Geochemistry and petrogenesis of the Tsirub nephelinite-basanite intrusions, Aus, southern Namibia.

Albertina Nakashole

Thesis submitted in fulfilment of the requirements for
the degree of Master of Science
University of Cape Town
August, 2007

Declaration

All the work presented in this thesis is my own, except otherwise where stated in the text.

A. N. Nakashole

TABLE OF CONTENTS

ACKNOWLEDGEMENTS

I would like to thank my supervisor, Anton le Roex, for his support and guidance during the course of my study. To my co-supervisor Dave Reid, thank you for your support with the geology of the area and other aspects of the study. I would like to extend my appreciation to my family for their love, support and encouragement and for believing in me. Financial support from the German Academic Service (DAAD) administered by The University Center for Studies in Namibia (TUCSIN) is highly appreciated. My supervisor is thanked for giving me a wonderful opportunity to participate in a research cruise, from Punta Arenas to Cape Town, aboard the German research vessel Polarstern. The geology team on this cruise sampled South Atlantic seamounts including the Discovery and Shona seamounts; I gained invaluable experience, thank you.

I am indebted to the following support staff in the Department of Geological Sciences at the University of Cape Town, Ernest Stout and Jonathan van Rooyen for preliminary sample preparations, David Wilson for thin-section preparations, Fayrooza Rawoort for sample preparation for ICP-MS analysis, Andreas Späth for assistance with ICP-MS and electron microprobe analyses, and Shireen Govender for Sr and Nd isotope analyses, thank you so much.

To my friends and colleagues Christel, Ndafunda, Ndapandula, Sigrid, Theresia, Zibizani thank you for the great time in Cape Town.

ABSTRACT

Nephelinite-basanite intrusions found on the Tsirub farm near Aus in southern Namibia are described for the first time. Their petrography is very similar to each other with texture ranging from porphyritic to microporphyritic where olivine is the dominant, and sometimes the only, phenocryst/microphenocryst phase, and less commonly clinopyroxene; the groundmass consist of clinopyroxene, olivine, Fe-Ti oxides and secondary generation amphibole. Rare felsic xenoliths comprising alkali feldspar (orthoclase) and clinopyroxene (diopside and aegirine-augite) occur in the two major intrusive bodies. Olivine phenocrysts/microphenocrysts are forsterite-rich (Fo_{74-92}), whereas the clinopyroxenes are diopsides ($Wo_{47-50}En_{37-43}Fs_{9-12}$). These rocks are all nepheline normative (e.g. SiO_2 = 38.7– 41.6 wt.%), relatively primitive (Mg# = 0.61 – 0.66), and can be classified as nephelinites and basanites; the Tsirub dyke shows the most primitive composition (Mg# = 0.71). CaO content is high (10.9 -12.9 wt.%), TiO_2 content is moderate to high (2.42 - 3.73 wt.%), whereas K_2O concentration is low (1.06 – 2.45 wt.%). On the basis of major (e.g. P_2O_5) and trace element variations the Tsirub North plug can be divided in an outer and inner intrusions (e.g. P_2O_5 = 1.03 – 1.27 wt.% for outer intrusion and 2.25 – 2.47 wt.% for inner intrusion).

Incompatible trace element contents are high with the Tsirub North (inner) plug showing the greatest abundances (e.g. Nb = 239- 267, Zr = 435 – 469 ppm), whereas the Tsirub North (outer) plug shows the least enrichment (e.g. Nb = 169 – 173, Zr = 395 - 449 ppm). La/Nb (0.34 – 0.61) and Zr/Nb ratios (1.73 – 2.37) are low whereas Ce/Pb ratio is high (e.g. 25.1 – 59.3), the latter suggesting insignificant amount of crustal contamination. Chondrite normalised REE patterns are steep (La/Yb_N ~ 32). Their primitive mantle normalised patterns are similar to each other consisting of strong Nb-Ta anomalies, moderate negative Pb anomaly and a striking strong negative K anomaly. Amphibole but not phlogopite is proposed to be the residual K-bearing phase responsible for the observed negative K anomaly. Initial Sr and Nd isotope ratios, calculated to an estimated age of 49 Ma, are similar (Tsirub dyke: $^{87}Sr/^{86}Sr_i$ = 0.70341 and $^{143}Nd/^{144}Nd_i$ = 0.51276, Tsirub North (outer) plug: $^{143}Nd/^{144}Nd_i$ = 0.51275 – 0.51278, Tsirub South plug: $^{87}Sr/^{86}Sr_i$ = 0.70342 – 0.70361 and $^{143}Nd/^{144}Nd_i$ = 0.51277 – 0.51278) and are restricted in ranges implying derivation from a common mantle source. An exception is the Tsirub North (inner) plug which has slightly lower initial $^{143}Nd/^{144}Nd$ ratios (0.512724 – 0.512732) suggesting a compositional distinct source. On the Nd-Sr correlation diagram, the

Tsirub intrusions plot in the depleted field suggesting a source with a long-term depletion in incompatible trace elements.

Fractional crystallization models do not support evolution of the entire Tsirub intrusions from a common magma on the basis of combined compatible and incompatible trace element variations. REE melting models indicate that the isotopically similar Tsirub intrusions may be related to each other by variable degrees of partial melting of a common amphibole-bearing spinel lherzolite (calculated assuming that the Tsirub dyke formed by 3% of partial melting). Quantitatively, these intrusions are formed by low degrees of partial melting, with the Tsirub North (outer) plug being formed by slightly higher degrees of partial melting (4-6%) relative to the Tsirub South plug (2-3%). The higher incompatible trace element contents of the compositionally distinct Tsirub North (inner) plug compared to the other Tsirub intrusions could indicate an origin by lower degrees of partial melting or derivation from a more enriched source.

The thermal stability field of amphibole, and the inferred presence of amphibole in the source, constrains the mantle source of the Tsirub intrusions to within the sub-continental lithospheric mantle (SCLM) rather than the convecting asthenosphere or a rising mantle plume. The contrasting isotope signature (requiring a source with long-term depletion in incompatible trace elements) and incompatible trace element signature (requiring an enriched source) could be explained by a recent metasomatic event. This event may be a result of fluids and/or small degree melts, released from a rising mantle plume, that infiltrated and metasomatised the SCLM and introduced amphibole. The ultimate cause of the melting that gave rise to the Tsirub rocks is unclear. The absence of an exact age for the Tsirub intrusions precludes direct comparison to the paleopositions of the Vema and Discovery plumes (the 49 Ma age of adjacent Dicker Willem carbonatite suggest a possible relationship to the Vema plume). Alternatively, the hydrous nature and subsequent thinning or uplift of the SCLM might have led to decompression melting of the metasomatised SCLM in the presence of amphibole and within the spinel stability field.

CHAPTER 1

INTRODUCTION

Continental alkaline rocks such as nephelinites, melilitites and basanites are relatively primitive mantle-derived rocks. These rock types are particularly abundant in extensional settings (e.g. Rhön area, Germany: Jung and Masberg, 1998; Jung and Hoernes, 2000) including the intensively studied East African Rift (e.g. Furman, 1995; Bedini *et al.*, 1997; Rogers *et al.*, 2000; le Roex *et al.*, 2001; MacDonald *et al.*, 2001; Keller *et al.*, 2006). In southern Africa, alkaline rocks have been reported from a number of isolated localities, including nephelinites (Spriggs, 1988) and phonolites (Lock and Marsh, 1981) from southern Namibia, basanite and tephrite plugs from Erongo area, northwest Namibia (Trumbull *et al.*, 2003) and melilitites from Namaqualand, South Africa (Rogers *et al.*, 1988 and 1992; Janney *et al.*, 2002).

The petrogenesis of continental alkaline rocks has received a lot of debate over the years (e.g. Rogers *et al.*, 1992; Wilson *et al.*, 1995; Franz *et al.*, 1999; MacDonald *et al.*, 2001; Janney *et al.*, 2002; Hoernle *et al.*, 2006; Jung *et al.*, 2006; Weinstein *et al.*, 2006) because these igneous rocks can provide valuable information in understanding the evolution and composition of, and process operating in, the Earth's upper mantle beneath continental areas. The primary concern of these studies has been to understand the location of mantle source regions of such rocks, whether they are generated within the sub-continental lithospheric mantle (SCLM), within the convecting asthenosphere, or whether they are products of direct melting of mantle plumes (e.g. White and McKenzie, 1989; Wilson and Downes, 1991; Cebriá and López-Ruiz, 1995; Panter *et al.*, 2000; Weinstein, 2000; Späth *et al.*, 2001; Shaw *et al.*, 2003). Most continental rocks generated during continental rifting and subsequent break up have been argued to have originated dominantly by decompression melting of ascending asthenosphere or actively upwelling mantle plumes with no or limited input from the SCLM (e.g. McKenzie and Bickle, 1988; White and McKenzie, 1989; Latin *et al.*, 1993). For example, Trumbull *et al.* (2003) have reported that Erongo basanite-tephrite plugs from northwest Namibia formed by decompression melting of the Tristan mantle plume. These authors argued that the initial magmas, Etendeka tholeiites, generated in the Erongo area are derived from partial melting within the lithosphere but with time extensive thinning of the lithosphere allowed decompression melting of the underlying Tristan mantle plume, giving rise to the Erongo basanite-tephrite plugs. Trumbull *et al.* (2003) based their argument for a

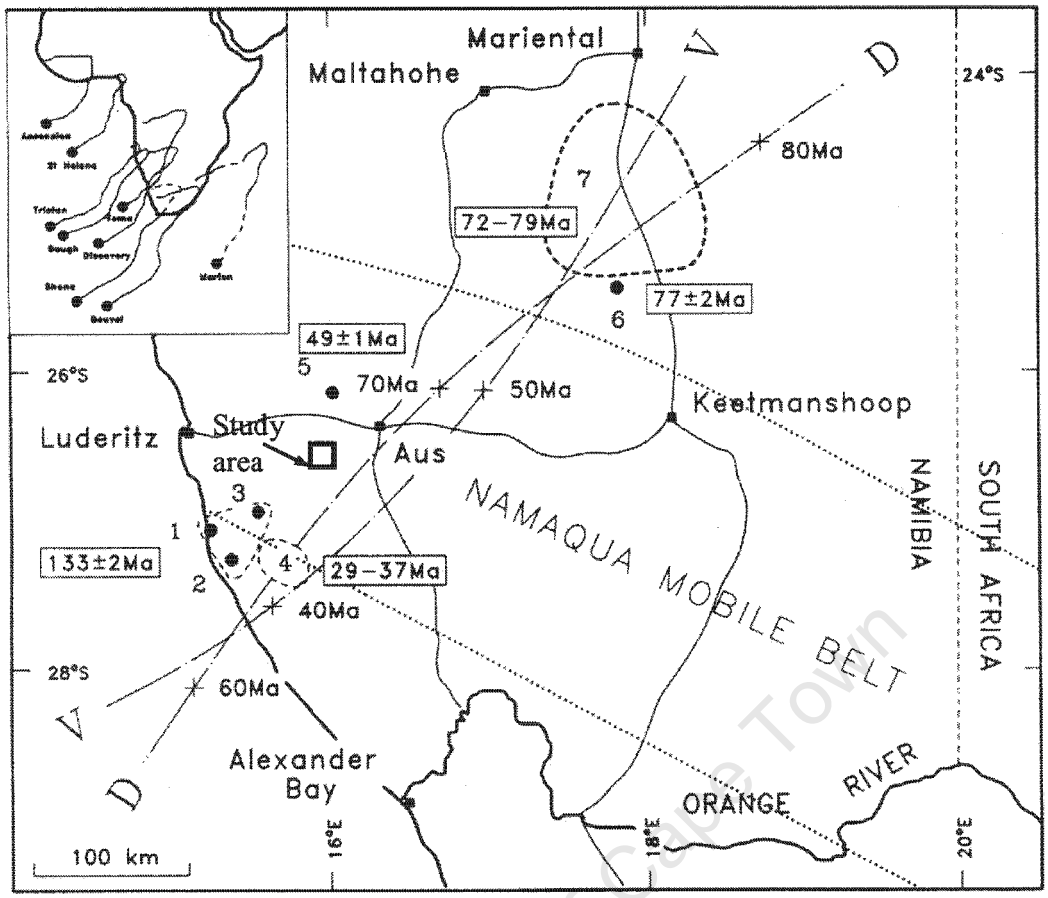

Fig. 2.1. Location of Tsirub intrusions in the Aus area (see appendix A for coordinates of individual samples), this study, and other alkaline, and related, igneous complexes from southern Namibia. Numbers outside the rectangles correspond to the complexes, 1 = Pomona, 2 = Granitiberg, 3 = Drachenfels 4 = Klinghardt phonolite field, 5 = Dicker Willem carbonatite, 6 = Gross Brukkaros, 7 = Gibeon kimberlite-carbonatite field. Numbers inside the rectangles corresponds to the age of the respective complexes. The discontinuous curves labelled V and D represent paleopositions of the Vema and Discovery plumes, respectively, in l0 Ma intervals (after Hartnady and le Roex, 1985; le Roex, 1986). The insert shows the tracks of South Atlantic plumes. The map is adapted from Reid *et al.* (1990).

2.2 Local geology

The first mention of post-Namaqua alkaline intrusives in the Aus region was by Jackson (1976) who described small plugs and narrow discontinuous dykes distributed south and west of Dicker Willem, including Tsirub (Fig. 2.2) and the neighbouring Diamond Area (Sperrgebiet). The country rocks in the study area, Tsirub farm, include biotite schist, biotite gneiss, Kubub granite gneiss, metaquartzite and Tsirub gneiss (Jackson, 1976). The biotite schists are generally grey and petrographically comprise feldspar, quartz and biotite. These schists occur associated with biotite gneisses in the northern part of Tsirub farm. The biotite gneisses are layered gneisses and are common in the northern part of the Tsirub farm. Kubub granite gneisses occur mostly in the

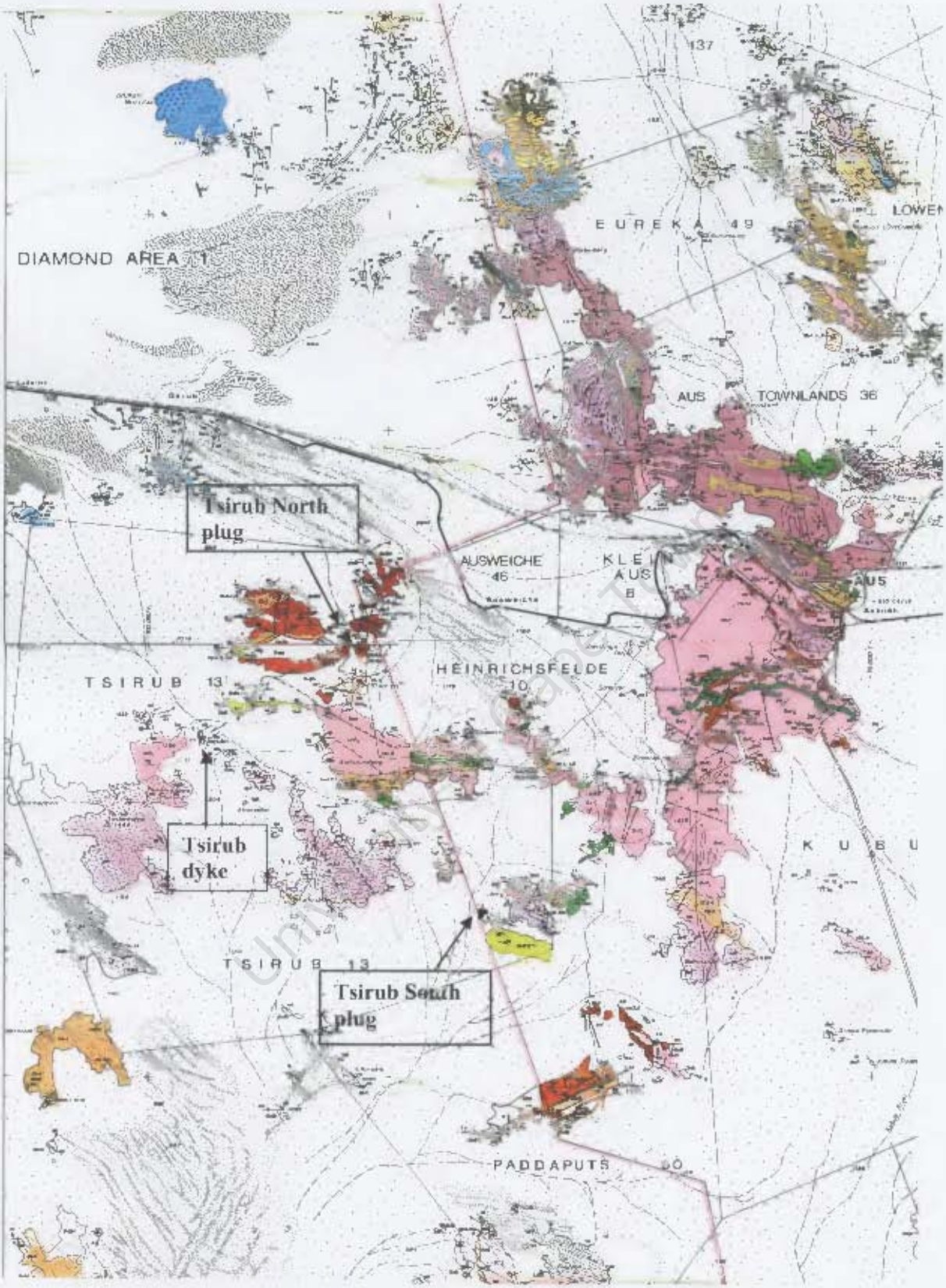

Fig. 2.2. Location of the Tsirub plugs (black) and dyke. Also shown on the map is the spatially associated Dicker Willem carbonatite (top left). All the other rocks represent metamorphic country rocks of the Namaqualand metamorphic complex. Scale is 1: 100 000. The map is after Jackson (1976).

Fig. 2.3. Tsirub North plug intruding a granitic country rock, looking west.

central part of the Aus area. Within the Tsirub farm, metaquartzites occur southeast of Tsirub South plug and northeast of Tsirub dyke. The Tsirub gneisses are common in the central part of the farm

The Tsirub intrusions lie on a roughly NNE-SSW lineament that could be projected towards Dicker Willem. No independent radiometric ages have been determined for these minor intrusives and so their temporal relationship with any of the recognised alkaline igneous events, mentioned previously, has yet to be established. The possible relationship between the Tsirub intrusions and the ijolitic members of Dicker Willem carbonatite will be discussed in this study. Field pictures of the Tsirub North and South plugs are shown in Figs. 2.3 to 2.5.

Fig. 2.4. Tsiruh South plug (arrow), looking northwest.

Fig. 2.5. The fine grained rocks of the Tsiruh South plug.

CHAPTER 3

PETROGRAPHY AND MINERAL CHEMISTRY

3.1 Introduction

Continental alkaline volcanic rocks such as basanite and nephelinite are usually classified by their bulk chemistry in the absence of coarse, easily recognizable minerals (e.g. Le Maitre, 2002). Phenocryst phases are dominated by olivine and clinopyroxene, but the dominant groundmass tends to be microcrystalline and therefore optically indeterminable.

Intrusions studied include a dyke (Tsirub dyke) cropping out next to the Tsirub farmhouse and two plugs, Tsirub North plug (intruding a granitic country rock) and Tsirub South plug, that occur in the NE corner and southern boundary of the Tsirub farm, respectively. The Tsirub North plug is further subdivided, on the basis of geochemistry as documented in Chapter 4, into an outer zone (Tsirub North (outer) plug) and an inner zone (Tsirub North (inner) plug) (Fig. 3.1). Two samples, AN-016 and AN-019, from the Tsirub North plug show geochemistry that is distinct from both the Tsirub North (outer) plug and Tsirub North (inner) plug, as discussed in the next chapter, and for this reason these two samples are treated separately. All the individual samples were examined for their petrography (presented in Appendix A) and a summary of the petrography of each intrusion is presented below. Selected minerals were analysed for their major element compositions. The petrography together with mineral chemistry will then be used to infer the conditions of fractional crystallization as to what minerals dominated the fractional crystallization process during the petrogenesis of these magmas.

3.2 Petrography

In the field, the Tsirub intrusions all display very dark outcrops with weathering surfaces (see Appendix A for co-ordinates of individual sampling sites). Rock surfaces are relatively smooth and reflect the aphanitic nature, except where occasional felsic xenoliths made up of feldspar and light and dark green clinopyroxene stud the relief. Freshly broken rock surfaces are sub-conchoidal and colours range from bluish to greenish dark gray (see Fig. 2.5). The xenoliths tend to be paler coloured because of their coarser and more feldspathic nature.

Fig. 3.1. Tsirub North plug intruding granitic country rock. The dashed outlines represent the outer and inner zones.

All samples had normal thin sections prepared, with the following systematic description based on microscopy. Sample numbers of rocks are given in square brackets. Photomicrographs of individual samples are presented in Appendix A and representative petrographic features are shown in Figs. 3.2 to 3.12.

3.2.1 Tsirub dyke

[AN-001]

The Tsirub dyke is sparsely porphyritic to microporphyritic with olivine and rare clinopyroxene phenocrysts/microphenocrysts set in a very fine-grained groundmass of clinopyroxene, olivine, minor Fe-Ti oxides and scattered secondary pleochroic brown amphibole. Amphibole does not appear to replace either olivine or clinopyroxene and is interpreted to have formed as result of reaction between Tsirub rocks and deutoric fluids. Anhedral to rarely subhedral or euhedral olivine phenocrysts (~10 vol.%, by visual estimation) dominate over clinopyroxene microphenocrysts (< 2 vol.%), and vary in length between 0.5 and 2.0 mm (Fig. 3.2a). Rare clinopyroxene microphenocrysts measure 0.5 - 1.5 mm in size and some show zoning.

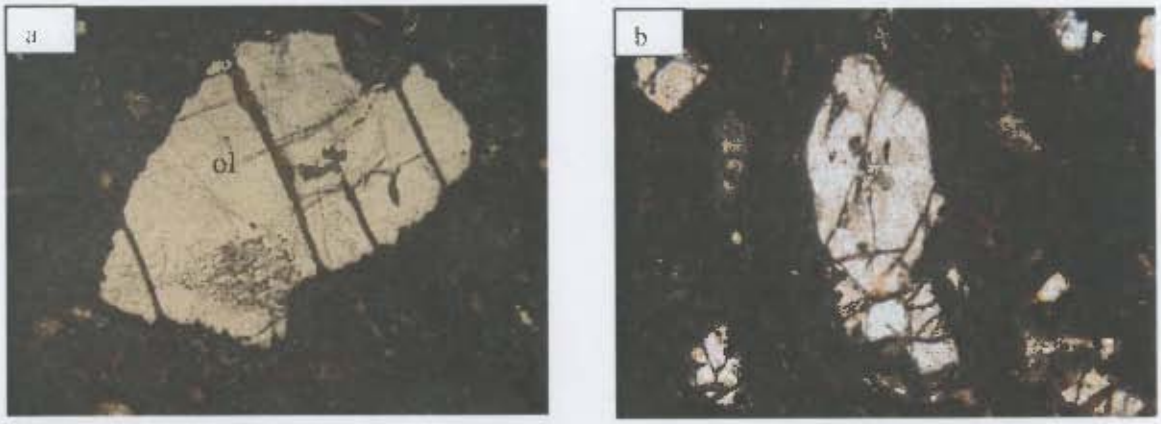

Fig. 3.2. (a) ***AN-001:*** Anhedral olivine (ol) phenocryst with alteration rims and cracks. Field of view is 2.5 mm across. Under plane polarised light. (b) ***AN-004:*** Euhedral olivine phenocryst (centre) in a fine grained groundmass of olivine, clinopyroxene and opaque Fe-Ti oxides. Field of view is 1 mm across; under plane polarised light.

3.2.2 Tsirub North (outer) plug

[AN-003, AN-004, AN-005, AN-006, AN-012, AN-014 and AN-015]

The Tsirub North (outer) plug is microporphyritic to rarely porphyritic in texture. Olivine is the dominant, and sometimes the only, microphenocryst phase (2 - 5 vol.%) measuring 0.3 - 1.4 mm in size. In terms of crystal habits, the majority of olivine microphenocrysts are anhedral, few are subhedral and rarely euhedral (Fig. 3.2b). Olivine microphenocrysts are commonly rimmed by, or completely altered to, serpentine (Fig. 3.3) and a few display compositional zoning with darker rims than cores (under crossed polars).

Clinopyroxene occurs in lesser proportions in the phenocryst assemblage (< 1 - 2.5 vol.%), but is more abundant in the groundmass. Clinopyroxene microphenocrysts are normally cream to light brown, elongate (with typical length of ~1mm) and anhedral (Fig. 3.3), but rare subhedral and euhedral crystals were also observed (Fig. 3.4a). These are relatively low in volume (< 3 vol.%). Normal compositional zoning occurs in some euhedral phenocrysts (Fig. 3.4a) with the exception of few anhedral or subhedral crystals which display sector zoning. Clinopyroxene microphenocrysts often occur in radiating clusters (Fig. 3.4b). The fine grained groundmass is made up of (in order of increasing abundance) clinopyroxene, Fe-Ti oxides, olivine and secondary generation brown secondary amphibole. A single sample (AN-012) contains vesicles constituting < 0.5% by volume.

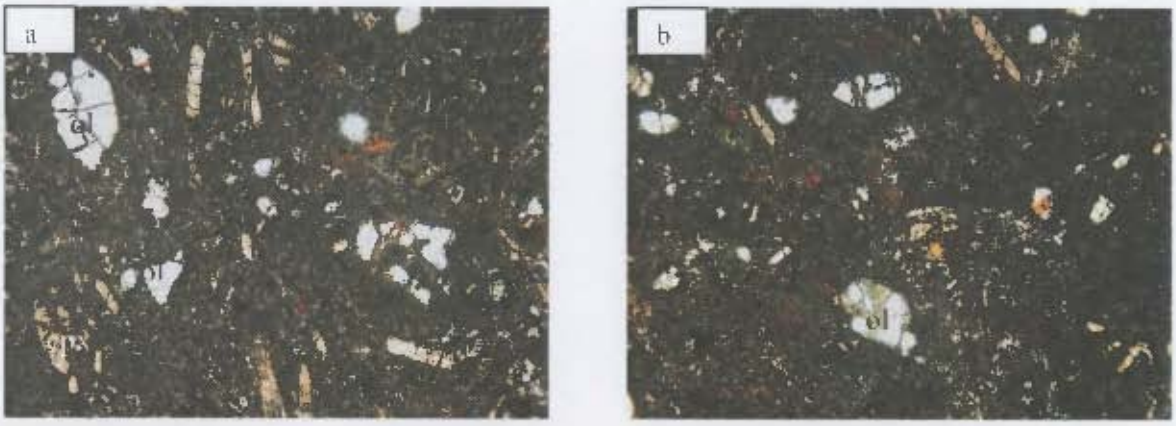

Fig. 3.3. (a) ***AN-013:*** Olivine (ol) and clinopyroxene (cpx) microphenocrysts embedded in a fine grained groundmass of clinopyroxene, opaque Fe-Ti oxides, olivine, and secondary amphibole. Note the euhedral olivine microphenocryst (top left). Field of view is 1.5 mm across; plane-polarised light. (b) ***AN-013:*** Serpentine rims and cracks on subhedral olivine microphenocrysts. Field of view is 1.8 mm across; under plane-polarised light.

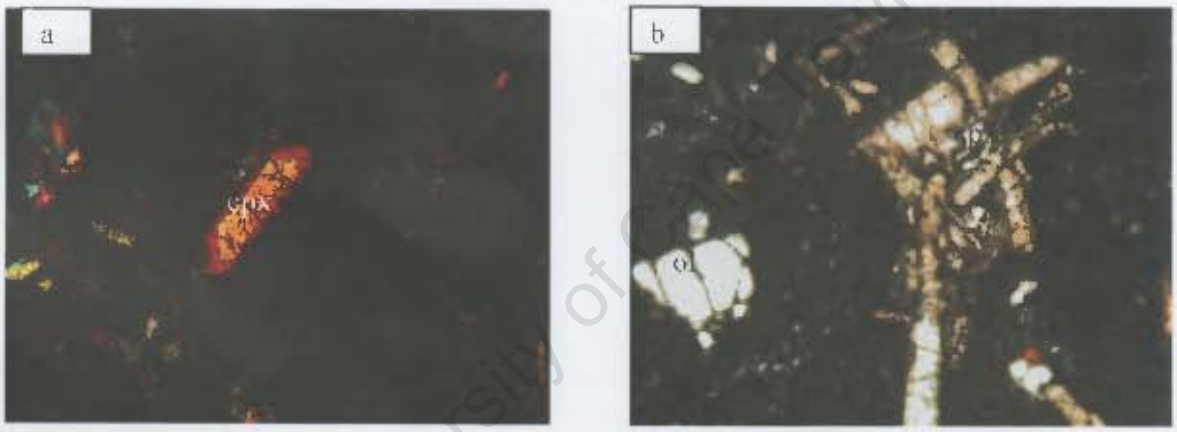

Fig. 3.4. (a) ***AN-003:*** Euhedral clinopyroxene microphenocryst showing compositional zoning. Field of view is 0.8 mm across; crossed polars. (b) ***AN-003:*** Clusters of radiating anhedral elongate clinopyroxene microphenocrysts. Field of view is 1.4 m across; under plane-polarised light.

Felsic xenoliths (< 2 vol.%) consisting of alkali feldspar and light and dark green clinopyroxene occur in this plug. Internal zonation is marked with light and dark green clinopyroxenes confined to the margins, with their prismatic habits aligned towards the feldspar filling the centre.

3.2.3 Tsirub North (inner) plug

[AN-007, AN-007A, AN-008, AN-009, AN-010, AN-011, AN-017 and AN-018]

The petrography of the inner zone of Tsirub North plug is characterised by a microporphyritic to rarely porphyritic texture with olivine being the dominant, and sometimes the only, microphenocryst phase. The majority of olivine microphenocrysts (0.3 - 1.5 mm in size and 1 - 3

vol.%) are anhedral and few are subhedral or euhedral (Fig. 3.5). A few olivine microphenocrysts show petrographic evidence of zoning with darker rims than cores (Fig. 3.5b), whereas a few are partially or completely replaced by serpentine. Clinopyroxene microphenocrysts (0.3 - 2.0 mm in size and < 1 vol.%) are rare, with a few displaying sector zoning (Fig. 3.6a). Together with clinopyroxene, Fe-Ti oxides, olivine and secondary brown amphibole (Fig. 3.6b) make up the fine grained groundmass.

A single spinel-bearing ultramafic xenolith comprising abundant olivine, subordinate clinopyroxene and minor spinel occurs in sample AN-017 (Fig. 3.7). Felsic xenoliths, similar to the ones observed in the Tsirub North (outer) plug, but higher in abundance (~ 4 vol.%) occur in this plug and are composed of feldspar and light and dark green clinopyroxenes. The constituent feldspar crystals show simple twinning. Clinopyroxene crystals are mostly confined to the margins and few are poikilitically enclosed within the larger feldspars (Figs. 3.8 and 3.9).

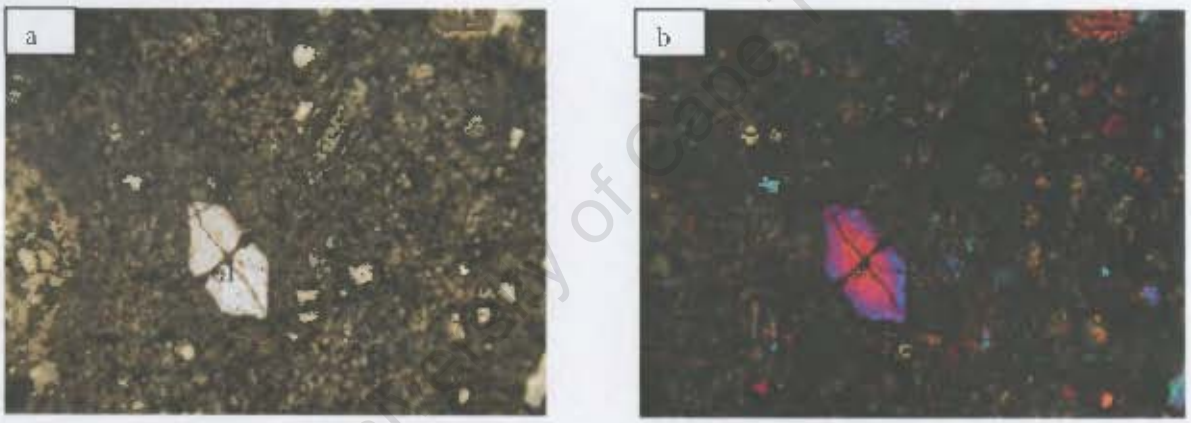

Fig. 3.5. (a) ***AN-018:*** Euhedral olivine microphenocryst showing compositional zoning. Field of view is 2 mm across. (b) Under crossed polars.

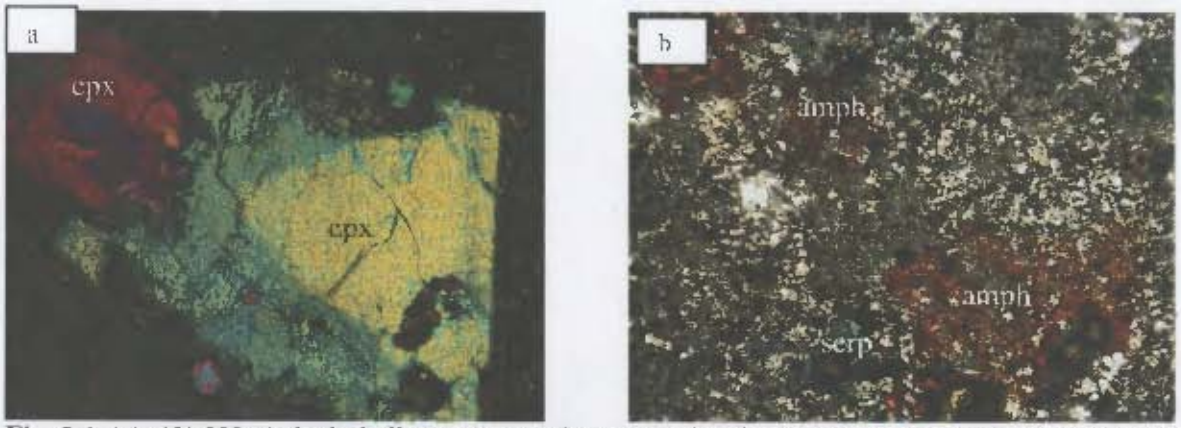

Fig. 3.6. (a) ***AN-008:*** Anhedral clinopyroxene phenocryst showing sector zoning. Field of view is 2.5 mm across; under crossed polars. (a) ***AN-011:*** Secondary brown amphibole (amph), serpentine (serp) and opaque Fe-Ti oxides that form part of the groundmass suite. Field of view is 2.5 mm across; plane polarised light.

vol.%) are anhedral and few are subhedral or euhedral (Fig. 3.5). A few olivine microphenocrysts show petrographic evidence of zoning with darker rims than cores (Fig. 3.5b), whereas a few are partially or completely replaced by serpentine. Clinopyroxene microphenocrysts (0.3 - 2.0 mm in size and < 1 vol.%) are rare, with a few displaying sector zoning (Fig. 3.6a). Together with clinopyroxene, Fe-Ti oxides, olivine and secondary brown amphibole (Fig. 3.6b) make up the fine grained groundmass.

A single spinel-bearing ultramafic xenolith comprising abundant olivine, subordinate clinopyroxene and minor spinel occurs in sample AN-017 (Fig. 3.7). Felsic xenoliths, similar to the ones observed in the Tsirub North (outer) plug, but higher in abundance (~ 4 vol.%) occur in this plug and are composed of feldspar and light and dark green clinopyroxenes. The constituent feldspar crystals show simple twinning. Clinopyroxene crystals are mostly confined to the margins and few are poikilitically enclosed within the larger feldspars (Figs. 3.8 and 3.9).

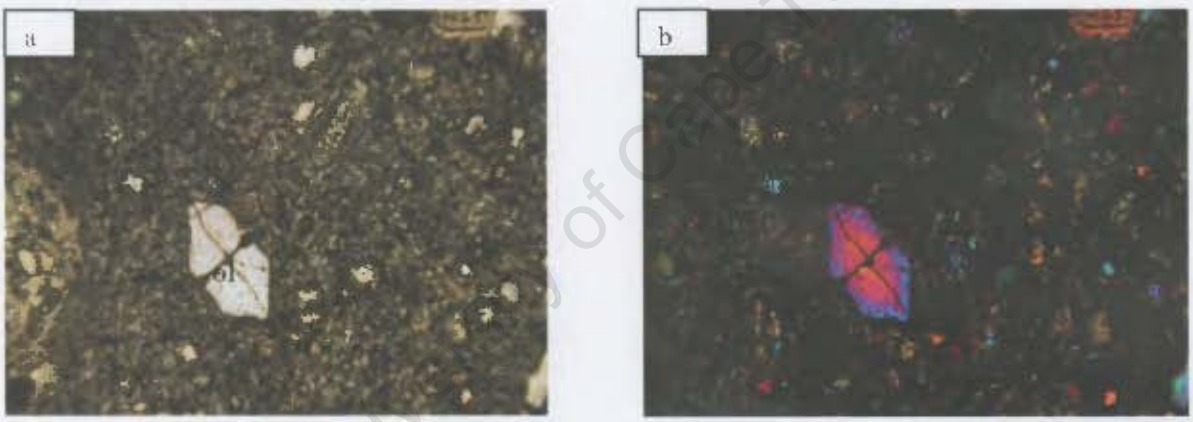

Fig. 3.5. (a) ***AN-018:*** Euhedral olivine microphenocryst showing compositional zoning. Field of view is 2 mm across. (b) Under crossed polars.

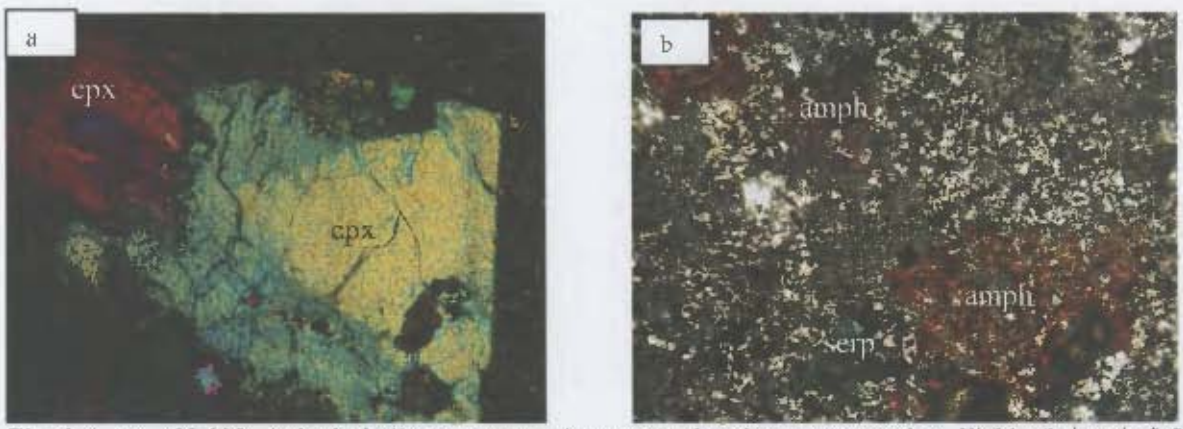

Fig. 3.6. (a) ***AN-008:*** Anhedral clinopyroxene phenocryst showing sector zoning. Field of view is 2.5 mm across; under crossed polars. (a) ***AN-011:*** Secondary brown amphibole (amph), serpentine (serp) and opaque Fe-Ti oxides that form part of the groundmass suite. Field of view is 2.5 mm across; plane polarised light.

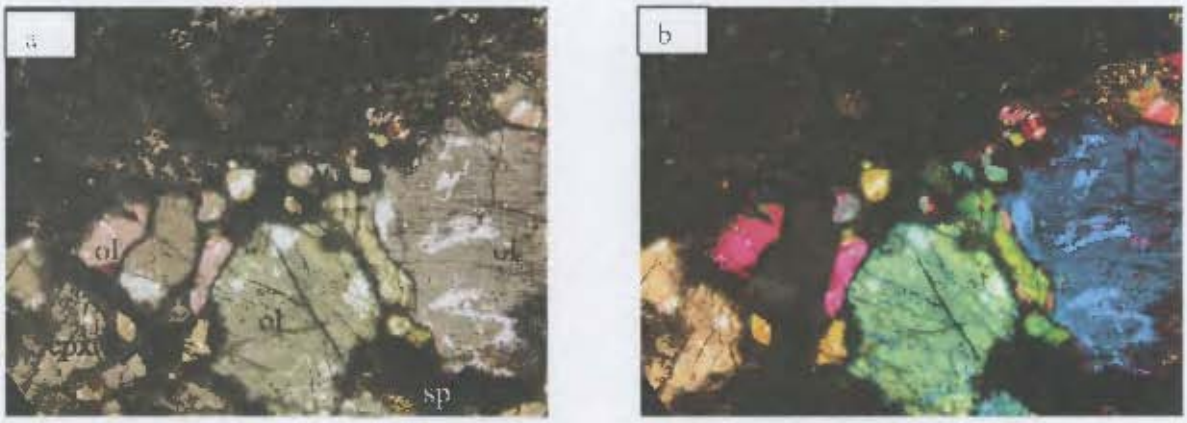

Fig. 3.7. (a) ***AN-017:*** Ultramafic xenolith comprising olivine (ol), clinopyroxene (cpx) and minor spinel (sp) from the Tsirub North (inner) plug. Note that the opaque spinel crystals fill the spaces between olivine and clinopyroxene crystals. Field of view is 3.0 mm across. (b) Under crossed polars.

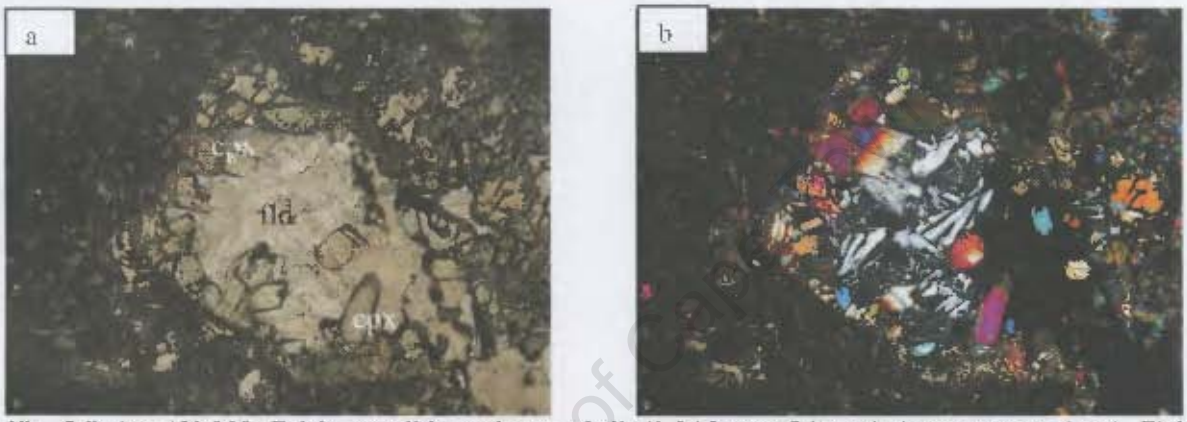

Fig. 3.8. (a) ***AN-018:*** Felsic xenolith made up of alkali feldspar (fld) and clinopyroxene (cpx). Field of view is 2.2 mm across. (b) Under crossed polars.

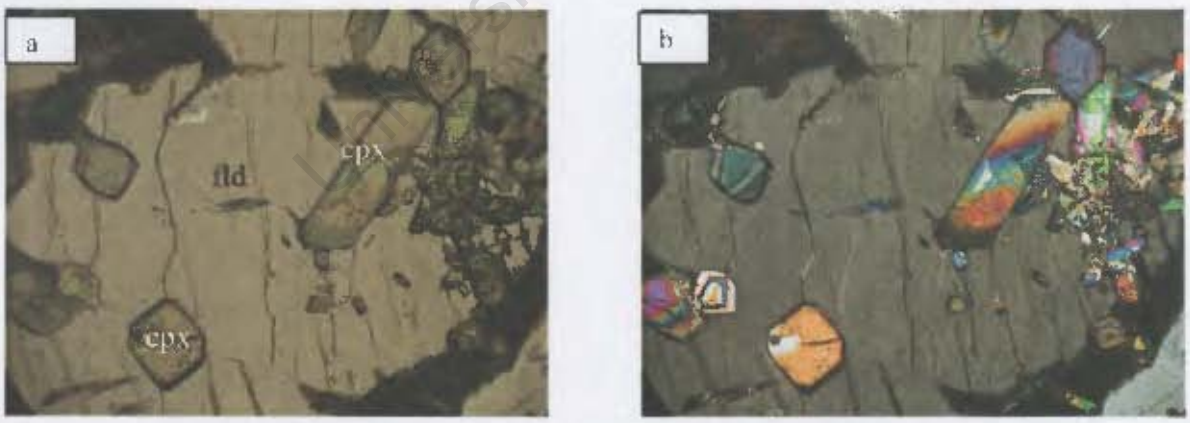

Fig. 3.9. (a) ***AN-007A:*** Clinopyroxene crystals poikilitically enclosed within a larger alkali feldspar. Field of view is 2.0 mm across (b) Under crossed polars.

In addition to showing similar petrography with the Tsirub North (inner) plug, samples AN-016 and AN-019 from the Tsirub North plug also consists of few euhedral olivine microphenocrysts (Fig. 3.10).

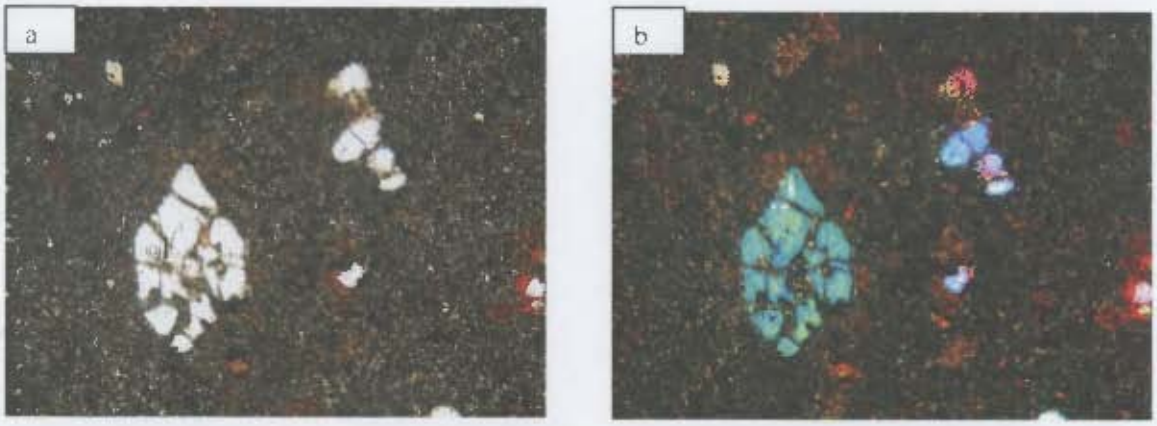

Fig. 3.10. (a) ***AN-016:*** Euhedral olivine microphenocryst (bottom left) set in a fine grained groundmass. Note the intensity of alteration on olivine. Field of view is 2.0 mm across. (b) Under crossed polars.

3.2.4 Tsirub South plug

[AN-021, AN-022, AN-023 and AN-024]

The Tsirub South plug is microporphyritic consisting of olivine and rare clinopyroxene microphenocrysts set in a fine grained groundmass. Olivine microphenocrysts, 0.3 – 1.1 mm in diameter, constitute less than 1 vol.% of the rock, are mostly anhedral but a few are subhedral in habit (Fig. 3.11) and zoned. Like in the samples from the Tsirub North plug, some olivine microphenocrysts are rimmed, or completely replaced, by serpentine while groundmass olivines are usually completely pseudomorphosed.

Clinopyroxene (< 0.5 vol.% and < 1mm in length) is less abundant in the microphenocryst assemblage but is more pronounced in the groundmass. The majority of the microphenocrysts are anhedral and elongate in shape (Fig. 3.12a), but few exhibit subhedral crystal habits. A few clinopyroxene microphenocrysts display normal compositional zoning with darker rims than cores. Clinopyroxene, opaque Fe-Ti oxides, olivine and secondary brown amphibole (Fig. 3.12b) make up the groundmass. Minor felsic xenoliths similar to those of the Tsirub North plug, but smaller in size, occur in a few samples.

In summary, the Tsirub intrusions are very similar in their petrography. The small difference between these intrusions is the higher abundance of felsic xenoliths in the Tsirub North (inner) plug and their absence in the Tsirub dyke. Another feature that distinguishes the Tsirub North (inner) plug from the other Tsirub intrusions is the occurrence of a single ultramafic xenolith in sample AN-017.

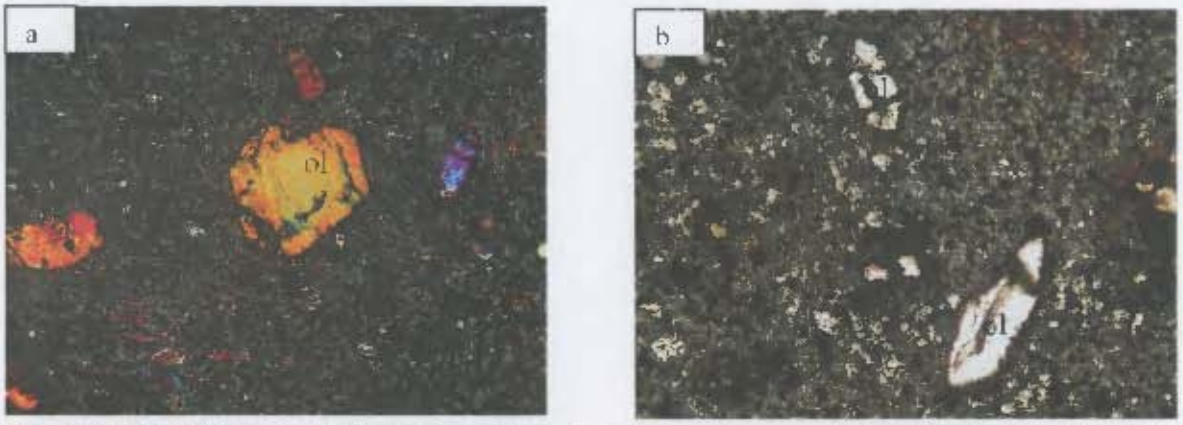

Fig. 3.11. (a) ***AN-021:*** Subhedral and anhedral olivine microphenocrysts in a fine grained groundmass of clinopyroxene, olivine and opaque Fe-Ti oxides. Field of view is 1.8 mm across; crossed polars. (b) ***AN-023:*** Moderately altered subhedral olivine microphenocrysts. Field of view is 1.0 mm across, plane polarised light.

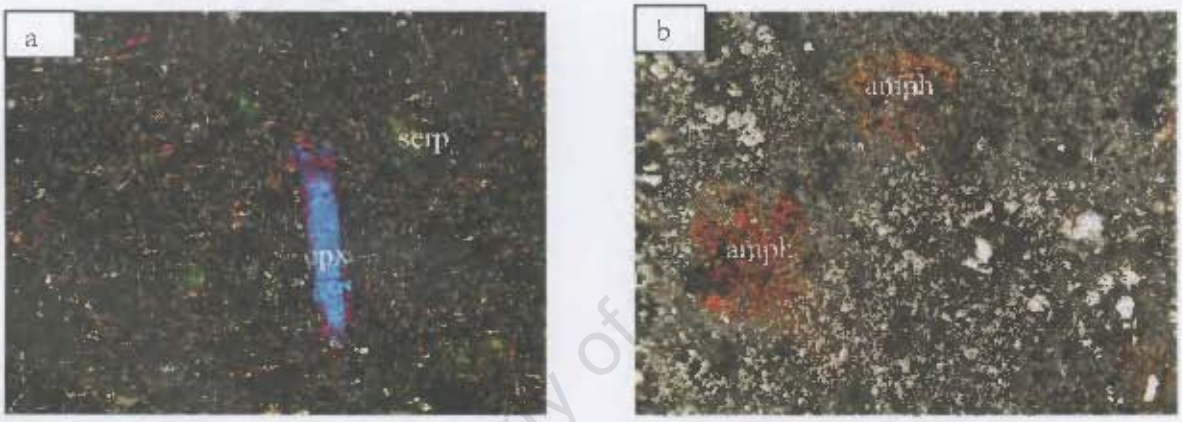

Fig. 3.12. (a) ***AN-021:*** Anhedral, elongate clinopyroxene microphenocryst and serpentine (serp). Field of view is 1.4 mm across. Picture taken under crossed polars. (b) ***AN-023:*** Brown secondary amphibole and opaque Fe-Ti oxides form part of the matrix assemblage, under plane-polarised light. Field of view is 2 mm across.

3.3 Mineral Chemistry

Electron microprobe analyses were conducted on selected primary mineral phases from selected samples (Tsirub dyke: AN-001; Tsirub North (inner) plug: AN-003, AN-005, AN-013 and AN-015; Tsirub North (inner) plug: AN-007, AN-007A, AN-008 and AN-017; Tsirub South plug: AN-021). Operating conditions for the electron microprobe are reported in Appendix B, section B.1. Individual analyses are reported in Appendix C, Tables C.2 and C.3, and representative analyses are given in Tables 3.1 to 3.5. Major element compositions of Fe-Ti oxides, ultramafic xenolith phases (olivine, clinopyroxene and spinel) and felsic xenolith phases (feldspar and clinopyroxene) were also analysed.

3.3.1 Olivine

Olivine analyses are reported in Table 3.1 and end-members are illustrated in Fig. 3.13.

The Tsirub dyke shows relatively primitive phenocryst olivine compositions (Fo_{89-90}) compared to the Tsirub North plug and Tsirub South plug, and has slightly more Mg-rich groundmass olivines (Fo_{81-91}) (Table 3.1; Fig. 3.13a). NiO concentrations are high (e.g. NiO = 0.34 – 0.40 wt.%) in both phenocryst and groundmass olivines. CaO concentration of olivine phenocryst cores (0.09 - 0.11 wt.%) are low and are similar to that of the groundmass olivines (Table 3.1). Following Roeder and Emslie (1970), the partition coefficient for Fe-Mg exchange between olivine and melt defined as K_D^{Fe-Mg} is 0.30 ± 0.03. This is illustrated in Fig. 3.14 where the most magnesium-rich olivine phenocrysts or microphenocrysts cores from each sample are plotted. Olivine phenocryst cores from the Tsirub dyke have equilibrium compositions (Fig. 3.14).

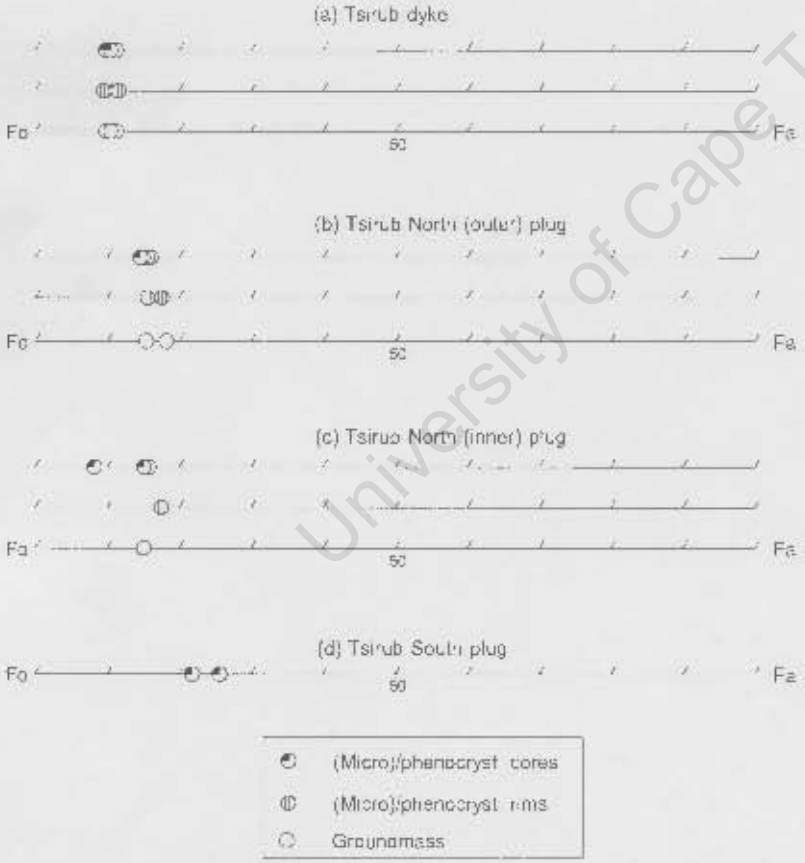

Fig. 3.13. Composition of olivine phenocryst/microphenocryst and groundmass olivine from selected Tsirub samples.

Table 3.1. Representative olivine analyses (in wt.%) from selected Tsirub samples. Abbreviations: p = phenocryst or microphenocryst, gm = groundmass, Fo = forsterite and Fs = fayalite, "-" = not detected. Total Fe reported as FeO*

	Tsirub dyke								Tsirub North (outer) plug								
	AN-001								AN-003			AN-005			AN-013		
	p (core)	p (rim)	p (core)	p (rim)	p	gm	gm	gm	p	p	gm	p (core)	p (rim)	gm	p (core)	p (rim)	gm
SiO_2	42.08	42.15	41.99	41.73	41.74	41.54	42.12	41.65	41.57	41.56	41.34	41.18	40.75	41.31	41.51	41.43	41.53
TiO_2	-	0.01	0.03	0.00	0.01	0.01	0.01	0.00	0.07	0.04	0.04	0.03	0.05	0.03	0.04	0.05	0.04
Al_2O_3	0.02	0.03	0.02	0.04	0.03	0.02	0.02	0.07	0.01	0.03	0.03	0.05	0.04	0.03	0.05	0.06	0.01
Cr_2O_3	0.03	0.03	0.01	0.03	0.02	0.01	0.02	0.02	0.03	0.02	0.04	0.03	0.03	0.02	0.04	0.04	0.04
FeO	9.19	8.92	10.60	10.78	9.78	11.34	8.86	9.25	14.64	14.37	14.11	13.81	16.16	16.53	13.52	14.32	14.20
MnO	0.13	0.13	0.13	0.14	0.11	0.15	0.13	0.13	0.24	0.27	0.25	0.21	0.33	0.32	0.23	0.24	0.23
MgO	47.66	47.87	47.07	46.50	47.35	46.37	47.54	47.57	43.22	43.45	43.48	43.93	42.44	41.55	44.40	43.52	43.70
CaO	0.10	0.10	0.09	0.09	0.11	0.11	0.10	0.11	0.40	0.39	0.35	0.28	0.35	0.36	0.29	0.32	0.37
NiO	0.39	0.37	0.35	0.35	0.39	0.34	0.40	0.38	0.15	0.17	0.15	0.17	0.15	0.14	0.18	0.15	0.14
Total	99.59	99.60	100.28	99.67	99.55	99.89	99.20	99.18	100.32	100.29	99.81	99.68	100.31	100.29	100.26	100.13	100.26
Fo	90.3	90.5	88.8	88.5	89.6	88.0	90.5	90.2	84.0	84.4	84.6	85.0	82.4	81.7	85.4	84.4	84.6
Fa	9.8	9.5	11.2	11.5	10.4	12.1	9.5	9.8	16.0	15.6	15.4	15.0	17.6	18.2	14.6	15.6	15.4

Table 3.1. Continued.

	Tsirub North (inner) plug					Tsirub South plug		
	AN-007			AN-017		AN-021		
	p (core)	p (rim)	gm	p	p	p	p	p
SiO_2	41.40	41.65	41.49	41.55	42.17	40.03	39.85	40.40
TiO_2	0.03	0.03	0.03	0.03	0.01	0.02	0.04	0.01
Al_2O_3	0.03	0.02	0.04	0.02	0.01	0.04	0.02	0.02
Cr_2O_3	0.03	0.03	0.05	0.01	0.02	-	0.01	0.02
FeO	14.54	15.96	13.89	13.92	7.79	22.80	22.96	20.03
MnO	0.22	0.30	0.26	0.20	0.11	0.74	0.78	0.54
MgO	43.48	42.10	43.78	44.01	48.72	36.91	37.46	40.35
CaO	0.28	0.38	0.31	0.23	0.05	0.48	0.44	0.33
NiO	0.14	0.11	0.17	0.24	0.36	0.08	0.07	0.09
Total	100.15	100.58	100.00	100.22	99.24	101.10	101.61	101.79
Fo	84.2	82.5	84.9	84.9	91.8	74.3	74.4	78.2
Fa	15.8	17.5	15.1	15.1	8.2	25.7	25.6	21.8

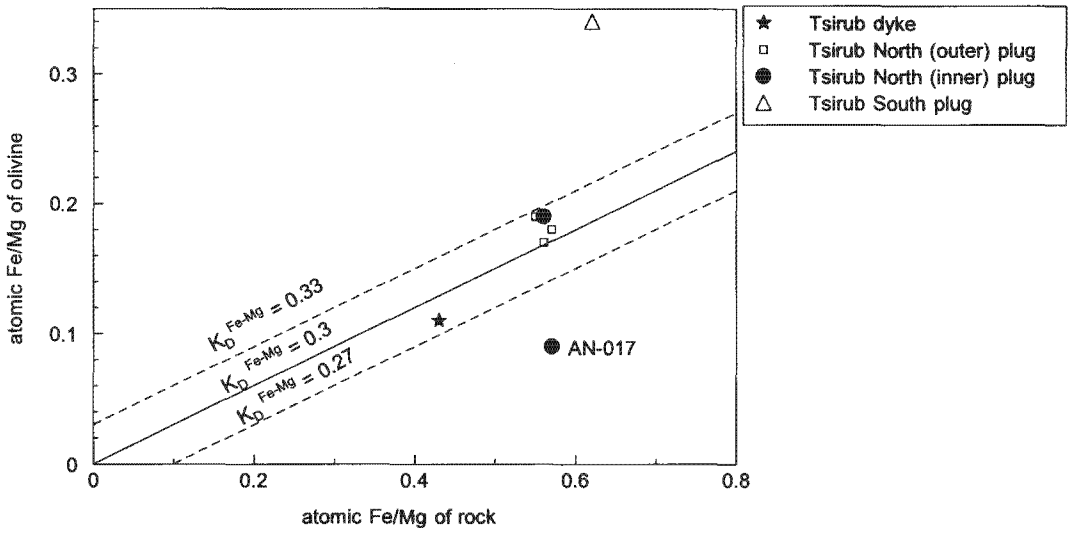

Fig. 3.14. Variation of atomic Fe/Mg ratio of olivine phenocryst/microphenocryst cores with atomic Fe/Mg ratio of their respective host rocks. Note that only the most magnesium-rich cores from each analysed sample are shown as representative of the liquidus olivine. The solid and broken lines represent the compositions of equilibrium liquidus olivine (Roeder and Emslie, 1970).

At Tsirub North, the analysed olivine microphenocrysts from the outer plug show similar forsterite contents (Fo_{84-85}) to that of their respective groundmass olivines (Fo_{82-84}). The inner plug, however, has olivine microphenocrysts extending to slightly higher Fo content (Fo_{85-92}) content than their respective groundmass olivines (Fo_{85}) (Table 3.1). Despite the optical zoning observed in thin sections, fosterite content does not vary significantly between the microphenocryst cores and rims in either the outer plug or the inner plug (e.g. outer plug: core = Fo_{85} and rim = Fo_{84}; inner plug: core = Fo_{84} and rim = Fo_{83}) (Figs. 3.13b and c). NiO content of olivine microphenocryst cores from the outer plug (NiO = 0.15 - 0.18 wt.%) is similar to those from the inner plug (NiO = 0.14 - 0.24 wt.%). CaO concentration for olivine microphenocrysts (0.29 – 0.40 wt.%) from the outer plug overlap with their respective groundmass olivine but the latter extend to slightly low CaO contents (0.35 – 0.37 wt.%); the same is true for those from the inner plug in microphenocryst (CaO = 0.23 – 0.28 wt.%) and groundmass olivine (CaO = 0.31 wt.%). Some of the analysed olivine microphenocrysts from the outer plug have compositions in equilibrium with their host rocks ($K_D^{Fe, Mg} = 0.30 – 33$) whereas one olivine microphenocryst from the inner plug is out of equilibrium ($K_D^{Fe, Mg} = 0.16$) (Fig. 3.14).

Only microphenocryst cores were analyzed in the Tsirub South plug because the groundmass olivines are heavily altered to serpentine (Appendix A, Fig. A.13a). Olivine microphenocrysts range in composition from Fo_{74} to Fo_{78}. In comparison to the Tsirub North plug, those from Tsirub South plug are less Mg-rich (Table 3.1; Fig. 3.13d), have lower NiO content (0.07 – 0.09

wt.%) and slightly higher CaO concentrations (0.33 – 0.48 wt.%). Olivine microphenocryst has composition out of equilibrium (Fig. 3.14).

3.3.2 Clinopyroxene

Clinopyroxene compositions are reported in Table 3.2 and are classified, based on Morimoto (1988), in Figs. 3.15 to 3.18.

The Tsirub dyke has unzoned clinopyroxene phenocrysts with CaO-rich core compositions of $Wo_{49-50}En_{38-41}Fs_{9-12}$ and rim compositions of $Wo_{49}En_{41-42}Fs_{9}$ (Table 3.2; Fig. 3.15). TiO_2 concentrations are high (TiO_2 – 2.27 – 2.77 wt.%) a feature common in clinopyroxenes of silica undersaturated alkaline rocks (Aoki and Kushiro, 1968). Al_2O_3 contents vary between 4.24 and 7.38 wt.%. Na_2O content is moderate (Na_2O = 0.36 – 0.67 wt.%). Following Morimoto (1988) classification, the clinopyroxenes are diopsides (Fig. 3.15).

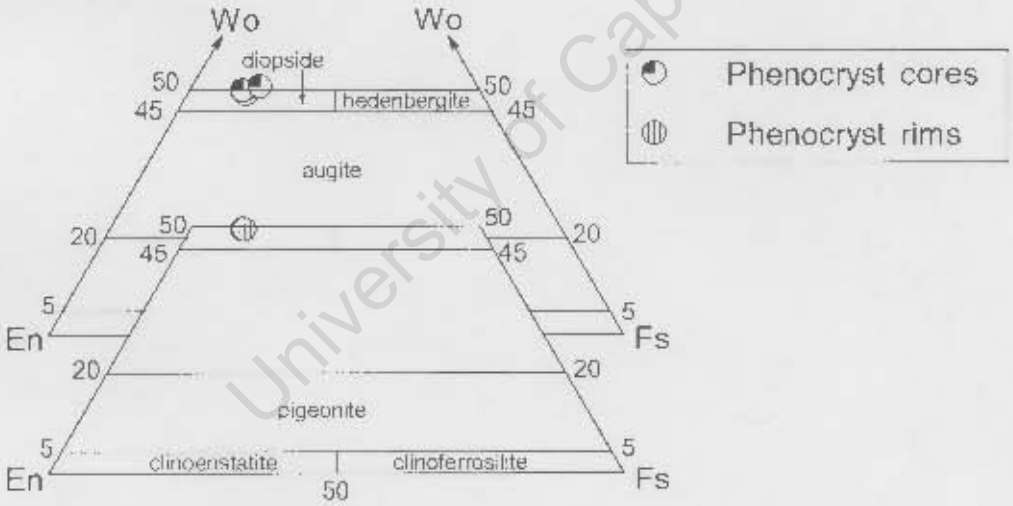

Fig. 3.15. Composition of clinopyroxene phenocryst (Ca-Mg-Fe) cores and rims from Tsirub dyke. Classification is according to Morimoto (1988).

At Tsirub North, clinopyroxene microphenocryst cores from the outer plug ($Wo_{47-50}En_{37-42}Fs_{10-13}$) and inner plug ($Wo_{47-48}En_{41-44}Fs_{9-12}$) are similar in composition to those in the Tsirub dyke (Table 3.2). Microphenocryst cores show similar compositions to that of rims (e.g. outer plug, core: CaO = 23.08 wt.% and rim: CaO – 23.14 wt.%; inner plug, core: CaO = 23.08 wt.% and rim: CaO = 23.14 wt.%). The outer plug and the inner plug have groundmass clinopyroxene compositions of

Table 3.2. Representative clinopyroxene analyses (in wt.%) from selected Tsirub samples Abbreviations: p = phenocryst, gm = groundmass, "-" = not detected). End-members calculated according to Morimoto *et al.* (1988).

	Tsirub dyke					Tsirub North (outer) plug								
	AN-001					AN-003			AN-005			AN-013	AN-015	
	p (core)	p (rim)	p	p (core)	p (rim)	p (core)	p (rim)	gm	p (core)	p (rim)	gm	gm	p (core)	p (rim)
SiO_2	49.24	48.94	49.26	46.51	48.86	48.76	48.28	47.34	44.16	42.41	48.03	48.32	48.19	43.06
TiO_2	2.27	2.51	2.28	2.77	2.40	2.77	2.61	2.89	4.75	5.31	2.90	4.16	2.64	5.10
Al_2O_3	4.24	4.64	4.62	7.38	4.49	4.19	4.80	4.84	7.93	9.12	4.37	2.78	4.77	8.63
Cr_2O_3	0.13	0.24	0.20	0.09	0.24	0.02	0.10	0.25	0.01	0.26	0.01	0.05	0.23	0.02
FeO	6.08	5.51	5.53	6.80	5.67	6.52	6.78	6.87	7.52	7.54	7.38	6.66	6.28	8.05
MnO	0.08	0.09	0.08	0.07	0.11	0.10	0.14	0.11	0.09	0.09	0.16	0.09	0.09	0.11
MgO	14.39	14.36	14.32	12.56	14.29	14.14	14.33	14.43	12.13	11.63	13.29	14.20	14.56	11.39
CaO	23.62	23.79	23.76	23.09	23.76	23.37	22.70	22.72	23.08	23.14	22.97	23.29	22.78	22.90
Na_2O	0.37	0.36	0.36	0.67	0.37	0.46	0.55	0.41	0.54	0.51	0.75	0.40	0.36	0.71
K_2O	0.01	-	0.01	0.01	-	-	0.11	0.04	-	0.01	0.02	0.00	0.00	0.02
Total	100.43	100.44	100.41	99.95	100.19	100.32	100.20	99.90	100.21	100.02	99.87	99.96	99.99	100.00
Fs	9.9	9.1	9.1	11.7	9.4	10.7	11.2	11.3	12.9	13.2	12.4	10.9	10.4	14.1
En	41.3	41.5	41.5	38.1	41.3	40.8	41.5	41.6	36.8	35.7	39.1	40.9	42.2	35.1
Wo	48.7	49.4	49.4	50.3	49.3	48.5	47.2	47.1	50.3	51.1	48.5	48.2	47.4	50.8

Note: Wo ($Ca_2Si_2O_6$) = 100*Ca/(Mg+Ca+ΣFe) where ΣFe = Fe^{2+}+Fe^{3} +Mn; En ($Mg_2Si_2O_6$) = 100*Mg/(Mg+Ca+ΣFe); Fs ($Fe_2Si_2O_6$) = 100* ΣFe/(Mg+Ca+ΣFe).

Table 3.2. Continued.

	Tsirub North (inner) plug											Tsirub South plug		
	AN-007			AN-007A		AN-008		AN-017				AN-021		
	p	gm	gm	p	p	p	p	p(core)	p(rim)	p(core)	p(rim)	p	p	p
SiO_2	49.68	47.36	48.84	51.86	51.92	49.15	48.80	48.23	48.88	50.21	51.04	48.43	46.42	51.55
TiO_2	3.03	4.90	3.79	1.62	1.15	1.54	1.75	1.73	1.66	1.28	1.69	2.48	3.34	1.82
Al_2O_3	2.23	3.26	2.55	1.02	1.24	4.64	5.08	6.23	6.18	4.43	1.66	4.69	5.48	1.66
Cr_2O_3	0.28	0.04	0.28	0.06	0.12	0.59	0.47	0.14	0.93	0.42	0.19	0.02	0.07	-
FeO	5.46	7.23	5.84	5.81	7.06	5.20	6.08	6.44	5.08	5.28	6.21	6.10	7.06	5.59
MnO	0.13	0.10	0.07	0.22	0.21	0.13	0.10	0.17	0.09	0.12	0.18	0.10	0.13	0.18
MgO	15.29	13.97	14.97	15.47	14.57	14.50	13.33	13.45	13.67	14.71	14.48	14.18	13.26	15.17
CaO	23.56	23.20	23.32	23.33	23.20	22.62	21.86	21.52	22.00	21.99	22.88	23.82	23.50	23.90
Na_2O	0.31	0.41	0.39	0.68	0.84	0.66	1.24	1.16	1.11	0.78	0.82	0.46	0.51	0.53
K_2O	0.01	0.01	0.01	0.01	0.01	0.01	0.14	0.03	0.02	0.02	0.02	0.00	0.00	0.01
Total	100.58	100.51	100.86	100.87	100.32	99.04	98.94	99.10	99.61	99.29	99.16	100.28	99.78	100.40
Fs	8.9	11.8	9.5	9.5	11.6	8.9	10.7	11.4	9.0	9.0	10.4	10.0	11.8	9.1
En	43.2	40.2	42.7	43.4	41.2	43.0	41.0	41.2	42.2	43.9	42.0	40.8	38.8	42.6
Wo	47.9	48.0	47.8	47.1	47.2	48.2	48.3	47.4	48.8	47.1	47.7	49.2	49.4	48.3

$Wo_{47-49}En_{39-42}Fs_{11-12}$ and $Wo_{48}En_{40-43}Fs_{9-12}$, respectively. TiO_2 contents are high, with the cores from the outer plug showing higher TiO_2 content (2.64 – 4.75 wt.%) than those from the inner plug (TiO_2 = 1.15 – 2.23 wt.%). TiO_2 increases with decreasing MgO for both sets of samples (Table 3.2). Microphenocrysts from the outer plug and inner plug show a wide range of Al_2O_3

concentration (4.19 – 7.93 wt.% for outer plug and 1.02 – 6.23 wt.% for inner plug). Na_2O concentrations are moderate and are not distinguishable from those of groundmass clinopyroxenes (e.g. outer plug: Na_2O = 0.36 wt.% - 0.54 wt.% for microphenocrysts and 0.40 – 0.75 wt.% for groundmass clinopyroxenes). Clinopyroxene compositions for microphenocryst cores and rims and groundmass clinopyroxenes are plotted in Figs 3.16 and 3.17 and are all diopsidic (Morimoto, 1988).

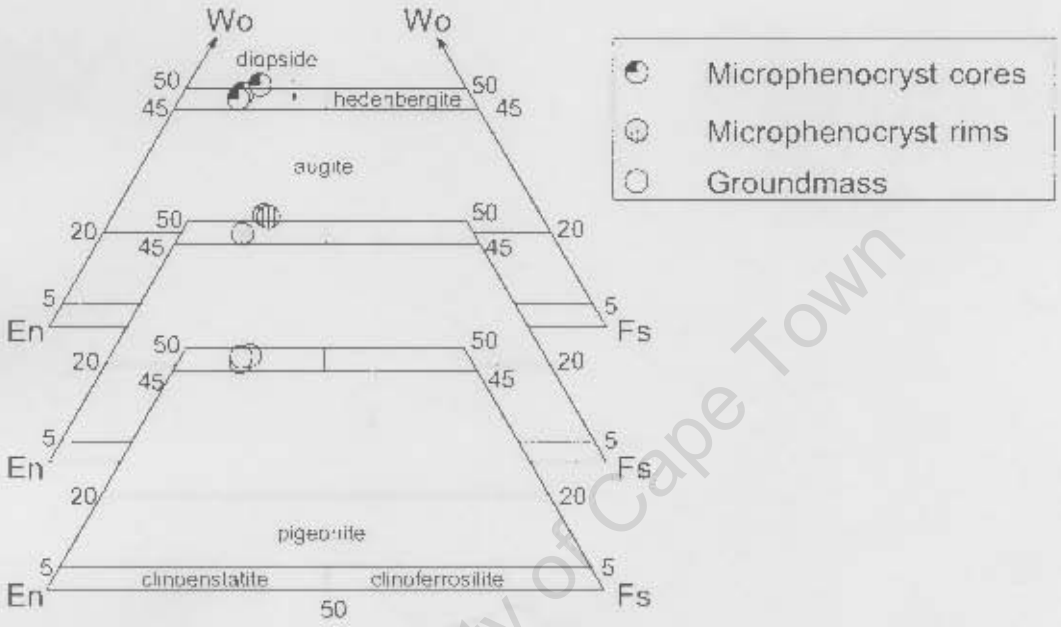

Fig. 3.16. Compositions of clinopyroxene (Ca-Mg-Fe) microphenocryst cores and rims, and groundmass clinopyroxene from Tsirub North (outer) plug. Classification is according to Morimoto (1988).

The Tsirub South plug has clinopyroxene microphenocryst core compositions of $Wo_{48-49}En_{39-43}Fs_{9-12}$ (Table 3.2), similar to those of the Tsirub North plug. TiO_2 (1.82 – 3.34 wt.%), Al_2O_3 (1.66 – 5.48 wt.%) and Na_2O (0.46 – 0.53 wt.%) concentrations (of the cores) are similar to those of the Tsirub North plug and Tsirub dyke. Following Morimoto's (1989) classification these clinopyroxenes are also diopsides (Fig. 3.18).

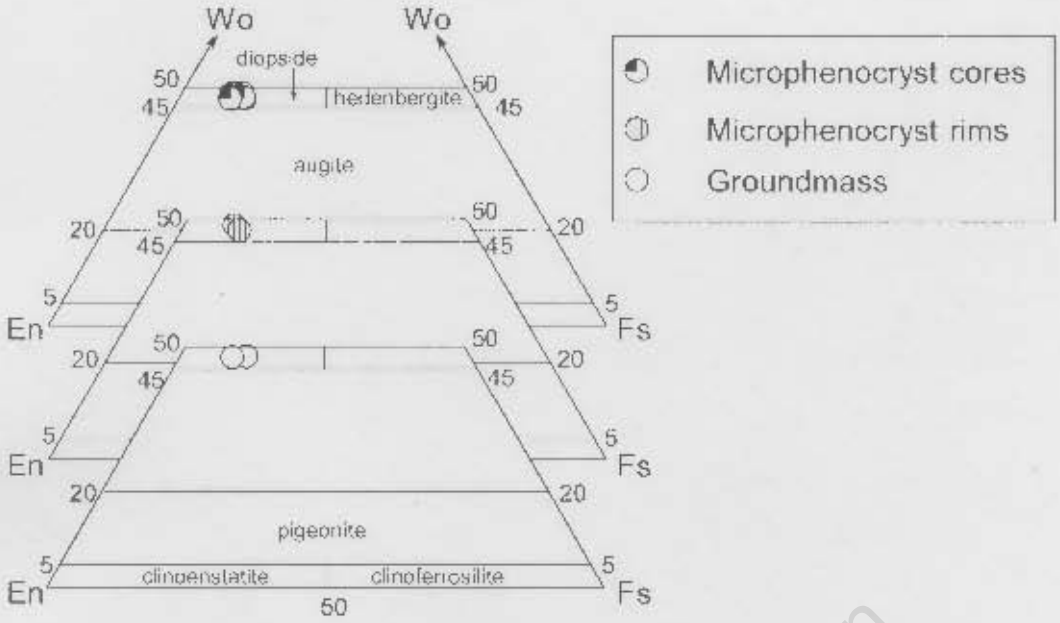

Fig. 3.17. Compositions of clinopyroxene (Ca-Mg-Fe) microphenocryst cores and rims, and groundmass clinopyroxene from Tsirub North (inner) plug. Classification is according to Morimoto (1988).

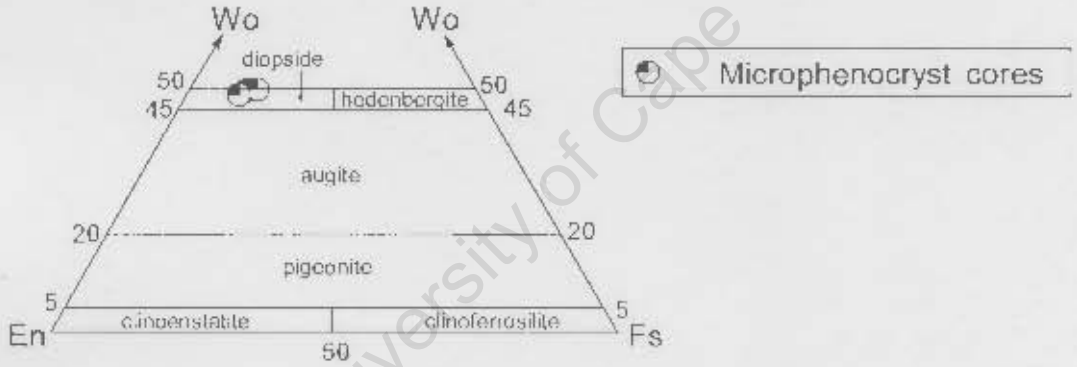

Fig. 3. 18. Composition of clinopyroxene (Ca-Mg-Fe) microphenocryst cores from Tsirub South plug. Classification is according to Morimoto (1988).

3.3.3 Fe-Ti oxides

The analysed Fe-Ti oxides presented in Table 3.3 are from the Tsirub North (inner) plug and are taken to be representative of Fe-Ti oxides from the Tsirub intrusions. Also reported in Table 3.3 is the Fe_2O_3 content estimated on the basis of stoichiometry assuming 32 oxygens and following Droop (1987). The Fe-Ti oxides are titanomagnetite in composition and consist of high total FeO (67.05 – 70.26 wt.%) and moderate TiO_2 (20.90 – 22.57 wt.%) contents. Calculated Fe_2O_3 content is 25.24 – 29.45 wt.%) (Table 3.3). MgO and Al_2O_3 concentrations are 3.38 - 3.96 wt.% and 0.22 – 0.73 wt.%, respectively. The analysed oxides contain a limited range of MnO content (1.00 – 1.14 wt.%).

Table 3.3. Representative Fe-Ti oxides analyses from the Tsirub North (inner) plug. FeO* represents the amount of total measured Fe. Fe_2O_3 calculated according to Droop (1987) on the basis of stoichiometry assuming 32 oxygens. Abbreviation: c = calculated.

	Fe-Ti oxides		
	AN-017		
SiO_2	0.04	0.07	0.18
TiO_2	21.82	20.90	22.57
Al_2O_3	0.26	0.22	0.73
Cr_2O_3	0.14	0.11	0.09
FeO*	69.44	70.26	67.05
MnO	1.00	1.02	1.14
MgO	3.73	3.38	3.96
CaO	0.17	0.31	0.30
Total	96.62	96.26	96.01
Fe_2O_3c	27.95	29.45	25.24
FeOc	44.29	43.76	44.34

3.3.4 Ultramafic xenolith

The single mantle xenolith found in sample AN-017 from the Tsirub North (inner) plug is a wehrlite, comprising olivine, clinopyroxene and minor spinel. Analyses of the constituent phases are presented in Table 3.4 and their respective end-members are shown in Fig. 3.19. Olivine is relatively iron-rich (Fo_{72-74}) with low NiO content (NiO ~ 0.10; Table 3.4). CaO concentration ranges between 0.15 and 0.20 wt.%. The clinopyroxenes are diopside ($Wo_{47-48}En_{41-42}Fs_{11}$) and have low TiO_2 content (0.94 – 1.09 wt.%), raised Al_2O_3 (6.21 – 6.68 wt.%) and moderate Na_2O concentrations (0.80 – 0.89 wt.%). The spinel is a hercynite having high Al_2O_3 (48.89 – 54.97 wt.%) and FeO contents (24.81 – 31.90 wt.%) and moderate MgO concentrations (13.01 – 15.97 wt.%). Cr_2O_3 content is low (1.65 – 4.21 wt.%).

3.3.5 Felsic xenolith

Analyses of feldspar and clinopyroxene making up the felsic xenoliths from the Tsirub North (inner) plug are reported in Table 3.5 and the minerals are classified in Fig. 3.20. Fe_2O_3 content of clinopyroxenes presented in Table 3.5 is calculated on the basis of 6 oxygens following Droop (1987). The analysed feldspars are alkali feldspars ($An_0An_{75-77}Ab_{23-25}$). A single feldspar from sample AN-008 ($Or_{48}Ab_{52}$) shows anomalously high Na_2O content of 7.21 wt.%. FeO and MgO contents are low and are 0.84 – 1.8 wt.% and 0.01 – 0.05 wt.%, respectively.

Table 3.4. Representative analyses of olivine, clinopyroxene and spinel that make up the ultramafic xenolith hosted in sample AN-017 from the Tsirub North (inner) plug. Abbreviations: p – phenocryst, gm – groundmass, "-" – not detected, and c = calculated). Clinopyroxene end-members are calculated following Morimoto (1988). FeO* represents measured total Fe. Fe_2O_3 and FeO concentrations of spinel are calculated on the basis of 32 oxygens following Droop (1987).

Olivine					Clinopyroxene					Spinel				
	AN-017					AN-017					AN-017			
SiO_2	39.97	40.44	39.97	40.43	SiO_2	48.94	49.34	48.93	48.99	SiO_2	0.07	0.05	0.05	0.04
TiO_2	-	0.01	0.03	0.01	TiO_2	1.05	0.94	1.09	1.03	TiO_2	1.51	0.89	0.85	0.83
Al_2O_3	0.01	0.01	-	0.01	Al_2O_3	6.60	6.21	6.51	6.68	Al_2O_3	49.89	54.97	54.02	49.98
Cr_2O_3	0.01	-	-	0.03	Cr_2O_3	0.13	0.06	0.05	0.09	Cr_2O_3	4.21	2.66	1.65	3.58
FeO	24.11	23.96	24.80	23.32	FeO	6.27	6.30	6.64	6.34	FeO*	29.18	24.81	28.67	31.90
MnO	0.31	0.37	0.33	0.34	MnO	0.15	0.10	0.15	0.16	MnO	0.21	0.15	0.22	0.29
MgO	37.10	36.68	36.19	37.35	MgO	13.78	13.61	13.76	13.70	MgO	14.90	15.97	15.05	13.01
CaO	0.15	0.20	0.18	0.15	CaO	21.92	22.00	21.77	21.71	CaO	0.02	0.06	-	0.02
NiO	0.11	0.10	0.10	0.11	NiO	-	-	-	-					
					Na_2O	0.83	0.80	0.82	0.89					
					K_2O	0.02	0.01	0.01	0.01					
Total	101.77	101.77	101.60	101.75	Total	99.69	99.38	99.73	99.59	Total	99.99	99.56	100.51	99.64
Fo	73.3	73.2	72.2	74.1	Fs	10.9	10.9	11.5	11.1	Fe_2O_3c	11.83	8.74	11.29	12.53
Fa	26.7	26.8	27.8	25.9	En	41.6	41.2	41.4	41.6	FeOc	18.53	16.95	18.51	20.62
					Wo	47.5	47.9	47.1	47.4					

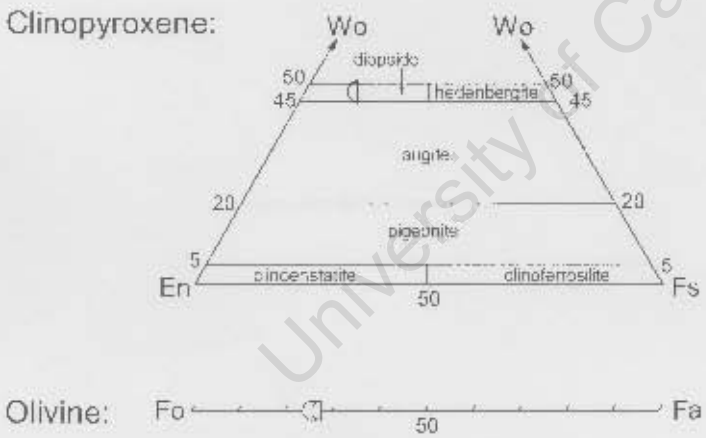

Fig. 3.19. Composition of olivine and clinopyroxene (Ca-Mg-Fe) that make up the ultramafic xenolith hosted by sample AN-017 from Tsirub North (inner) plug. Clinopyroxene classification is according to Morimoto (1988).

The light green clinopyroxenes are variable in composition enriched in CaO content ($Wo_{45-49}En_{43-46}Fs_{5-10}$) and have moderate to elevated Na_2O concentrations (0.55 – 3.19 wt.%). Al_2O_3 content is low (0.24 – 0.38 wt.%) (Table 3.5). These light green clinopyroxenes (excepting a single crystal) are diopsides (Morimoto, 1988). The dark green clinopyroxenes are enriched in FeO and have high Na_2O content (7.53 – 10.89 wt.%) indicating a significant aegirine component

Table 3.5. Representative analyses of feldspar and clinopyroxene (in wt.%) that make up the felsic xenolith from selected samples from the Tsirub North (inner) plug. Clinopyroxene end-members are after Morimoto *et al.* (1988). Fe_2O_3 calculated on the basis of 6 oxygens following Droop (1987). Symbol: "-" = not detected.

Feldspar						Light green clinopyroxene						Dark green clinopyroxene			
	AN-007A				AN-008		AN-007A		AN-008		AN-011		AN-007A		
SiO_2	65.09	65.37	64.66	64.74	62.58	SiO_2	53.47	53.54	53.64	53.87	53.80	53.73	52.67	53.22	53.04	53.26
TiO_2	0.05	0.08	0.05	0.08	0.19	TiO_2	0.90	1.21	0.41	0.58	0.53	0.52	4.77	3.21	4.00	5.34
Al_2O_3	18.44	18.07	18.63	18.29	19.23	Al_2O_3	0.24	0.38	0.27	0.36	0.27	0.08	0.36	0.31	0.33	0.40
Cr_2O_3	-	-	-	-	-	Cr_2O_3	-	0.02	0.17	0.05	0.04	0.03	-	-	-	-
FeO	1.19	1.28	0.95	1.21	0.84	FeO*	8.54	9.60	4.82	5.94	5.93	5.21	16.48	15.69	18.45	18.44
MnO	0.03	0.01	-	-	-	MnO	0.20	0.15	0.10	0.23	0.15	0.13	0.14	0.13	0.12	0.13
MgO	0.01	0.01	0.04	0.05		MgO	13.71	12.97	15.80	15.21	16.13	15.87	7.29	8.52	6.45	5.85
CaO	-	-	-	-	0.00	CaO	20.05	19.02	23.55	22.81	22.38	23.20	8.33	10.98	7.64	5.70
Na_2O	2.67	2.56	2.70	2.76	7.21	Na_2O	2.45	3.19	0.55	0.70	0.82	0.72	9.23	7.53	9.96	10.89
K_2O	13.02	13.29	13.10	12.87	9.94	K_2O	0.01	0.01	0.01	0.01	0.02	0.01	0.00	0.02	0.02	0.01
Total	100.50	100.66	100.13	99.99	99.99	Total	99.58	100.08	99.31	99.76	100.06	99.50	99.27	99.60	100.00	100.02
An	-	-	-	-	0.00	Fs	5.6	5.2	7.8	9.9	9.6	8.4	41.3	35.1	46.6	51.2
Ab	23.8	22.6	23.9	24.6	52.4	En	46.0	46.2	44.5	43.4	45.3	44.7	32.3	33.7	28.9	28.7
Or	76.2	77.4	76.1	75.4	47.6	Wo	48.4	48.6	47.7	46.7	45.1	46.9	26.5	31.2	24.6	20.1
						Q	82.4	77.2	96.1	95.0	94.1	94.8	36.2	47.3	31.6	26.1
						Ae	16.6	21.1	3.0	3.1	5.1	4.9	61.7	51.0	66.7	71.6
						Jd	1.0	1.7	0.9	1.9	0.8	0.3	2.1	1.7	1.7	2.3
						Fe_2O_3c	6.14	7.72	1.45	0.93	2.83	2.23	17.57	15.02	18.45	20.38
						FeOc	3.02	2.65	3.51	5.11	3.38	3.21	0.67	2.17	0.00	0.10

Note: Feldspar end-members: An = $An(CaAl_2Si_2O_8)$ = 100*Ca(Ca+Na+K), $Ab(NaAlSi_3O_8)$ = 100*Na(Ca+Na+K) and $Or(KAlSi_3O_8)$ = 100*K(Ca+Na+K). Clinopyroxene end-members (after Morimoto *et al.*, 1988): Wo ($Ca_2Si_2O_6$) = 100*Ca/(Mg+Ca+ΣFe) where ΣFe = Fe^{2+}+Fe^{3+}+Mn; En ($Mg_2Si_2O_6$) = 100*Mg/(Mg+Ca+ΣFe); Fs ($Mg_2Si_2O_6$) = 100* ΣFe/(Mg+Ca+ΣFe). Clinopyroxene end-members calculated for sodic clinopyroxene: Q (Wo, En, Fs) = 100*(Ca+Mg+Fe^{2+})/(Mg+Ca+Fe^{2+}+2Na), Jd ($NaAlSi_2O_6$)/Ae ($Na\,Fe^{3+}\,Si_2O_6$) = (Al/Fe^{3+})/(100*2Na)/(Mg+Ca+Fe^{2+}+2Na).

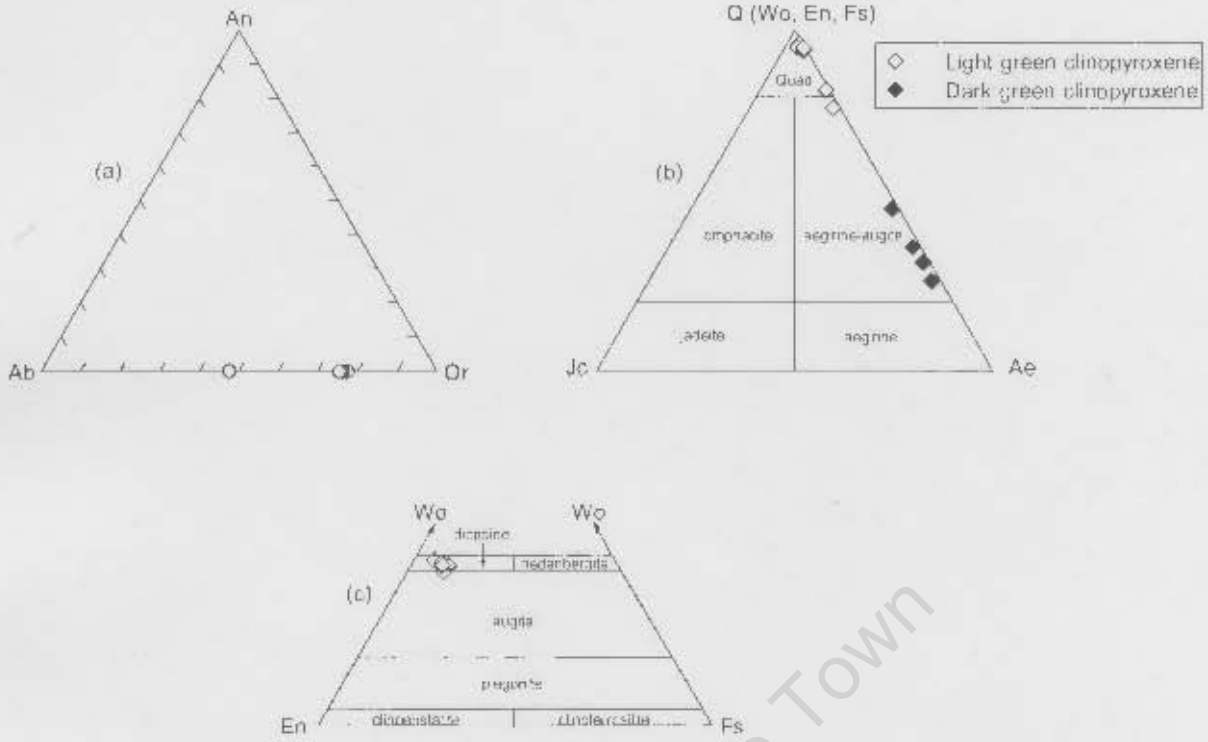

Fig. 3.20. Composition of feldspar (a) and clinopyroxene (b) that make up the felsic xenoliths from Tsirub North (inner) plug. Clinopyroxenes that plot in the Quad field (i.e. light green clinopyroxene) on the Q-Jd-Ae diagram in (b) are further classified on the Wo-En-Fs diagram in (c). Clinopyroxene classification is according to Morimoto (1988).

($Q_{26-47}Jd_2Ae_{51-72}$). TiO_2 is elevated (3.21 – 4.77 wt.%) and Al_2O_3 is very low (0.31 – 0.40 wt.%; Table 3.5). Calculated Fe_2O_3 content (calculated on the basis of 6 oxygens) is high (15.02 – 20.38 wt.%) (Table 3.5). According to Morimoto (1988) classification these are aegirine-augites (Fig. 3.20).

CHAPTER 4

MAJOR ELEMENT GEOCHEMISTRY

4.1 Introduction

A suite of 23 samples from Tsirub have been analysed for major element oxides by X-ray fluorescence (XRF) technique as described in Appendix B, section B.2. It should be noted that the felsic xenoliths mentioned in the previous chapter were removed from the samples before analysis. This chapter presents the description of the major element geochemistry for the Tsirub intrusions. The major elements were analysed in order to determine major element variations within each Tsirub intrusion and to determine variations between the Tsirub intrusions. The major element geochemistry, in conjunction with petrographic observations, will then be used to make inferences on the extent of fractional crystallization with particular emphasis on the minerals involved in the fractional crystallization process during the differentiation of the Tsirub magmas.

4.2 Major element geochemistry

Results of the major element analyses are reported in Table 4.1 and also shown on a total alkali-silica diagram in Fig. 4.1 (An analysis of the felsic country rock, SiO_2 = 68.8 wt.%, intruded by the Tsirub North plug is presented in Appendix C). The data were recalculated on a volatile free basis before plotting Fig. 4.1. In calculating the Mg#, reported in Table 4.1, a value of 0.2 was assumed for Fe_2O_3/FeO ratio (e.g. le Roex *et al.*, 1990; Späth *et al.*, 2001). Data for Schwarzeberg nephelinite (Spriggs, 1988) from southern Namibia and Erongo basanites and tephrites (Trumbull *et al.*, 2003) from northwest Namibia are also plotted on Fig. 4.1 for comparison.

The Tsirub rocks are classified based on Le Maitre's (2002) total alkali silica diagram (Fig. 4.1) and in conjunction with their CIPW norm values (in the case of Tsirub North (outer) plug). CIPW norm values are reported in Appendix C, Table C.1. The Tsirub dyke, Tsirub North (inner) plug, and Tsirub South plug all plot in the foidite (= nephelinite) field. Samples AN-016 and AN-019 from the Tsirub North plug also plot as nephelinites. These two samples are treated separately

Table 4.1. Major (in wt.%) and trace (in ppm) element analyses for Tsirub samples. All Fe reported as Fe_2O_3; Mg# = atomic Mg/(Mg + Fe^{2+}) calculated assuming Fe_2O_3/FeO = 0.2. *Analysed by XRF.

	Tsirub dyke	Tsirub North (outer) plug							
	AN-001	AN-003	AN-004	AN-005	AN-006	AN-012	AN-013	AN-014	AN-015
SiO_2	39.4	41.3	41.4	41.0	39.8	38.7	40.4	41.6	40.2
TiO_2	2.83	3.45	3.33	3.39	4.68	4.81	3.42	3.23	3.44
Al_2O_3	11.7	12.2	12.2	12.7	10.6	10.1	12.2	11.7	12.1
Fe_2O_3	11.6	11.8	11.7	12.0	13.9	14.0	11.8	11.3	11.7
MnO	0.20	0.19	0.18	0.19	0.17	0.16	0.18	0.18	0.19
MgO	12.0	9.43	9.22	9.63	9.47	9.25	9.37	8.70	9.40
CaO	11.2	11.2	10.9	12.1	11.1	11.0	11.5	14.6	11.3
Na_2O	4.48	4.38	5.30	4.19	3.84	2.94	4.69	2.16	4.62
K_2O	1.86	1.42	1.11	1.67	3.89	1.26	1.06	0.64	1.42
P_2O_5	1.42	1.03	1.07	1.11	1.27	1.06	1.05	1.12	1.03
H_2O-	0.37	0.31	0.31	0.28	0.17	0.96	0.31	0.40	0.21
LOI	2.07	2.34	2.24	2.14	0.42	5.07	3.23	3.74	3.33
Total	99.11	99.05	98.97	100.37	99.25	99.24	99.27	99.36	98.99
Mg#	0.71	0.65	0.65	0.65	0.61	0.61	0.65	0.64	0.65
ICP-MS:									
Sc	16.7	21.8	22.0	22.3	23.5	24.3	23.2	20.2	20.6
Ni	309	134	131	131	123	130	134	135	140
Cr	393	233	225	233	302	350	245	236	249
Co	44.6	42.2	41.8	42.0	51.9	53.7	42.9	43.3	44.1
V	183	243	224	247	288	226	251	252	252
Cu	39.1	53.6	39.5	50.9	69.6	67.1	51.1	53.2	54.9
Zn	84.9	86.6	87.4	85.3	93.0	102	87.0	88.3	88.0
Rb	57.8	85.5	64.2	62.6	112.7	50.3	75.9	64.3	111
Sr	1260	909	917	1155	1059	1957	1004	965	921
Cs	1.14	1.11	1.22	1.06	1.06	2.08	1.15	0.97	1.21
Ba	934	1094	1101	1109	1559	1531	1062	1071	1084
Y	26.0	24.2	25.1	25.5	22.3	19.2	23.3	21.8	24.4
Zr	402	407	398	395	449	444	404	400	400
Nb*	201	171	173	171	170	152	169	170	169
Hf	8.85	9.53	9.25	9.23	11.1	11.2	9.59	9.34	9.19
Ta	13.9	12.3	12.2	12.1	11.7	11.3	12.2	12.2	10.7
Pb	4.41	4.07	4.66	4.33	1.07	8.20	3.18	3.07	3.46
Th	10.3	9.05	9.06	8.78	7.66	5.80	8.03	7.40	8.20
U	2.88	1.93	1.92	1.95	1.89	1.85	1.47	1.48	1.62
La	85.2	58.6	60.2	61.0	67.0	51.8	59.4	58.3	59.2
Ce	167	117	117	120	148	116	117	115	116
Pr	18.8	13.2	13.0	13.1	17.5	13.9	13.0	12.7	12.0
Nd	70.4	50.9	50.1	50.6	67.8	54.6	49.9	48.6	47.3
Sm	10.8	8.44	8.38	8.44	10.3	8.73	8.53	8.19	7.84
Eu	3.27	2.59	2.63	2.61	3.02	2.50	2.59	2.53	2.61
Gd	8.80	7.27	7.38	7.40	8.10	6.60	7.10	6.92	6.98
Tb	1.14	0.99	1.00	1.01	1.02	0.87	0.98	0.94	0.93
Dy	5.64	5.12	5.22	5.24	4.94	4.21	4.98	4.82	4.77
Ho	1.02	0.95	0.99	1.00	0.89	0.76	0.94	0.91	0.86
Er	2.46	2.34	2.43	2.49	2.16	1.82	2.30	2.20	2.24
Tm	0.32	0.33	0.34	0.34	0.28	0.24	0.32	0.31	0.29
Yb	1.92	1.90	2.01	2.04	1.68	1.48	1.93	1.80	1.84
Lu	0.28	0.28	0.30	0.31	0.24	0.21	0.28	0.26	0.26

Table 4.1. Continued.

	Tsirub North plug									
	Tsirub North (inner) plug								AN-016 and AN-019	
	AN-007	AN-007A	AN-008	AN-009	AN-010	AN-011	AN-017	AN-018	AN-016	AN-019
SiO_2	39.9	38.9	39.8	40.3	38.7	39.6	39.3	39.6	39.5	40.1
TiO_2	2.56	2.51	2.42	2.42	2.47	2.52	2.51	2.48	3.73	2.99
Al_2O_3	12.4	11.8	11.8	12.1	12.4	11.9	11.8	12.1	11.3	12.8
Fe_2O_3	11.8	11.6	11.4	11.4	11.6	11.6	11.6	11.6	12.8	12.1
MnO	0.22	0.21	0.21	0.21	0.20	0.21	0.21	0.21	0.18	0.19
MgO	9.25	9.54	8.93	9.22	9.34	9.51	8.93	8.97	9.48	9.89
CaO	12.6	12.8	12.5	12.7	12.6	12.9	12.4	12.5	11.5	11.8
Na_2O	4.94	4.19	5.06	5.39	4.91	4.45	4.95	5.01	4.83	5.22
K_2O	2.18	1.86	1.51	1.45	2.12	1.97	2.68	2.00	1.87	1.84
P_2O_5	2.25	2.47	2.43	2.37	2.30	2.46	2.43	2.25	1.54	1.81
H_2O-	0.43	0.51	0.32	0.22	0.34	0.35	0.35	0.16	0.18	0.10
LOI	2.32	2.76	2.56	1.76	3.05	2.37	2.42	2.27	2.34	1.76
Total	100.83	99.06	98.93	99.55	100.08	99.88	99.70	99.06	99.18	100.51
Mg#	0.65	0.66	0.65	0.65	0.65	0.66	0.64	0.64	0.63	0.66
ICP-MS:										
Sc	17.3	18.8	18.5	19.2	18.9	18.8	17.9	19.2	22.4	20.4
Ni	129	130	129	132	128	129	133	135	125	119
Cr	194	193	182	187	175	184	191	197	252	214
Co	38.4	38.6	38.5	38.7	38.5	38.6	39.1	39.9	49.2	44.6
V	187	190	185	185	179	201	187	210	267	225
Cu	47.0	47.6	42.3	47.8	47.0	43.4	42.2	45.8	59.9	62.4
Zn	91.5	92.1	91.4	91.6	82.6	91.5	91.9	91.4	88.5	85.4
Rb	56.8	42.3	57.6	56.2	54.6	47.4	45.1	45.7	53.8	78.8
Sr	1879	1976	1935	1883	1842	1937	1932	1910	1347	1461
Cs	1.03	0.95	1.18	1.13	1.09	0.87	0.86	0.98	1.05	1.02
Ba	1353	1442	1311	1392	963	1199	1298	1472	1477	1365
Y	37.8	38.0	37.1	36.5	36.6	37.3	39.4	41.0	27.2	29.4
Zr	469	451	444	440	450	454	435	445	402	375
Nb*	267	245	246	239	247	251	251	250	184	184
Hf	9.32	9.01	8.84	8.76	8.79	9.13	8.72	9.02	9.37	7.88
Ta	14.9	14.1	13.6	13.3	13.8	14.1	12.8	13.6	10.4	9.69
Pb	6.58	4.39	3.44	4.11	6.83	7.23	3.50	5.62	4.60	5.96
Th	18.7	17.7	18.3	18.1	18.6	18.3	17.5	17.7	10.6	13.0
U	3.93	3.80	3.96	4.07	3.06	4.05	4.03	4.10	3.20	3.05
La	148	147	147	146	150	148	145	145	92.8	105
Ce	278	278	280	277	283	281	271	271	186	198
Pr	31.6	31.6	31.5	30.9	31.9	31.8	29.7	29.6	20.3	20.6
Nd	114	113	113	111	114	114	111	110	78.4	77.4
Sm	15.8	16.1	15.9	15.6	16.0	16.2	15.3	15.4	11.3	11.2
Eu	4.63	4.60	4.62	4.46	4.50	4.60	4.55	4.57	3.37	3.36
Gd	12.2	11.9	12.0	11.7	12.0	12.1	11.7	11.8	8.66	8.61
Tb	1.57	1.57	1.55	1.53	1.53	1.57	1.46	1.48	1.06	1.11
Dy	7.70	7.63	7.57	7.54	7.41	7.62	7.37	7.50	5.37	5.62
Ho	1.41	1.40	1.40	1.38	1.36	1.39	1.33	1.36	0.96	1.00
Er	3.45	3.42	3.37	3.31	3.32	3.39	3.36	3.49	2.38	2.53
Tm	0.48	0.47	0.47	0.47	0.46	0.47	0.44	0.47	0.31	0.33
Yb	2.83	2.83	2.80	2.78	2.73	2.77	2.74	2.84	1.92	2.07
Lu	0.42	0.42	0.42	0.42	0.41	0.41	0.38	0.40	0.26	0.29

Table 4.1. Continued.

	Tsirub South plug			
	AN-021	**AN-022**	**AN-023**	**AN-024**
SiO_2	39.0	39.4	38.9	39.1
TiO_2	3.30	3.25	3.36	3.26
Al_2O_3	12.3	12.3	12.7	12.2
Fe_2O_3	12.6	12.5	12.7	12.4
MnO	0.21	0.21	0.21	0.21
MgO	8.87	9.05	9.04	9.13
CaO	12.1	12.1	12.8	12.4
Na_2O	4.81	5.12	4.76	4.30
K_2O	2.45	2.55	2.86	2.48
P_2O_5	1.59	1.55	1.58	1.62
H_2O-	0.29	0.15	0.10	0.17
LOI	1.93	1.43	1.69	2.33
Total	99.30	99.58	100.79	99.67
Mg#	0.62	0.63	0.62	0.63
ICP-MS:				
Sc	19.7	19.1	18.9	19.0
Ni	105	108	107	105
Cr	168	172	162	166
Co	42.3	43.0	42.3	42.0
V	221	225	217	220
Cu	46.1	47.2	42.1	45.1
Zn	87.4	86.6	85.8	87.8
Rb	55.7	61.5	66.5	69.5
Sr	1359	1374	1383	1455
Cs	1.32	0.86	1.07	1.20
Ba	1160	1223	1148	1116
Y	31.4	32.1	30.9	31.1
Zr	406	410	399	397
Nb*	205	220	209	206
Hf	9.16	8.88	8.83	8.78
Ta	12.7	12.9	12.5	12.3
Pb	3.39	1.04	3.04	3.65
Th	11.2	12.0	11.3	11.3
U	2.70	2.45	2.78	2.24
La	95.4	100	96.1	96.2
Ce	179	190	180	181
Pr	18.8	19.9	18.9	19.0
Nd	72.3	76.9	73.5	73.2
Sm	11.3	11.7	11.1	11.3
Eu	3.44	3.62	3.47	3.52
Gd	9.20	9.29	9.15	9.10
Tb	1.16	1.19	1.17	1.16
Dy	6.01	6.12	5.89	6.01
Ho	1.09	1.08	1.08	1.06
Er	2.68	2.72	2.64	2.68
Tm	0.35	0.36	0.34	0.35
Yb	2.16	2.22	2.11	2.17
Lu	0.30	0.31	0.29	0.30

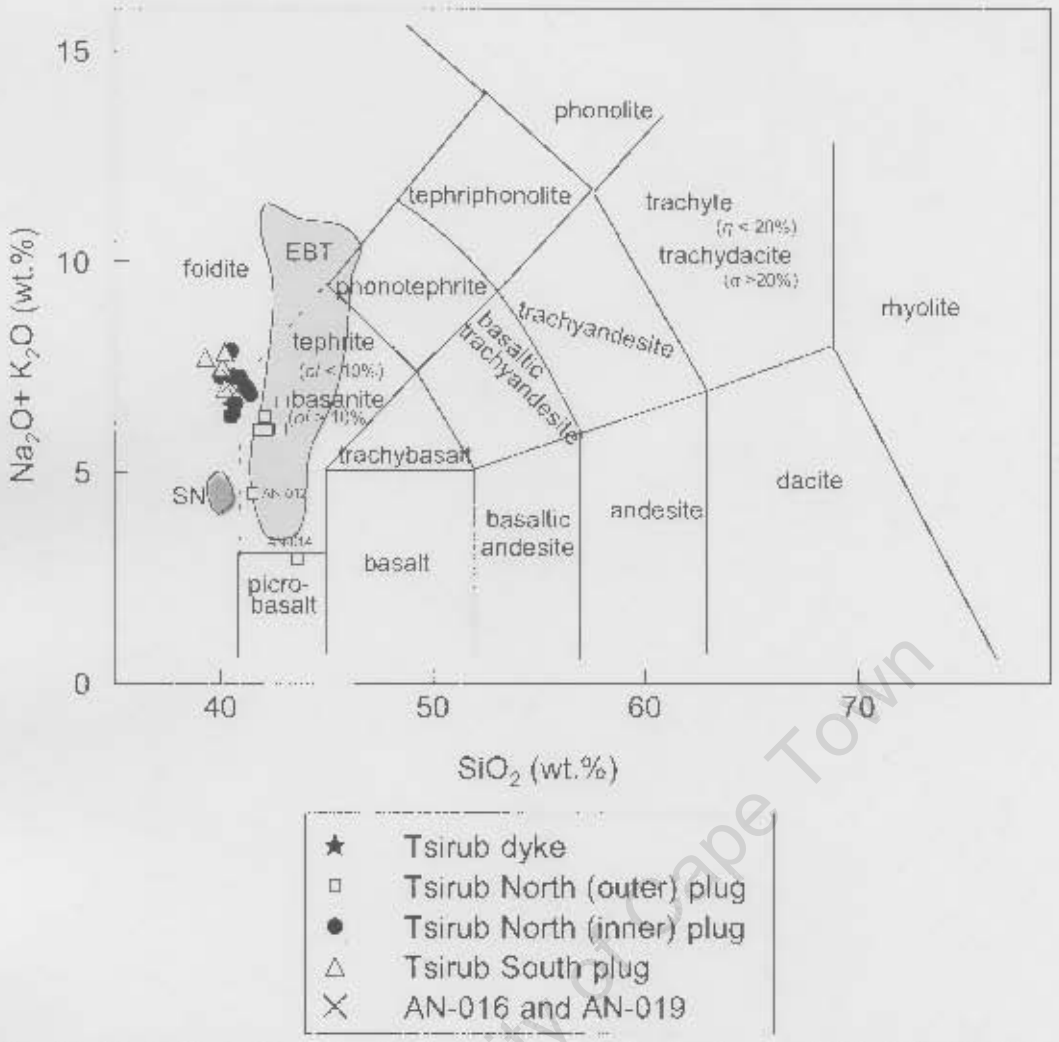

Fig. 4.1. Total alkali-silica classification diagram for Tsirub plugs and dyke (after Le Maitre, 2002). Data for the Schwarzeberg nephelinite (SN) is from Spriggs (1988), Erongo basanite and tephrites (EBT) from Trumbull *et al.* (2003).

from this point forward because they are geochemically distinct, e.g. see Fig 4.2g, and 5.2, from the outer and inner plug samples. The entire samples from Tsirub North (outer) plug (excepting AN-014) plot in the basanite/tephrite field. Sample AN-014 plots on the boundary between the basanite/tephrite field and picrobasalt field owing to its low total alkali content of 2.80 wt.%. To identify if the Tsirub North (outer) plug samples are basanites or tephrites their normative olivine values were used. According to Le Maitre (2002), basanites have > 10 wt.% normative olivine whereas tephrites are defined by < 10 wt.% normative olivine. Therefore, on the basis of their high normative olivine values (10.2 - 14.6 wt.%; Table C.1, Appendix C) samples from the Tsirub North (outer) plug are classified as basanites. All the Tsirub samples, except AN-012 and AN-014, have high normative nepheline values (18 – 24 wt.%). Samples AN-012 (ne – 11 wt.%)

and AN-014 (ne = 7 wt.%) are anomalous, having significantly lower normative nepheline values.

In comparison to the Schwarzeberg nephelinite, the Tsirub samples have higher total alkali contents but comparable SiO_2 content (Fig. 4.1). On the same diagram (Fig. 4.1) the Tsirub North (outer) plug plot within the field defined by the Erongo basanites and tephrites (Trumbull *et al.*, 2003). The Tsirub dyke, Tsirub North (inner) plug, samples AN-016 and AN-019 and Tsirub South plug will be referred to as nephelinites whereas the Tsirub North (outer) plug will be referred to as basanites.

The variations of selected major elements with MgO content as an index of differentiation are shown in Fig. 4.2 where the data was recalculated on a volatile free basis before plotting. MgO, and not SiO_2, was chosen as an index of differentiation because it is a much more sensitive indicator of degree of evolution of basaltic rocks compared to SiO_2 (Fitton *et al.*, 1991). Data for Schwarzeberg nephelinite (Spriggs, 1988) from southern Namibia is also plotted on Fig. 4.2 for comparison.

The Tsirub dyke shows the most primitive MgO content (12.0 wt.%) and Mg# (0.71) (Mg# = atomic $Mg/(Mg + Fe^{2+})$; assuming $Fe_2O_3/FeO = 0.2$) among the Tsirub intrusions. TiO_2 content is relatively high (2.83 wt.%), which is typical of nephelinites (Le Bas, 1987). CaO content of the Tsirub dyke is high (11.2 wt.%) and is similar to that of the Tsirub North (outer) plug (Fig. 4.2e). P_2O_5 concentration (1.42 wt.%) is moderate (Fig. 4.2g) whereas K_2O (1.86 wt.%) content is relatively low.

At Tsirub North, the outer plug (e.g. Mg# = 0.61 – 0.65) and the inner plug (Mg# – 0.64 – 0.66) shows limited internal variations in Mg# (Table 4.1). SiO_2 concentration is low and it ranges between 38.7 and 41.6 wt.% for the basanite samples and between 38.7 and 40.3 wt.% for the nephelinite samples. CaO is positively correlated with MgO in both the outer plug and inner plug (CaO = 12.4 – 12.9 wt.% and MgO – 8.93 – 9.54 wt.%) with the outer plug (MgO – 9.22 – 9.63 wt.%) extending to lower CaO content (10.9 – 12.1 wt.%) (Fig. 4.2e). Sample AN-014 from the outer plug is displaced to relatively lower MgO content (8.70 wt.%) and much higher CaO concentration (14.6 wt.%). The anomalous behaviour of this sample is also reflected in its elevated LOI value (3.74 wt.%). The inner plug is readily distinguishable from the outer plug (TiO_2 – 3.23 and 3.45 wt.% and P_2O_5 = 1.03 – 1.27 wt.%) by its relatively lower TiO_2 content

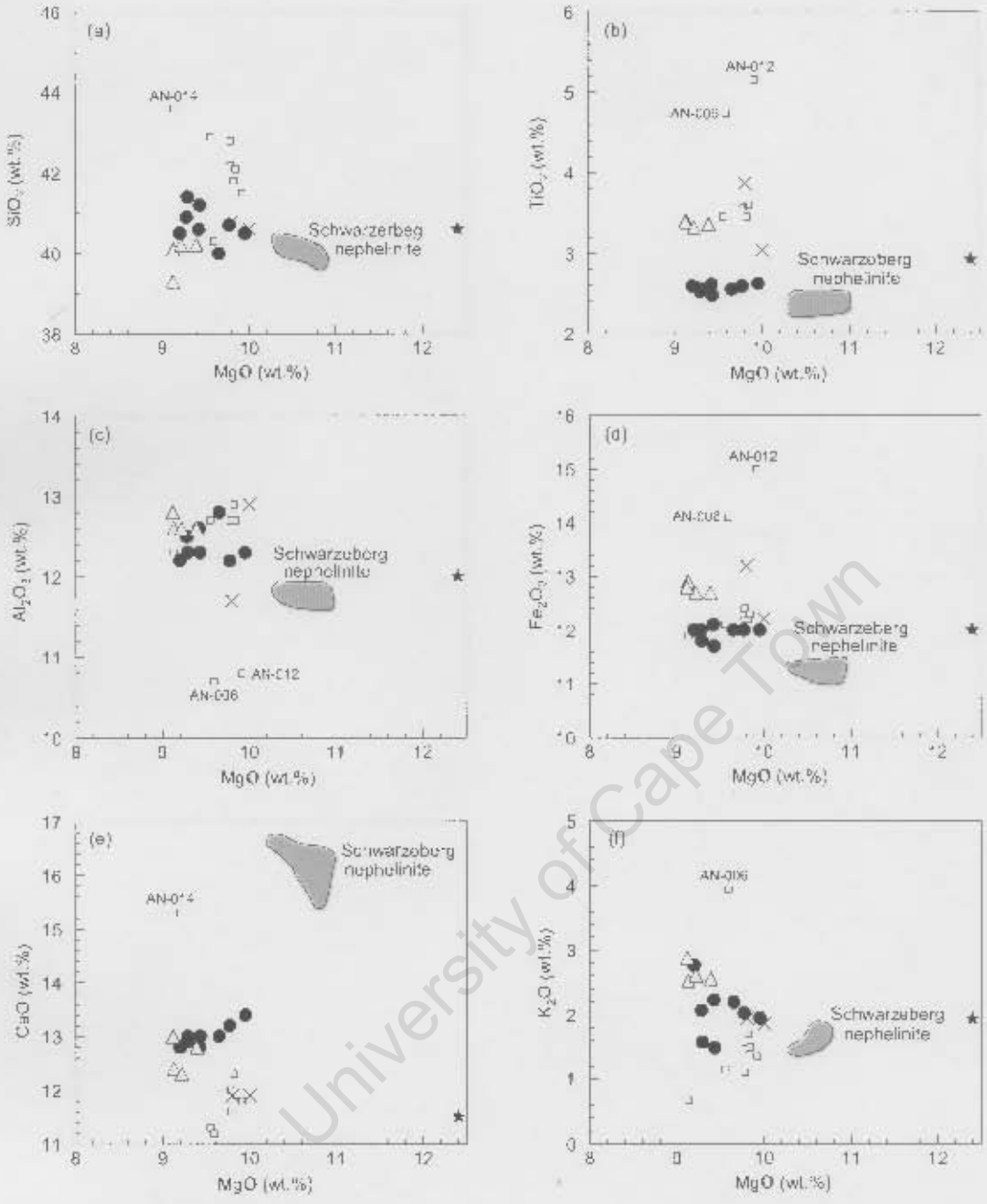

Fig. 4.2. Variations of selected major elements with respect to MgO, as an index of differentiation, in Tsirub rocks. The gray fields represent Schwarzeberg nephelinite data (Spriggs, 1988). Symbols are as in Fig. 4.1.

(2.42 – 2.56 wt.%) and higher P_2O_5 concentration (2.25 – 2.47 wt.%). Al_2O_3 and Fe_2O_3 concentrations are high and overlap between the two sets of samples (Al_2O_3 = 11.7 –12.7 wt.% and Fe_2O_3 = 11.7 – 12.0 wt.% for outer plug, Al_2O_3 = 11.7 – 12.7 wt.% and Fe_2O_3 = 11.7 – 12.0 wt.% for inner plug) (Table 4.1; Figs. 4.2c and d). Samples AN-006 and AN-012 from the outer plug are displaced to relatively high TiO_2 and Fe_2O_3 contents (AN-006: TiO_2 – 4.68 wt.% and

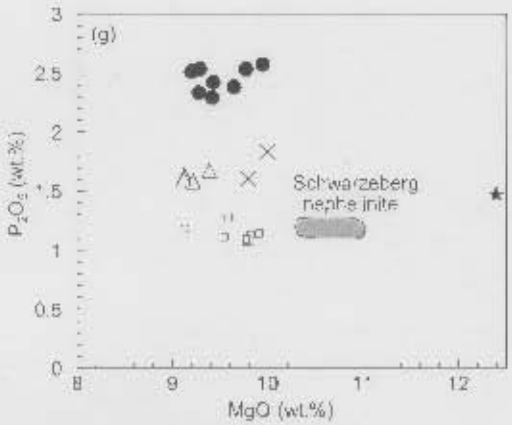

Fig. 4.2. Continued.

Fe_2O_3 = 13.9 wt.%; AN-012: TiO_2 = 4.81 wt.% and 14.0 wt.%) and lower Al_2O_3 concentrations (Al_2O_3 = 10.6 wt.% for AN-006 and 10.1 wt.% for AN-012). The anomalous behaviour of these two samples is consistent with their greater abundance of much altered olivine microphenocrysts (see Appendix A) and elevated LOI value (5.07 wt.%) in the case of sample AN-012. Although the inner plug (K_2O = 1.45 – 2.68 wt.%) lacks any correlation between K_2O and MgO, the outer plug with K_2O – 0.64 – 1.67 wt.% displays a scattered positive correlation between K_2O and MgO (Fig. 4.2f). In addition to showing anomalous TiO_2, Al_2O_3 and Fe_2O_3 concentrations, sample AN-006 from the outer plug is also displaced to higher K_2O content (3.89 wt.%).

Samples AN-016 and AN-019 from the Tsirub North plug have SiO_2 and K_2O contents (SiO_2 = 39.5 – 40.1 wt.% and K_2O = 1.84 – 1.87 wt.%) similar to that of the Tsirub North (inner) plug whereas their CaO abundances (AN-016: 11.5 wt.%; AN-019: 11.8 wt.%) are similar to that of the Tsirub North (outer) plug. P_2O_5 concentrations (1.54 – 1.81 wt.%) for these two samples are intermediate between the Tsirub North (outer) plug and Tsirub North (inner) plug (Fig. 4.2g).

The Tsirub South plug shows a limited range in major element composition and the four nephelinite samples form a cluster (e.g. MgO – 8.87 – 9.13 wt.%) (Fig. 4.2). SiO_2 content (38.9 – 39.4 wt.%) and TiO_2 content (3.25 – 3.36 wt.%) of this plug are similar to that of the Tsirub North (inner) plug and Tsirub North (outer) plug, respectively. CaO concentration is high: a feature characteristic of nephelinitic rocks (e.g. Le Bas, 1987). In comparison to the other Tsirub intrusions the Tsirub South plug shows slightly higher Fe_2O_3 contents (12.4 – 12.7 wt.%). Al_2O_3 concentration is high (12.1 – 12.8 wt.%) whereas the P_2O_5 content (1.55 – 1.62 wt.%) is similar to

that of samples AN-016 and AN-019 from the Tsirub North plug (Fig. 4.2g). This plug shows higher K_2O concentration (2.45 – 2.86 wt.%) compared to other Tsirub intrusions.

In general terms, all the Tsirub intrusions, except the Tsirub dyke, show similar MgO content. The Tsirub dyke has relatively primitive MgO abundances. The Tsirub North (outer) plug is readily distinguished from the other Tsirub intrusions by its slightly higher SiO_2 content and lower P_2O_5 contents. The Tsirub North (inner) plug has relatively lower TiO_2 content relative to the other Tsirub intrusions whereas the Tsirub South plug can be distinguished on the basis of its slightly higher Fe_2O_3 and K_2O concentrations.

In comparison to the Schwarzeberg nephelinite, the Tsirub nephelinites and basanites show lower MgO (excepting the Tsirub dyke) and CaO concentrations but higher TiO_2, Al_2O_3 and Fe_2O_3 concentrations (Fig. 4.2).

CHAPTER 5

TRACE ELEMENT GEOCHEMISTRY

5.1. Introduction

The concentration of trace elements in rocks is controlled by their concentration in the source region, by chemical fractionation during partial melting and by fractional crystallization during ascent. Mantle derived magmas that have undergone limited fractional crystallization yield rocks with high concentration of compatible trace elements and such rocks are termed primary magmas (Frey *et* al., 1978). Continental mafic alkaline rocks including nephelinites and basanites are enriched in trace elements particularly in the incompatible trace elements. Such high concentrations of incompatible trace elements are frequently interpreted to be a result of low degrees of partial melting or derivation from an enriched source (e.g. Erlank *et al.*, 1982; Zhang & O'Reilly, 1997; Cebriá *et al.*, 2000; Späth *et al.*, 2001).

Since the concentration of incompatible trace elements is inversely proportional to the degrees of partial melting (assuming no influence of residual phases that accommodate certain incompatible elements such as Nb in rutile) such elements are useful in constraining the degrees of partial melting. Incompatible trace elements that are somewhat compatible in certain minor mantle phases are useful in constraining the nature of residual mineralogy at the time of partial melting. Such elements include Nb compatible in phases such as rutile and ilmenite (Green, 1995). The role of a minor residual phase can be recognized by the lack of correlation between an incompatible trace element accommodated in a minor phase (assuming no influence of secondary alteration which affects mobile incompatible trace elements) and other incompatible trace elements of similar incompatibility. Rare earth elements (REE) in particular are useful in discriminating between partial melting within the garnet stability field and spinel stability field because the heavy REE such as Yb are compatible in garnet whereas the light REE are incompatible in garnet. In contrast, both the light and heavy REE are equally incompatible in spinel such that partial melting in the spinel stability field does not cause fractionation of the heavy REE from the light REE as in garnet stability field (e.g. Wilson, 1989; Ellam, 1992; Pearce, 1996; Bernstein *et al.*, 2000; Siebel *et al.*, 2000; Keller *et al.*, 2006).

The Tsirub samples have been analysed for trace element concentrations using inductively coupled mass spectrometry (ICP-MS) technique following procedures documented in Appendix B, section B.3. Results of these analyses are reported in Table 4.1. The Tsirub samples were analysed in order to determine trace element variations within each Tsirub intrusion and to determine trace element variations between the Tsirub intrusions. The trace element geochemistry will then be used to evaluate petrogenetic processes such as partial melting and to make inferences on source region characteristics such as the type of residual minerals at the time of melt extraction. The REE elements in particular will be used in partial melting modelling in order to quantify the degrees of partial melting that gave rise to the Tsirub intrusions and to determine whether partial melting took place in the garnet stability field or the spinel stability field. The latter four aspects are discussed in Chapter 7.

5.2 Compatible trace elements

The variation of selected compatible trace elements with MgO in the Tsirub nephelinites and basanites is shown in Fig. 5.1.

Ni and Cr concentrations of the Tsirub dyke (Ni = 309 ppm and Cr = 393 ppm) are similar to that documented for primary magmas (Ni = 300 – 400 ppm, Frey *et al.*, 1978). Co concentration is moderate (44.6 ppm) whereas Sc content is low (16.7 ppm).

At Tsirub North, the outer plug is slightly more enriched in the compatible trace elements, except for Ni, than the inner plug. Ni concentration overlap between the two sets of samples (outer plug: Ni = 123 – 140 ppm and inner plug: Ni = 128 – 135 ppm) and it shows no correlation with MgO (Fig. 5.1a). Like Ni, Co content in both the outer plug (Co = 41.8 – 44.1 ppm) and inner plug (Co = 38.4 – 39.9 ppm) lack any correlation with MgO concentration. Cr content is moderate for both the outer plug (225 – 249 ppm) and inner plug (175 – 197 ppm). Samples AN-006 and AN-012 from the outer plug are displaced to higher Cr and Co contents (AN-006: Cr = 302 ppm and Co = 51.9 ppm, AN-012: Cr = 350 ppm and Co = 53.7 ppm). The outer plug defines a small range of, low, Sc content (20.2 – 24.3 ppm) and the same is true for the inner plug (17.3 – 19.2 ppm) (Table 4.1; Fig. 5.1d).

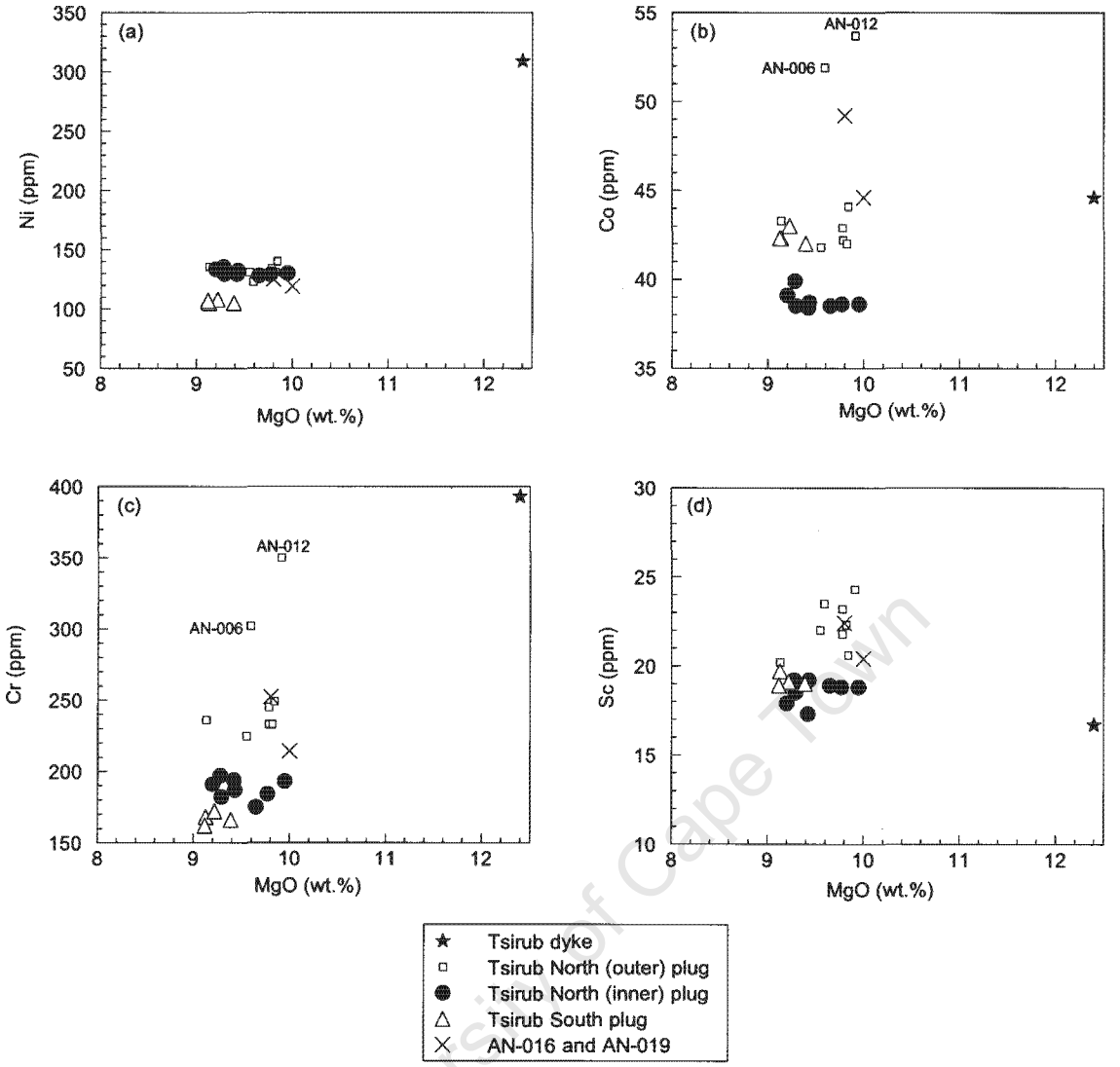

Fig. 5.1. Variation of selected compatible trace elements with MgO concentration (as an index of differentiation) in Tsirub intrusions.

Samples AN-016 (Ni = 125 ppm and Co = 49.2 ppm) and AN-019 (Ni = 119 ppm and Co = 44.6 ppm) from the Tsirub North plug show comparable Ni content to, but higher Co concentration than, the Tsirub North (outer) plug and Tsirub North (inner) plug. Their Cr, Sc and V contents are more comparable to those of the Tsirub North (outer) plug but slightly higher than for the Tsirub North (inner) plug (e.g. Sc = 20.4 - 22.4 ppm versus 20.2 – 24.3 ppm for Tsirub North (outer) plug; Fig. 5.1).

The Tsirub South plug defines relatively restricted ranges in compatible trace elements (e.g. Ni, Co, Sc). Ni (105 – 108 ppm) and Cr contents (162 – 172 ppm) do not show any correlation with MgO and are slightly lower than for Tsirub North plug. Sc concentration (18.9 – 19.7 ppm) in

this plug is low and is similar to the Tsirub North (inner) plug. Co contents vary between 42.0 and 43.0 ppm.

5.3 Incompatible trace elements

High field strength elements (HFSE) and large ion lithophile elements (LILE) data are presented in Table 4.1 and shown on variation diagrams in Fig. 5.2. Data for Schwarzeberg nephelinite (Spriggs, 1988) is also plotted on Fig. 5.2 for comparison.

The Tsirub dyke is enriched in HFSE most notably in Nb (194 ppm) and Zr (402 ppm). Th (10.3 ppm) and U contents (2.88 ppm) are moderate and low, respectively (Table 4.1; Fig. 5.2). Y and Hf contents are 26.0 ppm and 8.85 ppm, respectively. In terms of the LILE, this dyke has slightly lower Ba content (934 ppm) but shows similar Rb content (57.8 ppm) to the Tsirub North and South plugs.

At Tsirub North, the outer plug and inner plug are variably enriched in HFSE with the most enrichment in Nb and Zr a feature also observed in the Tsirub dyke (Table 4.1; Fig. 5.2). The inner plug is much more enriched in the HFSE (e.g. Nb = 231 – 256 ppm) than the outer plug (Nb = 145 – 168 ppm) for a given magnesium number, consistent with the higher alkali content of the former. For example, samples AN-007 (Zr = 469 ppm, Nb = 256 ppm) and AN-009 (Zr = 440 ppm, Nb = 231 ppm) from the inner plug, show much higher Zr and Nb contents than samples AN-004 (Zr = 398 ppm, Nb = 166 ppm) and AN-013 (Zr = 404 ppm, Nb = 164 ppm), from the outer plug, despite showing the same magnesium number of 0.65 (Table 4.1). These two plugs define tight clusters on a variation diagram of Nb versus La. The compositional ranges of Th and U are narrow (e.g. Th = 7.66 – 9.06 ppm for outer plug and 17.5 – 18.7 ppm for inner plug).

LILE in Tsirub North magmas are not correlated with each other and they also do not show any correlation with other incompatible trace elements with comparable degree of incompatibility such as Nb (Fig. 5.2e). For example, the outer plug and inner plug show a considerable scatter between Rb and K (Fig. 5.2f) and between Rb and Ba (not shown). The outer plug displays a wider range of Rb concentrations (50.3 – 85.5 ppm) that extends to higher values compared to the narrow range depicted by the inner plug (Rb = 42.3 – 56.8 ppm).

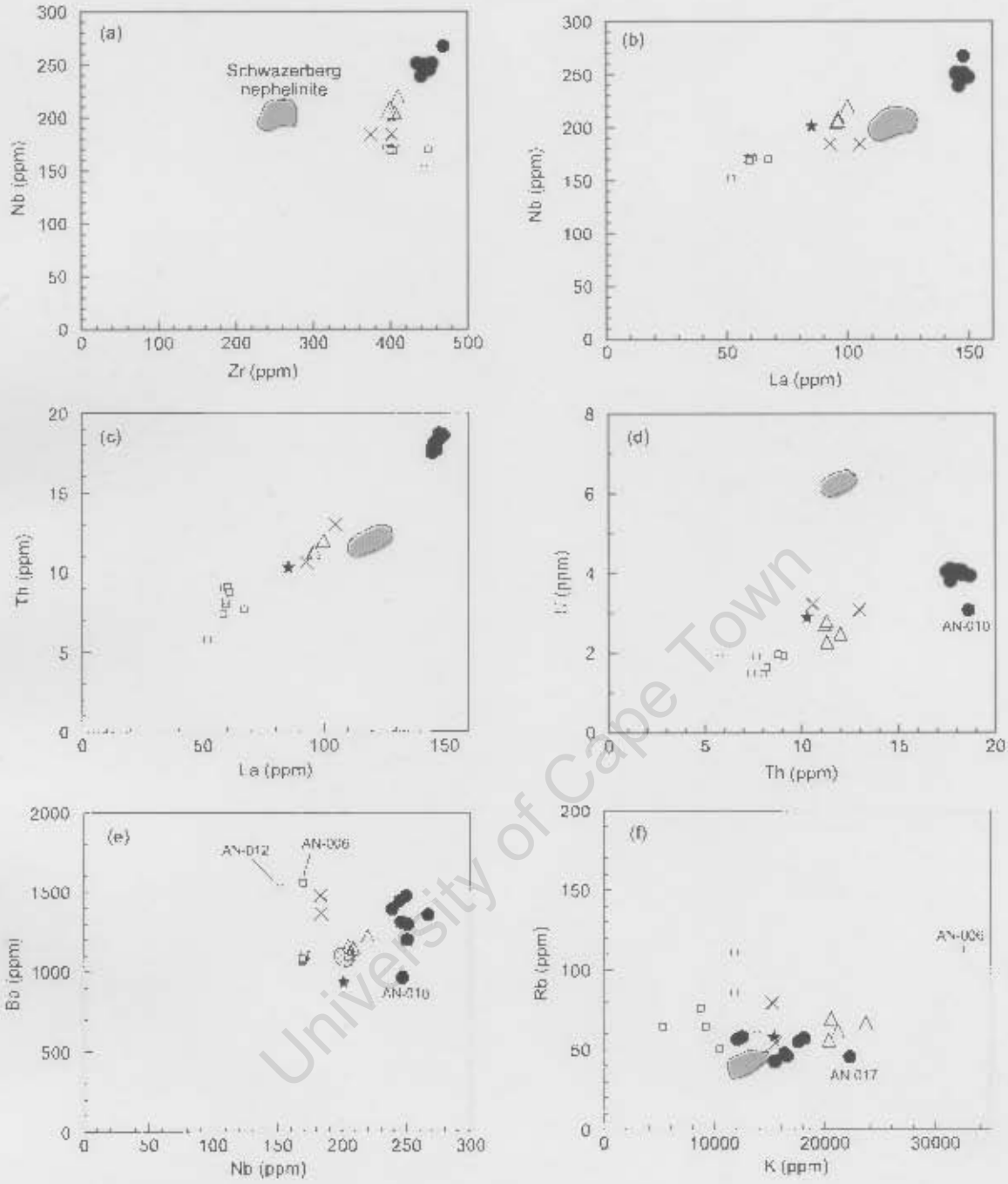

Fig. 5.2. Variation of selected high field strength elements (HFSE) and large ion lithophile elements (LILE) among the Tsirub nephelinites and basanites. The gray field represents Schwarzeberg nephelinite data (Spriggs, 1988). Symbols are as in Fig. 5.1.

La, Th and U concentrations of samples AN-016 (Nb – 180 ppm and Th = 10.6 ppm) and AN-019 (Nb – 185 ppm and Th = 13.0 ppm) are similar to those of the Tsirub dyke and Tsirub South plug. Ba content for these two samples is high (1477 ppm and 1365 ppm).

Like the Tsirub North plug, the Tsirub South plug also shows considerable HFSE enrichment. The latter plug is characterized by restricted ranges of Nb (201 – 215ppm), Zr (397 – 410 ppm) and Th concentrations (11.2 – 12.0 ppm). Both Nb and Th increase with increasing La concentration (Table 4.1). On the variation diagrams of Nb versus Zr, Nb versus La and Th versus La, the Tsirub South plug define a tight cluster. U concentration ranges between 2.24 and 2.78 ppm and is similar to that of Tsirub dyke. There is no correlation between LILE e.g. Rb versus K (Fig. 5.2f) and Rb versus Ba (not shown). For example there is considerable scatter between Rb (55.7 – 69.5 ppm) and K a feature also observed in the other Tsirub intrusions as stated previously.

In comparison to the Schwarzeberg nephelinite, all the Tsirub samples show much higher Zr content but lower U content (Fig. 5.2a and d). Nb and Th contents of the Tsirub dyke, samples AN-016 and AN-019 and Tsirub South plug are similar to those of the Schwazeberg nephelinite.

5.3.1 Incompatible trace element ratios

Incompatible trace element ratios are reported in Table 5.1 and shown graphically in Fig. 5.3. It should be noted that samples AN-006 and AN-012 for the Tsirub North (outer) plug are excluded in calculating the average Ce/Pb ratio, reported in Table 5.1, of the Tsirub North (outer) plug because of their anomalously high and low Ce/Pb ratios, respectively (see Table 4.1). Also AN-022 from the Tsirub South plug is excluded in calculating the average Ce/Pb ratio of the Tsirub South plug because it has anomalously high Ce/Pb ratio owing to its much lower Pb content (see Table 4.1).

The Tsirub dyke shows La/Nb (0.42) and Zr/Nb (2.00) ratios similar to the Tsirub South plug. Ba/Nb ratio is also comparable to the Tsirub South plug and the Tsirub North (inner) plug. Nb/U and Ce/Pb ratios are 69.7 and 37.9, respectively (Table 5.1).

At Tsirub North, the outer plug and inner plug show variable incompatible trace elements ratios. The outer plug has slightly higher Zr/Nb ratio (2.46 ± 0.21) but slightly lower La/Nb ratio (0.35 ± 0.02) than the inner plug (Zr/Nb = 1.80 ± 0.04 and La/Nb = 0.59 ± 0.02) (Fig. 5.3). Both display a negative correlation between Zr/Nb ratio and Nb (Fig. 5.3b). The outer plug also shows a good

Table 5.1. Incompatible trace element ratios and average incompatible trace element ratios for Tsirub samples. Subscript $_N$ denotes chondrite normalised (values from Sun and McDonough, 1989).

	Tsirub dyke	Tsirub North (outer) plug								
	AN-001	AN-003	AN-004	AN-005	AN-006	AN-012	AN-013	AN-014	AN-015	Average + s.d
Zr/Nb	2.00	2.38	2.30	2.31	2.63	2.92	2.39	2.36	2.37	2.46 ± 0.21
Nb/Ta	14.4	13.9	14.1	14.1	14.6	13.4	13.9	13.9	15.8	14.2 ± 0.74
La/Nb	0.42	0.34	0.35	0.36	0.39	0.34	0.35	0.34	0.35	0.35 ± 0.02
Ba/Nb	4.65	6.41	6.36	6.50	9.14	10.1	6.29	6.32	6.41	7.19 ± 1.51
Ce/Pb	37.9	28.9	25.1	27.7	138*	14.1*	36.8	37.4	33.6	31.6 ± 5.09
$(La/Yb)_N$	31.9	22.1	21.5	21.4	28.6	25.1	22.1	23.2	23.1	23.4 ± 2.43
$(La/Sm)_N$	5.08	4.48	4.64	4.67	4.19	3.83	4.50	4.59	4.87	4.47 ± .032

	Tsirub North (inner) plug								
	AN-007	AN-007A	AN-008	AN-009	AN-010	AN-011	AN-017	AN-018	Average + s.d
Zr/Nb	1.76	1.84	1.80	1.84	1.82	1.81	1.73	1.78	1.80 ± 0.04
Nb/Ta	17.9	17.3	18.1	18.0	17.9	17.8	19.6	18.4	18.1 ± 0.66
La/Nb	0.55	0.60	0.60	0.61	0.61	0.59	0.58	0.58	0.59 ± 0.02
Ba/Nb	5.07	5.88	5.33	5.83	3.89	4.77	5.16	5.88	5.23 ± 0.68
Ce/Pb	42.3	63.4	81.5	67.5	41.4	38.9	77.3	48.3	57.6 ± 15.9
$(La/Yb)_N$	37.4	37.3	37.8	37.5	39.4	38.3	38.0	36.7	37.8 ± 0.75
$(La/Sm)_N$	6.04	5.90	5.97	6.01	6.04	5.88	6.13	6.10	6.01 ± 0.08

	AN-016 and AN-019			Tsirub South plug				
	AN-016	AN-019	Average + s.d	AN-021	AN-022	AN-023	AN-024	Average + s.d
Zr/Nb	2.19	2.04	2.11 ± 0.11	1.98	1.86	1.91	1.92	1.92 ± 0.05
Nb/Ta	17.6	19.0	18.3 ± 0.98	16.2	17.0	16.7	16.7	16.7 ± 0.34
La/Nb	0.50	0.57	0.54 ± 0.05	0.47	0.46	0.46	0.47	0.46 ± 0.01
Ba/Nb	8.04	7.41	7.72 ± 0.44	5.65	5.55	5.48	5.41	5.53 ± 0.10
Ce/Pb	40.5	33.2	36.8 ± 5.14	53.0	183*	59.3	49.6	53.9 ± 4.90
$(La/Yb)_N$	34.7	36.3	35.5 ± 1.16	31.7	32.5	32.6	31.8	32.1 ± 0.46
$(La/Sm)_N$	5.28	6.05	5.67 ± 0.54	5.46	5.55	5.61	5.51	5.54 ± 0.06

* Note that samples AN-006 and AN-012 from the Tsirub North (outer) plug are excluded in calculating the average Ce/Pb because of their anomalously high and low Ce/Pb ratios, respectively. Also AN-022 from Tsirub South plug is excluded in calculating the average Ce/Pb because it has anomalously high Ce/Pb ratio owing to its much lower Pb content (see Table 4.1).

positive correlation between Ta/La and Nb/La ratios (Fig. 5.3d). In addition to higher HFSE/HFSE ratios, the outer plug has slightly higher Ba/Nb ratio (7.19 ± 1.51) than the inner plug (5.23 ± 0.68) (Table 5.1; Fig. 5.3f). Samples AN-006 (Ba/Nb = 9.14) and AN-012 (Ba/Nb = 10.1) from the outer plug are displaced to relatively high Ba/Nb ratio due to their anomalously high Ba contents. Nb/U and Ce/Pb ratios are high (e.g. Ce/Pb = 31.6 ± 5.09 for outer plug and 57.6 ± 15.6 for inner plug) and are slightly higher than those of OIB (Nb/U_{OIB} = 47, Ce/Pb_{OIB} = 25; Sun and McDonough, 1989).

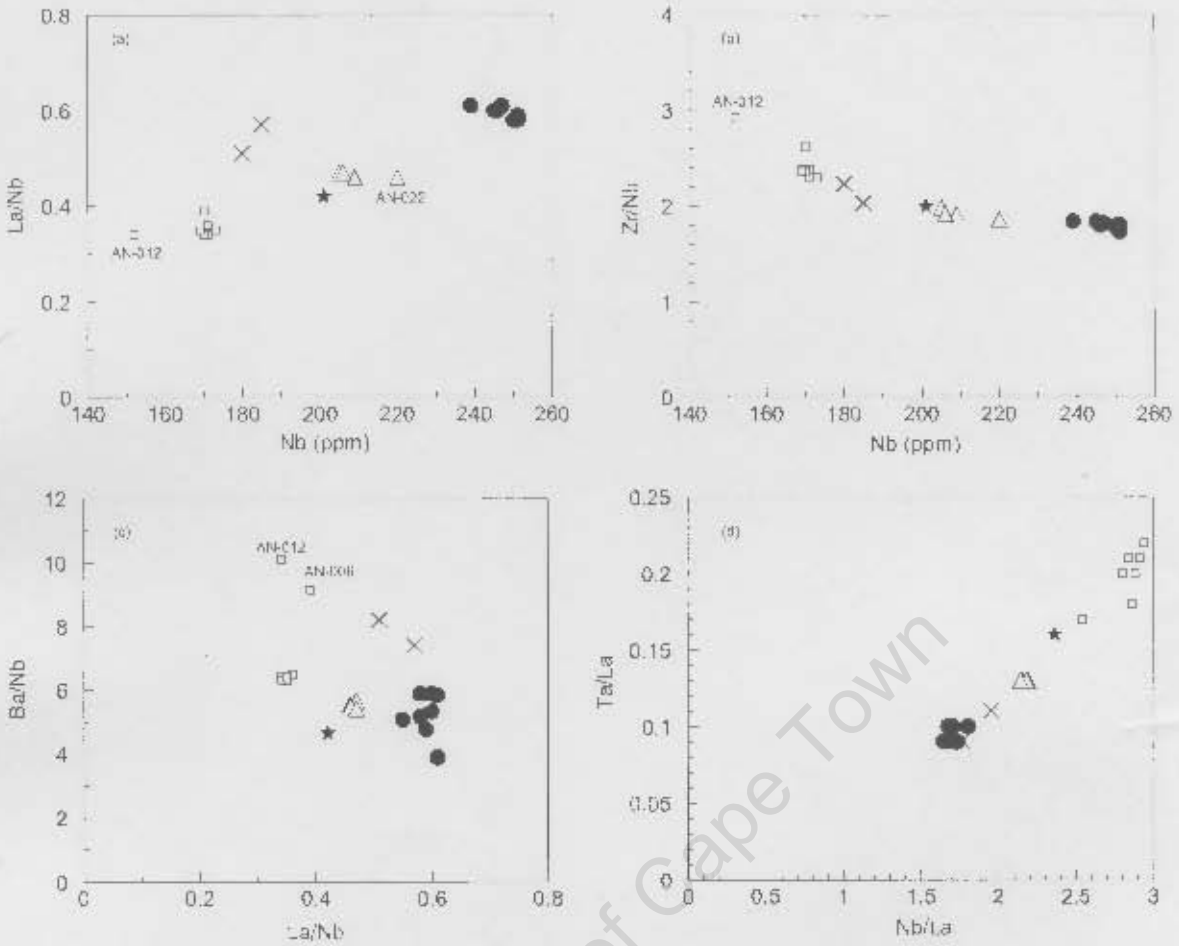

Fig. 5.3. Selected incompatible trace element ratios for Tsirub samples. Symbols are as in Fig. 5.1.

Samples AN-016 (Ba/Nb = 8.04) and AN-019 (Ba/Nb = 7.41) have slightly higher Ba/Nb ratios than the Tsirub North (outer) plug and Tsirub North (inner) plug. Their La/Nb and Zr/Nb ratios (La/Nb = 0.54 ± 0.05 and Zr/Nb = 2.11 ± 0.11) are intermediate between those of the Tsirub North (outer) plug and Tsirub North (inner) plug (Table 5.1; Fig. 5.3a and b)

Like the Tsirub dyke and samples AN-016 and AN-019, the Tsirub South plug shows La/Nb ratio (0.46 ± 0.01) intermediate between the Tsirub North (outer) plug and Tsirub North (inner) plug (Fig. 5.3a). The Tsirub South plug has a limited range of Ba/Nb (5.41 – 5.65) and Zr/Nb ratios (1.92 ± 0.05). The most striking geochemical features for this plug are the constant Th/La (0.12) and Th/Nb ratios (0.06). Nb/U ratio (72.8 – 89.8) and Ce/Pb ratio (53.9 ± 4.9) are high (Sun and McDonough, 1989).

Overall, all the Tsirub nephelinites and basanites are characterized by relatively moderate Ba/Nb ratio, low La/Nb and Zr/Nb ratios (Table 5.1; Fig. 5.3). These define a narrow negative trend between Zr/Nb ratio and Nb (Fig. 5.3b) and a positive trend between Ta/La and Nb/La (Fig. 5.3d). On the variation diagram of La/Nb versus Nb, the Tsirub samples fall on a positive trend except the outstanding samples AN-016 and AN-019 that are offset from this trend i.e. have much higher La/Nb ratio for a given Nb value.

5.3.2 Rare earth elements patterns

The chondrite normalised rare earth element (REE) patterns of the Tsirub intrusions are shown in Fig. 5.4 and their La/Yb_N ratios (where $_N$ denotes chondrite normalised) are reported in Table 5.1. In Fig. 5.4a, the average chondrite normalised REE abundances for each intrusion are plotted.

The Tsirub dyke shows steep chondrite REE patterns (La/Yb_N = 31.9; La as high as 359 times chondrite and Yb = 11.3 times chondrite) with no Eu anomaly (Fig. 5.4b). At Tsirub North, the outer plug and the inner plug show subparallel steep chondrite normalised REE patterns (Fig. 5.4c and d) where the latter shows steeper patterns (La/Yb_N = 37.8 ± 0.75) than the former (La/Yb_N = 23.4 ± 2.43). The inner plug is enriched in La and Yb up to 633 and 16.7 times chondrite, respectively, whereas the outer plug has La and Yb abundances up to 283 and 12.0 times chondrite, respectively. In addition, the inner plug also shows higher absolute light REE concentrations than the outer plug for a given magnesium number. Samples AN-016 (La/Yb_N = 34.7) and AN-019 (La/Yb_N = 36.3) also show light REE enriched chondrite normalised REE patterns (Fig. 5.4e), and samples from Tsirub South plug have La/Yb_N = 31.7 – 32.6 (Fig. 5.4f), with La and Yb enrichment up to 424 and 13.1 times chondrite, respectively.

Overall, the Tsirub intrusions show steep subparallel chondrite normalised REE patterns with the Tsirub North (inner) plug showing the highest chondrite normalised REE abundances whereas the Tsirub North (outer) plug shows the lowest chondrite normalised REE abundances.

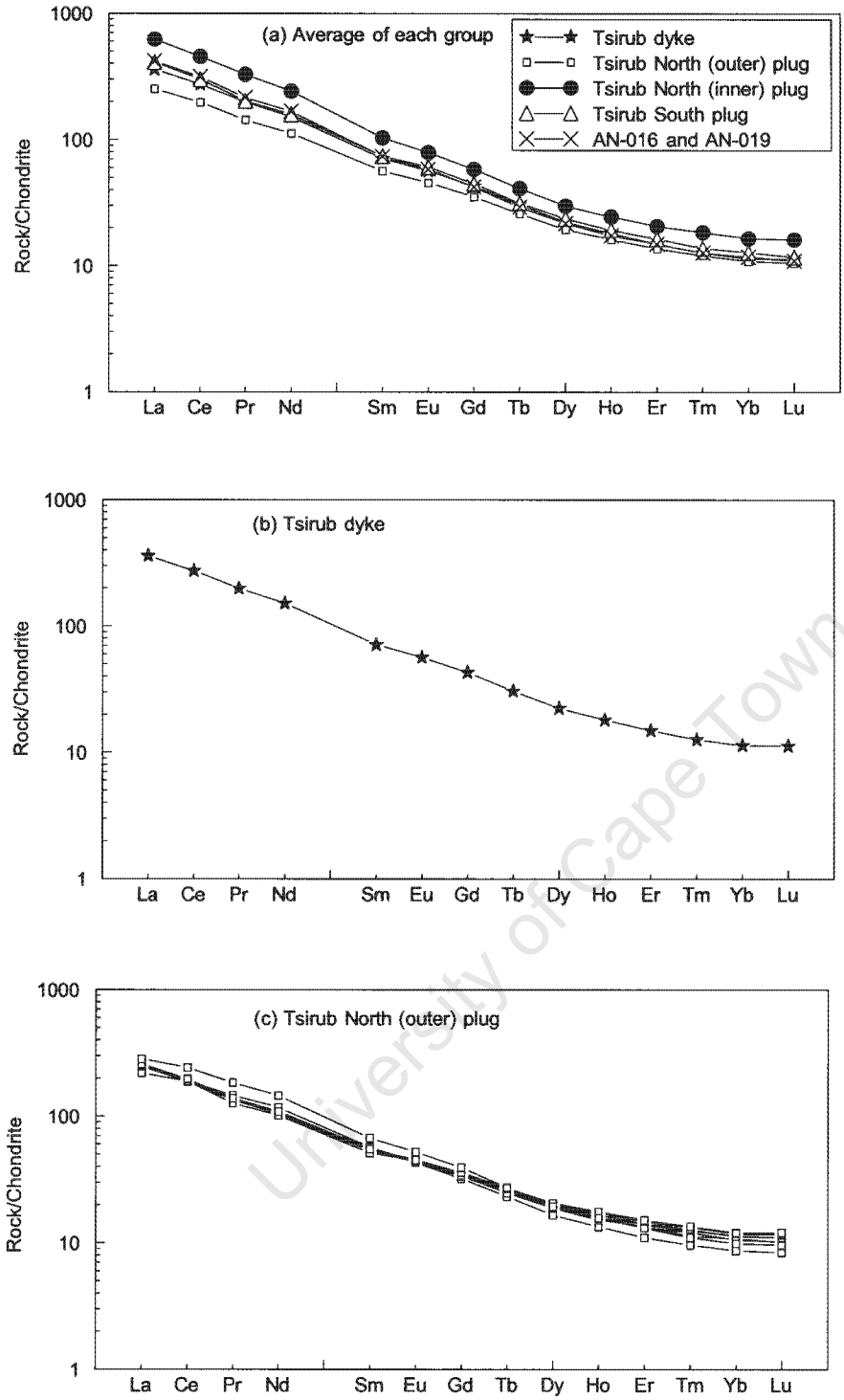

Fig. 5.4. Chondrite normalized REE patterns of Tsirub samples. In (a), the average chondrite normalised REE values of each compositional group are plotted. Chondrite normalising values are taken from Sun and McDonough (1989).

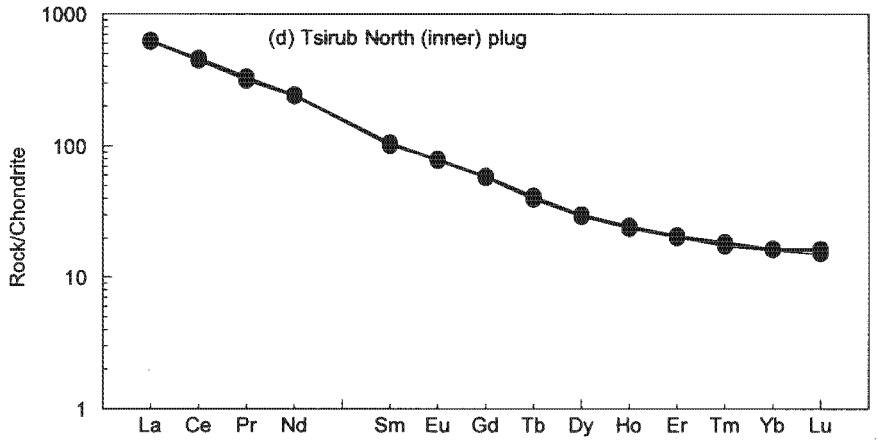

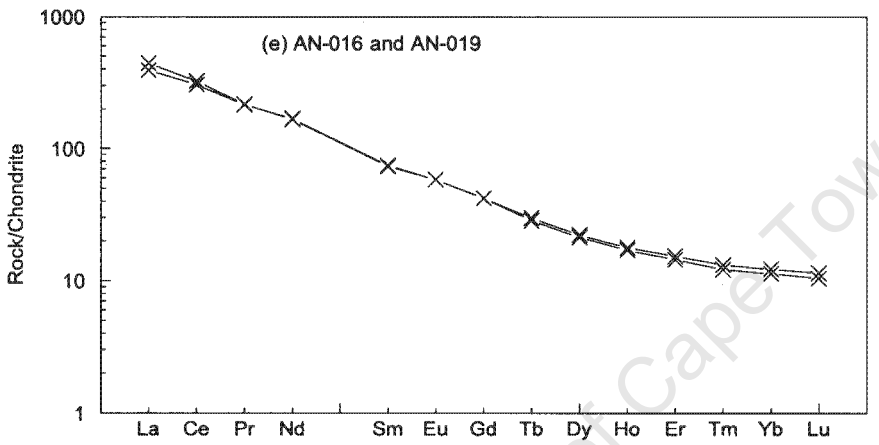

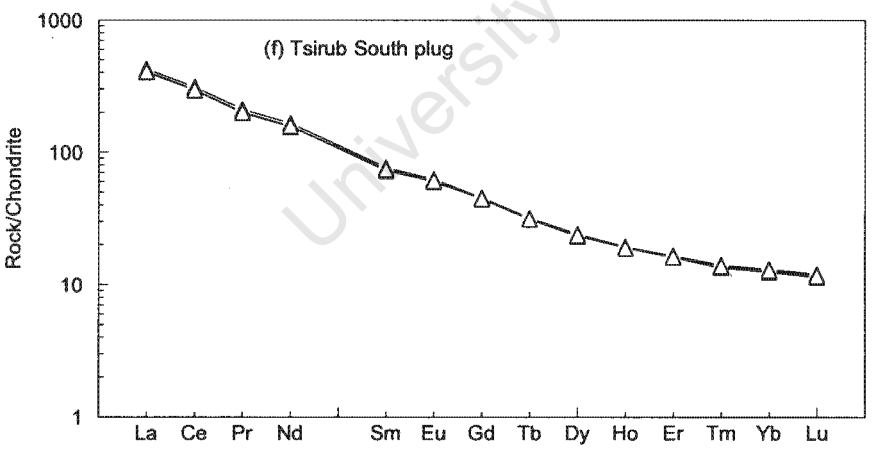

Fig. 5.4. Continued.

5.3.3 Primitive mantle normalised patterns

Incompatible trace elements in Tsirub samples are normalised to primitive mantle in Fig. 5.5 where the incompatible trace elements are arranged in order of decreasing incompatibility from left to right. Primitive mantle normalising values are taken from Sun and McDonough (1989).

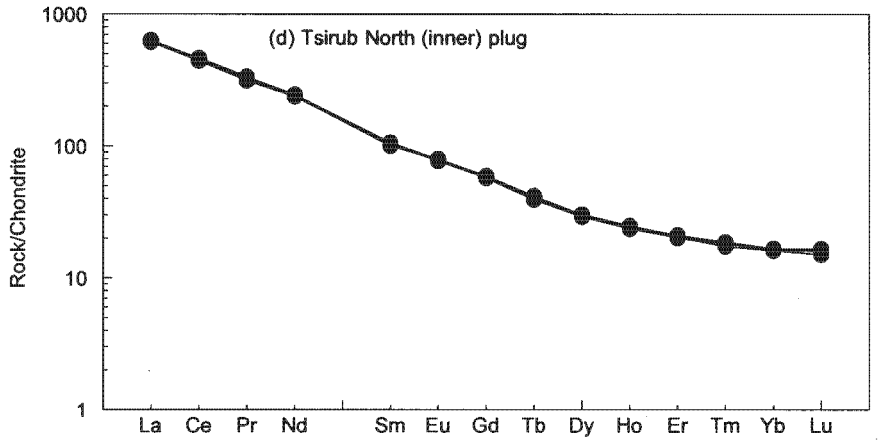

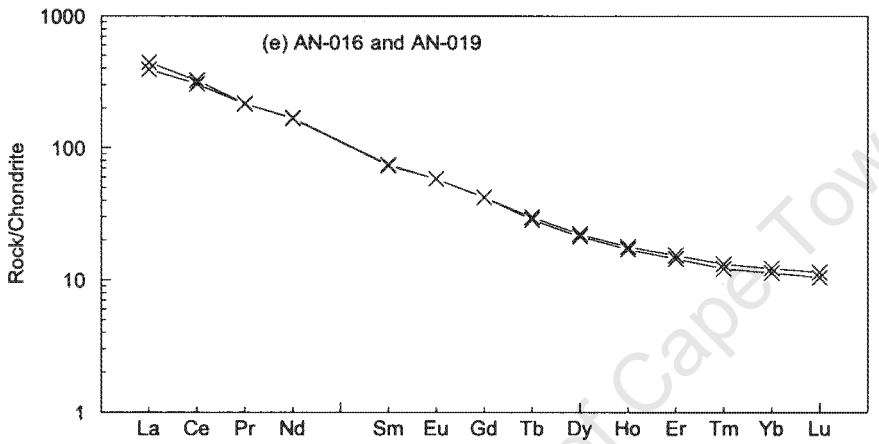

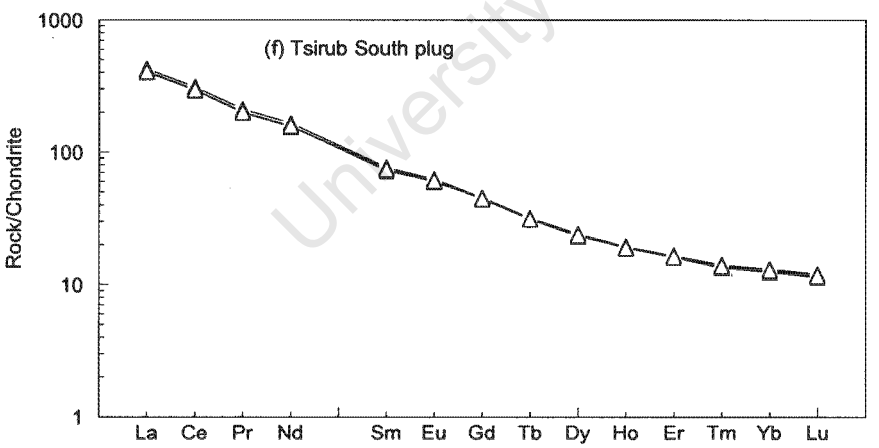

Fig. 5.4. Continued.

5.3.3 Primitive mantle normalised patterns

Incompatible trace elements in Tsirub samples are normalised to primitive mantle in Fig. 5.5 where the incompatible trace elements are arranged in order of decreasing incompatibility from left to right. Primitive mantle normalising values are taken from Sun and McDonough (1989).

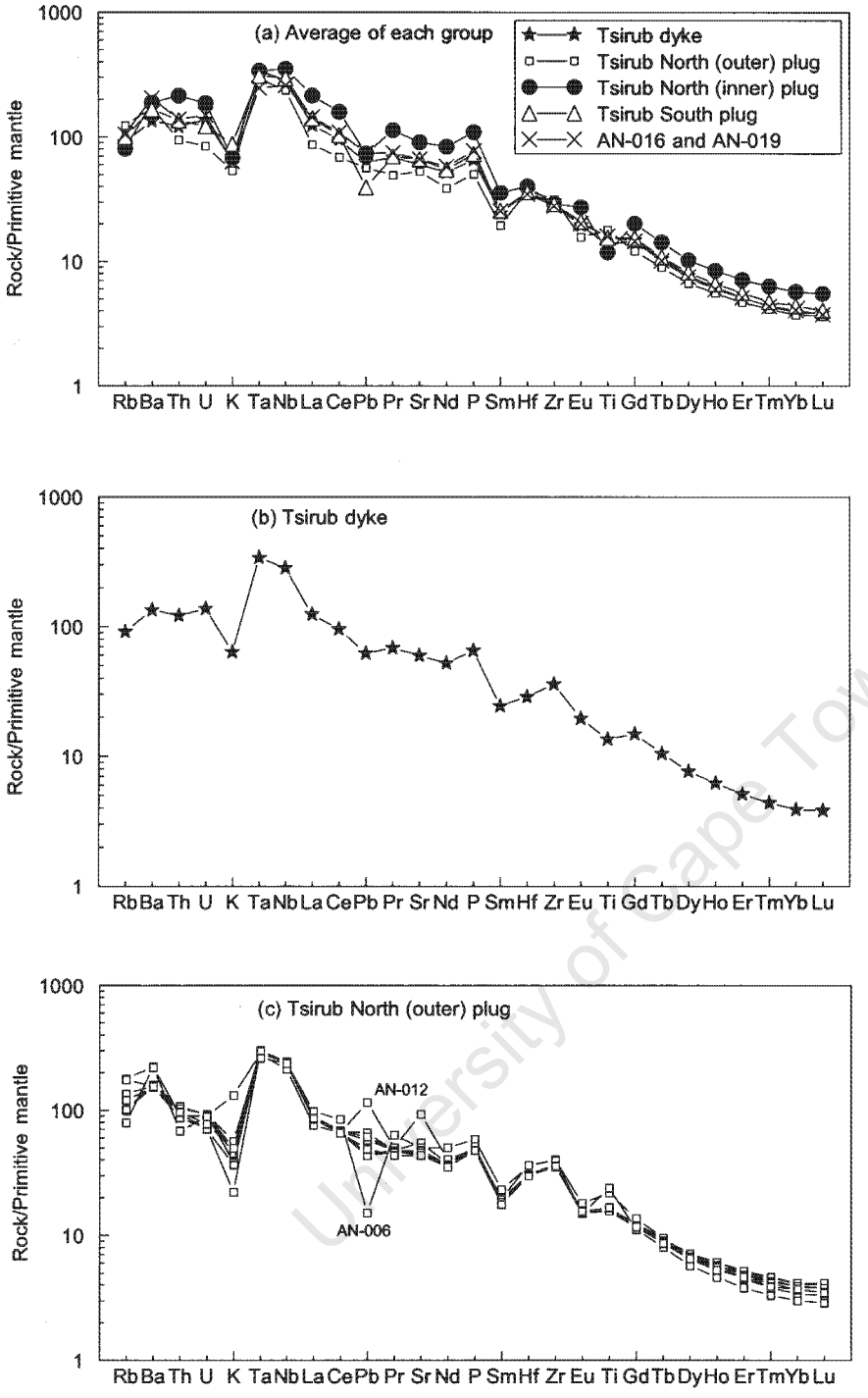

Fig. 5.5. Primitive mantle normalised patterns for Tsirub samples. Primitive mantle normalising values are taken from Sun and McDonough (1989).

The Tsirub samples are all enriched in incompatible trace elements relative to the primitive mantle, with strong enrichment (100 – 200 times primitive mantle) in the most highly incompatible trace elements (e.g. Ba, Th, Nb, Ta, La) relative to the less incompatible trace elements (~ 5 times primitive mantle) (Fig. 5.5a). Nb and Ta concentrations are typically 300 –

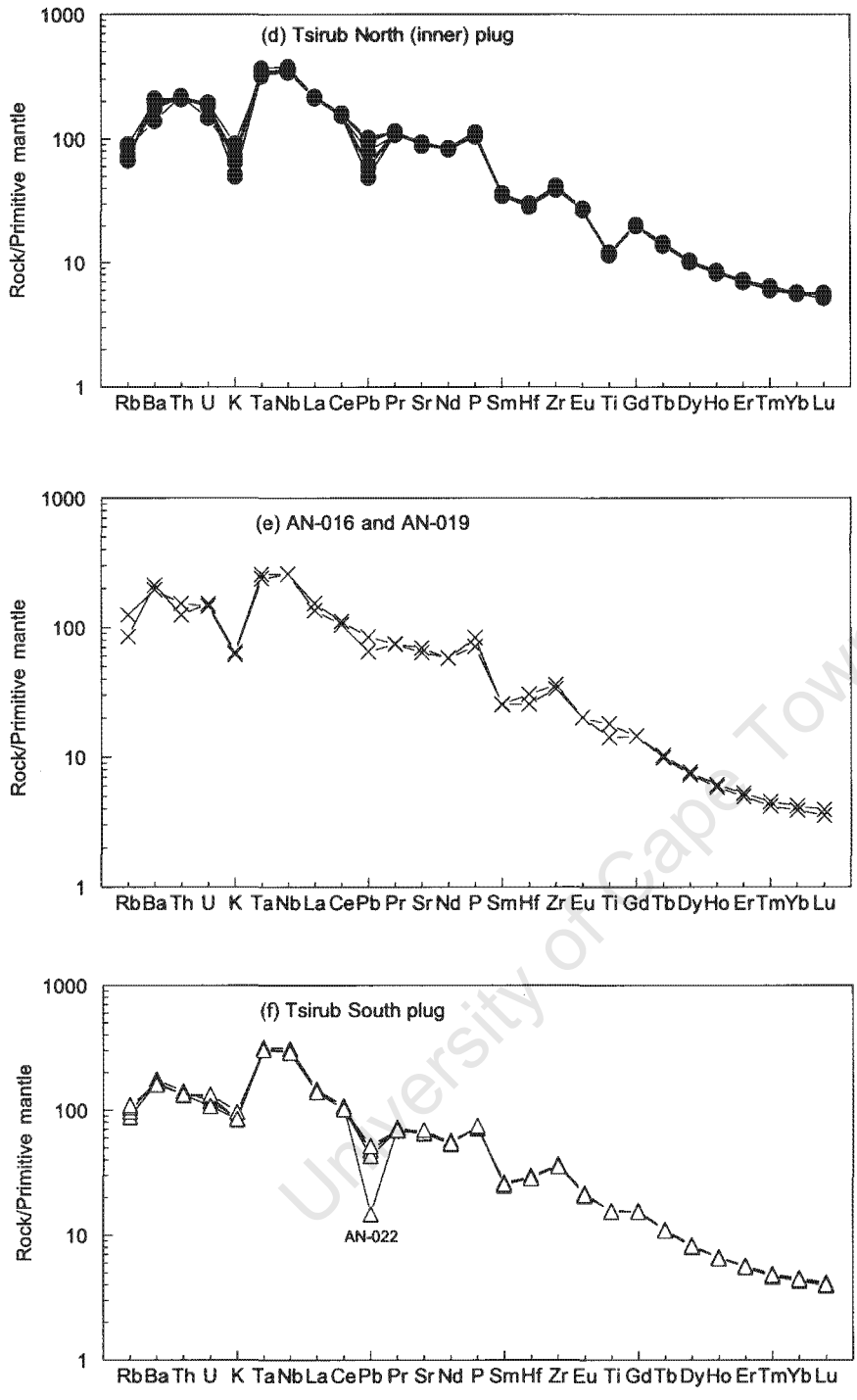

Fig. 5.5. Continued.

400 times primitive mantle. Overall, the primitive mantle normalised patterns for samples from each locality are similar having relative depletion in K compared to Th, U, La (e.g. K/Th = 1500 for Tsirub dyke, 1278 ± 369 for Tsirub North (outer) plug; 853 ± 126 for Tsirub North (inner) plug, 1323 ± 206 for AN-016 and AN-019 and 1876 ± 151 for Tsirub South plug), strong relative

enrichment in Nb-Ta and Zr-Hf and relative enrichment in P. Pb is variably enriched to depleted relative to the adjacent elements whereas the Tsirub North (inner) plug and Tsirub South plug have small negative Pb anomalies. Sample AN-022 from the Tsirub South plug is anomalous in showing a strong negative Pb anomaly relative to the other samples from the same plug (Fig. 5.5f). The entire samples of the Tsirub North (outer) plug, excepting AN-006 and AN-012, lack any Pb anomaly (Fig. 5.5c). One of these two anomalous samples, AN-012, has a positive Pb anomaly that may be due to crustal contamination or secondary alteration given its high LOI value (5.07 wt.%; Table 4.1). Another anomalous sample, from the Tsirub North (outer) plug, in terms of Pb abundance is sample AN-006 showing a negative Pb anomaly. Ti is also variably enriched to depleted relative to the adjacent elements whereas the Tsirub North (outer) plug shows a small positive Ti anomaly (Fig. 5.5d) and the Tsirub North (inner) plug has a small negative Ti anomaly.

Overall, the primitive mantle normalised patterns of the Tsirub samples are typical of continentally emplaced alkaline rocks (e.g. Panter *et al.*, 2006).

CHAPTER 6

ISOTOPE GEOCHEMISTRY

6.1 Introduction

Sr and Nd isotope ratios have been used in petrogenetic studies of alkaline rocks over the years as geochemical tracers of the nature of mantle source (depleted versus enriched source). Isotope ratios are good geochemical tracers of mantle sources compared to trace element ratios because unlike trace elements, they are not affected by fractionation events such as fractional crystallization and partial melting, nor are they affected by the nature of residual mineralogy of the source and are therefore characteristic of the source from which a magma is derived. For example La/Nb ratio, which is often used to discriminate between the lithospheric mantle and asthenospheric mantle (DePaolo and Daley, 2000), is in part controlled by the nature of the residual mineralogy because Nb is compatible in rutile (D^{Nb} =16 – 30, Ryerson and Watson, 1987) and ilmenite (Rollinson, 1993). Nb, which otherwise has similar incompatibility with La, will therefore be fractionated from La if rutile or ilmenite is present in the mantle residue at the time of partial melt extraction in which case the La/Nb ratio of the melt will not reflect that of the source

Applications of Sr and Nd isotopes have been useful in distinguishing between sub-continental lithospheric mantle (SCLM) and asthenospheric mantle sources for continental alkaline rocks (e.g. Paslick *et al.*, 1995; MacDonald, *et al.*, 2001; Janney *et al.*, 2002; Hoernle *et al.*, 2006). The asthenospheric mantle consists of high $^{143}Nd/^{144}Nd$ and low $^{87}Sr/^{86}Sr$ isotope ratios and therefore plots in the depleted mantle quadrant on the Nd-Sr isotope correlation diagram (e.g. Altherr *et al.*, 1990; Dosso *et al.*, 1991; le Roex *et al.*, 1992; Mahoney *et al.*, 1992; Volker *et al.*, 1993; Janney *et al.*, 2005; Nauret *et al.*, 2006). Therefore rocks derived from the asthenospheric mantle can be recognised on the basis of high Nd and low Sr isotope ratios. The Sr and Nd isotopic composition of the SCLM has been determined by a number of authors using mantle xenoliths, hosted by continental alkaline rocks, which are interpreted to represent direct samples of the SCLM (e.g. Menzies and Wass, 1983; Stosch and Lugmair, 1986; Witt-Eickschen and Kramm, 1998; Witt-Eickschen *et al.*, 1998; Pearson and Nowell, 2002; Witt-Eickschen *et al.*, 2003) therefore their

isotope ratios reflect that of the SCLM. Pioneering isotopic studies (e.g. Menzies and Murthy, 1980b; Richardson *et al.*, 1985; Hawkesworth *et al.*, 1990a; Carlson and Irving, 1994; Fan *et al.*, 2000; Pearson and Nowell, 2002; Downes *et al.*, 2003) on SCLM-derived xenoliths including xenoliths from southern Africa (Menzies and Murthy, 1980b; Richardson *et al.*, 1985; Hawkesworth *et al.*, 1990a) revealed that the SCLM ($^{87}Sr/^{86}Sr$ = 0.70223 – 0.70952 and $^{143}Nd/^{144}Nd$ = 0.51216- 0.51289) is variable in terms of Sr and Nd isotopic compositions because it plots in both the depleted field and enriched field on the Nd-Sr isotope correlation diagram.

Continental alkaline rocks have generally variable Sr and Nd isotopic compositions (e.g. Spriggs, 1988; Cebriá and López-Ruiz, 1995; Wilson *et al.*, 1995; Späth *et al.*, 2001; Janney *et al.*, 2002; Shaw *et al.*, 2003; Keller *et al.*, 2006). For example, Späth *et al.* (2001) reported a depleted Sr and Nd isotopic signature for Chyulu Hills nephelinites and basanites, southern Kenya. Similarly, Spriggs (1988) obtained low Sr isotope ratios (0.703728 – 0.703893) for Schwarzeberg nephelinite from southern Namibia. In contrast, le Roex *et al.* (2001) reported $^{143}Nd/^{144}Nd$ ratios for alkali basalts and basanites from Kenya Rift valley as low as 0.51239, i.e. have no depleted isotopic signature.

Since Rb, which decays to Sr by radioactive decay, is a mobile element the Rb-Sr system is sensitive to alteration and thus the $^{87}Sr/^{86}Sr$ ratio may be disturbed by alteration over time (Faure, 1986). The Rb-Sr system is also sensitive to crustal contamination because the continental crust is enriched in Rb such that crustal contamination results in elevated $^{87}Sr/^{86}Sr$ ratios (Davies *et al.*, 1985; Paslick *et al.*, 1995). It is therefore not easy to isolate the effects of alteration and crustal contamination on Sr isotopic composition. Unlike the Rb-Sr system, the Sm-Nd system is not affected by secondary alteration because Sm and Nd are immobile elements and therefore $^{143}Nd/^{144}Nd$ ratios remain unchanged by alteration. Also $^{143}Nd/^{144}Nd$ ratio is insensitive to crustal contamination because the concentrations of Sm and Nd in the continental crust are not that different to those in mafic magmas. Since isotope ratios are subject to changes in parent/daughter ratios due to secondary factors such as alteration and crustal contamination. It is the initial ratio that is of petrogenetic relevance and thus measured ratios need to be corrected for age.

Selected samples from each of the Tsirub intrusions have been analysed for Sr and Nd isotope ratios by mass spectrometer following procedures presented in Appendix B, section B.4. The $^{87}Sr/^{86}Sr$ and $^{143}Nd/^{144}Nd$ ratios of selected Tsirub samples were analysed in order to characterize their Sr and Nd isotope geochemistry and to document isotopic variations and similarities

between the three Tsirub intrusions. The isotope geochemistry is used to evaluate whether the composition of the Tsirub samples has been affected by alteration and crustal contamination, to document if the Tsirub intrusions are derived from a common mantle source, and to infer the nature and type of mantle from which the Tsirub rocks are derived i.e. whether they are produced by partial melting within the SCLM or the asthenospheric mantle. The latter three aspects are discussed in Chapter 7.

6.2 Sr and Nd isotopes

Results of Sr and Nd isotope analyses of selected Tsirub samples are reported in Table 6.1 and illustrated on a Nd-Sr isotope correlation diagram in Fig. 6.1. Also plotted for comparison on Fig. 6.1 are the Sr and Nd isotopic compositions of continental alkaline rocks and related rocks from southern Namibia and neighbouring South Africa (Spriggs, 1988; Davies *et al.*, 2001; Coe, 2004; Nowell *et al.*, 2004; Becker and le Roex, 2006) including Dicker Willem carbonatite (Cooper and Reid, 1998) and Namaqualand melilitites (Janney *et al.*, 2002). Isotope data of Erongo basanites and tephrites from northwest Namibia (Trumbull *et al.*, 2003) are also plotted on Fig. 6.1 for comparison. Since the age of the Tsirub rocks has not yet been determined, the initial $^{87}Sr/^{86}Sr$ and $^{143}Nd/^{144}Nd$ ratios presented in Table 6.1 were calculated using the age of the spatially related Dicker Willem carbonatite dated at 49 Ma (Reid *et al.*, 1990) and equations 6.1 and 6.2, respectively.

$$^{87}Sr/^{86}Sr = (^{87}Sr/^{86}Sr)_i + {}^{87}Rb/^{86}Sr(e^{\lambda t} - 1) \quad (6.1)$$

$$^{143}Nd/^{144}Nd = (^{143}Nd/^{144}Nd)_i + {}^{147}Sm/^{144}Nd(e^{\lambda t} - 1) \quad (6.2)$$

Where i = initial

λ = decay constant (Rb-Sr: 1.42×10^{-11} yr^{-1}; Sm-Nd: 6.54×10^{-12} yr^{-1})

t = age of rock (in million years)

Age correction to 49 Ma years leads to a correction of < 0.0001 for $^{87}Sr/^{86}Sr$ and < 0.00003 for $^{143}Nd/^{144}Nd$ ratios. ε_{Nd} presented in Table 6.1 is a measure of the deviation of $^{143}Nd/^{144}Nd$ ratio from a hypothetical chondritic uniform reservoir (CHUR) at time *(t)* and is calculated from equation 6.3 (DePaolo and Wasserburg, 1976). The epsilon values for the Tsirub samples were calculated in order to make inferences about the type of mantle source from which they are

derived i.e. depleted versus enriched mantle. A positive epsilon Nd value indicates derivation from a time-averaged depleted mantle source, whereas a negative epsilon Nd value point to an enriched mantle source (DePaolo and Wasserburg, 1976).

$$\varepsilon_{Nd} = [(^{143}Nd/^{144}Nd_{sample,\,t})/(^{143}Nd/^{144}Nd_{CHUR,\,t}) - 1] \times 10^4 \qquad (6.3)$$

Table 6.1. Measured and initial whole rock Sr and Nd isotope data for selected Tsirub samples. Initial Sr and Nd isotope ratios are calculated assuming an age of 49 Ma (Reid *et al.*, 1990). Subscripts m = measured, i = initial. Errors quoted for $^{87}Sr/^{86}Sr$ and $^{143}Nd/^{144}Nd$ represent $2\sigma_{mean}$ on in-run statistics and apply to the last quoted digits of the ratio.

	Tsirub dyke	Tsirub North plug					Tsirub South plug	
		Tsirub North (outer) plug		Tsirub North (inner) plug		AN-016 and AN-019		
	AN-001	AN-004	AN-005	AN-009	AN-011	AN-019	AN-021	AN-022
Rb (ppm)	57.8	64.2	62.6	56.2	47.4	78.8	55.7	61.5
Sr (ppm)	1260	917	1155	1883	1937	1461	1359	1374
Rb/Sr	0.05	0.07	0.05	0.03	0.02	0.05	0.04	0.04
$^{87}Rb/^{86}Sr$	0.133	0.202	0.157	0.086	0.071	0.156	0.119	0.129
$^{87}Sr/^{86}Sr_m$	0.703505	0.704039	0.704550	0.703512	0.703513	0.703455	0.703506	0.703695
2σ error	16	18	25	22	24	24	9	54
$^{87}Sr/^{86}Sr_i$	0.703412	0.703898	0.704441	0.703452	0.703463	0.703346	0.703423	0.703605
Sm (ppm)	10.8	8.38	8.44	15.6	16.2	11.2	11.3	11.7
Nd (ppm)	70.4	50.1	50.6	111	114	77.4	72.2	76.9
Sm/Nd	0.15	0.17	0.17	0.14	0.14	0.14	0.16	0.15
$^{147}Sm/^{144}Nd$	0.092	0.101	0.100	0.085	0.086	0.087	0.094	0.092
$^{143}Nd/^{144}Nd_m$	0.512786	0.512779	0.512814	0.512751	0.512759	0.512804	0.512805	0.512796
2σ error	22	14	20	10	16	24	12	7
$^{143}Nd/^{144}Nd_i$	0.512756	0.512747	0.512781	0.512724	0.512732	0.512776	0.512775	0.512767
$(\varepsilon Nd)_o$	2.88	2.76	3.43	2.20	2.36	3.24	3.26	3.09
$(\varepsilon Nd)_i$	3.54	3.36	4.03	2.90	3.06	3.93	3.91	3.75

Parameters used: λ for Rb-Sr = 1.42×10^{-11} yr^{-1} and for Sm-Nd = 6.54×10^{-12} yr^{-1};
$^{143}Nd/^{144}Nd_{CHUR} = 0.512638$ and $^{147}Sm/^{144}Nd_{CHUR} = 0.1967$

The Tsirub dyke ($^{87}Sr/^{86}Sr_i$ = 0.703412 and $^{143}Nd/^{144}Nd_i$ = 0.512756) plots within the depleted mantle quadrant at 49 Ma (ε_{Ndi} = 3.54) suggesting a relatively recent enrichment event to explain the high incompatible trace elements concentrations reported in Chapter 5. This explanation is also suggested for all the other Tsirub samples because they all show the same characteristics. This aspect is discussed further in Chapter 7.

Although the Tsirub North (outer) plug has similar initial Nd isotope ratios to the other Tsirub intrusions, it shows a wide range of, and more radiogenic, initial $^{87}Sr/^{86}Sr$ ratios (0.703898 – 0.704441), for a small variation in initial $^{143}Nd/^{144}Nd$ (0.512747 – 0.512781). The fact that this plug shows similar initial Nd isotope ratios (insensitive to alteration; Faure, 1986) to the other Tsirub intrusions may suggest that the initial Sr isotope composition of this plug has been

changed either by alteration (e.g. samples AN-006, AN-012 and AN-014) or crustal assimilation. Secondary alteration in the Tsirub North (outer) plug is evidenced by serpentine that partially or completely replaces olivine. The effect of alteration and crustal contamination on the composition of the Tsirub rocks is discussed further in the next chapter.

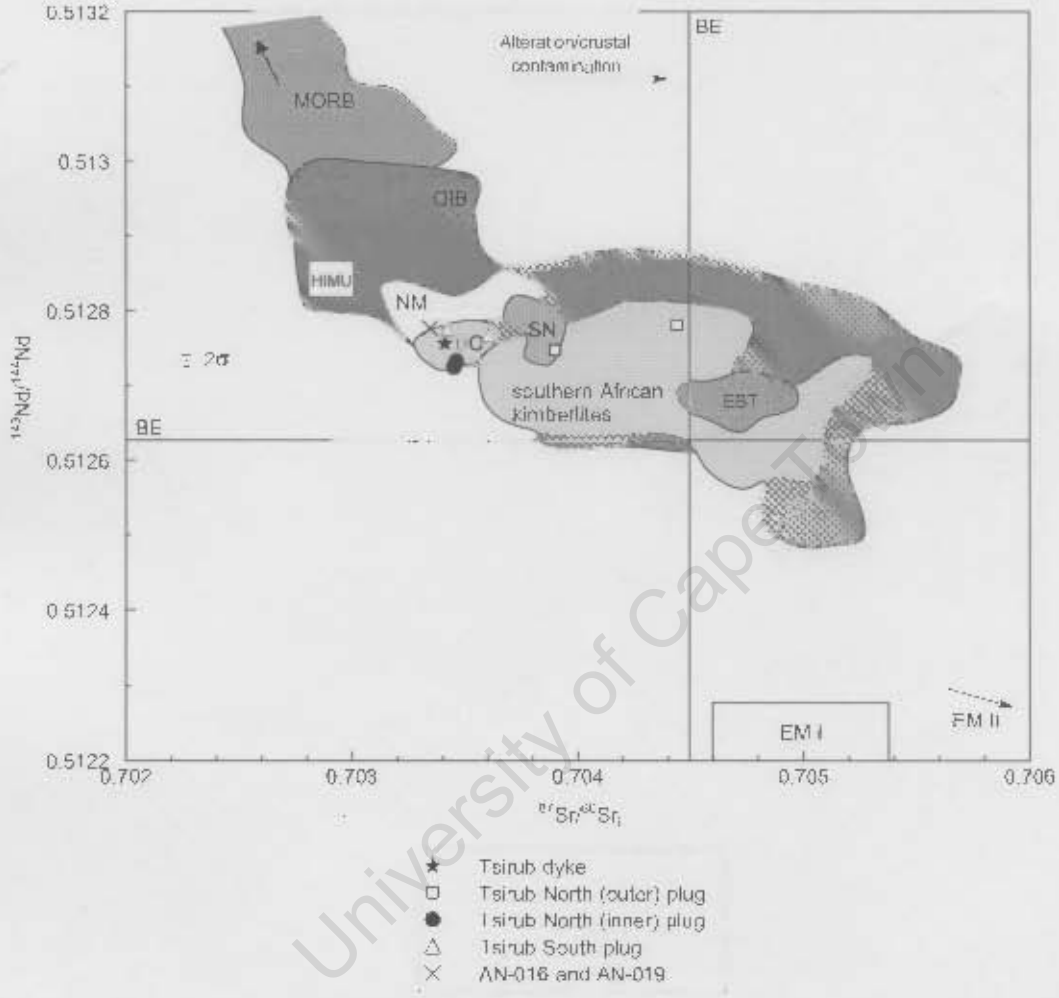

Fig. 6.1. Initial Nd-Sr isotope ratio correlation diagram for the Tsirub samples at 49 Ma. BE = Bulk Earth. Analytical error bars are shown and represent $2\sigma_{mean}$ errors. The compositions of the hypothetical mantle reservoirs (HIMU, EMI and EMII) are from Zindler and Hart (1986) and Hart (1988). Data for Dicker Willem carbonatite (DC) is from Cooper and Reid (1998), Schwarzeberg nephelinite (SN) from Spriggs (1988), Namaqualand melilitites (NM) from Janney *et al.* (2002), Erongo basanites-tephrites (EBT) from Trumbull *et al.* (2003), southern African kimberlites from Spriggs (1988); Davies *et al.* (2001); Coe (2004); Nowell *et al.* (2004); Becker and le Roex (2006). MORB data is from Zindler and Hart (1986) and references therein; Hegner and Pallister (1989); Altherr *et al.* (1990); Dosso *et al.* (1991); le Roex *et al.* (1992); Schilling *et al.* (1992); Mahoney *et al.* (1992); Volker *et al.* (1993); Janney *et al.* (2005); Naumet *et al.* (2006). Field for OIB include data from St Helena (Chaffey *et al.*, 1989), Cape Verde (Davies *et al.*, 1989), Tristan da Cunha (le Roex *et al.*, 1990), Inaccessible (Cliff *et al.*, 1991), Azores (Davies *et al.*, 1989; Widom *et al.*, 1997), Comores Archipelago (Späth *et al.*, 1996; Class and Goldstein, 1997; Class *et al.*, 1998), Canary Islands (Thomas *et al.*, 1999), Trindade (Siebel *et al.*, 2000), Martin Vaz (Siebel *et al.*, 2000), and Samoa island (Workman *et al.*, 2004).

On the Nd-Sr isotope correlation diagram, the Tsirub North (inner) plug plots in the depleted mantle guardant (ε_{Ndi} = 2.90 – 3.06) and they show narrow ranges of low initial $^{87}Sr/^{86}Sr$ (0.703452 – 0.703463) and $^{143}Nd/^{144}Nd$ ratios (0.512724 – 0.512732) (Fig. 6.1).

Samples AN-016 and AN-019, from the Tsirub North plug, with $^{87}Sr/^{86}Sr_i$ = 0.703346 and $^{143}Nd/^{144}Nd_i$ = 0.512776, show similar initial Sr and Nd isotope ratios to the other Tsirub samples and they plot in the depleted mantle quadrant (ε_{Ndi} = 3.93) on the Nd-Sr isotope correlation diagram.

The Tsirub South plug ($^{87}Sr/^{86}Sr_i$ = 0.703423 – 0.703605 and $^{143}Nd/^{144}Nd_i$ = 0.512767 – 0.512775) plots in the depleted mantle field (ε_{Ndi} = 3.75 – 3.91) on the Nd-Sr isotope correlation diagram.

In terms of inter-group variations, all the Tsirub intrusions excepting the Tsirub North (inner) plug show similar initial $^{87}Sr/^{86}Sr$ and $^{143}Nd/^{144}Nd$ ratios suggesting that the Tsirub dyke, Tsirub North (outer) plug, samples AN-016 and AN-019 and Tsirub South plug are derived from a common mantle source as discussed further in the next chapter. An exception to similar initial $^{87}Sr/^{86}Sr$ among the above groups (Tsirub dyke, Tsirub North (outer) plug, samples AN-016 and AN-019 and Tsirub South plug) is the Tsirub North (outer) plug that is displaced to elevated initial $^{87}Sr/^{86}Sr$ ratio as mentioned previously and attributed to alteration/crustal contamination. Tsirub North (inner) plug shows slightly lower initial $^{143}Nd/^{144}Nd$ relative to the other Tsirub intrusions implying that this plug is derived from a distinct source and this is further illustrated in Fig. 6.2 where the Tsirub intrusions are plotted on variation diagrams of initial $^{87}Sr/^{86}Sr$ and $^{143}Nd/^{144}Nd$ versus 1/Sr and 1/Nd, respectively. If the two altered samples from the Tsirub North (outer) plug, whose initial $^{87}Sr/^{86}Sr$ ratio has been disturbed by alteration/crustal contamination, are ignored there is a suggestion of a correlation between initial $^{87}Sr/^{86}Sr$ ratio and 1/Sr (Fig. 6.2a) but most particularly between $^{143}Nd/^{144}Nd$ and 1/Nd. In addition, on the variation diagram of $^{143}Nd/^{144}Nd$ versus 1/Nd the Tsirub dyke, samples AN-016 and AN-019 and the Tsirub South plug form a cluster whereas the Tsirub North (inner) plug occurs at much lower initial $^{143}Nd/^{144}Nd$ ratio (Fig. 6.2b) further supporting a different source for the latter.

In comparison to other continental alkaline rocks and related rocks from southern Namibia and neighbouring South Africa, the Tsirub intrusions (except the altered samples from the Tsirub North (outer) plug) plot in the field defined by the Dicker Willem carbonatite (Cooper and Reid,

1998) but have slightly lower initial $^{143}Nd/^{144}Nd$ ratio and comparable initial $^{87}Sr/^{86}Sr$ to that of the Namaqualand melilitites from the Western Cape olivine melilitite province, South Africa (Janney *et al.*, 2002) and southern African kimberlites (Spriggs, 1988; Davies *et al.*, 2001; Coe, 2004; Nowell *et al.*, 2004; Becker and le Roex, 2006), respectively. As a whole the Tsirub intrusions have similar initial Nd isotope ratios, but slightly lower initial Sr isotope ratios, to that of the Schwarzeberg nephelinite. When compared to the Erongo basanites and tephrites, northwest Namibia (Trumbull *et al.*, 2003) the Tsirub rocks are characterised by even much lower initial Sr isotope ratios.

When compared in Fig. 6.1 to the field of the global ocean island basalts (OIB) (e.g. Cliff *et al.*, 1991; le Roex *et al.*, 1990; Späth *et al.*, 1996; Class *et al.*, 1998; Thomas *et al.*, 1999; Workman *et al.*, 2004) that sample deep seated mantle plumes, the Tsirub intrusions plot in the OIB field suggesting that they carry a mantle plume signature. The role of a mantle plume in the generation of the Tsirub intrusions is discussed in Chapter 7. As a whole, the initial $^{143}Nd/^{144}Nd$ ratios of the Tsirub intrusions are much lower than those of mid-ocean ridge basalts (MORB) (e.g. Zindler and Hart, 1986 and references therein; Hegner and Pallister, 1989; Altherr *et al.*, 1990; le Roex *et al.*, 1992; Schilling *et al.*, 1992; Volker *et al.*, 1993; Janney *et al.*, 2005) that sample the asthenospheric mantle (le Roux *et al.*, 2002b).

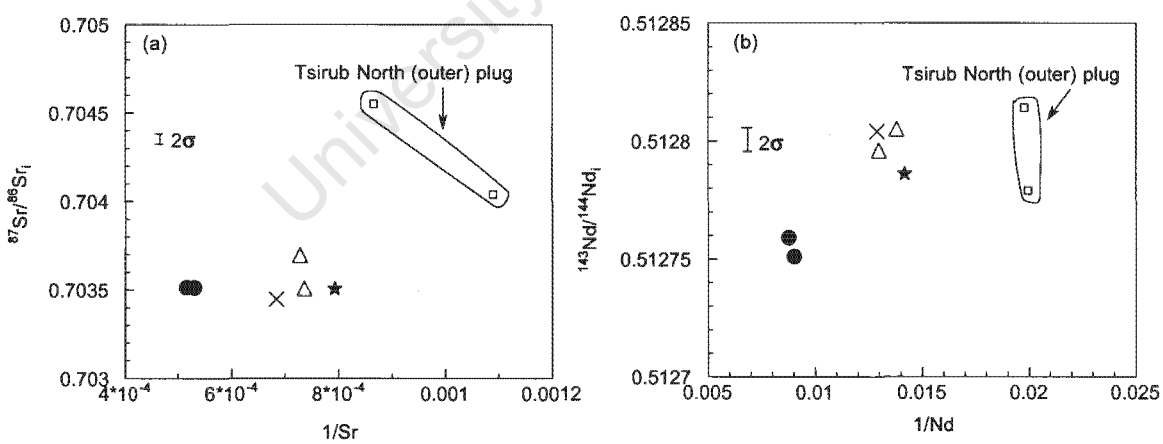

Fig. 6.2. Variations of initial Sr and Nd isotope ratios between the Tsirub intrusions. Analytical error bars are shown and represent $2\sigma_{mean}$ errors. Symbols are as in Fig. 6.1.

CHAPTER 7

PETROGENESIS

7.1 Introduction

The enrichment of incompatible trace elements in continental alkaline rocks has prompted igneous petrologists as early as in the 1970s (e.g. Gast, 1968; Kay and Gast, 1973; Frey *et al.* 1978) to conduct experiments to investigate the origin of such enrichment. The experimental work of Brey (1978); Olafsson and Eggler (1983); and Kushiro (1996) concluded that incompatible trace element enrichment in such rocks is due to derivation from low degrees of partial melting of a carbonated peridotite at high pressures, e.g. 20 -25 kbar for nephelinitic magmas. The work of Frey *et al.* (1978); Sun and Hanson (1975) and Menzies and Murphy (1980c) have proposed that a metasomatic event prior to low degrees of partial melting partially contributes to the high incompatible elements in continental alkaline rocks. Studies of natural continental alkaline rocks also reached similar conclusions and have attributed high concentrations of incompatible trace elements to low degrees of partial melting (e.g. Simonetti *et al.*, 1998; Panter *et al.*, 2000; MacDonald *et al.*, 2001; Jung *et al.*, 2006; Keller *et al.*, 2006) of a metasomatically enriched mantle source (Wass and Rogers, 1980; Hawkesworth *et al.*, 1990b; le Roex *et al.*, 2001; Späth *et al.*, 2001).

Although the location of the mantle source region of alkaline rocks has received a lot of debate over the years (e.g. Wilson and Downes, 1991; Cebriá and López-Ruiz, 1995; Wilson *et al.*, 1995; Weinstein, 2000; Späth *et al.*, 2001; Janney *et al.*, 2002; Jung *et al.*, 2006) this issue is still poorly resolved. The common question is whether continental alkaline rocks are derived by partial melting within the sub-continental lithospheric mantle (SCLM), within the asthenospheric mantle, or by direct melting of a mantle plume. Various geochemical parameters that can distinguish between these mantle sources have been put forward. Trumbull *et al.* (2003) argued that the Erongo basanite-tephrite plugs from northwest Namibia formed by direct melting of a mantle plume, the Tristan plume. These authors argued that the initial magmas, Etendeka tholeiites, generated in the Erongo area are derived from partial melting within the SCLM but with time extensive thinning of the lithosphere allowed decompression melting of the underlying and rising Tristan mantle plume, giving rise to the Erongo basanite-tephrite plugs. Trumbull *et al.* (2003) based their argument for a mantle plume origin on the basis that the Erongo basanite-

tephrite plugs have Sr, Nd and Pb isotope ratios that closely resemble those of the Tristan plume as sampled by basalts on Tristan da Cunha island. Authors in favour of an asthenospheric mantle source (Jung and Masberg, 1998) argue that depleted Nd-Sr isotopic signatures are indicative of an asthenospheric mantle source. In contrast, some workers argue that relative K depletion in many primitive mafic alkaline magmas is characteristic of amphibole-bearing lithospheric mantle sources (Wass and Rogers, 1980; Francis and Ludden, 1995; le Roex *et al.*, 2001; Späth *et al.*, 2001; Weinstein *et al.*, 2006). In addition, a plume signature in continental alkaline rocks (i.e. with incompatible trace element signatures and isotope ratios that are similar to that of OIB) that show a relative K depletion, has been attributed to involvement of a mantle plume in their generation where a mantle plume serves only as a source of heat and as a source of incompatible trace element-rich fluids that metasomatise, and introduce metasomatic amphibole into, the overlying SCLM (e.g. Späth *et al.*, 2001)

Before discussing the petrogenesis of the Tsirub intrusions, the role of alteration and crustal contamination in contributing to their observed elemental and isotopic composition is considered. Thereafter, relationships between the Tsirub intrusions will be discussed as to whether they are related to each other by variable degrees of fractional crystallization or partial melting. Degrees of partial melting giving rise to the Tsirub rocks are quantified using quantitative forward modelling of REE, with particular emphasis on constraints that can be placed on the modal mineralogy (e.g. spinel lherzolite versus garnet lherzolite) of the mantle source region. The physical location of the mantle source region, i.e. whether it is located within or below the SCLM, will then be considered.

7.2 Role of alteration and crustal contamination

Before using geochemical data to make inferences on petrogenetic processes and source region characteristics, the effects of alteration and crustal contamination on the composition of the concerned rocks must first be evaluated. Secondary alteration can modify the concentration of mobile elements such as Ba, Rb and K. The composition of continentally emplaced alkaline rocks may be modified during crustal contamination whereby the concentration of elements that are significantly enriched (e.g. Pb; Hofmann *et al.* 1986) or depleted (e.g. Nb, Ta; Green, 1995; Weaver, 1991b) in the continental crust may increase or decrease, respectively. In this section the

role of alteration and crustal contamination on the major and trace element and isotope composition of the Tsirub samples is evaluated.

The effect of alteration on the major element composition of the Tsirub rocks can be inferred from their volatile contents that are reported as LOI in Table 4.1. Elevated LOI values suggest significant alteration. The majority of Tsirub samples show moderate LOI contents i.e. below 3.00 wt.%. Samples AN-012 (LOI = 5.07 wt.%) and AN-014 (LOI = 3.74 wt.%), from the Tsirub North (outer) plug have more elevated LOI values and therefore these two samples may have suffered significant alteration. In addition, one of these samples, AN-012, is anomalous in showing a positive Pb anomaly as reported in Chapter 5. This positive Pb anomaly might be caused either by alteration or crustal contamination (e.g. le Roex *et al.*, 2001). The lack of correlation between mobile incompatible trace elements and immobile incompatible trace elements is often taken to indicate some degree of alkali element mobility during alteration (Weinstein, 2000). Given their similar degrees of incompatibility, K, Rb, Ba and Nb (Späth *et al.*, 2001) are expected to show similar geochemical behaviour during partial melting but K, Rb, Ba can be fractioned from Nb (and other immobile incompatible trace elements) during secondary alteration due to their mobile nature. The effect of alteration on Tsirub samples is illustrated in Fig. 7.1 where mobile incompatible trace elements (K, Rb) are plotted versus immobile incompatible trace elements of similar incompatibility (e.g. Nb). The lack of correlation between K, Rb and Zr or Nb suggests that K and Rb were mobilized during secondary processes. For example, the size of the present-day negative K anomaly observed in the Tsirub rocks, as reported in Chapter 5, could be smaller or larger than the initial anomaly prior to alteration. Petrographic evidence for low temperature alteration in the Tsirub nephelinites and basanites is provided by the presence of serpentine, which partially or completely replaces olivine (see Chapter 3).

Since alteration and crustal contamination can both result in elevated Sr isotope ratios (Dejonghe *et al.*, 1998; Harris *et al.*, 1999; MacDonald *et al.*, 2001; Kokfelt *et al.*, 2006; Panter *et al.*, 2006) it is sometimes difficult to separate the effect of the two processes. Therefore the wide range of elevated initial Sr isotope ratios for a small variation in initial Nd isotope ratios in the Tsirub North (outer) plug suggest that its Rb-Sr system has not remained closed, but was disturbed by alteration or crustal contamination. From this point forward, samples that show extreme signs of alteration (i.e. high LOI contents, highly altered olivine phenocrysts) such as AN-006, AN-012 and AN-014 (Table 4.1) are excluded from the quantitative geochemical modelling and interpretations presented in this chapter.

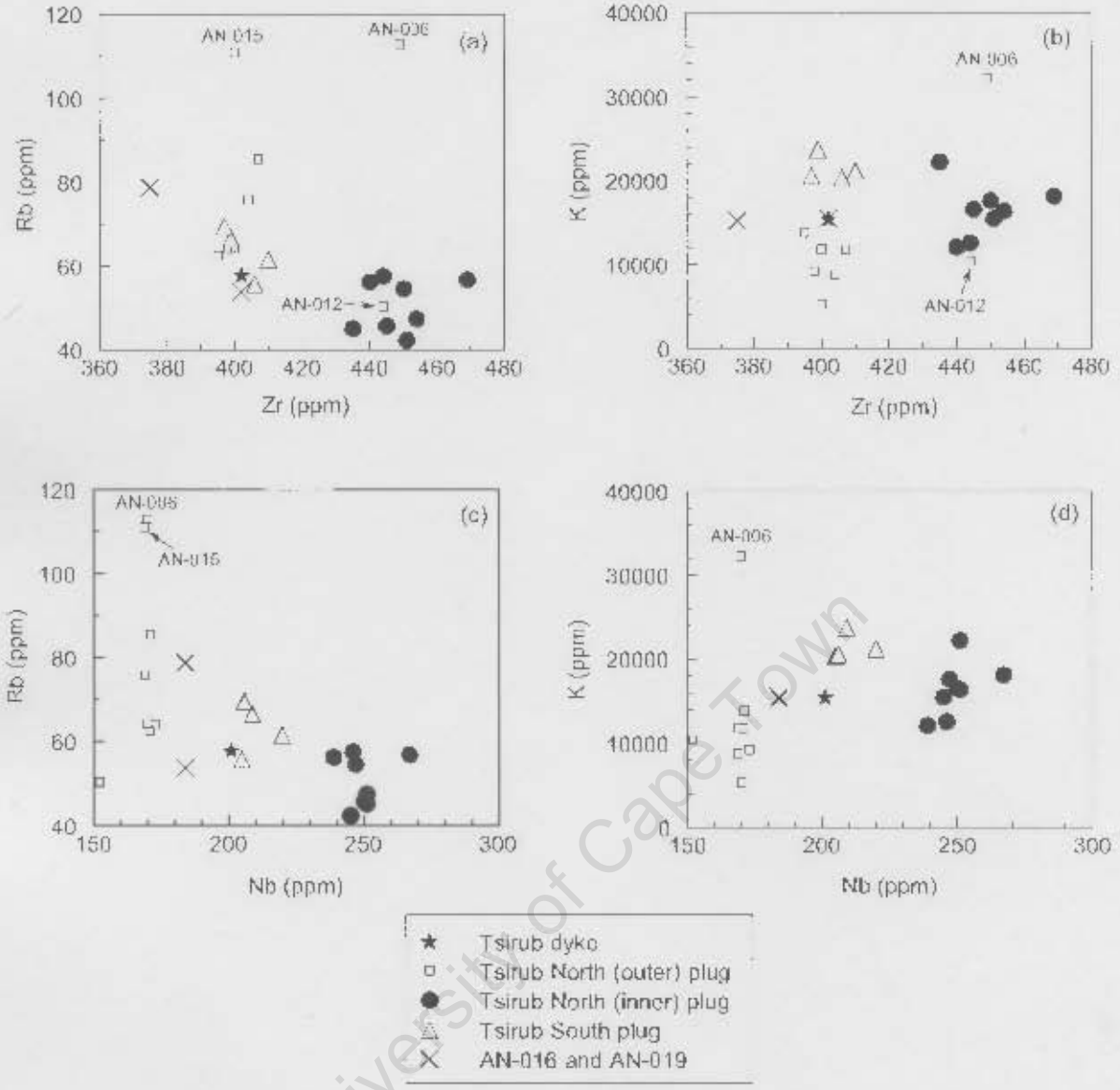

Fig. 7.1. Variations of selected highly mobile incompatible trace elements with immobile incompatible trace elements of comparable degree of incompatibility.

The presence of the felsic xenoliths comprising alkali feldspar and clinopyroxene in some of the Tsirub intrusions including the Tsirub North (inner) plug, as reported in Chapter 3, indicate interaction of the parental magmas with the continental crust shortly prior to eruption. However, the absence of a positive Pb anomaly suggests that the amount of felsic continental crust assimilated by the parental magmas was small (Panter *et al.*, 2000; le Roex *et al.*, 2001). Additionally, the occurrence of an ultramafic xenolith in the Tsirub North (inner) plug suggests rapid ascend *en route* to the surface, and therefore limited time interaction of the host magma with the surrounding continental crust.

7.3 Relationship between the Tsirub intrusions

The question addressed in this section is whether the observed variations in major and trace element concentrations within the Tsirub intrusions is a result of variable degrees of fractional crystallization of a common primitive magma or a consequence of variation in the degrees of partial melting of a common source. Rocks that share a common mantle source are often recognised on the basis of similar isotope ratios (e.g. Rogers *et al.*, 1992; Franz *et al.*, 1999; Gibson *et al.*, 2006), parallel chondrite normalised REE patterns (Zhang and O'Reilly, 1997; Franz *et al.*, 1999) and near identical incompatible trace elements ratios (le Roex *et al.*, 2001). On the basis of their similar initial Sr and Nd isotope ratios, the Tsirub dyke, Tsirub North (outer) plug, samples AN-016 and AN-019 and the Tsirub South plug are suggested to be derived from a common mantle source and therefore their relationships will be evaluated. The Tsirub North (inner) plug has lower initial Nd isotope ratios, but similar Sr isotope ratios to the other Tsirub samples (see Chapter 6, Fig. 6.1), suggesting derivation from a distinct source and therefore this plug will be treated separately.

7.3.1 Fractional crystallization

Fractional crystallization is one of the important petrogenetic processes that may significantly change the composition of primitive magmas. This process results in a decrease of major element oxides and compatible trace elements accommodated in the fractionating phases, accompanied by a relative increase in the concentration of major element oxides (not accommodated in the fractionating phases) and incompatible trace elements. Fractional crystallization of olivine results in a decrease of MgO, Ni and Co concentrations (the latter two being compatible in olivine; Hart and Davis, 1978; Cox *et al.*, 1979) and the increase of other major oxides and incompatible trace elements. In comparison, clinopyroxene fractional crystallization causes decrease in CaO and MgO content (e.g. Zhi *et al.*, 1990; Hoernle and Schmincke, 1993; Class *et al.*, 1994; Späth *et al.*, 2000; le Roux *et al.*, 2002a; Mattsson and Oskarsson, 2005) and increase in other major elements oxides (e.g. Al_2O_3) and incompatible trace elements contents. Therefore MgO and CaO concentrations of a magma undergoing both olivine and clinopyroxene fractional crystallization are expected to decrease with increasing degrees of fractional crystallization and its composition progressively moves away that of a typical primary magma (Mg# = 0.68 - 0.75, Ni = 300 – 400 ppm; Sun and Hanson, 1975b; Frey *et al.*, 1978). Mg# below this range are frequently taken to

indicate the effect of fractional crystallization (Jung and Masberg, 1998; Sayona *et al.*, 2000; Keller *et al.*, 2006; Weinstein *et al.*, 2006) whereas values greater than 0.75 indicate accumulation of mafic phases such as olivine (e.g. Hart and Davis, 1978; Späth *et al.*, 2000). The Mg# of the Tsirub intrusions (Mg# = 0.61 – 0.66) falls slightly below the range widely accepted for primary melts, consistent with effect of minor olivine and clinopyroxene fractional crystallization. An exception is the Tsirub dyke (Mg# = 0.71 and Ni = 309 ppm) which shows a typical primary magma composition. Minor, rather than extensive, amount of fractional crystallization within each intrusion is supported by the limited variation of Mg# shown by the analysed samples.

Since olivine and clinopyroxene are the only phenocryst/microphenocryst phases in the Tsirub samples, the two critical oxides to consider are MgO and CaO. The depletion of CaO content with degreasing MgO, reported in Chapter 4, provides evidence for clinopyroxene fractionation. This argument is further strengthened by the positive correlation between CaO/Al_2O_3 ratio and MgO (not shown). Equally important, the dominance of olivine over clinopyroxene in the phenocryst/microphenocryst assemblage suggests that olivine dominated the early fractional crystallization history of the Tsirub intrusions.

To determine if the Tsirub dyke, Tsirub North (outer) plug and Tsirub South plug may be related by variable degrees of olivine and clinopyroxene fractionation from a common primitive magma, variation diagrams of Ni and selected incompatible trace elements (Nb, Th and Ce) versus MgO as index of differentiation are plotted in Fig. 7.2. Since the Tsirub dyke has the most primitive composition in terms of its Mg#, Ni and Cr contents it is assumed to be the parental magma. Also shown in Fig. 7.2 are fractional crystallization trends of olivine alone and combined olivine plus clinopyroxene in the ratio of 6:4. This ratio was chosen based on the dominance of olivine over clinopyroxene in these rocks. MgO content calculated by continuously removing the composition of the fractionating phases, olivine and clinopyroxene, from the Tsirub dyke and using the equation MgO = [MgO(rock)*(1-F] – [MgO(mineral)*(F/100)]. The most primitive olivine (MgO = 47.66 wt.%) and clinopyroxene (MgO = 14.39 wt.%) phenocrysts were chosen as starting compositions. Variation in Ni, Nb, Th and Ce concentration during fractional crystallization is calculated using fractional crystallization equation of Gast (1968) and partition coefficients (except for Ni) presented in Table 7.1. The partition coefficient for Ni in olivine was calculated using the equation 124/MgO - 0.9 (Hart and Davis, 1978). Since the partition coefficient for Ni in olivine changes with variations in MgO content, i.e. with degrees of fractionation, the partition

coefficient for Ni was calculated for each degree of fractionation. For example, the Ni partition coefficient for 8% olivine fractionation was calculated using MgO content calculated for 7% fractionation. It is clear that the slopes of olivine and combined olivine and clinopyroxene fractional crystallization trends are similar suggesting that the role of clinopyroxene during the differentiation of the Tsirub dyke is minor. The calculated fractional crystallization trends also indicate that the Tsirub North (outer) plug and the Tsirub South plug are not obviously related to the Tsirub dyke by olivine plus clinopyroxene fractionation. Rather, it is suggested that each of the Tsirub intrusions represent a distinct magma body that underwent independent minor olivine and clinopyroxene fractional crystallization.

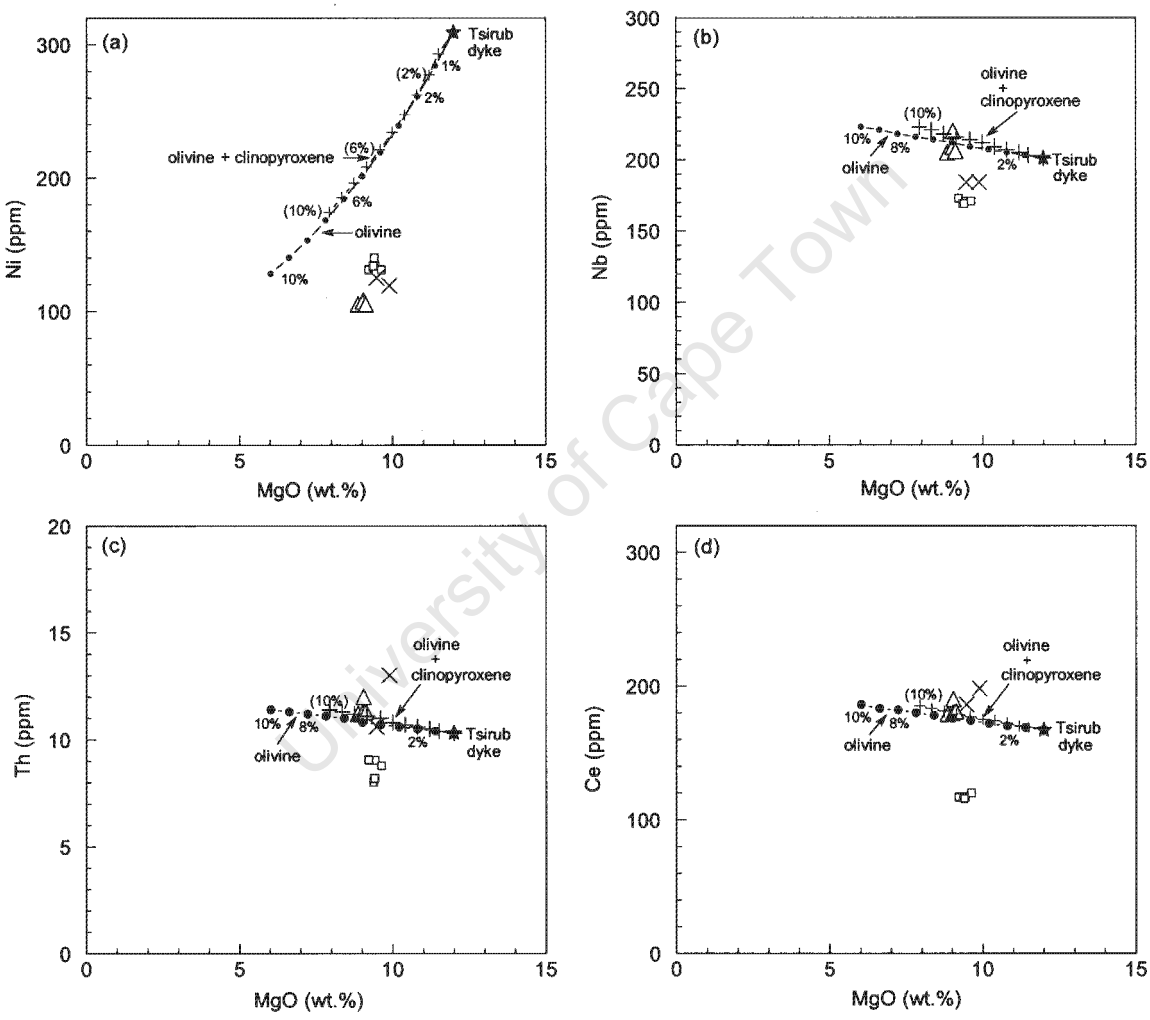

Fig. 7.2. Plot of Ni, Nb, Th and Ce (in ppm) versus MgO (in wt.%). Also shown are the fractional crystallization trends of olivine and combined olivine and clinopyroxene in the ratio 6:4. Variation in Ni concentration during fractional crystallization is calculated using fractional crystallization equation of Gast (1968). Partition coefficients for Ni in olivine and clinopyroxene used are 124/MgO - 0.9 and 2, respectively (Späth *et al.*, 1996 and references therein). Incompatible trace element variation calculated as for Ni using partition coefficients presented in Table 7.1. MgO content calculated by continuously removing the composition of the fractionating phases from the Tsirub dyke. Symbols are as in Fig 7.1.

7.3.2 Partial melting

As mentioned earlier, high concentration of incompatible trace elements in primitive alkaline rocks is often argued to indicate origin by low degrees of partial melting (e.g. Erlank *et al.*, 1982; Pearce, 1996; Bernstein *et al.*, 2000; Cebriá *et al.*, 2000; MacDonald *et al.*, 2001; Keller *et al.*, 2006) of a metasomatically enriched mantle source (e.g. Wass and Rogers, 1980; le Roex *et al.*, 2001; Späth *et al.*, 2001). Therefore, the relative degrees of partial melting for primitive lavas may be inferred from the concentration of incompatible trace elements as carried out below for the Tsirub intrusions. Thereafter, the degrees of partial melting giving rise to the Tsirub rocks are quantified using REE modelling approach.

7.3.2.1 Relative degrees and depth of partial melting

The high concentrations of incompatible trace elements e.g. Nb, Zr in the Tsirub rocks (coupled with their silica undersaturated nature) suggests that they are derived from relatively low degrees of partial melting. Further evidence for origin by low degrees of partial melting is provided by high La/Yb_N ratios (e.g. $La/Yb_N = 36.7 - 39.4$ for Tsirub North (inner) plug). The high La/Yb_N ratio may also suggests a role of residual garnet because garnet has higher partition coefficients for heavy REE relative to the light REE (e.g. Wilson, 1989; Bernstein *et al.*, 2000; Kamber, 2000; Siebel *et al.*, 2000; Jung *et al.*, 2006; Keller *et al.*, 2006), or a strongly light REE enriched source. The lower incompatible trace elements contents of the Tsirub North (outer) plug relative to the other Tsirub intrusions (that appear to share a common mantle source) suggests that the former is generated by comparatively higher degrees of partial melting than the latter.

According to Gast (1968) and Fiegenson *et al.* (1996) systematic variations in REE concentrations for a set of cogenetic lavas can be used to constrain the degrees or conditions of mantle partial melting using constrained forward modelling approach. A number of workers have used this quantitative REE modelling approach in constraining the amount of degrees of partial melting for similar mafic continental alkaline rocks (Jung and Masberg, 1998; le Roex *et al.*, 2001; Späth *et al.*, 2001; Jung *et al.*, 2006; Keller *et al.*, 2006). A similar approach is followed in quantifying the amount of partial melting that produced the Tsirub intrusions where the Tsirub dyke, the Tsirub North (outer) plug, samples AN-016 and AN-019, and the Tsirub South plug are assumed to share a common mantle source (see section 7.3). On the basis of distinctively lower

initial Nd isotope ratios, the Tsirub North (inner) plug is inferred to be from a compositionally distinct source and it will therefore be treated separately. Before conducting partial melting modelling on the Tsirub intrusions, the cause of the strong K anomaly on their primitive mantle normalised patterns (see Fig. 5.5) is first evaluated to determine whether this anomaly is caused by a residual mineral phase that should be included in the residual source mineralogy used in the partial melting modelling.

7.3.2.2 Origin of K anomaly

It was reported in Chapter 5 that the Tsirub intrusions show a strong negative K anomaly on their primitive mantle normalised patterns (see Fig. 5.5). This relative K depletion may be caused by fractionation of a K-bearing mineral phase such as amphibole or phlogopite or it could be inherited from their mantle source where a residual K-bearing phase was present at the time of partial melting (e.g. Wilson and Downes, 1991; Haase and Devey, 1994; Class and Goldstein, 1997; Hart *et al.*, 1997; Thomas *et al.*, 1999; Furman, 2007). Both amphibole (D^K = 1.36; Dalpé and Baker, 1994) and phlogopite (D^K = 3.67; LaTourrette *et al.*, 1995) are common minor K-bearing phases in the upper mantle (Gast, 1968; Sun and Hanson, 1975b; Hanson and Langmuir, 1978) and their presence in the mantle residue at the time of melt extraction can significantly fractionate K from other incompatible trace elements of (otherwise) similar incompatibility such as Th, Nb and La. The common existence of amphibole and phlogopite in the upper mantle has been confirmed by several authors who reported occurrences of these two minerals in mantle xenoliths (e.g. Dawson *et al.*, 1970; Mitchell, 1984; Dawson and Smith, 1988; Johnson *et al.*, 1997; Grégoire *et al.*, 2002 and 2003), including amphibole-bearing mantle xenoliths hosted in Gibeon kimberlites, southern Namibia (Franz *et al.*, 1996b).

Fractionation of amphibole or phlogopite as a possible cause of the observed relative K depletion is ruled out on the basis of absence of primary amphibole or phlogopite phenocrysts (or microphenocrysts) and the lack of correlation between K and La (Fig. 7.3), suggesting that the relative K depletion reflects conditions at the time of partial melting. Therefore a residual amphibole or phlogopite at the time of melt extraction is responsible for the relative K depletion in the Tsirub rocks. Numerous studies have attempted to identify geochemical parameters that can distinguish residual phlogopite control from residual amphibole control (e.g. Clague and Frey, 1982; Greenough, 1988; Adam *et al.*, 1993; Späth *et al.*, 2001). Following the work of Greenough (1988) and Adam *et al.* (1993), phlogopite has a stronger affinity for Ba (D^{Ba} = 2.90)

whereas amphibole has a low partition coefficient for Ba (D^{Ba} = 0.5). Partial melting in the presence of phlogopite will therefore yield partial melts with significantly lower Ba concentrations relative to melts generated in the presence of amphibole where Ba will behave as an incompatible element. For example, Rogers *et al.* (1988 and 1992) have argued for a residual phlogopite as the cause of a negative K anomaly in the Namaqualand melilitites, South Africa, on the basis of low Ba concentrations. Primitive mantle normalised ratios involving Ba and an incompatible trace element, as a numerator, that is equally incompatible in both phlogopite and amphibole such as Nb ($D^{Nb}_{phlogopite}$ = 0.14, $D^{Nb}_{amphibole}$ = 0.2; McKenzie and O'Nions, 1991; Adam *et al.*, 1993) will therefore be much higher in partial melts generated in the presence of phlogopite compared to melts generated in the presence of amphibole. For example the Namaqualand melilitites that have been argued to have originated in the presence of phlogopite have Nb/Ba_{PM} in the range of 1.59 – 4.42 (Rogers *et al.* 1992). The low primitive mantle normalised Nb/Ba ratio (up to 2.0) in the Tsirub rocks (e.g. Nb/Ba_{PM} = 1.8 ± 0.03 for Tsirub South plug) point to a residual amphibole.

Recent work by Späth *et al.* (2001) on primitive alkaline lavas from Chyulu Hills, southern Kenya, concluded that partial melting in the presence of phlogopite produces melts with much higher K content (K > 3000 ppm) compared to partial melting in the presence of amphibole (K < 3000 ppm). To further isolate residual amphibole from phlogopite, the approach of Späth *et al.* (2001) is employed by plotting the Tsirub data on a variation diagram of K versus La showing fields of melts in equilibrium with residual phlogopite and amphibole (Fig. 7.3). Clearly, the Tsirub data are consistent with residual amphibole rather than phlogopite. The proposed residual amphibole is suggested to be of metasomatic origin (Class and Goldstein, 1997; Nielson and Neller, 1987; Haase *et al.*, 2004; Jung *et al.*, 2006; Furman, 2007) and this aspect is discussed in more detail in section 7.5. On a similar note, Franz *et al.* (1996b) documented the occurrence of amphibole in spinel-bearing mantle xenoliths hosted in Gibeon kimberlites from southern Namibia, located a few kilometres from the Tsirub rocks, and this provide further support for the inferred residual amphibole. A number of workers have also inferred amphibole as the residual K-bearing hydrous mineral to account for strong relative K depletion in similar continental alkaline rocks (e.g. Francis and Ludden, 1995; Jung and Masberg, 1998; le Roex *et al.*, 2001; Weinstein *et al.*, 2006) and alkaline rocks emplaced in oceanic settings (Späth *et al.*, 1996; Class and Goldstein, 1997). In contrast, Rogers *et al.* (1988 and 1992) proposed a residual phlogopite in the mantle source of Namaqualand melilitites from neighbouring South Africa, as documented earlier.

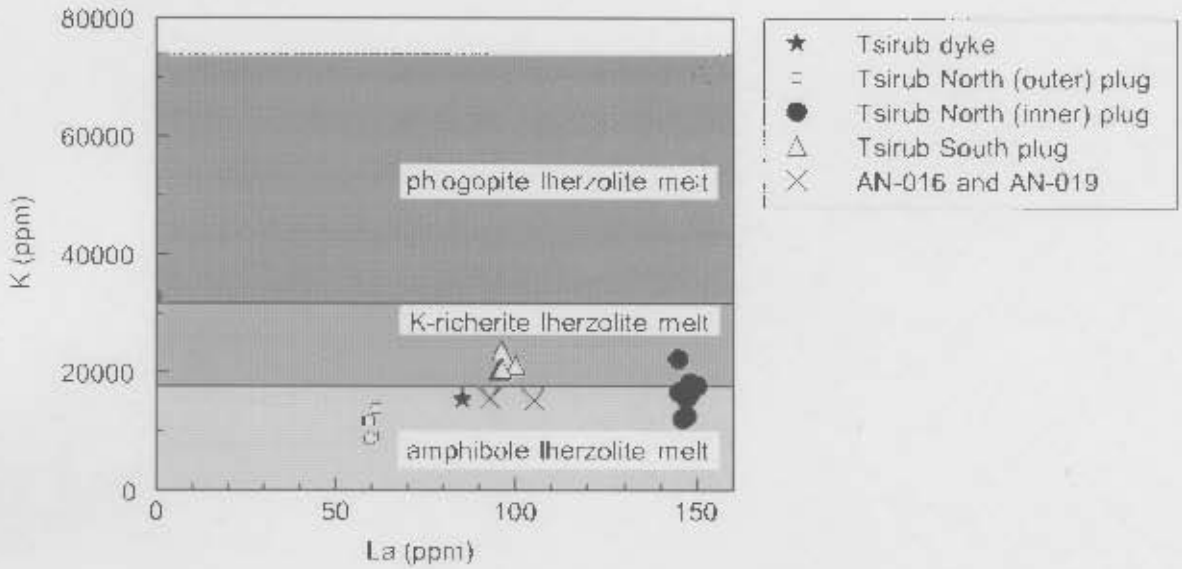

Fig. 7.3. Variation diagram of K versus La showing fields of melts in equilibrium with residual phlogopite and amphibole (after Späth *et al.*, 2001).

7.3.2.3 Constrains on the degrees of partial melting

To quantify the degrees of partial melting for the Tsirub intrusions and to evaluate if the Tsirub intrusions (except the Tsirub North (inner) plug) are related to a common mantle source by variable degrees of partial melting, constrained forward REE modelling approach was followed. REE modelling was conducted using modal batch melting equation of Shaw (1970) presented in equation 7.1, partition coefficients reported in Table 7.1 and starting and melt modes given in Table 7.2. The REE modelling was undertaken to test for the presence of garnet or spinel in the source i.e. depth of melting. The composition of the predicted source is calculated from the Tsirub dyke (AN-001) assuming 3% of partial melting. Sample AN-001 (Mg# = 0.71, Ni = 309 ppm and Cr = 393 ppm) was chosen because it shows close-to-primary compositions in terms of its Mg#, Ni and Cr contents among the Tsirub intrusions as mentioned previously.

$$C_l/C_o = 1/[F + D(1-F)] \qquad (7.1)$$

Where C_l = concentration of trace element in the melt

C_o – concentration of trace element in the source

F – degrees of partial melting

D = bulk partition coefficient calculated from the proportions of the phases left in the source at the time of melt separation

Table 7.1. Partition coefficients used in partial melting modelling, after Späth *et al.* (2001) and references therein. Abbreviations: Opx = orthopyroxene, Cpx = clinopyroxene, and Amph = amphibole.

	Rb	Ba	Th	U	K	Ta	Nb	La	Ce	Pb	Pr	Sr	Nd	P
Olivine	0.001	0.001	0.0001	0.001	0.001	0.001	0.001	0.001	0.001	0.001	0.001	0.001	0.001	0.001
Opx	0.001	0.001	0.0001	0.001	0.001	0.001	0.001	0.001	0.001	0.001	0.001	0.001	0.001	0.001
Cpx	0.001	0.001	0.0026	0.001	0.01	0.01	0.01	0.05	0.08	0.08	0.1	0.12	0.12	0.1
Garnet	0.001	0.001	0.001	0.001	0.001	0.001	0.001	0.01	0.02	0.02	0.05	0.001	0.09	0.05
Spinel	0.001	0.001	0.001	0.001	0.001	0.001	0.001	0.01	0.001	0.01	0.01	0.01	0.001	0.01
Amph	0.3	0.5	0.05	0.05	1.36	0.2	0.2	0.04	0.07	0.07	0.11	0.376	0.142	0.7

	Sm	Hf	Zr	Eu	Ti	Gd	Tb	Dy	Ho	Er	Tm	Yb	Lu
Olivine	0.0007	0.001	0.001	0.0095	0.001	0.0015	0.001	0.001	0.001	0.001	0.001	0.0011	0.001
Opx	0.01	0.01	0.01	0.013	0.1	0.016	0.019	0.022	0.022	0.03	0.03	0.1	0.1
Cpx	0.26	0.2	0.2	0.15	0.17	0.2	0.25	0.3	0.3	0.28	0.29	0.2	0.2
Garnet	0.13	0.1	0.1	0.32	0.1	0.3	0.6	0.9	1.4	2	3	4	6
Spinel	0.001	0.01	0.01	0.001	0.01	0.001	0.001	0.0015	0.01	0.003	0.01	0.01	0.01
Amph	0.188	0.8	0.8	0.351	1.4	0.304	0.301	0.322	0.01	0.297	0.01	0.22	0.01

Table 7.2. Modal mineralogy used in constrained forward models, after Wass and Rogers (1980), Greenough (1988) and Johnson *et al.* (1990). Abbreviations: Opx = orthopyroxene, Cpx = clinopyroxene, and Amph = amphibole.

	Garnet (5%) lherzolite		Garnet (1%) lherzolite		Spinel (2%) lherzolite	
	Starting mode	Melt mode	Starting mode	Melt mode	Starting mode	Melt mode
Olivine	0.53	0.05	0.53	0.05	0.53	0.05
Opx	0.22	0.05	0.22	0.05	0.22	0.10
Cpx	0.15	0.34	0.19	0.34	0.18	0.33
Garnet	0.05	0.06	0.01	0.06	-	-
Spinel	-	-	-	-	0.02	0.02
Amph	0.05	0.50	0.05	0.50	0.05	0.50

Results of model melts calculated from a garnet-bearing source (containing 5% garnet) are shown in Fig. 7.4 together with the composition of the predicted source. The predicted garnet-bearing source is enriched in the light REE relative to the heavy REE (e.g. La ~ 14 times chondrite and Yb ~ 3 times chondrite). It is clear that model melts calculated from a source containing 5% residual garnet closely resemble the observed REE compositions in Tsirub South plug and samples AN-016 and AN-019 from the Tsirub North plug. Quantitatively, the Tsirub South plug and samples AN-016 and AN-019 from the Tsirub North plug could have formed by 2 - 3% of partial melting of a similar source to that giving rise to the Tsirub dyke. However, observed heavy REE compositions in the Tsirub North (outer) plug cannot be accounted for in this model (Fig. 7.4a). Even a small amount of garnet (as low as 1% garnet) cannot account for the heavy REE compositions in the Tsirub North (outer) plug.

Like garnet, spinel is a common upper mantle aluminous mineral and its role in the source of the Tsirub lavas is evaluated by conducting forward REE partial melting modelling on spinel-bearing

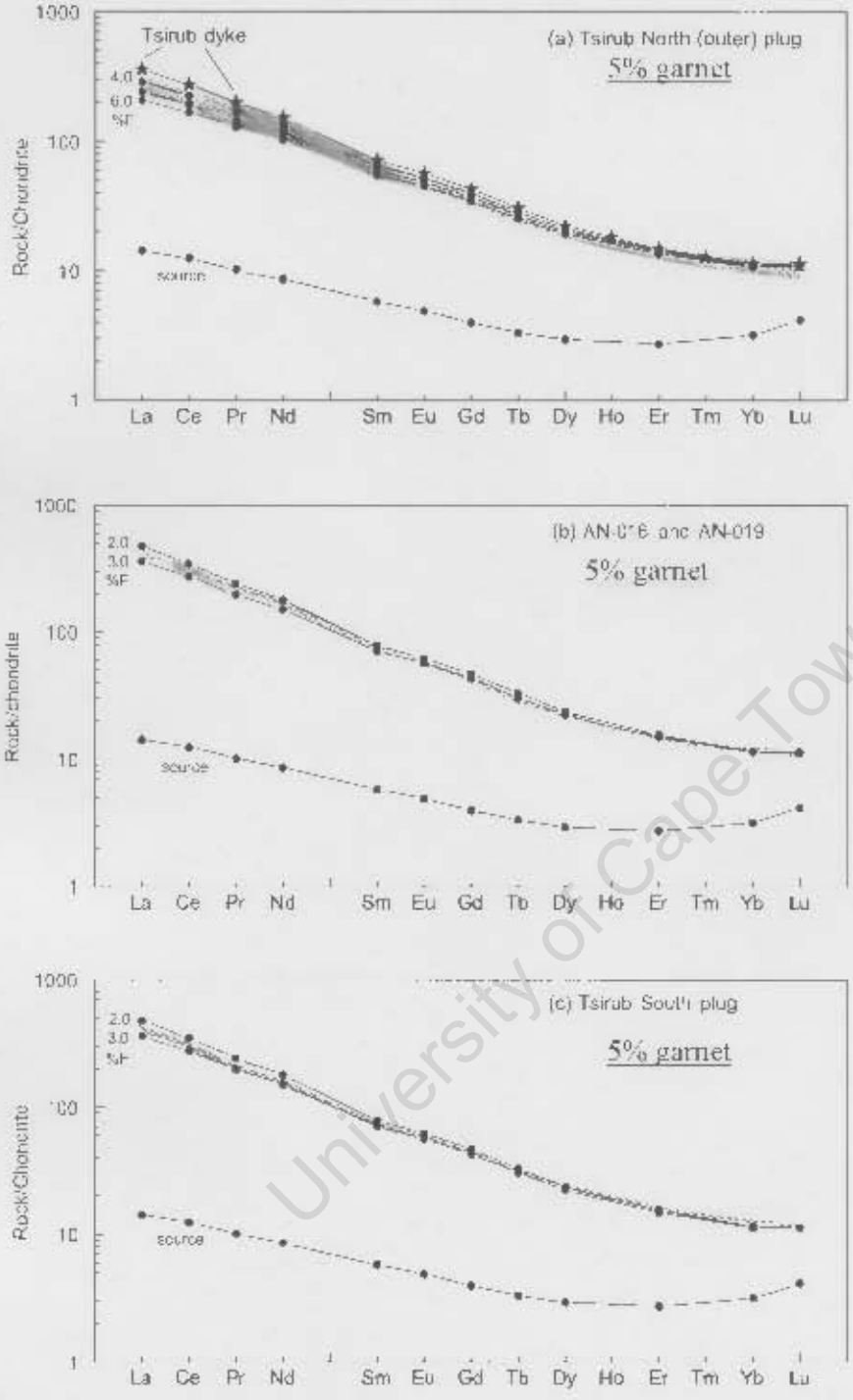

Fig. 7.4. Chondrite normalised REE patterns for partial model melts of an amphibole bearing garnet lherzolite containing 5% garnet. Source composition calculated by assuming AN-001 (from Tsirub dyke) is derived by 3% melting. The shaded fields represent the observed range of REE compositions in Tsirub rocks (i.e. Tsirub dyke, samples AN-016 and AN-019, and Tsirub South plug). Degrees of partial melting (%F) are in percent and are in steps of 1%. Partition coefficients are from Späth *et al.* (2001) and references therein. Starting and melt modes are from Wass and Rogers (1980), Greenough (1988) and Johnson *et al.* (1990) and are reported in Table 7.2. Chondrite normalising values are from Sun and McDonough (1989).

mineralogy using mineral-melt partition coefficients listed in Table 7.1 and starting and melt modes presented in Table 7.2. The spinel-bearing hypothetical source is calculated from sample AN-001 assuming 3% of partial melting. Results of model melts calculated from a spinel-bearing source containing 2% spinel are displayed in Fig. 7.5. The predicted spinel-bearing source is light REE enriched (~12 times chondrite) and has heavy REE abundances slightly higher than chondritic (~1.5 times chondrite). It is clear that the observed range of light REE compositions in the Tsirub intrusions correspond well to the shape of the REE patterns of model melts calculated from an amphibole-bearing spinel lherzolite source containing 2% spinel and 5% amphibole. Most importantly, the range in heavy REE abundances of the Tsirub intrusions is better accounted for by melting in the spinel field. Considering Fig. 7.5, the model melts suggests that the Tsirub South plug and samples AN-016 and AN-019 are generated by slightly lower degrees (2 - 3%) of partial melting than the Tsirub North (outer) plug (4 - 6% partial melting), consistent with the lower incompatible trace element contents of the latter. These conclusions are in line with the work of Green (1970), Gast (1978) and Frey *et al.* (1978) who have proposed degrees of melting for alkaline rocks as low as 3-7%.

The degree of partial melting required to generate the Tsirub North (inner) plug, argued earlier to be from a compositionally distinct source (see section 7.3), is difficult to model because it shows a limited variation in the REE abundances. However, the higher incompatible trace elements concentration of this plug could suggest either origin from a source more enriched in incompatible trace elements relative to the source shared by the other Tsirub intrusions, or an origin by relatively lower degrees of partial melting.

In summary, from the above quantitative modelling it is proposed that the Tsirub intrusions (excepting the Tsirub North (inner) plug) appear to be related to each other by variable degrees of partial melting of a common amphibole-bearing source located in the spinel stability field. In comparison the Tsirub North (inner) plug is generated from a compositionally slightly distinct mantle source, probably more enriched in incompatible trace elements than the source shared by the other Tsirub intrusions.

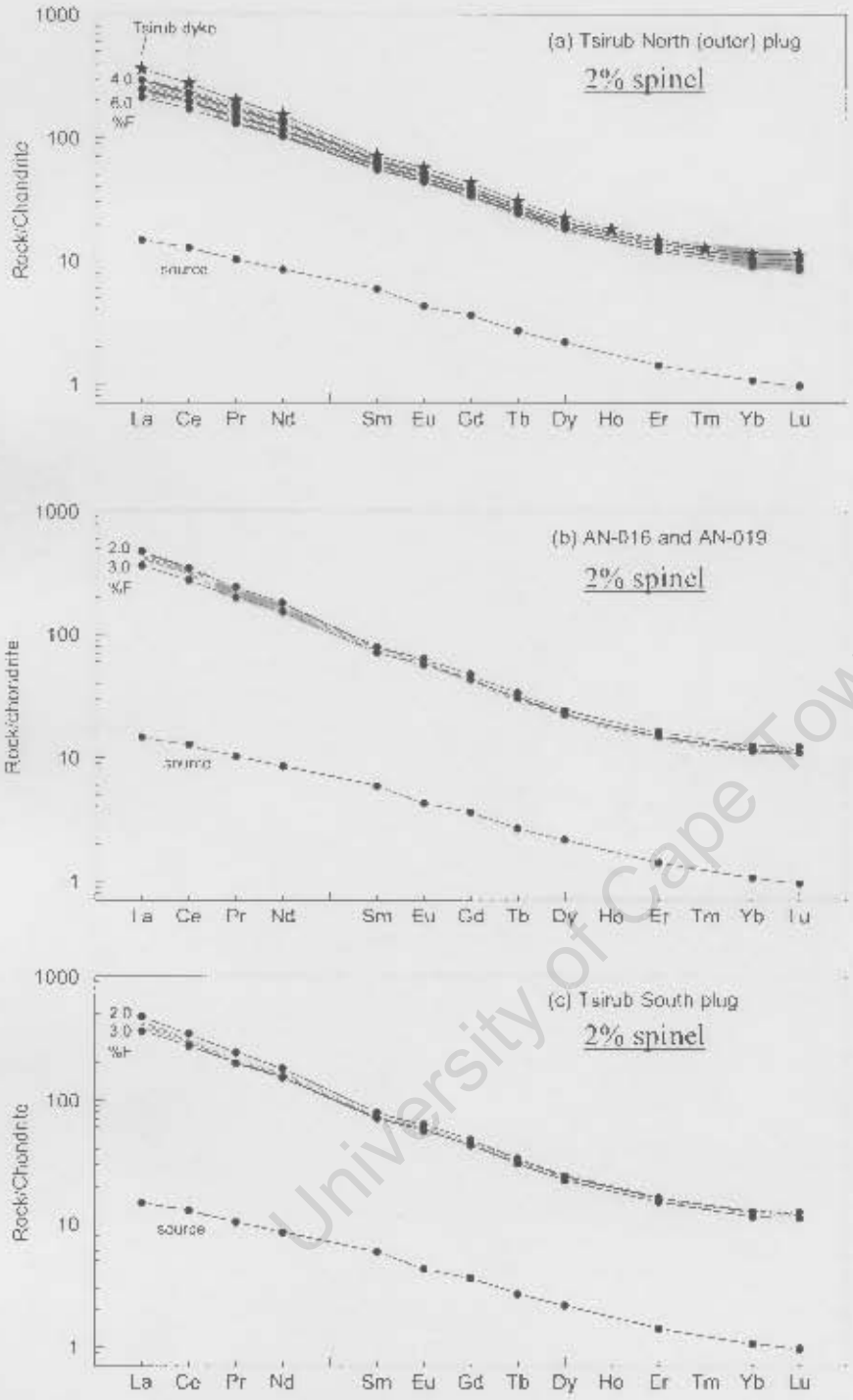

Fig. 7.5. Chondrite normalised REE patterns for model partial melts of an amphibole-bearing spinel lherzolite source containing 2% spinel. Source composition calculated by assuming AN-001 (from Tsirub dyke) is derived by 3% melting. The shaded fields represent the observed range of REE compositions. Partition coefficients, starting and melt modes, and chondrite normalising values are as in Fig. 7.4.

7.3.2.4 The effect of amphibole on incompatible trace element patterns

To illustrate whether the presence of 5% residual amphibole (see Table 7.2) can produce the magnitude of relative K depletion comparable to that displayed by the Tsirub nephelinites and basanites incompatible trace elements partial melt modelling of an amphibole-bearing spinel lherzolite for an extended suite of trace elements, including K, has been undertaken. The approach was similar to that described for the REE. However, K was treated as a stoichiometric constituent of amphibole using the approach of Greenough (1988) which is based on the assumptions that the entire amount of a given stoichiometric element is accommodated in a single, minor, solid phase. The behaviour of that particular element during partial melting, where the minor phase in which it is accommodated remains in the residue after melt extraction, is therefore independent of the degrees of partial melting and the amount of the minor residual phase present in the source, but is dependent on the proportion of the minor residual phase entering the melt (Greenough, 1988). The concentration of K in amphibole during partial melting can therefore be modelled using equation 7.2 that takes into account the concentration of the major element in the minor phase and the proportion that the minor phase contributes to the melt.

$$C_L = C_m * P \qquad (7.2)$$

Where C_L = concentration of major element in melt

C_m = concentration of major element in minor phase

P = proportion of melt composed of minor phase (i.e. melt mode of minor mineral)

Results of the above modelling approach are shown in Fig. 7.6 where element abundances have been normalised to primitive mantle values. The incompatible trace elements compositions, except K, of the predicted spinel-bearing source (calculated from sample AN-001 assuming 3% of partial melting) and model melts were calculated using equation 7.1. The primitive mantle normalised K concentration for the predicted source was assumed to lie mid-way between Nb and La (i.e. the source had no K anomaly), whereas K content for the model melts was calculated assuming K as a stoichiometric component of amphibole containing 1.02 wt.% K_2O (Dawson and Smith, 1973; Best, 1974; Zanetti *et al.*, 1996) and contributing 50% of the melt (Wass and Rogers, 1980). It is clear from Fig. 7.6 that the calculated model melts closely resemble the observed primitive mantle normalised patterns. The magnitude of the negative K anomaly in the

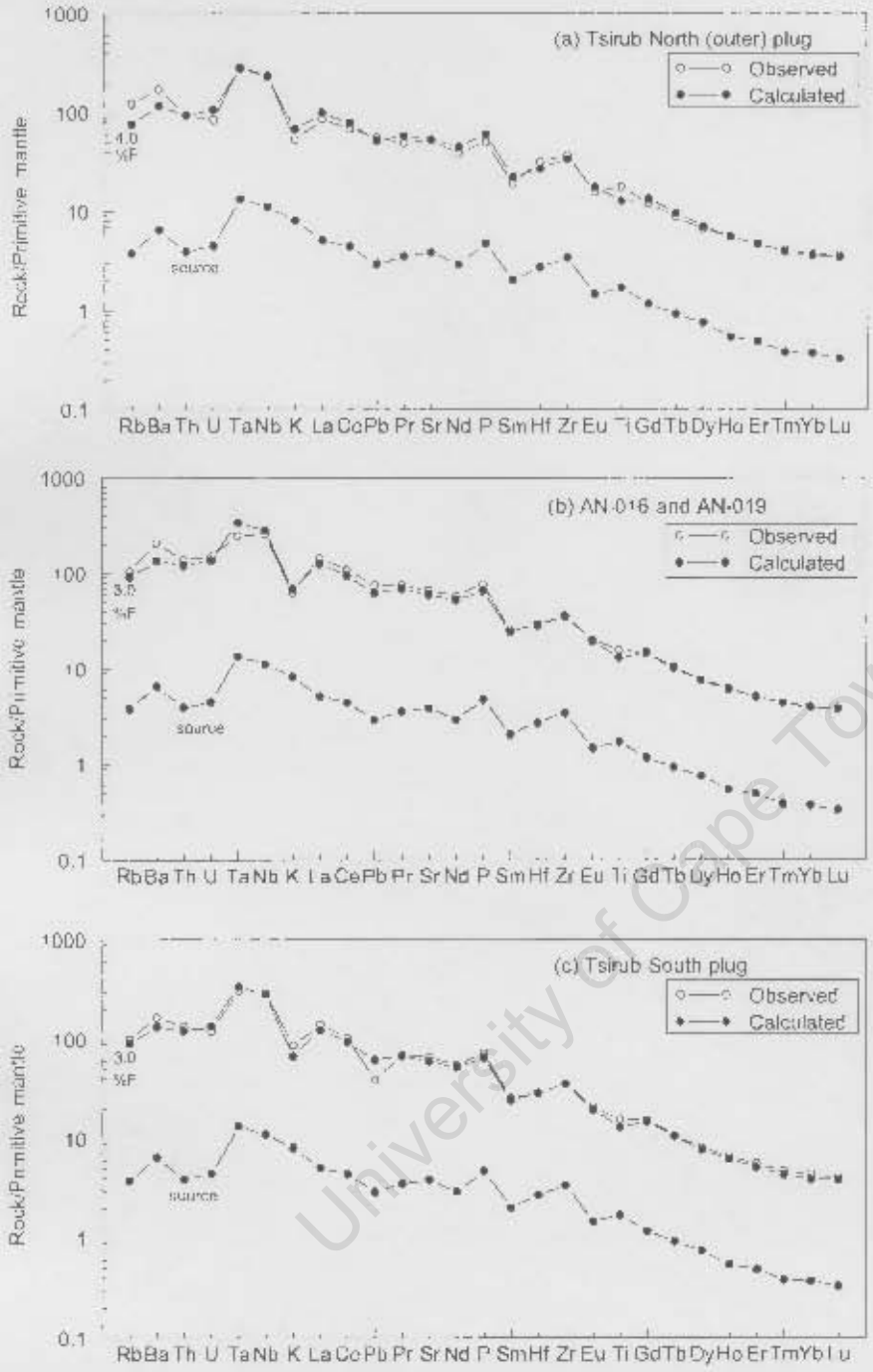

Fig. 7.6. Primitive mantle normalised incompatible trace element patterns for model, non-modal equilibrium batch melts (*solid circles*) of an amphibole-bearing spinel lherzolite. The patterns with *open circles* represent the average of observed compositions. Source composition calculated by assuming AN-001 (from Tsirub dyke) is derived by 3% melting except for K where the primitive mantle normalised K concentration was assumed to be intermediate between Nb and La. K for the model melts was treated as stoichiometric constituent of amphibole (K_2O = 1.02 wt.%,) using the approach of Greenough (1988). Partition coefficients, starting and melt modes, are as in Fig. 7.4. Primitive mantle normalising values are from Sun and McDonough (1989).

model melts is also similar to the observed K anomaly, confirming the likely importance of amphibole in the source of the Tsirub intrusions.

The magnitude of a negative K anomaly in a melt can be measured by ratios involving K and other incompatible trace elements with similar degree of incompatibility such as La or Th. During partial melting in the presence of amphibole, which retains K, the concentrations of La and Th are expected to decrease with increasing degrees of partial melting such that the K/La and K/Th ratios are directly proportional to the degrees of partial melting. This aspect is illustrated in Fig. 7.7 where melting trends calculated for an amphibole-bearing spinel lherzolite (containing 5% initial amphibole), with K/Nb and K/Th ratios similar to primitive mantle values, are shown. For comparison purposes, the Tsirub North (inner) plug from a compositionally distinct source is also plotted on Fig. 7.7. The Tsirub intrusions all fall along the calculated melting trend strengthening the earlier argument for a residual amphibole. The Tsirub North (outer) plug with La and Th contents lower than that of the other Tsirub intrusions generated by lower degrees of partial melting e.g. Tsirub South plug, is slightly displaced to lower K/La and K/Th. Given the mobile nature of K in a weathering environment, the displacement of this plug could be explained by secondary alteration during which some of K was lost from this plug. Since the Tsirub North (inner) plug, proposed earlier to be from a distinct source, falls on the calculated melting trend this is taken to suggest that this plug is derived by lower degrees of partial melting of a distinct source.

7.4 Mantle source region location

The mantle source region of continental alkaline rocks has received substantial debate over the years as to whether such rocks are derived from the sub-continental lithospheric mantle (SCLM) or from sub-lithospheric sources (convecting asthenospheric mantle or mantle plumes) (e.g. White and McKenzie, 1989; Wilson *et al.*, 1992; Cebriá and López-Ruiz, 1995; Simonetti and Bell, 1995; Rogers, *et al.*, 2000; Janney *et al.*, 2002; Shaw *et al.*, 2003; Jung *et al.*, 2006). Evidence put forward in favour of the asthenospheric mantle includes depleted Nd-Sr isotopic signature (Jung and Masberg, 1998). In contrast, there is growing evidence that many continentally emplaced alkaline rocks are derived from within the SCLM. Such evidence includes relative K depletion argued to be indicative of residual amphibole in the mantle source (Dawson and Smith, 1973; Best, 1974; Zanetti *et* al., 1996). Since amphibole is thermally unstable in either the convecting asthenospheric mantle or mantle plumes (Class and Goldstein, 1997) the source of continental alkaline rocks showing a relative K depletion is argued to be located within the SCLM (Francis and Ludden, 1995; le Roex *et al.*, 2001; Späth *et al.*, 2001, Weinstein *et al.*, 2006).

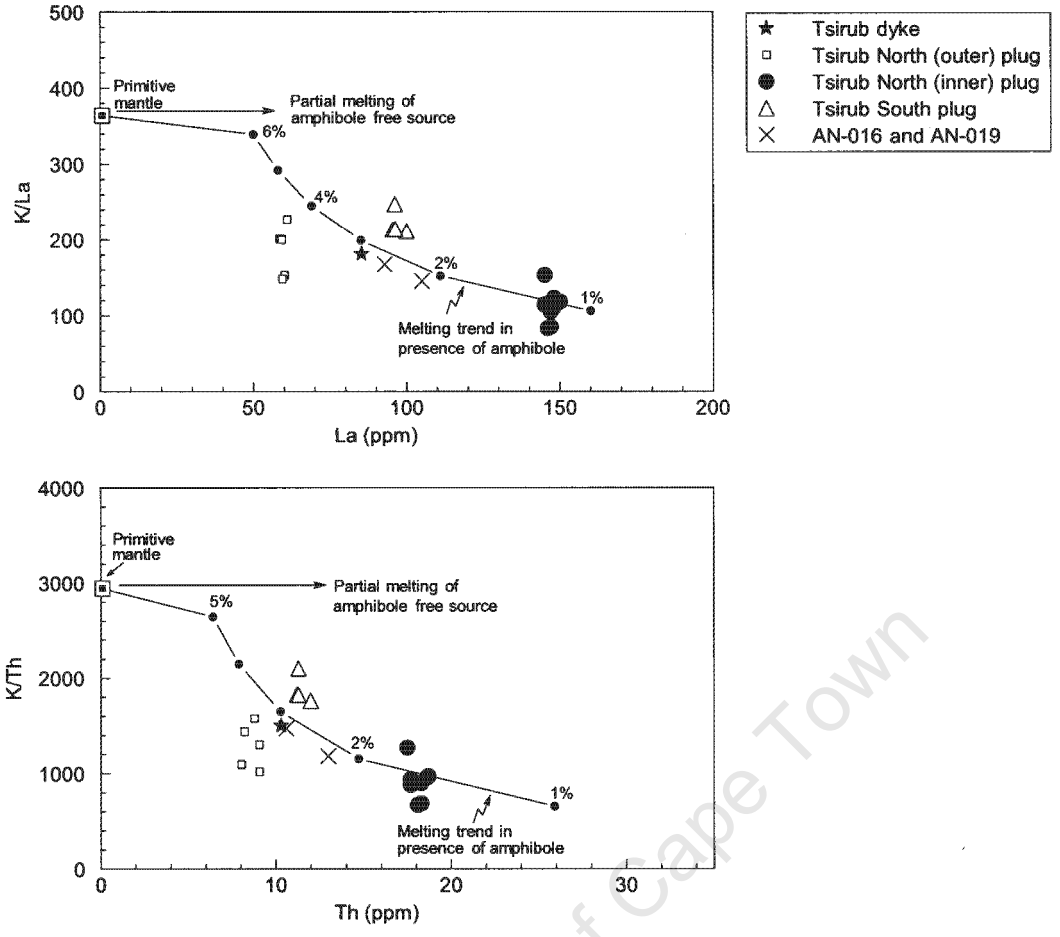

Fig. 7.7. Variation of magnitude of negative K anomaly (K/La and K/Th) with La and Th concentrations. Melting trends and K concentration calculated as in Fig. 7.6 assuming 5% initial amphibole in the source. Primitive mantle values are from Sun and McDonough (1989).

Experimental studies of Olafsson and Eggler (1983) and Mengel and Green (1989) have constrained the upper stability limit of pargasitic or kaersutitic amphibole to less than 30 kbar. Class and Goldstein (1997) have compared the thermal stability field of pargasitic and kaersutitic amphibole (~ 800 - 1100 °C) with typical asthenosphere (~ 1250 °C, McKenzie and Bickle, 1988) and mantle plume (~ 1480 °C, McKenzie and Bickle, 1988) adiabats and concluded that both pargasitic and kaersutitic amphibole are stable in the relatively cooler SCLM, but are unstable under conditions characteristic of the convecting asthenospheric mantle or hotter mantle plume. Considering earlier arguments around the evidence for a residual amphibole in the mantle source region of the Tsirub nephelinites and basanites, it is suggested that their mantle source is located within the SCLM as opposed to the convecting asthenospheric mantle or mantle plume.

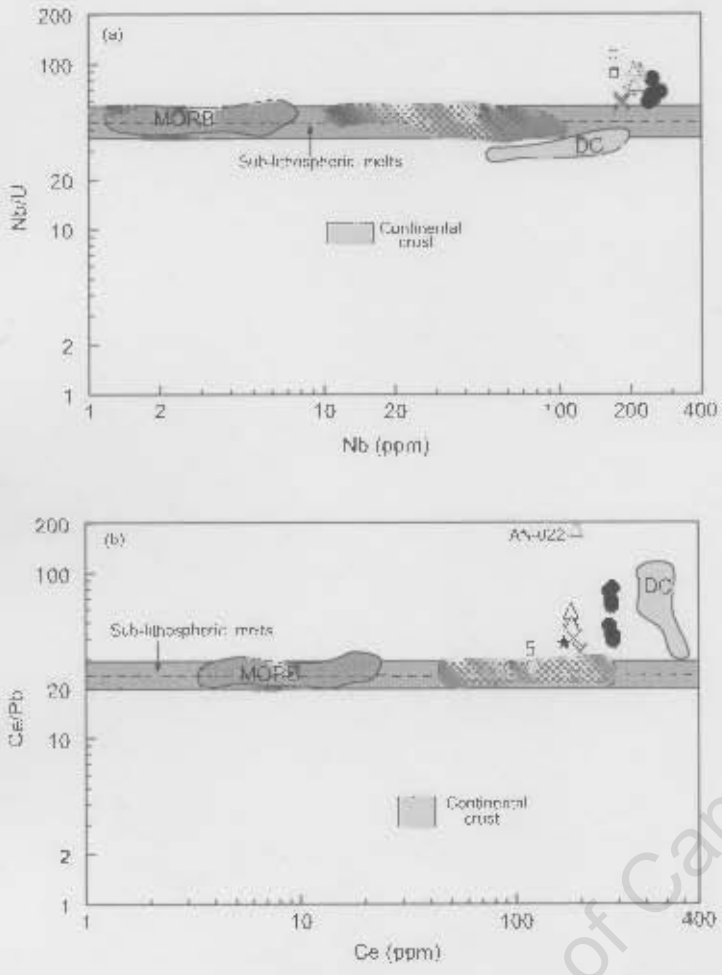

Fig. 7.8. Variations of Nb/U and Ce/Pb ratios with Nb and Ce concentrations. Also shown are fields delineating the ranges of Nb/U and Ce/Pb values expected in magmas generated from sub-lithospheric sources (Hofmann *et al.*, 1986). Data for Dicker Willem carbonatite (DC) from Cooper and Reid (1998), MORB and OIB from Hofmann *et al.* (1986) and references therein, continental crust from Taylor and McLennan (1981 and 1985); Weaver and Tarney (1984); Rudnick and Fountain (1995). Symbols are as in Fig. 7.7.

Hofmann *et al.* (1986) have constrained Nb/U and Ce/Pb ratios of MORB and OIB sampled from sub-lithospheric sources (convecting asthenospheric mantle or mantle plumes) to be 47 ± 10 and 25 ± 10, respectively. Figure 7.8 presents comparison of Nb/U and Ce/Pb ratios between sub-lithospheric melts and Tsirub intrusions. For comparison purposes, the Dicker Willem carbonatite (Cooper and Reid, 1998) that is spatially related to the Tsirub intrusions is also plotted on Fig 7.8. It is clear that the Tsirub rocks have slightly higher Nb/U and Ce/Pb ratios than sub-lithospheric melts, suggesting that their source is geochemically distinct from that of the sub-lithospheric mantle-derived MORB and OIB. Moreover, the Sr and Nd isotopic composition of the SCLM beneath southern Africa has been determined from ultramafic xenoliths (Menzies and Murthy, 1980b; Kramers *et al.*, 1981; Richardson *et al.*, 1985; Jones, 1987; Hawkesworth *et al.*, 1990a)

including xenoliths hosted in Gibeon kimberlites from southern Namibia (Jones, 1987; Davies *et al.*, 2001). These isotope data are compared to that of the Tsirub intrusions in Fig. 7.9. In comparison to the SCLM (that plots in the depleted quadrant), the Tsirub rocks show slightly lower initial Nd isotope ratios but similar Sr isotope ratios. The fact that these rocks have much lower initial Nd isotope ratios than those of MORB (e.g. Altherr *et al.*, 1990; le Roex *et al.*, 1992; Volker *et al.*, 1993; Janney *et al.*, 2005) (Fig.7.9) generally accepted to have sampled the asthenosphere (e.g. le Roux, *et al.*, 2002b) provide further support for an origin within the SCLM.

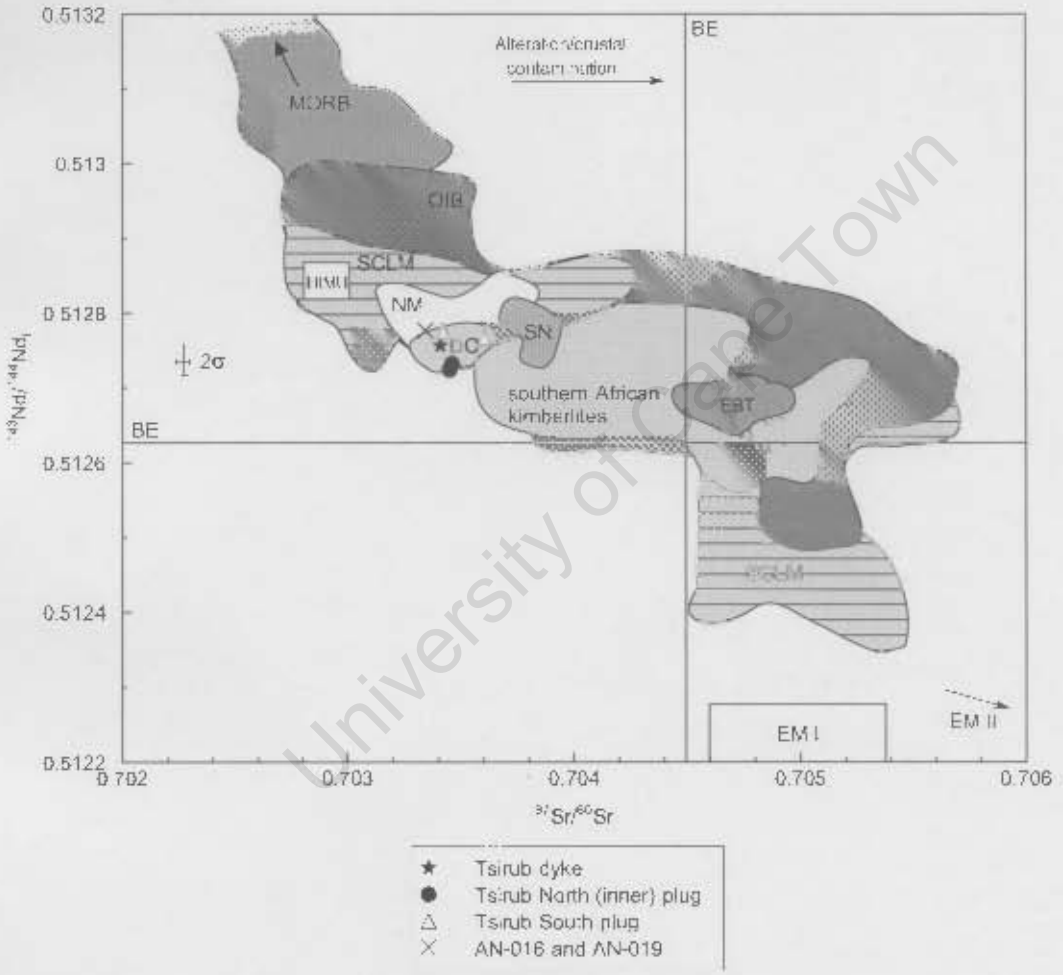

Fig. 7.9 Initial Nd-Sr isotope ratio correlation diagram for the Tsirub rocks. BE – Bulk Earth. Analytical error bars are shown and represent $2\sigma_{mean}$ errors. Also shown are fields representing isotopic composition of sub-continental lithospheric mantle (SCLM) beneath southern Africa (Menzies and Murthy, 1980b; Kramers *et al.*, 1981; Richardson *et al.*, 1985; Jones, 1987; Hawkesworth *et al.*, 1990a; Davies *et al.*, 2001). Data sources for HIMU, EMI and EMII, Dicker Willem carbonatite (DC), Schwarzeberg nephelinite (SN), Namaqualand melilitites (NM), Erongo basanites-tephrites (EBT), southern African kimberlites, MORB and OIB are as in Fig 6.1.

In summary, it is argued that the mantle source regions of the Tsirub nephelinites and basanites including the compositionally distinct Tsirub North (inner) plug is located within the SCLM rather than the convecting asthenospheric mantle as suggested by their relative K depletion requiring a residual amphibole, which is thermally unstable in the asthenosphere.

7.5 The cause of magmatism, evolution of source region and relationship to other local alkaline volcanics

In this section, processes that initiated partial melting within the SCLM and evolution of the mantle source region are discussed as well as the relationship of the Tsirub rocks to other local continental alkaline volcanics such as Schwarzeberg nephelinite (Spriggs, 1988) and spatially located Dicker Willem carbonatite (Cooper and Reid, 1998) from southern Namibia.

It has been proposed in the previous section that the source of the Tsirub rocks is located within the SCLM. The question being addressed here is what triggered partial melting in the cooler SCLM and not in the asthenosphere? As mentioned in Chapter 1, the Tsirub intrusions occur on a broad NNE-SSW lineament, with other alkaline intrusives such as Schwarzeberg nephelinite and Gibeon kimberlites, and magmatism along this lineament has been linked to the Vema and Discovery hotspots (Duncan, 1981; Morgan, 1983; Hartnady and le Roex, 1985; le Roex, 1986). The initial Sr and Nd isotope ratios of the Tsirub rocks are similar to those of OIB (e.g. Cliff *et al.*, 1991; Späth *et al.*, 1996; Widom *et al.*, 1997; Class *et al.*, 1998; Thomas *et al.*, 1999; Siebel *et al.*, 2000; Workman *et al.*, 2004), see Chapter 6, suggesting that these rocks carry a geochemical mantle plume signature thus arguing for the involvement of a mantle plume in their generation. A number of authors have also reported a geochemical plume signature in alkaline complexes from continental settings including the East African Rift (Stein and Hofmann, 1992; le Roex *et al.*, 2001; Späth *et al.*, 2001). Similarly, Class and Goldstein (1997), Class *et al.* (1998) and Mattielli *et al.* (1999) documented a plume signature in alkaline volcanics emplaced on oceanic islands. Contrasting models for the generation of continental alkaline rocks that bear a plume signature have been put forward (Stein and Hofmann, 1992; le Roex *et al.*, 2001; Späth *et al.*, 2001; Trumbull *et al.*, 2003). Trumbull *et al.* (2003) argued that the Erongo basanite-tephrite plugs from northwest Namibia formed by direct melting of a mantle plume, as stated previously. In contrast, studies of continentally emplaced alkaline rocks by Stein and Hoffmann (1992), le Roex *et al.* (2001) and Späth *et al.* (2001) argued that such rocks with a plume signature showing

a relative K depletion are not formed by direct partial melting of a mantle plume but rather formed by partial melting within a metasomatised lithospheric mantle where a mantle plume serves as a source of heat and/or a source of fluids that infiltrate into, and metasomatise, the overlying lithospheric mantle.

Hartnady and le Roex (1985) and le Roex (1986) have established the tracks of the Vema and Discovery hotspots (Fig. 7.10) which have been linked to some alkaline magmatism in southern Namibia, as mentioned previously (e.g. Spriggs, 1988). For example, the 70 Ma kimberlite magmatism at Gibeon in southern Namibia has been attributed to the Discovery plume (Spriggs, 1988). Discovery and Vema plume were beneath southern Namibia (i.e. Tsirub area) at 70 Ma and 49 Ma, respectively (Hartnady and le Roex, 1985; le Roex, 1986). The model proposed for the Tsirub intrusions involves fluids released from a rising mantle plume migrating into the overlying dry SCLM. These fluids are proposed to have been responsible for mantle metasomatism needed to explain the high incompatible trace elements observed in the Tsirub rocks. The ultimate cause of the melting that gave rise to the Tsirub nephelinite/basanite magmatism is unclear. The absence of an exact age for the Tsirub intrusions precludes direct comparison to the paleopositions of the Vema and Discovery plumes (although the inferred age of ~ 49 Ma suggest a possible relationship to the Vema plume). Alternatively, the hydrous nature (i.e. amphibole-bearing) and subsequent thinning (possibly caused by a rising Vema plume) or uplift of the SCLM might have led to decompression melting of the metasomatised SCLM in the presence of amphibole and within the spinel stability field. Independent evidence for thinning, as the ultimate case of melting, is not available because there is no published geophysical work from the study area. However, thermobarometric work done by Franz *et al.* (1996b) on ultramafic xenoliths from Gibeon kimberlites, southern Namibia obtained a geothermal gradient of 44 mW/m^2 for the lower lithosphere of southern Namibia (see Fig. 7.10 for location of Gibeon kimberlites, marked "7", relative to the study area), suggesting a thinner lithosphere than that typical of the cratonic regions to the west.

In order to evaluate the relationship of the Tsirub rocks to other local and regional alkaline volcanics i.e. Schwarzeberg nephelinite, (Spriggs, 1988) and spatially located rocks (Dicker Willem carbonatite, Cooper and Reid, 1998), their incompatible trace element ratios (Fig. 7.11) and Sr and Nd isotope ratios are compared. La/Nb ratio and Ba/Nb ratio of the Tsirub rocks are similar to those of the Dicker Willem carbonatite and Schwarzeberg nephelinite, respectively. As

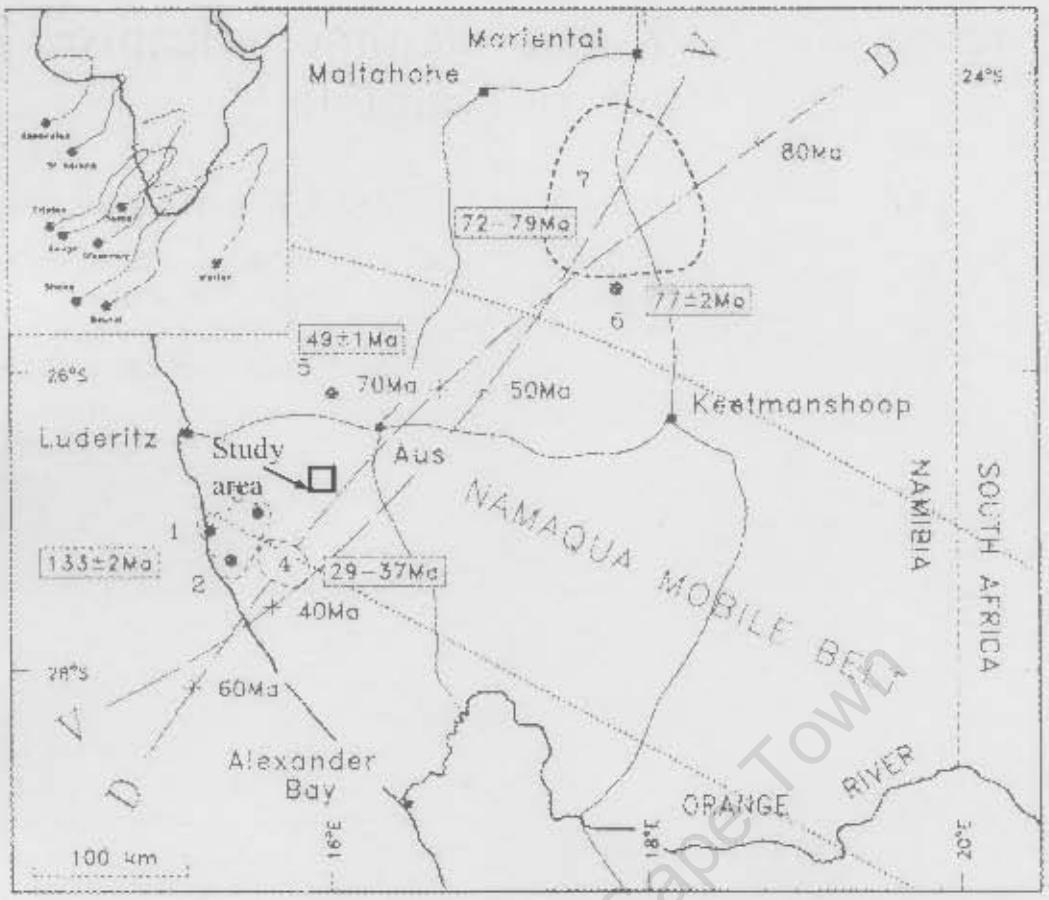

Fig. 7.10. Palcopositions of the Vema (V) and Discovery hotspots, shown as discontinuous curves. The respective positions of the two hotspots are marked by the numbers along the discontinuous curves in 10 Ma intervals (after Hartnady and le Roex, 1985; le Roex, 1986). The map is from Reid *et al.* (1990).

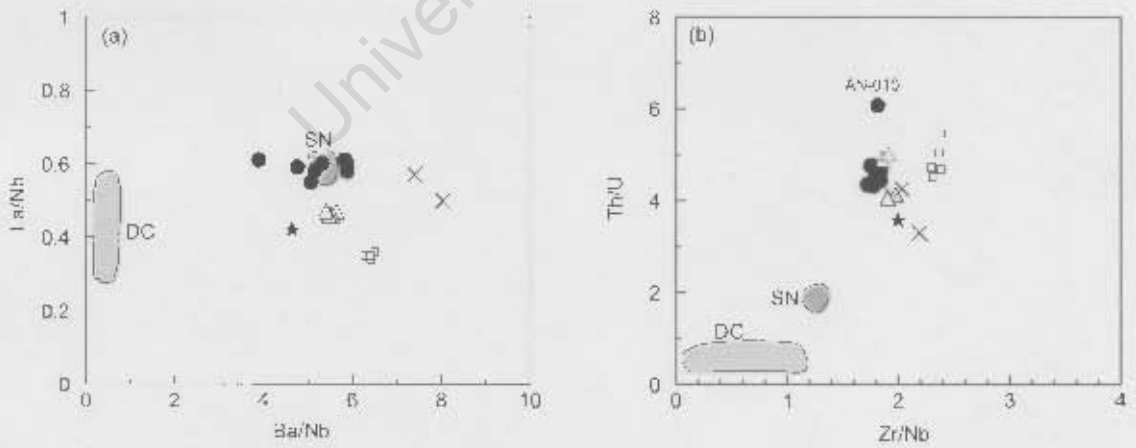

Fig. 7.11. Comparison of Tsirub rocks to Dicker Willem carbonatite (DC) (Cooper and Reid, 1998) and Schwarzeberg nephelinite (SN) (Spriggs, 1988) in terms of their incompatible trace element ratios.

reported in Chapter 6, the Tsirub intrusions show similar Nd isotope ratios to Dicker Willem carbonatite and Schwarzeberg nephelinite (see Fig. 6.1). Given their similar initial Sr and Nd isotope ratios and incompatible trace element ratios it is proposed that the Tsirub intrusions may share a genetic relationship to Dicker Willem carbonatite and Schwarzeberg nephelinite.

CHAPTER 8

SUMMARY AND CONCLUSION

8.1 Introduction

The Tsirub alkaline intrusions from the Aus region, southern Namibia occur along a broad NNE-SSW lineament of Cretaceous alkaline intrusions (Gross Brukkaros volcano, Klinghardt phonolite field, Gibeon kimberlites) including the Dicker Willem carbonatite and Luderitz alkaline province. Three separate intrusions are recognized; two major plugs (Tsirub North and Tsirub South) and a spatially associated dyke (Tsirub dyke). In detail the Tsirub North plug can be subdivided on the basis of geochemistry into an outer zone and inner zone. Following the classification scheme of Le Maitre (2002), the Tsirub intrusions are largely nephelinites, an exception being the Tsirub North (outer) plug which can be classified as basanite.

8.2 Petrography and mineral chemistry

The Tsirub intrusions show very similar petrography. They are porphyritic (Tsirub dyke) or microporphyritic (Tsirub North (outer) plug, Tsirub North (inner) plug, and Tsirub South plug) in texture in which phenocrysts/microphenocrysts of olivine and clinopyroxene are embedded in a fine grained groundmass. Olivine is the dominant (micro) phenocryst phase whereas clinopyroxene is common in the groundmass assemblage ± Fe-Ti oxides ± olivine ± secondary amphibole. Some olivine crystals are partially or completely altered to serpentine. The small petrographic difference between the Tsirub intrusions is the occurrence of rare felsic xenoliths (few mm wide) consisting of alkali feldspar (orthoclase) and clinopyroxene (diopside and aegirine-augite) in the Tsirub North (outer) plug, Tsirub North (inner) plug and Tsirub South plug, and their absence in the Tsirub dyke. Another feature of the Tsirub North (inner) plug is the occurrence of a single ultramafic xenolith consisting of olivine, clinopyroxene and spinel (hercynite).

Olivine phenocryst/microphenocryst cores in the Tsirub dyke are forsterite-rich (Fo_{89-90}), but more iron-rich in the Tsirub South plug (Fo_{74-78}). Those in the Tsirub North (inner) plug (Fo_{85-92})

extend to slightly higher fosterite contents relative to those in the Tsirub North (outer) plug (Fo_{84-85}). Clinopyroxene phenocryst/microphenocryst cores are diopsidic in composition and indistinguishable between the different intrusions (e.g. Tsirub dyke = $Wo_{49-50}En_{38-41}Fs_{9-12}$, Tsirub North (outer) plug = $Wo_{47-50}En_{37-42}Fs_{10-13}$ and Tsirub North (inner) plug = $Wo_{47-48}En_{41-44}Fs_{9-12}$). The groundmass Fe-Ti oxides (FeO = 67.05 – 70.34 wt.% and TiO_2 = 20.45 – 22.57 wt.%) are titanomagnetite in composition.

8.3 Bulk rock geochemistry

The Tsirub samples are nepheline normative and silica undersaturated rocks (e.g. SiO_2 = 38.7–41.6 wt.%). The Tsirub dyke has a relatively primitive Mg# (0.71), whereas the other Tsirub intrusions are less MgO-rich; Tsirub North (outer) plug (0.61 – 0.65), Tsirub North (inner) plug (0.64 – 0.66), and Tsirub South plug (0.62 – 0.63). A positive correlation of CaO with MgO, together with petrographic observations, is taken to suggest fractional crystallization of olivine and clinopyroxene with olivine the major fractionating phase. TiO_2 contents are high (e.g. 3.25 – 3.36 wt.%) with the Tsirub North (inner) plug showing slightly lower concentrations (2.42 – 2.56 wt.%). Three compositional groups within the Tsirub North plug are readily distinguishable by their P_2O_5 concentration. The Tsirub North (inner) plug shows highest P_2O_5 concentration (2.25 – 2.47 wt.%), samples AN-016 and AN-019 (1.54 – 1.81 wt.% P_2O_5) are intermediate, and the Tsirub North (outer) plug has the lowest P_2O_5 concentration (1.03 – 1.27 wt.%).

The concentrations of incompatible trace elements in the Tsirub rocks are high, with the Tsirub North (inner) plug showing the greatest enrichment whereas the Tsirub North (outer) plug shows the least enrichment. For example, the Tsirub North (inner) plug has Nb and Zr concentrations as high as 256 ppm and 469 ppm, respectively, whereas the Tsirub North (outer) plug has Nb and Zr concentrations of 168 and 449 ppm, respectively. Chondrite normalised rare earth element patterns are steep (e.g. $La/Yb_N \sim 32$) suggesting influence of a residual garnet or a strongly light REE enriched source.

The Tsirub samples are characterized by low La/Nb (0.34 – 0.61) and Zr/Nb (1.73 – 2.37) ratios and high Ce/Pb (25.1 – 59.3) and Nb/U ratios with the Tsirub North (inner) plug extending to slightly higher Ce/Pb values (41.4 – 81.5). On primitive mantle normalised diagrams they show similar incompatible trace elements patterns with strong positive Nb-Ta anomalies, moderate

negative Pb anomaly and a strong negative K anomaly; the latter is attributed to a residual K-bearing phase at the time of melt extraction.

As a whole the Tsirub intrusions plot in the depleted field on the Nd-Sr isotope correlation diagram, implying a source with long-term depletion in incompatible trace elements. The Tsirub dyke ($^{87}Sr/^{86}Sr_i$ = 0.703412 and $^{143}Nd/^{144}Nd_i$ = 0.512756), Tsirub North (outer) plug ($^{143}Nd/^{144}Nd_i$ = 0.512747 – 0.512781), Tsirub South plug ($^{87}Sr/^{86}Sr_i$ = 0.703423 – 0.703605 and $^{143}Nd/^{144}Nd_i$ = 0.512767 – 0.512775) and samples AN-016 and AN-019 ($^{87}Sr/^{86}Sr_i$ = 0.703346 and $^{143}Nd/^{144}Nd_i$ = 0.512776) have similar, and limited range of, initial $^{143}Nd/^{144}Nd$ ratios (calculated at an assumed age of 49 Ma) and have similar initial $^{87}Sr^{86}Sr$ ratios suggesting a common mantle source. Elevated $^{87}Sr/^{86}Sr_i$ ratios in the Tsirub North (outer) plug (0.703898 – 0.704441) are attributed to alteration or crustal contamination. In comparison, the Tsirub North (inner) plug ($^{87}Sr/^{86}Sr_i$ = 0.703452 – 0.703463) has slightly lower initial $^{143}Nd/^{144}Nd$ ratios (0.512724 – 0.512732) relative to the other Tsirub intrusions, suggesting a compositionally slightly distinct source.

8.4 Alteration and crustal contamination

The lack of correlation between mobile incompatible trace elements (K, Rb and Ba) and immobile incompatible trace elements of similar degree of incompatibility (e.g. Nb, La) within the Tsirub intrusions indicates that these rocks have suffered a certain degree of alteration during which K, Rb and Ba were mobilised. Petrographic evidence for secondary alteration is provided by the presence of serpentine which partially or completely replaces olivine.

The presence of felsic xenoliths in some samples indicates a certain degree of crustal assimilation shortly before eruption. However, the amount of continental crust assimilated by the parental magmas appears to be small because the Tsirub rocks have high Ce/Pb and Nb/U ratios and they lack a positive Pb anomaly or negative Nb anomaly.

8.5 Relationship between the Tsirub intrusions and the degrees of partial melting

Whereas each of the Tsirub intrusions shows limited compositional variations there are clear differences between the intrusions. However, this latter variation does not conform to expected result of crystal fractionation. It appears therefore, that the compositional difference between the intrusions is not the result of magmatic evolution from a common parent magma.

Quantitative REE modelling relating the Tsirub dyke, Tsirub North (outer) plug, Tsirub South plug and samples AN-016 and AN-019 to a common mantle source (calculated assuming that the Tsirub dyke formed by 3% of partial melting) indicates that they could be related to each other by variable degrees of partial melting from a common amphibole-bearing spinel lherzolite. Partial melt models indicate that Tsirub North (outer) plug formed by slightly higher degrees of partial melting (4 - 6%) relative to the Tsirub South plug (2 - 3 %) and samples AN-016 and AN-019 (2 - 3%). The apparent garnet signature observed in the Tsirub samples (i.e. high La/Yb_N) is attributed to a strong light REE enrichment in the mantle source region, rather than to residual garnet. The degrees of partial melting for the compositionally distinct Tsirub North (inner) plug are difficult to model because it shows limited variation in REE elements. Nevertheless, higher incompatible trace elements contents of this plug, and steeper REE patterns, relative to the other Tsirub intrusions (that share a common mantle source) suggest derivation by lower degrees of partial melting or from a more enriched source.

8.6 Location of mantle source and the cause of magmatism

The strong negative K anomaly on the primitive mantle normalised diagram is shown to have originated as result of residual amphibole rather than phlogopite. The temperature stability limits of amphibole constrain the mantle source of these rocks to within the sub-continental lithospheric mantle (SCLM), rather than the convecting asthenosphere or a rising mantle plume. The contrasting requirement of the incompatible trace elements which require an enriched mantle source, and the isotope ratios which require a long-term depleted source, are explained as result of a recent metasomatic event superimposed on a previously depleted mantle. This metasomatism is attributed to rising fluids and/or small degree melts from either the Vema or Discovery plumes that were located beneath this region prior to the inferred time of magmatism. The geodynamic model envisaged in the generation of the Tsirub intrusions involved fluids and/or small degree melts released from a rising mantle plume migrating into a dry SCLM. These fluids led to the

formation of amphibole and lowering of the solidus temperature. The ultimate cause of the melting that gave rise to the Tsirub nephelinite/basanite magmatism in unclear. The absence of an exact age for the Tsirub intrusions precludes direct comparison to the paleopositions of the Vema and Discovery plumes (although the inferred age of ~ 49 Ma suggest a possible relationship to the Vema plume). Alternatively, the hydrous nature and subsequent thinning or uplift of the SCLM might have led to decompression melting of the metasomatised SCLM in the presence of amphibole and within the spinel stability field.

REFERENCES

Adam, J., Green, T. H. and Sie, S. H. (1993). Proton microprobe determined partitioning of Rb, Sr, Ba, Y, Zr, Nb and Ta between experimentally produced amphiboles and silicate melts with variable F content. *Chemical Geology* **109,** 29-49.

Altherr, R., Henjes-Kunst, F. and Baumann, A. (1990). Asthenosphere versus lithosphere as possible sources for basaltic magmas erupted during the formation of the Red Sea: constraints from Sr, Pb and Nd isotopes. *Earth and Planetary Science Letters* **96,** 269-286.

Aoki, K.-I. and Kushiro, I. (1968). Some clinopyroxenes from ultramafic inclusions in Dreiser Weiher, Eifel. *Contribution to Mineralogy and Petrology* **18**, 326-337.

Becker, M. and le Roex, A. P. (2006). Geochemistry of South African On- and Off-craton, Group I and Group II kimberlites: petrogenesis and source region evolution. *Journal of Petrology* **47,** 673-703.

Bedini, R. M., Bidinier, J.-L., Dautria, J.-M. and Morten, L. (1997). Evolution of LILE-enriched small melt fractions in the lithospheric mantle: a case study from the East African Rift. *Earth and Planetary Science Letters* **153,** 67-83.

Bell, K. and Peterson, T. (1991). Nd and Sr isotope systematics of Shombole Volcano, East Africa, and the links between nephelinites, phonolites and carbonatites. *Geology* **19**, 582-585.

Bell, K. and Tilton, G. R. (2001). Nd, Sr and Pb isotope compositions of the East African carbonatites: evidence for mantle mixing and plume inhomogeneity. *Journal of Petrology* **42,** 1927-1945.

Bernstein, S., Leslie, A. G., Higgins, A. K. and Brooks, C. K. (2000). Tertiary alkaline volcanics in the Nunatak Region, Northeast Greenland: new observations and comparison with Siberian maymechites. *Lithos* **53**, 1-20.

Best, M. G. (1974). Mantle-derived amphibole within inclusions in alkalic-basaltic lavas. *Journal of Geophysical Research* **79,** 2107-2113.

Brey, G. and Green, D. H. (1977). Systematic study of liquidus phase relations in olivine melilitite + H2O + CO2 at high pressures and petrogenesis of a melilitite magma. *Contributions to Mineralogy and Petrology* **61,** 141-162.

Brey, G. (1978). Origin of olivine melilitites: chemical and experimental constraints. *Journal of Volcanology and Geothermal Research* **3,** 61-88.

Carlson, R. W. and Irving, A. J. (1994). Depletion and enrichment history of subcontinental lithospheric mantle: an Os, Sr, Nd and Pb isotopic study of ultramafic xenoliths from the northwestern Wyoming Craton. *Earth and Planetary Science Letters* **126,** 457-472.

Cebriá, J. M. and López-Ruiz, J.(1995). Alkali basalts and leucitites in an extensional intracontinental plate setting: The late Cenozoic Calatrava Volcanic Province (central Spain). *Lithos* **35**, 27-46.

Cebriá, J. M., López-Ruiz, J., Doblas, M., Oyarzun, R., Hertogen, J. and Benito, R. (2000). Geochemistry of the Quaternary alkali basalts of Gorratxa (NE Volcanic Province, Spain): a case of double enrichment of the mantle lithosphere. *Journal of Volcanology and Geothermal Research* **102**, 217-235.

Chaffey, D. J., Cliff, R. A. and Wilson, B. M. (1989) Characterization of the St Helena magma source. In: Saunders, A. D. and Norry, M. J. (eds). Magmatism in ocean basins. Geological Society **42**(special publication), pp 257-276.

Clague, D. A. and Frey, F. A. (1982). Petrology and trace element geochemistry of the Honolulu volcanics, Ohau: implications for the oceanic mantle below Hawaii. *Journal of Petrology* **23,** 447-504.

Class, C., Altherr, R., Volker, F., Eberz, G. and McCulloh, M. T. (1994). Geochemistry of Pliocene to Quaternary alkali basalts from the Huri Hills, northern Kenya. *Chemical Geology* **113,** 1-22.

Class, C. and Goldstein, S. L. (1997). Plume-lithosphere interaction in the ocean basins: constraints from the source mineralogy. *Earth and Planetary Science Letters* **150**, 245-260.

Class, C., Goldstein, S. L., Altherr, R. and Bachélery, P. (1998). The process of plume-lithosphere interaction in the ocean basins – the case of Grande Comore. *Journal of Petrology* **39,** 881-903.

Cliff, R. A., Baker, P. E. and Mateer, N. J. (1991). Geochemistry of Inaccessible Island volcanics. *Chemical Geology* **92,** 251-260.

Cooper, A. F. and Reid, D. L. (1998). Nepheline sövites as parental magmas in carbonatite complexes: evidence from Dicker Willem, southwest Namibia. *Journal of Petrology* **39,** 2123-2136.

Cox, K. J., Bell, J. D. and Pankhurst, R. J. (1979). *The interpretation of Igneous rocks*. Chapman and Hall, London. 450 pp.

Coe, N. (2004). Petrogenesis of Swartruggens and Star Group II kimberlite dyke swarms, South Africa. *Unpublished M.Sc thesis,* University of Cape Town.

Dalpé, C. and Baker, D. R. (1994). Partition coefficients for rare-earth elements between calcic amphibole and Ti-rich basanitic glass at 1.5 Gpa, 1100°C. *Mineralogical Magazine* **58a,** 207-208.

Davies, G. R., Gledhill, A. and Hawkesworth, C. (1985). Upper crustal recycling in southern Britain: evidence from Nd and Sr isotopes. *Earth and Planetary Science Letters* **75,** 1-12.

Davies, G. R., Norry, M. J., Gerlach, D. C. and Cliff, R. A. (1989). A combined chemical and Pb-Sr-Nd isotope study of the Azores and Cape Verde hotspots: the geodynamic implications). In: Saunders, A. D. and Norry, M. J. (eds). Magmatism in ocean basins. Geological Society **42** (special publication), pp 231-255.

Davies, G. R., Spriggs, A. J. and Nixon, P. H. (2001). A non-cognate origin for the Gibeon Kimberlite Megacryst Suite, Namibia: Implications for the origin of the Namibian kimberlites. *Journal of Petrology* **42** 159-172.

Dawson, J. B., Powell, D. G. and Reid, A. M. (1970). Ultrabasic xenoliths and lavas from Lashaine volcano, northern Tanzania. *Journal of Petrology* **11,** 519-548.

Dawson, J. B. and Smith, J. V. (1973). Alkalic pyroxenite xenoliths from the Lashine volcano, northern Tanzania. *Journal of Petrology* **14,** 113-131.

Dawson, J. B. and Smith, J. V. (1988). Metasomatised and veined upper-mantle xenoliths from the Pello Hill, Tanzania: evidence for anomalously-light mantle beneath the Tanzanian sector of the East African Rift Valley. *Contributions to Mineralogy and Petrology* **100,** 510-527.

Dejonghe, L., Denaiffe, D. and Weis, D. (1998). Strontium isotope geochemistry of anhydrites and calcite pseudomorphs after anhydrite from Palaeozoic formations in Belgium. *Chemical Geology* **144**, 63-71.

DePaolo, D. J. and Wasserburg, G. J. (1976) Nd isotopic variation and petrogenetic models. *Geophysical Research Letters* **3,** 249-252.

DePaolo, D. J. and Daley, E. E. (2000). Neodymium isotopes in basalts of southwest basin and range and lithospheric thinning during continental extension. *Chemical Geology* **169,** 157-185.

Dosso, L., Hanan, B. B., Bougault, H., Schilling, J.-G. and Joron, J.-L. (1991). Sr-Nd-Pb geochemical morphology between 10° and 17° N on the Mid-Atlantic Ridge: a new MORB isotope signature. *Earth and Planetary Science Letters* **106,** 29-43.

Downes, H., Reichow, M. K., Mason, P. R. D., Beard, A. D. and Thirlwall, M. F. (2003). Mantle domains in the lithosphere beneath the French Massif Central: trace element and isotopic evidence from mantle clinopyroxenes. *Chemical Geology* **200,** 71-87.

Droop, G. T. R. (1987). A general equation for estimating Fe^{3+} concentrations in ferromagnesian silicates and oxides from microprobe analyses, using stoichiomentric criteria. *Mineralogical Magazine* **51,** 431-435.

Duncan, R. A. (1981). Hotspots in the Southern Oceans: An absolute frame of reference for the motions of the Gondwana continents. *Tectonophysics* **74,** 29-42.

Ellam, R. M. (1992). Lithospheric thickness as a control on basalt geochemistry. *Geology* **20**, 153-156.

Erlank, A. J., Allsopp, H. L., Hawsworth, C. J. and Menzies, M. A. (1982). Chemical and isotopic characteristics of the upper mantle metasomatism in peridotite nodules from the Bulfoentein kimberlite. *Terra Cognita* **2,** 216-263.

Erlank, A. J., Marsh, J. S., Duncan, A. R., Miller, R. M., Hawkesworth, C. J., Betton, P. J. And Rex, D. C. (1984). Geochemistry and petrogenesis of the Etendeka volcanic rocks from SWA/Namibia. *Geological Society of South Africa* **13** (special publication), 195-245.

Fan, W. M., Zhang, H. F., Baker, J., Jarvis, K. E., Mason, P. R. D. and Menzies. (2000). On and off the North China craton: where is the Archean Keel? *Journal of Petrology* **41,** 933-950.

Faure, G. (1986). *Principles of Isotope Geochemistry*. 2nd Edition. John Wiley and Sons, Canada. 589 pp.

Fiegenson, M. D., Patino, L .C. and Carr, M. J. (1996). Constraints on partial melting imposed by rare earth element variations in Mauna Kea basalts. *Journal of Geophysical Research* **101,** 11815-11829.

Fitton, J. G. and Dunlop, H. M. (1985). The Cameroon line, West Africa, and its bearing on the origin of oceanic and continental alkali basalt. *Earth and Planetary Science Letters* **72,** 23-33.

Francis, D. and Ludden, J. (1995). The signature of amphibole in mafic alkaline lavas, a study in northern Canadian Cordillera. *Journal of Petrology* **36,** 1171-1191.

Franz, L., Brey, G. P. and Okrusch, M. (1996a). Steady state geotherm, thermal disturbances, and tectonic development of the lower lithosphere underneath the Gibeon Kimberlite Province, Namibia. *Contributions to Mineralogy and Petrology* **126,** 181-198.

Franz, L., Brey, G. P. and Okrusch, M. (1996b). Requilibration of ultramafic xenoliths from Namibia by metasomatic processes at the mantle boundary. *Journal of Geology* **104,** 599-615.

Franz, G., Steiner, G., Volker, F., Pudlo, D. and Hammerschmidt, K. (1999). Plume related alkaline volcanism in central Africa-the Meidob Hills (W Sudan). *Chemical Geology* **157,** 27-47.

Frey, F. A., Green, D. H. and Roy, S. D. (1978). Integrated models of basalt petrogenesis: a study of quartz tholeiites and olivine melilitites from South Eastern Australia utilizing geochemical and experimental petrological data. *Journal of Petrology* **19,** 463-513.

Frimmel, H. E., Hartnady, C. J. H. and Koller, F. (1996). Geochemistry and tectonic setting of magmatic units in the Pan-African Gariep Belt, Namibia. *Chemical Geology* **130,** 101-121.

Frimmel, H. E. and Frank, W. (1998). Neoproterozoic tectono-thermal evolution of the Gariep Belt and its basement, Namibia and South Africa. *Precambrian Research* **90,** 1-28.

Furman, T. (1995). Melting of metasomatized subcontinental lithosphere: undersaturated mafic lavas from Rungwe, Tanzania. *Contributions to Mineralogy and Petrology* **122,** 97-115.

Furman, T. (2007). Geochemistry of East African Rift basalts: An overview. *Journal of African Earth Sciences* **48,** 147-160

Gast, P. W. (1968). Trace element fractionation and the origin of tholeiitic and alkaline magma types. *Geochimica et Cosmochimica Acta*. **32,** 1057-1086.

Germs, J. G. B. and Gresse, P. G. (1991). The foreland basin of the Damara and Gariep orogens in Namaqualand and southern Namibia: strategic correlations and basin dynamics. *South African Journal of Geology* **94,** 159-169.

Gibson, S. A., Thompson, R. N. and Day, J. A. (2006). Timescales and mechanisms of plume-lithosphere interactions: $^{40}Ar/^{39}Ar$ geochronology and geochemistry of alkaline igneous rocks from the Paraná-Etendeka large igneous province. *Earth and Planetary Science Letters* **251,** 1-17.

Govindaraju, K. (1989). Compilation of working values and sample description of 272 geostandards. *Geostandards Newsletter* **13** (special issue), 1-113.

Govindaraju, K. (1994). Compilation of working values and sample description of 383 geostandards. *Geostandards Newsletter* **18** (special issue), 158.

Green, T. H. (1970). A review of experimental evidence on the origin of basaltic and nephelinitic magmas: *Physics Earth and Planetary Interiors* **3,** 221-235.

Green, T. H. (1995). Significance of Nb/Ta as an indicator of geochemical processes in the crust-mantle system. *Chemical Geology* **120,** 347-359.

Greenough, J. D. (1988). Minor phases in the earth's mantle: evidence from trace-and minor element patterns in primitive alkaline magmas. *Chemical Geology* **69** 177-192.

Grégoire, M., Bell, D. R. and le Roex, A. P. (2002) Trace element geochemistry of glimmerite and MARID xenoliths: their relationship to kimberlite and to phlogopite-bearing peridotite revisited. *Contributions to Mineralogy and Petrology* **142,** 603-625.

Grégoire, M., Bell, D. R. and le Roex, A. P. (2003). Garnet lherzolites from the Kaapvaal Craton (South Africa): trace element evidence for a metasomatic history. *Journal of Petrology* **44,** 629-657.

Gresse, P. G. and Germs, G. J. B. (1993). The Nama foreland basin: sedimentation, major unconformity bounded sequences and multisided active advance. *Precambrian Research* **63,** 247-252.

Haase, K. M. and Devey, C. W. (1994). Petrology and geochemistry of Vesteris Seamount, Greenland Basin-an intraplate alkaline volcano of no-plume origin. *Journal of Petrology* **35,** 295-328.

Haase, K. M., Goldschmidt, B. and Garbe-Schönberg, C.-D. (2004). Petrogenesis of tertiary continental intra-plate lavas from the Westerwald region, Germany. *Journal of Petrology* **45,** 883 – 905.

Hanson, G. N. and Langmuir, C. H. (1978). Modeling of major elements in mantle-melt systems using trace element approaches. *Geochimica et Cosmochimica Acta* **42,** 725-741.

Harris, C., Marsh, J. S. and Milner, S. C. (1999). Petrology of the alkaline core of the Messum igneous complex, Namibia: evidence for the progressively decreasing effect of crustal contamination. *Journal of Petrology* **40,** 1377-1397.

Hart, S. R. and Davis, K. E. (1978). Nickel partitioning between olivine and silicate melt. *Earth and Planetary Science Letters* **40,** 203-219.

Hart, S. R. and Brooks, C. (1977). The geochemistry and evolution of early Precambrian mantle. *Contributions to Mineralogy and Petrology* **61,** 109-128.

Hart, S. R. (1988). Heterogeneous mantle domains: signatures, genesis and mixing chronologies. *Earth and Planetary Science Letters* **90**, 273-296.

Hart, S. R., Blusztajn, J., LeMasurie, W. E. and Rex, D. C. (1997). Hobbs Coast Cenozoic volcanism: implications for the West Antarctic rift system. *Chemical Geology* **139,** 223-248.

Hartnady, C. J. and le Roex, A. P. (1985). Southern Ocean hotspot tracks and the Cenozoic absolute motion of the Africa, Antarctic and South American plates. *Earth and Planetary Science Letters* **75**, 245-257.

Hawkesworth, C. J., Erlank, A. J., Kempton, P. D. and Waters, F. G. (1990a). Mantle metasomatism: isotope and trace-element trends in xenoliths from Kimberley, South Africa. *Chemical Geology* **85,** 19-34.

Hawkesworth, C. J., Kempton, P. D., Rogers, N. W., Ellam, R. M. and van Calsteren, P. W. (1990b). Continental mantle lithosphere and shallow level enrichment processes in the Earth's mantle. *Earth and Planetary Science Letters* **96,** 256-268.

Hegner, E. and Pallister, J. S. (1989). Pb, Sr, Nd isotopic characteristics of Tertiary Red Sea rift volcanics from the central Saudi Arabian coastal plain. *Journal of Geophysical Research* **94B,** 7749-7755.

Hoernle, K. and Schmincke, H.-U. (1993a). The petrology of the tholeiites through melilite nephelinites on Gran Canaria, Canary Islands: crystal fractionation, accumulation and depths of melting. *Journal of Petrology* **34,** 573-597.

Hoernle, K. and Schmincke, H.-U. (1993b). The role of partial melting in the 15-Ma geochemical evolution of Gran Canaria: a blob model for the Canary hotspot. *Journal of Petrology* **34,** 599-626.

Hoernle, K., White, J. D. L. van den Bogaard, P., Hauff, F., Coombs, D. S., Werner, R., Timm, C., Garbe-Schönberg, D., Reay, A. and Cooper, A. F. (2006). Cenozoic intraplate volcanism on New Zealand: Upwelling induced by lithospheric removal. *Earth and Planetary Science Letters* **248,** 350-367.

Hofmann, A. W., Jochum, K. P., Seufert, M. and White, W. M. (1986). Nb and Pb in oceanic basalts: new constraints on mantle evolution. *Earth and Planetary Science Letters* **79,** 33-45.

Jackson, M. P. A. (1976). High-grade metamorphism and migmatization of the Namaqua Metamorphic Complex around Aus in the southern Namib Desert, South West Africa. *Precambrian Research Unit*, **18**. 299 pp.

Janney, P. E. and le Roex, A. P., Carlson, R. W. and Viljoen, K. S. (2002). A chemical and multi-isotope study of the Western Cape olivine melilitite province, South Africa: Implications for the sources of kimberlites and the origin of the HIMU signature in Africa. *Journal of Petrology* **43,** 2339-2370.

Janney, P. E., le Roex, A. P. and Carlson, R. W. (2005). Hafnium isotope and trace element constraints on the nature of mantle heterogeneity beneath the central Southwest Indian Ridge (13°E to 47°E). *Journal of Petrology* **46,** 2427-2464.

Janse, A. J. A. (1969). Gross Brukkaros, a probable carbonatite volcano in the Nama Plateau of South West Africa. *Geological Society of America Bulletin* **80**, 573-586.

Johnson, K. T. M., Dick, H. J. B. and Shimizu, N. (1990). Melting in the oceanic upper mantle: an ion microprobe study of diopsides in abyssal peridotites. *Journal of Geophysical Research* **95**, 2661-2678.

Johnson, L. J., Jones, A. P., Church, A. A. and Taylor, W. R. (1997). Ultramafic xenoliths and megacrysts from a melilitite tuff cone, Deeti, northern Tanzania. *Journal of African Earth Sciences* **25,** 29-42.

Jones, R. A. (1987). Strotium and Nd isotopic and rare element evidence for the genesis of megacrysts in kimberlites from southern Africa. In: Nixon, P. H. (ed). *Mantle xenoliths*. John Wiley and Sons Ltd, Great Britain. pp 711-724.

Jung, S. and Masberg, P. (1998). Major-and trace-element systematics and isotope geochemistry of Cenozoic mafic volcanic rocks from the Vogelsberg (central Germany): constraints on the origin of the continental alkaline and tholeiitic basalts and their mantle sources. *Journal of Volcanology and Geothermal Research* **86**, 151-177.

Jung, S., Mezger, K. and Hoernes, S. (1998). Petrology and geochemistry of syn- to post-collisional metaluminous A-type granites- a major and trace element and Nd–Sr–Pb–O-isotope study from the Proterozoic Damara Belt, Namibia. *Lithos* **45,** 147-175.

Jung, S. and Hoernes, S. (2000). The major- and trace-element and isotope (Sr, Nd, O) geochemistry of Cenozoic alkaline rift-type volcanic rocks from the Rhön area (central Germany): petrology, mantle source characteristics and implications for asthenosphere-lithosphere interactions. *Journal of Volcanology and Geothermal Research* **99**, 27-53.

Jung, C., Jung, S., Hoffer, E. and Berndt, J. (2006). Petrogenesis of Tertiary mafic alkaline magmas in the Hocheifel, Germany. *Journal of Petrology* **47**, 1637-1671.

Kay, R. and Gast, P. W. (1973). The rare earth element content and origin of alkali-rich basalts. *Journal of Geology* **81,** 287-310.

Kamber, B. S. and Collerson, K. D. (2000). Role of "hidden" deeply subducted slabs in mantle depletion. *Chemical* Geology **166**, 241-254.

Keller, J., Zaitsev, A. N. and Wiedenmann, D. (2006). Primary magmas of Oldoinyo Lengai: The role of olivine melilitites. *Lithos* **91**, 150-172.

Kokfelt, T, F., Hoenle, K., Hauff, F., Fiebig, J., Werner, R. and Garbe-Schönberg, D. (2006). Combined trace element and Pb-Nd-Sr-O isotope evidence for recycled oceanic crust (upper and lower) in the Eceland mantle plume. *Journal of Petrology* **47,** 1705-1749.

Kramers, J. D., Smith, C. B., Lock, N. P., Harmon, R. S. and Boyd, F. R. (1981). Can kimberlites be generated from an ordinary mantle? *Nature* **291,** 53-56.

Kröner, A. (1973). Comments on "Is the African Plate stationary?" *Nature* **243,** 29-30.

Kurszlaukis, S., Franz, L. and Brey, G. P. (1999). The Blue Hills Intrusive Complex in southern Namibia – relationship carbonatites and monticellite picrites. *Chemical Geology* **160,** 1-18.

Kushiro, I. (1996). Partial melting of a fertile mantle peridotite at high pressures: an experimental study using aggregates of diamond. In: Basu, A. and Hart, S.R. (eds). *Earth Processes: Reading the Isotopic Code. American Geophysical Union, Geophysical Monogram* **95,** pp 109-122.

Latin, D., Norry, M. J. and Tarzey, R. J. E. (1993). Magmatism in the Gregory Rift, East Africa: evidence for melt generation by a plume. *Journal of Petrology* **34,** 1007-1027.

LaTourrette, T., Herving, R. L., Holloway, J. R. (1995). Trace-element partitioning between amphibole, phlogopite and basanite melt. *Earth and Planetary Science Letters* **135,** 13-30.

Le Bas, M. J. (1987). Nephelinites and carbonatites. In: Fitton, J. G. and Upton, B. G. J. (eds). *Alkaline Igneous Rocks*. Geological Society of London **30**(special publication), 53-83.

Le Maitre, R. W. (ed), Streckheisen, A., Zanettin, B., Le Bas, M. J., Bonin, B., Batemen, P., Bellieni, G., Dudek, A., Etremova, S., Keller, J., Lameyer, J., Sabine, P. A., Schmid, R., Sørensen, H. and Woolley, A. (2002). *Igneous Rocks: A Classification and Glossary of Terms*. 2nd Edition. Recommendations of the International Union of Geological Sciences Subcommission on the sytematics of igneous rocks. Cambridge University Press. 236 pp.

le Roex, A. P. and Dick, H. J. B. (1981). Petrography and geochemistry of basaltic rocks from the Conrad fracture zone on the America-Antarctica Ridge. *Earth and Planetary Science Letters* **54,** 117-138.

le Roex, A. P. (1986). Geochemical correlation between southern African kimberlites and South Atlantic hotspots. *Nature* **324**, 243-245.

le Roex, A. P., Cliff, R. A. and Adair, B. J. I. (1990). Tristan da Cunha, South Atlantic: geochemistry and petrogenesis of a basanite-phonolite lava series. *Journal of Petrology* **31**, 779-812.

le Roex, A. P., Dick, H. J. B. and Watkins, R. T. (1992). Petrogenesis of anomalous K-enriched MORB from the Southwest Indian Ridge: 11°53'E to 14°38'E. *Contributions to Mineralogy and Petrology* **110,** 253-268.

le Roex, A. P. and Lanyon, R. (1998). Isotope and trace element geochemistry of Cretaceous Damaraland lamprophyres and carbonatites, northwestern Namibia: evidence for plume-lithosphere interactions. *Journal of Petrology* **39**, 1117-1146.

le Roex, A. P., Späth, A. and Zartman, R. E. (2001). Lithospheric thickness beneath southern Kenya Rift: implications from basalt geochemistry. *Contributions to Mineralogy and Petrology* **142,** 89-106.

le Roux, P. J., le Roex, A. P. and Schilling, J.-G. (2002a). Crystallization processes beneath the southern Mid-Atlantic Ridge (40-55°S), evidence for high-pressure initiation of crystallization. *Contributions to Mineralogy and Petrology* **142,** 582-602.

le Roux, P. J., le Roex, A. P., Schilling, J.-G., Shimizu, N., Perkins, W. W. and Pearce, N. J. G. (2002b). Mantle heterogeneity beneath the southern Mid-Atlantic Ridge: trace element evidence for contamination of ambient asthenospheric mantle. *Earth and Planetary Science Letters* **203,** 479-498.

Liati, A., Franz, L., Gebauer, D. and Fanning, C. M. (2004). The timing of mantle and crustal events in South Namibia, as defined by SHRIMP-dating of zircon domains from a garnet peridotite xenolith of the Gibeon Kimberlite Province. *Journal of African Earth Sciences* **39,** 147-157.

Lock, B. E. and Marsh, J. S. (1981). Tertiary phonolite volcanism in the Klinghardt Mountains of South West Africa/Namibia. *Transactions of the Geological Society of South Africa* **84,** 1-6.

MacDonald, R., Rogers, N. W., Fitton, J. G., Black, S. and Smith, M. (2001). Plume-lithosphere interactions in the generation of the basalts of the Kenya Rift, East Africa. *Journal of Petrology* **42,** 877-900.

Mahoney, J. J., le Roex, A. P., Peng, Z., Fisher, R. L. and Natland, J. H. (1992). Southwestern limits of Indian Ocean Ridge mantle and the origin of low $^{206}Pb/^{204}Pb$ mid-ocean ridge basalts: isotope sytematics of the Southwest Indian Ridge (17°-50°E). *Journal of Geophysical Research* **97,** 19771-19790.

Marsh, J. S. (1975). The Luderitz alkaline province, South West Africa: Descriptive petrology of the Granitberg Foyalite Complex. *Transactions of the Geological Society of South Africa* **78,** 215-224.

Marsh, J. S. (1987). Evolution of a strongly differentiated suite of phonolites from the Klinghardt Mountains, Namibia. *Lithos* **20**, 41-58.

Marsh, J. S., Erlank, A. J. and Duncan, A. R. (1991). Preliminary geochemical data for dolerite dykes and sills of the southern part of the Etendeka Igneous Province. *Communications of the Geological Survey of Namibia* **7,** 71-73.

Mattielli, N., Weis, D., Scoates, J. S., Shimizu, N., Mennessier, J.-P., Grégoire, M., Cottin, J.-Y. and Giret, A. (1999). Evolution of heterogeneous lithospheric mantle in a plume environment beneath the Kerguelen Archipelago. *Journal of Petrology* **40,** 1721-1744.

Mattsson, H. B. and Oskarsson, N. (2005). Petrogenesis of alkaline basalts at the tip of a propagating rift: evidence from the Heimaey volcanic centre, south Iceland. *Journal of Volcanology and Geothermal Research* **147,** 245-267.

McKenzie, D. and Bickle, M. J. (1988). The volume and composition of melt generated by extension of lithosphere. *Journal of Petrology* **29,** 625-679.

McKenzie, D. and O'Nions, R. K. (1991). Partial melt distribution from inversion of rare earth element concentrations. *Journal of Petrology* **32,** 1021-1091.

Mengel, K. and Green, D. H. (1989). Stability of amphibole and phlogopite in metasomatised peridotite under water-saturated and water-undersaturated conditions. In: Ross, J., Jaques, A. L., Ferguson, J., Green, D. H., O'Reilly, S. Y., Danchin, R. V. and Janse, A. J. A. (eds). *Kimberlites and Related Rocks.* Geological Society of Australia. Blackwell Scientific Publications, Carlton Australia **1**(special issue), pp 571-581.

Menzies, M. and Murthy, V. R. (1980a). Enriched mantle: Nd and Sr isotopes in diopsides from kimberlite nodules. *Nature* **283,** 634-636.

Menzies, M. and Murthy, V. R. (1980b). Nd and Sr isotope geochemistry of hydrous mantle nodules and their host alkali basalts: implications for local heterogeneities in metasomatically veined mantle. *Earth and Planetary Science Letters* **46,** 323-334.

Menzies, M. and Murthy, V. R. (1980c). Mantle metasomatism as a precursor to the genesis of alkaline magmas-isotopic evidence. *American Journal of Science* **280A,** 622-638.

Menzies, M. and Wass, S. Y. (1983). CO_2- and LREE-rich mantle below eastern Australia: a REE and isotopic study of alkaline magmas and apatite-rich mantle xenoliths from the Southern Highlands Province, Australia. *Earth and Planetary Science Letters* **65,** 287-302.

Mitchell, R. H. (1984). Garnet lherzolites from the Hanaus-I and Louwrensia kimberlites of Namibia. *Contributions to Mineralogy and Petrology* **86,** 178-188.

Morgan, J. W. (1983). Hotspot tracks and the early rifting of the Atlantic. *Tectonophysics* **94,** 123-139.

Morimoto, N., Fabries, J., Ferguson, A. K., Ginzburg, I. V., Ross, M. Seifert, F. A., Zussman, J., Aoki, K. and Gottardi, G. (1988). Nomenclature of pyroxenes. *American Mineralogist.* **73,** 1123-1133.

Nauret, F., Abouchami, W., Galer, S. J. G., Hofmann, A. W., Hémond, C., Chauvel, C. and Dyment. (2006). Correlated trace element-Pb isotope enrichments in Indian MORB along 18-20°S, Central Indian Ridge. *Earth and Planetary Science Letters* **245,** 137-152.

Nielson, J. E. and Noller, J. S. (1987). Processes of mantle metasomatism; constraints from observations of composite peridotite xenoliths. In: Morris, E.M. and Pasteris, J.D. (eds) . *Mantle metasomatism and alkaline magmatism.* Geological Society of America **215** (special paper), pp 61-76.

Nowell, G. M., Pearson, D. G., Bell, D. R., Carlson, R. W., Smith, C. B., Kempton, P. D. and Noble, S. R. (2004). Hf isotope sytematics of kimberlites and their megacrysts: new constrains on their source regions. *Journal of Petrology* **45,** 1583-1612.

Olafsson, M. and Eggler, D. M. (1983). Phase relations of amphibole, amphibole-carbonate and phlogopite-carbonate peridotite: petrologic constraints on the asthenosphere. *Earth and Planetary Science Letters* **64,** 305-315.

Panter, K. S., Hart, S. R., Kyle, P., Blusztanjn, J. and Wilch, T. (2000). Geochemistry of Late Cenozoic basalts from the Crary Mountains: characterization of mantle sources in Marie Byrd Land, Antarctica. *Chemical Geology* **165**, 215-241.

Panter, K. S., Blusztanjn, J., Hart, S. R., Kyle, P. R., Esser, R. and McIntosh, W. C. (2006). The origin of HIMU in the SW Pacific: evidence from intraplate volcanism in southern New Zealand and subantarctic islands. *Journal of Petrology* **47**, 1676-1704.

Paslick, C., Halliday, A., James, D. and Dawson, J. B. (1995). Enrichment of the continental lithosphere by OIB melts: Isotopic evidence from the volcanic province of northern Tanzania. *Earth and Planetary Science Letters* **130,** 109-126.

Pearce, J. A. (1996). A user's guide to basalt discrimination diagrams. In Wyman, D. A. (ed). *Trace element geochemistry of volcanic rocks: applications for massive sulphide exploration: Geological Association of Canada, Short Course Notes* **12**, 79-113.

Pearson, D. G. and Nowell, G. M. (2002). The continental lithospheric mantle: characteristics and significance as a mantle reservoir. *Philosophical Transactions of the Royal Society of London* **A360,** 2383-2410.

Reid, D. L., Cooper, A. F., Rex, D. C. and Harmer, R. E. (1990). Timing of post-Karoo alkaline volcanism in southern Namibia. *Geological Magazine* **127**, 427- 433.

Reid, D. L. and Rex, D. C. (1994). Cretaceous dyke associated with the opening of the South Atlantic: the Mehlberg dyke, northern Richtersveld. *South African Journal of Geology* **92**, 135-145.

Richardson, S. H., Erlank, A. J. and Hart, S. R. (1985). Kimberlite-borne garnet xenoliths from old enriched subcontinental lithosphere. *Earth and Planetary Science Letters* **75,** 116-128.

Roeder, P.L. and Emslie, R. F. (1970). Olivine liquid equilibrium. *Contributions to Mineralogy and Petrology* **29**, 275-289.

Rogers, N. W., Hawkesworth, C. J. and Palacz, Z. A. (1988). The geochemistry of olivine melilitites from southern Africa and controls on U/Pb fraction in the upper mantle. *Chemical Geology* **70** (special issue), 56.

Rogers, N. W., Hawkesworth, C. J. and Palacz, Z. A. (1992). Phlogopite in the generation of olivine melilitites from Namaqualand, South Africa and implications for element fractionation processes in the upper mantle. *Lithos* **28**, 347-365.

Rogers, N., Macdonald, R., Fitton, J. G., George, R., Smith, M. and Barreiro, B. (2000). Two mantle plume beneath the East African rift system: Sr, Nd and Pb isotope evidence from Kenya Rift basalts. *Earth and Planetary Science Letters* **176,** 387-400.

Rollinson, H. R. (1993). *Using geochemical data: evaluation, presentation and interpretation.* Longman Group UK Limited. 352 Pp.

Rudnick, R. L and Fountain, D. M. (1995). Nature and composition of the continental crust: a lower crustal perspective. *Reviews of Geophysics* **33,** 267-309.

Ryerson, F. J. and Watson, E. B. (1987). Rutile saturation in magmas: implications for Ti-Nb-Ta depletion in island-arc basalts. *Earth and Planetary Science Letters* **86,** 225-239.

Sajona, F. G., Maury, R. C., Pubellier, M., Leterrier, J., Bellon, H. and Cotton, J. (2000). Magmatic source enrichment by slab derived melts in a young post-collision setting, central Mindanao (Philippines). *Lithos* **54**, 173-206.

Schilling, J. G., Kingsley, R. H., Hanan, B. B. and McCully, B. L. (1992). Nd-Sr-Pb isotopic variations along the Gulf of Aden: evidence for mantle plume-continental lithosphere interaction. *Journal of Geophysical Research* **97,** 10927-10966.

Shaw, D. M. (1970). Trace element fractionation during anatexis. *Geochimica et Cosmochica Acta.* **34,** 237-243.

Shaw, J. E., Baker, J. A. Menzies, M. A., Thirlwall, M. F. and Ibrahim, K. M. (2003). Petrogenesis of the largest intraplate volcanic field on the Arabian Plate (Jordan): a mixed lithosphere-asthenosphere source activated by lithospheric extension. *Journal of Petrology* **44**, 1657-1679.

Siebel, W., Becchio, R., Volker, F., Hansen, M. A. F., Viramonte, J., Trumbull, R. B. Haase, G. and Zimmer, M. (2000). Trindade and Matrín Vaz Islands, South Atlantic: Isotopic (Sr, Nd, Pb) and trace element constraints on plume related magmatism. *Journal of South American Earth Sciences* **13**, 79-103.

Simonetti, A. and Bell, K. (1994). Nd, Pb and Sr isotopic data from the Napak carbonatite-nephelinite centre, eastern Uganda: an example of open system crystal fractionation. *Contributions to Mineralogy and Petrology* **115,** 356-366.

Simonetti, A. and Bell, K. (1995). Nb, Pb and S isotopic data from the Mount Elgon volcano, eastern Uganda-western Kenya: Implications for the origin and evolution of nephelinite lavas. *Lithos* **36,** 141-153.

Späth, A., le Roex, A. P. and Duncan. R. A. (1996). The geochemistry of lavas from the Comores Archipelago, western Indian Ocean: petrogenesis and mantle source region characteristics. *Journal of Petrology* **37**, 961-991.

Späth, A., le Roex, A. P. and Opiyo-Akech, N. (2000). The Petrology of the Chyulu Hills Volcanic Province, southern Kenya. *Journal of African Earth Sciences* **31**, 337-358.

Späth, A., le Roex, A. P. and Opiyo-Akech, N. (2001). Plume-lithosphere interaction and the origin of continental rift-related alkaline volcanism-the Chyulu Hills Volcanic Province, southern Kenya. *Journal of Petrology* **42**, 765-787.

Spriggs, A. J. (1988). An isotopic and geochemical study of kimberlites and associated alkaline rocks from Namibia. *Unpublished PhD Thesis.* University of Leeds.

Stein, M. and Hofmann, A. L. (1992). Fossil plume head beneath the Arabian lithosphere? *Earth and Planetary Science Letters* **114,** 193-209.

Stosch, H.-G. and Lugmair, G. W. (1986). Trace element and Sr and Nd isotope geochemistry of peridotite xenoliths from the Eifel (West Germany) and their bearing on the evolution of subcontinental lithosphere. *Earth and Planetary Science Letters* **80,** 281-298.

Sun, S.-S. and Hanson, G. N. (1975a). Evolution of the mantle: geochemical evidence from alkali basalt. *Geology* **3,** 297-302.

Sun, S.-S. and Hanson, G. N. (1975b). Origin of Ross Island basanitoids and limitations upon the heterogeneity of mantle sources for alkali basalts and nephelinites. *Contributions to Mineralogy and Petrology* **52,** 77-106.

Sun, S.-S. and McDonough, W. F. (1989). Chemical and isotopic sytematics of oceanic basalts: implications for mantle composition and processes. In: Saunders, A.D. and Nory, M.J. (eds). *Magmatisim in the Ocean Basins*. Geological Society of London, **42** (special publication), pp 313-345.

Taylor, S. R. and McLennan, S. M. (1981). The composition and evolution of the continental crust: rare earth element evidence for sedimentary rocks. *Philosophical Transactions of the Royal Society of London* **A301,** 381-399.

Taylor, S. R. and McLennan, S. M. (1985). *The continental crust: its composition and evolution.* Oxford, Blackwell. 312 pp.

Thomas, L. E., Hawkesworth, C. J., Van Calsteren, P., Turner, S. P. and Rogers, N. W. (1999). Melt generation beneath ocean islands: A U-Th-Ra isotope study from Lanzarote in the Canary Islands. *Geochimica et Cosmochimica Acta* **63,** 4081-4099.

Trumbull, R. B., Bühn, B., Romer, R. L. and Volker, F. (2003). The petrology of basanite-tephrite intrusions in the Erongo complex and implications for a plume origin of Cretaceous alkaline complexes in Namibia. *Journal of Petrology* **44,** 93-111.

Volker, F., McCulloch, M. T. and Altherr, R. (1993). Submarine basalts from the Red Sea: new Pb, Sr and Nd isotopic data. *Geophysical Research Letters* **20,** 927-930.

Wallace, M. E. and Green, D. H. (1988). An experimental determination of primary carbonatite magma composition. *Nature* 335, 343-346.

Wass, S. Y. and Rogers, N. W. (1980). Mantle metasomatism -precursor to alkaline continental volcanism. *Geochimica et Cosmochimica Acta* **44,** 1811-1823.

Waters, D. J. (1989). Metamorphic for the heating and cooling of Namaqualand granulites. In: Daly, J. S., Cliff, R. A. and Yardley, B. W. D. (eds). *Evolution of Metamorphic Belts*. Geological Society of London. pp 357-363.

Weaver, B. L. and Tarney, J. (1984). Empirical approach to estimating the composition of the continental crust. *Nature* **310,** 575-577.

Weaver, B. L. (1991a). The origin of oceanic island basalt end-member compositions: trace element and isotopic constraints. *Earth and Planetary Science Letters* **104,** 381-397.

Weaver, B. L. (1991b). Trace element evidence for the origin of ocean-island basalts. *Geology* **19,** 123-126.

Weinstein, Y. (2000). Spatial and temporal geochemical variability in basin-related volcanism, northern Israel. *Journal of African Earth Sciences* **30,** 865-886.

Weinstein, Y., Navon, O., Altherr, R. and Stein, M. (2006). The role of lithospheric mantle heterogeneity in the generation of Plio-Pleistocene alkali basaltic suites from NW Harrat Ash Shaam (Israel). *Journal of Petrology* **47,** 1017-1050.

White, R and McKenzie, D. (1989). Magmatism at rift zones: the generation of volcanic continental margins and flood basalts. *Journal of Geophysical Research* 94, 7685-7729.

Widom, E., Carlson, R. W., Gill, J. B and Schmincke, H.-U. (1997). Th-Sr-Nd-Pb isotope and trace element evidence fro the origin of the São Miguel, Azores, enriched mantle source. *Chemical Geology* **140,** 49-68.

Willis, J. P. (1999). Instrumental parameters and data quality for routine major and trace element determinations by WDXRFS, University of Cape Town, Cape Town.

Wilson, M. (1989). *Igneous Petrogenesis: a global tectonic approach.* Unwin Hyman Ltd, Uk. 446 pp.

Wilson, M. and Downes, H. (1991). Tertiary-Quaternary extension-related alkaline magmatism in Western and Central Europe. *Journal of Petrology* **32,** 811-849.

Wilson, M., Rosenbaum, J. M., Dunworth, E. A. and Larsen, G. (1992). Are melilitites partial melts of the thermal boundary layer? *Eos, Transactions, American Geophysical Union.* **73,** 325.

Wilson, M., Rosenbaum, J. M. and Dunworth, E. A. (1995). Melilitites: partial melts of the thermal boundary layer? *Contributions to Mineralogy and Petrology* **119**, 181-196.

Witt-Eickschen, G., and Kramm, U. (1998). Evidence for multiple stage of the subcontinental lithospheric mantle beneath the Eifel (Germany) from pyroxenite and composite pyroxenite/peridotite xenoliths. *Contributions to Mineralogy and Petrology* **131,** 258-272.

Witt-Eickschen, G., Kaminsky, W., Kramm, U. and Harte, B. (1998). The nature of young vein metasomatism in the lithosphere of the West Eifel (Germany): geochemical and isotopic constraints from composite mantle xenoliths from the Meerfelder Maar. *Journal of Petrology* **39,** 155-185.

Witt-Eickschen, G., Seck, H. A., Mezger, K., Eggins, S. M. and Altherr. (2003). Lithospheric mantle evolution beneath the Eifel (Germany): constraints from Sr-Nd-Pb isotopes and trace element abundances in spinel peridotite and pyroxenite xenoliths. *Journal of Petrology* **44,** 1077-1095.

Workman, R. K., Hart, S. R., Jackson, M., Regelous, M., Farley, K. A., Blusztajn, J., Kurz, M. and Staudigel, H. (2004). Recycled metasomatized lithosphere as the origin of the enriched

mantle II (EM2) end member: evidence from Samoan volcanic chain. *Geochemistry, Geophysics, Geosystems* **5,**

Worthington, T. J., Hekinian, R., Stoffers, P., Kuhn, T. and Hauff, F. (2006). Osbourn Trough: Structure, geochemistry and implications of a mid-Cretaceous paleospreading ridge in the South Pacific. *Earth and Planetary Science Letters* **245,** 685-701.

Zannetti, A., Vannucci, R., Bottazzi, P., Oberti, R. and Ottolini, L. (1996). Infiltration metasomatism at Lherz as monitored by systematic ion-microprobe investigations close to a hornblendite vein. *Chemical Geology* **134,** 113-133.

Zindler, A. and Hart, S. R. (1986). Chemical dynamics. *Annual Review of Earth and Planetary Sciences* **14,** 493-571.

Zindler, A. (1980). Geochemical processes in the Earth's mantle and the nature of crust-mantle interactions: evidence from the studies of Nd and Sr isotope ratios in mantle-derived igneous rocks and lherzolite nodules. *Unpublished Ph.D thesis*. Massachusetts Institute of Technology.

Zhang, M. and O'Reilly, S. Y. (1997). Multiple sources for basaltic rocks from Dubbo, eastern Australia: geochemical evidence for plume-lithosphere interaction. *Chemical Geology* **136,** 33-54.

Zhi, X., Song, Y., Frey, F. A., Feng, J. and Zhai, M. (1990). Geochemistry of Hannuoba basalts, eastern China: Constraints on the origin of continental alkalic and tholeiitic basalt. *Chemical Geology* **88,** 1-33.

APPENDIX A

PETROGRAPHIC DESCRIPTIONS

A.1 Tsirub dyke

AN-001: Sparsely porphyritic olivine nephelinite

This sample is a sparsely porphyritic to microporphyritic rock with olivine and rare clinopyroxene phenocrysts/microphenocrysts set in a fine-grained groundmass. Anhedral to rarely subhedral olivine phenocrysts/microphenocrysts are 0.5 - 2.0 mm in size, constitute ~ 10 vol.% of the rock. Thin brown alteration rims surround most olivine crystals (Fig. A.1). Rare clinopyroxene crystals (< 2 vol.%), measure 0.5 -1.5 mm in size. Some crystals show simple to complex zoning with darker rims than cores and many have sieve texture cores. The fine grained groundmass is made up of olivine, clinopyroxene, minor Fe-Ti oxides and scattered pleochroic brown secondary amphibole aggregates.

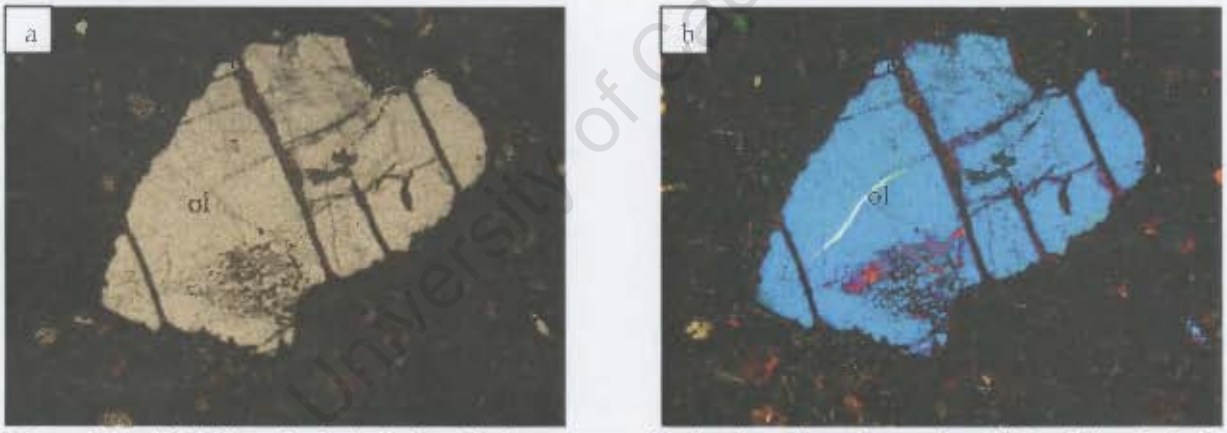

Fig A.1 (a) ***AN-001:*** Anhedral olivine (ol) phenocryst with interior alteration cracks. Field of view is 2.5 mm across. (b) Under crossed polars.

A.2 Tsirub North (outer) plug

AN-003: microporphyritic basanite

This sample is a microporphyritic rock with microphenocrysts of olivine and clinopyroxene set in a very fine grained groundmass. Anhedral to rarely subhedral and euhedral olivine microphenocrysts, 0.3 -1.4 mm in size, constitute ~5 vol.% of the rock, and many are rimmed by serpentine alteration rims. Elongate, 0.3 - 1mm long, anhedral to rarely subhedral, clinopyroxene microphenocrysts constitute ~2 vol.% of the rock and sometimes occur in radiating clusters (Fig.

A.2). Olivine, lath-shaped clinopyroxene, and minor opaque Fe-Ti oxides and secondary brown amphibole make up the fine-grained groundmass. Felsic xenoliths comprising feldspar and green euhedral and anhedral needle-shaped clinopyroxen (diopside and aegirine-augite). Clinopyroxene crystals are mostly confined to the edges of the xenoliths and a few are poikilitically enclosed within larger feldspar crystals

AN-004: microporphyritic basanite

This sample is a microporphyritic rock with olivine and rare brown clinopyroxene microphenocrysts set in a fine grained groundmass. Olivine microphenocrysts (3.5 vol.%), are 0.3 -1.3 mm in size, majority are anhedral, few are subhedral and very few are euhedral. Many are enclosed in thin brown alteration rims with few being completely altered to brown colour. Brown elongate clinopyroxene microphenocrysts, 0.3 - 0.8 mm in size, form ~2 vol.% of the rock, these are anhedral to rarely subhedral, and sometimes occur in clusters. A single sector zoned clinopyroxene crystal occurs in this sample. Lath-like clinopyroxene dominates the groundmass, with minor olivine, brown pleochroic secondary amphibole and black Fe-Ti oxides. Like in sample AN-003, felsic xenoliths composed of alkali feldspar and clinopyroxene (diopside and aegirine augite) occur in this sample (Fig. A.3a).

AN-005: microporphyritic basanite

This sample is a sparsely microporphyritic with olivine and rare brown clinopyroxene microphenocrysts set in a very fine groundmass. Olivine phenocrysts, 0.3 - 0.8 mm in size, constitute 4.5 vol.% of the rock, few are zoned with darker rims than cores. Most are anhedral, minor subhedral and very few are euhedral, many have thin dark brown alteration veinlets or thin alteration rims (Fig. A.3b). Few crystals show zoning with darker rims than cores. Anhedral clinopyroxene (<1 vol.%) measure 0.3 - 0.7 mm in size, these are all anhedral and few are zoned with darker rims than cores. Felsic xenoliths consisting of dominant feldspar and anhedral needle-shaped and rarely subhedral clinopyroxene occur in this sample. The fine grained groundmass is made up of clinopyroxene, olivine, minor secondary brown amphibole and Fe-Ti oxides.

AN-006: microporphyritic basanite

This sample is a microporphyritic rock in which olivine microphenocrysts are set in a very fine grained groundmass. Anhedral to rarely subhedral olivine microphenocrysts, 0.3 – 0.8 mm in size, form 1.5 vol.% of the rock, majority are rimmed by dark brown alteration rims and the smaller ones are completely pseudomorphosed by serpentine (Fig. A.4a). Lath-like

clinopyroxene, minor olivine, opaque Fe-Ti oxides and secondary amphibole constitute the fine grained groundmass. Minor felsic xenoliths made up of alkali feldspar and clinopyroxene occur in this sample.

AN-006B: vesicular microporphyritic basanite

This sample is a vesicular microporphyritic rock with olivine and minor brown clinopyroxene microphenocrysts set in a very fine grained matrix. Olivine microphenocrysts, 2.5 vol.%, measure 0.3 - 0.5 mm in size, most are anhedral with occasional subhedral and euhedral crystals, and few exhibit compositional zoning with darker rims than cores. They are enclosed in, mostly thin to thick, brown alteration rims and few consist of brown alteration cracks. Elongate, 0.3 - 0.6 mm long, anhedral clinopyroxene microphenocrysts (<0.5 vol.%) commonly show sector zoning. Carbonate vesicles, 0.8 - 2.4 mm long, form 15 vol.% of the rock. The fine matrix is made up of olivine and clinopyroxene in equal abundance, and black opaque Fe-Ti oxides. Minor, felsic xenoliths were observed.

AN-012: vesicular microporphyritic basanite

This sample is vesicular microporphyritic rock in which altered olivine microphenocrysts (Fig. A.4b) are set in a fine grained groundmass. Olivine microphenocrysts, 0.3 - 0.9 mm in size, constitute 2 vol.% of the rock, these are mostly anhedral, and few are subhedral or euhedral. And many are enclosed in thick brown alteration rims of serpentine. Carbonate vesicles constitute < 0.5 vol.% of the rock. Clinopyroxene is only present in the groundmass together with olivine and few black Fe-Ti oxides.

AN-013: densely microporphyritic basanite

This sample is a microporphyritic rock in which olivine and brown clinopyroxene microphenocrysts are embedded in a fine grained groundmass. Olivine microphenocrysts, 0.3 - 0.8 mm long, form approximately 3 vol.% of the rock, many are anhedral, few are subhedral and very few are euhedral. Most are partially altered to, e.g. along cracks, or completely replaced by, serpentine. Elongate clinopyroxene microphenocrysts, 2.5 vol.%, range between 0.3 - 0.7 mm in length, they are mostly anhedral with few being subhedral or euhedral (Fig. A.5). The euhedral clinopyroxene crystals show zoning with darker rims than cores. Lath-like clinopyroxene, 3 vol.% of the matrix, olivine, brown secondary amphibole and black Fe-Ti oxides make up the fine grained groundmass.

AN-014: densely microporphyritic basanite

This sample is a densely microporphyritic rock in which olivine and brown clinopyroxene are set in a fine grained groundmass. Olivine microphenocrysts, 0.3 - 0.8 mm in size, make up 3.5 vol.% of the rock, most are anhedral with few subhedral and very rarely euhedral ones and many are rimmed by, and few are completely altered to, serpentine. Brown clinopyroxene microphenocrysts, 0.4 - 1.3 mm, constitute 2.5 vol.% of the rock, many are anhedral and few are subhedral in habits (Fig. A.6a). A single cluster of clinopyroxene microphenocrysts occur in this sample. Minor felsic xenoliths comprising feldspar and clinopyroxene; some of the clinopyroxenes are poikilitically enclosed. Lath-like clinopyroxene, minor olivine, brown secondary amphibole and black Fe-Ti oxides make up the fine grained groundmass.

AN-014A: vesicular microporphyritic basanite

This sample is a vesicular microporphyritic highly altered rock in which rare olivine and brown clinopyroxene are set in a fine grained matrix. Minor olivine microphenocrysts, < 1vol.%, range between 0.2 - 0.8 mm in size, many are anhedral with few being subhedral or euhedral. These are severely altered and most are rimmed by thick brown alteration rims. Rare clinopyroxene microphenocrysts, < 0.5 vol.%, range between 0.3 and 0.8 mm in size, some from clusters composed of at least four crystals. The fine grained matrix is made up of olivine and clinopyroxene. A single felsic xenolith composed of feldspar hosting lath-shaped clinopyroxene occurs in this sample. This sample is similar to AN-006B, but it has larger carbonate vesicles. Like sample AN-006B, the vesicles are filled by carbonates, possibly calcite, with some crystals showing simple twinning.

AN-015: microporphyritic basanite

This sample is a microporphyritic rock with olivine and minor brown clinopyroxene set in a fine grained groundmass. Olivine microphenocrysts, 0.3 - 0.8 mm in size, make up 2.5 vol.% of the rock, most are anhedral and few subhedral or euhedral, and few are rimmed by, or completely altered to, serpentine. Brown clinopyroxene, < 1 vol.%, measure 0.3 - 1.0 mm in size, most are anhedral, few are subhedral and very few are euhedral. Few subhedral crystals exhibit zoning with darker rims than cores (Fig. A.6b). Felsic xenoliths composed of feldspar and clinopyroxene (mostly needle shaped) occur in this sample. Lath-like clinopyroxene and minor olivine, pleochroic brown secondary amphibole and black Fe-Ti oxides make up the fine grained groundmass.

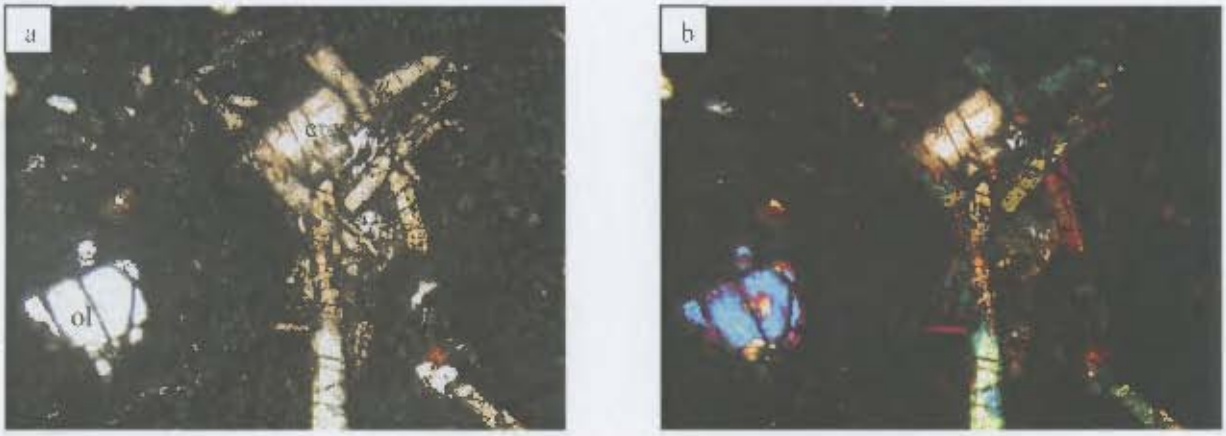

Fig. A.2 (a) ***AN-003:*** Clusters of elongate clinopyroxene (cpx) microphenocrysts. Field of view is 1.4 mm across. (b) Under crossed polars.

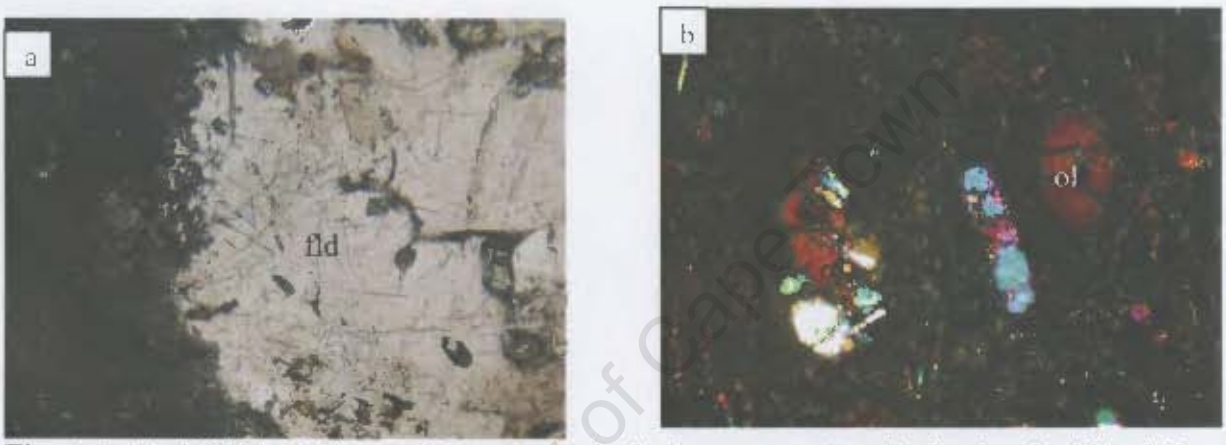

Fig. A.3 (a) ***AN-004:*** Felsic xenoliths composed of clinopyroxene "needles"enclosed within feldspar (fld); under crossed polars. Field of view is 1 mm across. (b) ***AN-005:*** Altered anhedral and subhedral olivine microphenocrysts, note the single elongate clinopyroxene microphenocryst (top left). Field of view is 1 mm across, picture taken under crossed polars.

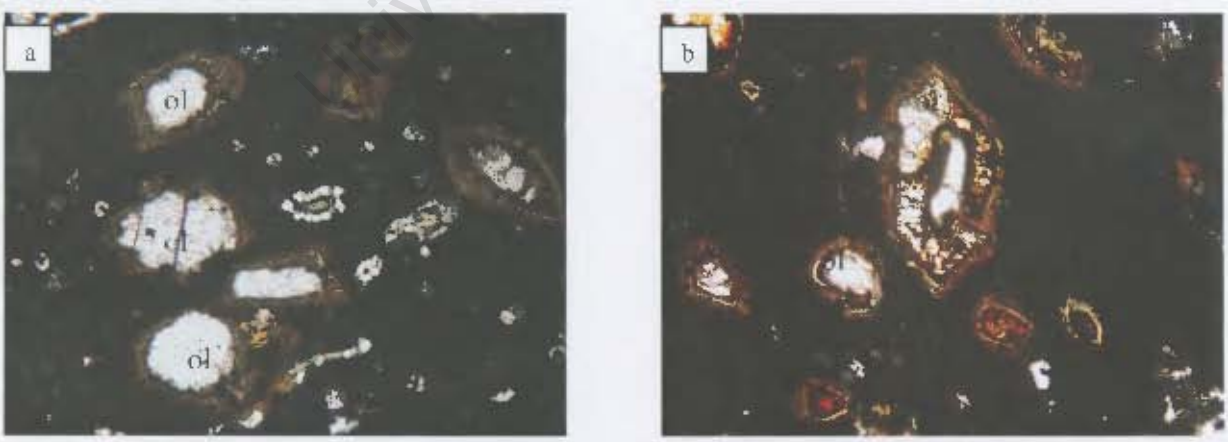

Fig. A.4 (a) ***AN-006:*** Very altered anhedral olivine microphenocrysts enclosed in brown alteration rims. Under plane polarized light. Field of view is 2.5 mm across. (b) ***AN-012:*** Very altered olivine microphenocrysts, note the subhedral olivine microphenocryst in the centre, under plane polarized light. Field of view is 1.2 mm across.

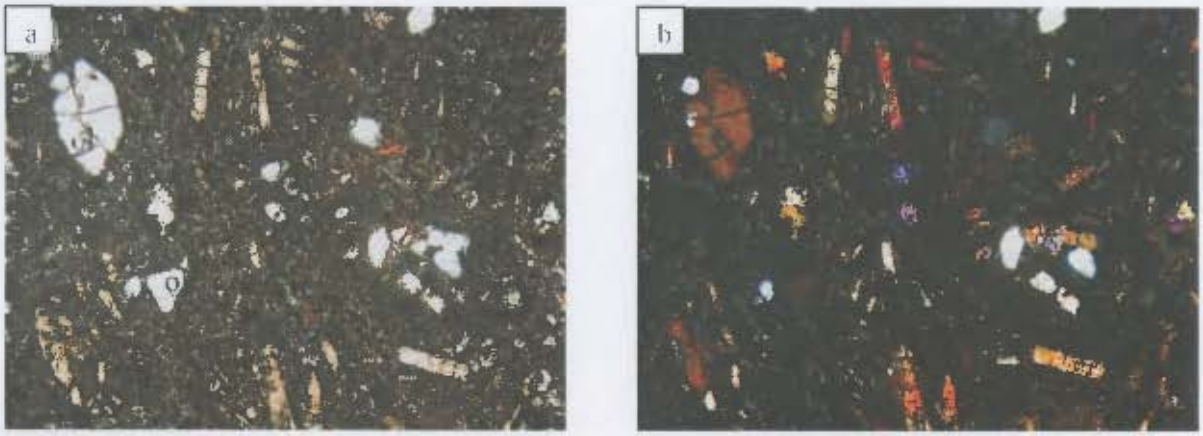

Fig. A.5 (a) ***AN-013:*** Euhedral and anhedral olivine and clinopyroxene (light brown) microphenocrysts embedded in a fine grained groundmass of clinopyroxene, ± Fe-Ti oxides and secondary amphibole (dark brown). Under plane polarized light. Field of view is 1.5 mm across. (b) Under crossed polars.

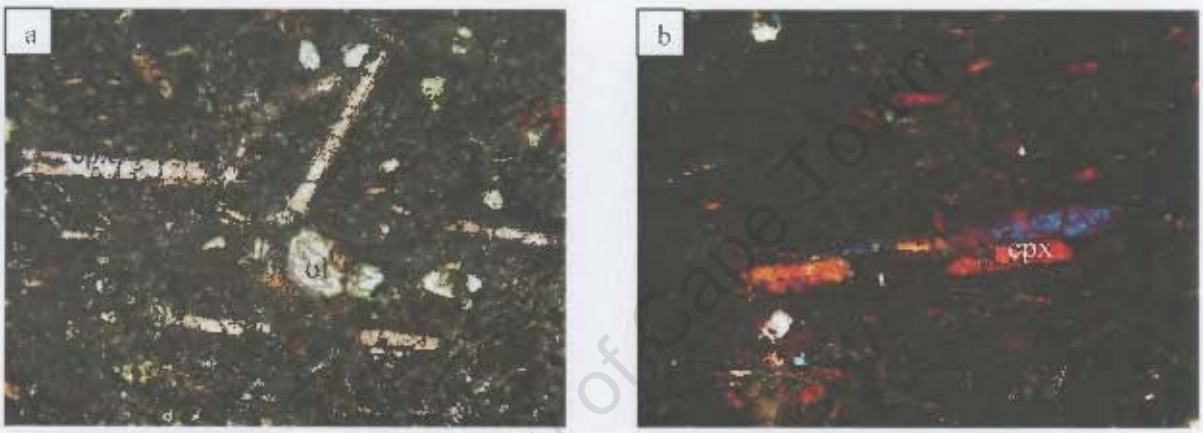

Fig. A.6 (a) ***AN-014:*** Anhedral clinopyroxene microphenocrysts, note the olivine microphenocrysts that are partially or completely altered to green serpentine. Under plane polarized light. Field of view is 1.8 mm across. (b) ***AN-015:*** Anhedral elongate clinopyroxene phenocryst. Under crossed polars. Field of view is 1.4 mm across.

A.3 Tsirub North (inner) plug

AN-007: sparsely microporphyritic nephelinite

This sample is a sparsely microporphyritic with olivine and rare brown clinopyroxene microphenocrysts set in a fine grained groundmass. Olivine is the dominant microphenocryst phase. It forms anhedral to rarely subhedral 0.3 – 1.5 mm long crystals (1.5 vol.%); the majority are partially replaced along the crystal edges by, or completely altered to, serpentine (Fig. A.7a). Minor crystals are enclosed in brown alteration rims. Anhedral clinopyroxene microphenocrysts, 0.3- 0.6 mm in size, constitute <0.5 vol.% of the rock.. The fine grained groundmass is mostly made up of clinopyroxene and minor olivine, opaque Fe-Ti oxides and pleochroic secondary amphibole. Felsic xenoliths composed of dominant feldspar and clinopyroxene occur in this

sample. Feldspar mostly occurs in the centre of the xenoliths whereas clinopyroxenes are dominantly confined to the edges, most of those that occur in the centre are poikilitically enclosed within larger feldspars.

AN-007A: very sparsely microporphyritic nephelinite

This sample is a very sparsely microporphyritic in which olivine and very minor brown clinopyroxene microphenocrysts are set in a fine-grained groundmass. Anhedral olivine microphenocrysts, 0.4 - 0.8 mm in size, constitute < 1 vol.% of the rock, few show zoning with darker rims than cores and most are replaced by serpentine. Minor lath-shaped clinopyroxene microphenocrysts, 0.4 - 0.8 mm in size, constitute << 0.5 vol.% of the rock (Fig. A.7b). The fine grained groundmass is made up of abundant lath-like clinopyroxene, minor olivine and brown secondary amphibole. Felsic xenoliths composed of dominant feldspar and light and dark clinopyroxene occur in this sample. Feldspar mostly occurs in the centre of the xenoliths whereas clinopyroxenes are dominantly confined to the edges, many of the few that occur in the centre are poikilitically enclosed within larger feldspars.

AN-008: sparsely porphyritic nephelinite

This sample is similar to AN-007A and is sparsely microporphyritic in which olivine and rare brown clinopyroxene microphenocrysts are set in a very fine grained groundmass. Anhedral to rarely subhedral olivine microphenocrysts, 0.3 - 0.5 mm in size, form 1.5 vol.% of the rock, few crystals are enclosed in thin serpentine rims or brown alteration rims. Some are zoned with darker rims than cores. Brown clinopyroxene microphenocrysts, < 0.5 vol.%, measure 0.3 – 2.0 mm in length, these are anhedral to rarely subhedral in habits and few display sector zoning (Fig. A.8a). The fine grained groundmass consists of lath-like clinopyroxene, olivine, brown secondary amphibole and Fe-Ti oxides. Clinopyroxene dominates the groundmass suite. Felsic xenoliths comprising needle-shaped clinopyroxene together and alkali feldspar.

AN-009: microporphyritic nephelinite

This sample is a microporphyritic rock in which olivine and minor brown clinopyroxene microphenocryts are set in a fine grained groundmass. Olivine microphenocrysts, 0.3 - 0.7 mm in size, form 3 vol.% of the rock, most are anhedral with few being subhedral and some exhibit zoning with darker rims than cores. Some crystals, mostly the smaller ones, are completely replaced by serpentine. A single olivine microphenocryst, with a core of recrystallized porphyroblast? occurs in this sample (Fig. A.8b). Anhedral to moderately subhedral, 0.3 - 0.7 mm

long, clinopyroxene microphenocrysts constitute << 0.5 vol.% of the rock. Clinopyroxene, olivine and, in equal abundance, and secondary amphibole make up the groundmass suite. This sample has felsic xenoliths consisting of alkali feldspar and subhedral clinopyroxene. The centres of the xenoliths are dominated by feldspar but their margins are largely occupied by made clinopyroxenes.

AN-010: microporphyritic nephelinite

This sample is a microporphyritic rock with olivine and very minor clinopyroxene microphenocrysts set in a fine grained groundmass. Olivine microphenocrysts, 0.3 - 0.7 mm long, constitute 2.5 vol.% of the rock, many are anhedral with few subhedral ones, and the vast majority are surrounded by thin to thick brown alteration rims (Fig. A.9a). A single zoned crystal with a darker rim than core occurs in this sample. Very rare clinopyroxene microphenocrysts, 0.3 - 0.8 mm in length, make up < 0.5 vol.% of the rock, these are anhedral elongate crystals. The fine grained groundmass is made up of olivine, clinopyroxene, opaque Fe-Ti oxides and secondary amphibole. This sample has felsic xenoliths consisting of alkali feldspar and subhedral clinopyroxene. The centres of the xenoliths are dominated by feldspar but their margins are largely occupied by made clinopyroxenes.

AN-011: very sparsely microporphyritic nephelinite

This sample is a very sparsely microporphyritic rock with rare olivine and brown clinopyroxene microphenocrysts set in a fine grained groundmass. Olivine microphenocrysts, 0.3 – 2.0 mm in length, constitute < 1 vol.% of the rock, they are anhedral in habits and most are replaced, along the crystal edges, by serpentine. Few crystals are zoned with darker rims than core. Clinopyroxene microphenocrysts, 0.3 - 0.9 mm in length, make up << 0.5 vol.% of the rock and are anhedral, except a single highly altered euhedral crystal. The fine grained groundmass is made up of lath-like clinopyroxene, olivine, brown secondary amphibole (Fig. A.9b) and black Fe-Ti oxides. The fine grained groundmass is made up of olivine, clinopyroxene, opaque Fe-Ti oxides and secondary amphibole. This sample consists of felsic xenoliths consisting of alkali feldspar and anhedral to rarely subhedral clinopyroxene.

AN-017: very sparsely microporphyritic nephelinite

This sample is a very sparsely microporphyritic rock with olivine phenocrysts set in a fine grained groundmass. Olivine microphenocrysts, 0.3 - 0.6 mm in size, constitute 1 vol.% of the rock, many are anhedral and few are subhedral, some display zoning with darker rims than cores.

Most have "dissolved" grain boundaries and some are rimmed by serpentine (Fig. A.10a). The fine grained groundmass is made up of olivine, minor pleochroic brown secondary amphibole and black Fe-Ti oxides. Felsic xenoliths composed of alkali feldspar and clinopyroxene occur scattered in this sample.

AN-018: sparsely microporphyritic nephelinite

This sample is a very sparsely microporphyritic rock in which olivine and very rare brown clinopyroxene are set in a very fine grained groundmass. Olivine microphenocrysts, 0.3 - 0.9 mm, make up 1.5 vol.% of the rock, majority are anhedral and few are subhedral or euhedral. Few are zoned with darker rims than cores (Fig. A.10b). The smaller crystals are replaced by serpentine. Clinopyroxene microphenocrysts, 0.3-1.0 mm, constitute <1 vol.% of the rock, many are anhedral in habit. Clinopyroxene, olivine, minor secondary amphibole and black Fe-Ti oxides constitute the groundmass. Felsic xenoliths, similar to the ones observed in other samples from the same plug, consisting of large, >3mm in size, feldspar crystals and subhedral to euhedral clinopyroxenes occur in this sample.

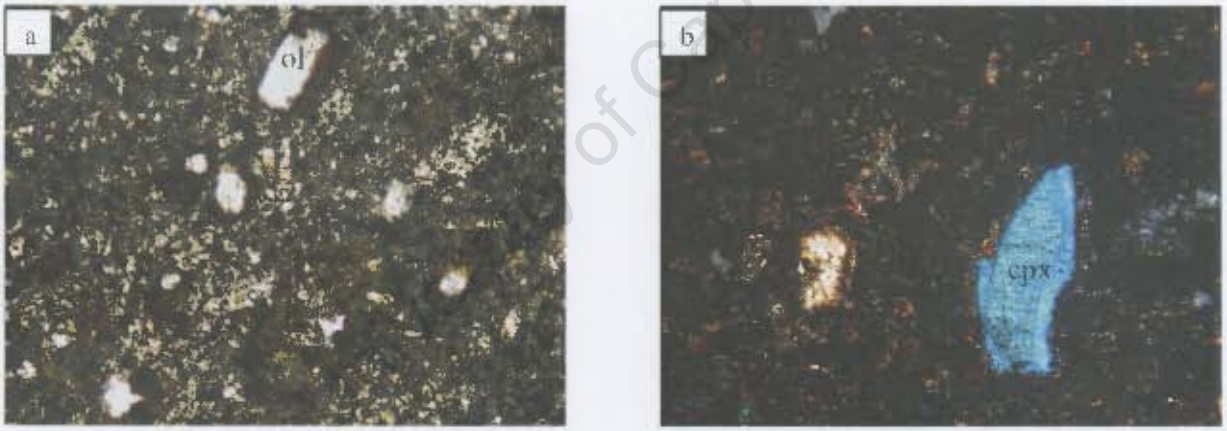

Fig. A.7 (a) ***AN-007:*** Scattered anhedral olivine microphenocrysts enclosed in alteration rims. Under plane polarized light. Field of view is 2.5 mm across. (b) ***AN-007A:*** Subhedral clinopyroxene microphenocryst. Under crossed polars. Field of view is 2.5 mm across.

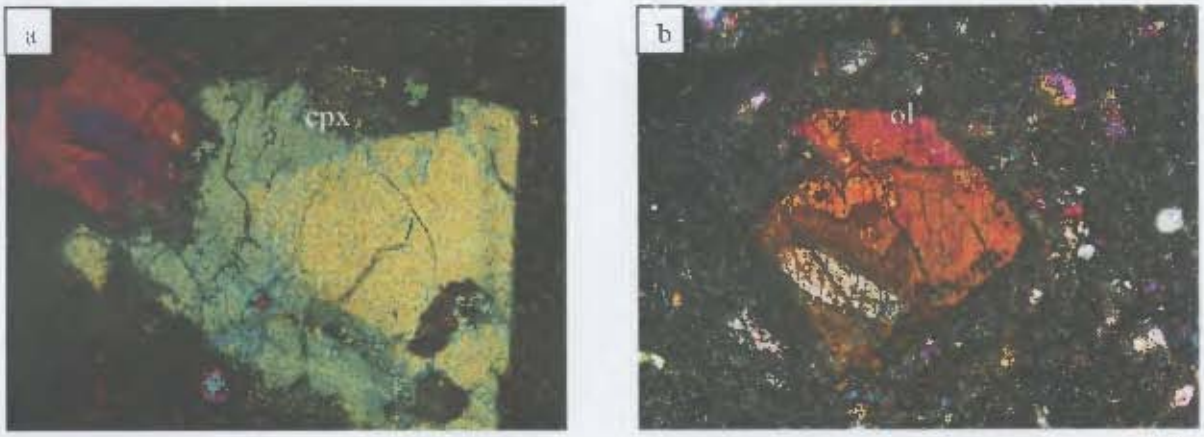

Fig. A.8 (a) ***AN-008:*** Sector zoned anhedral clinopyroxene phenocryst, under crossed polars. Field of view is 2.5 mm across. (b) ***AN-009:*** Anhedral olivine phenocryst (centre) with a recrystallized core of a porphyroblast? Under crossed polars. Field of view is 1.5 mm across.

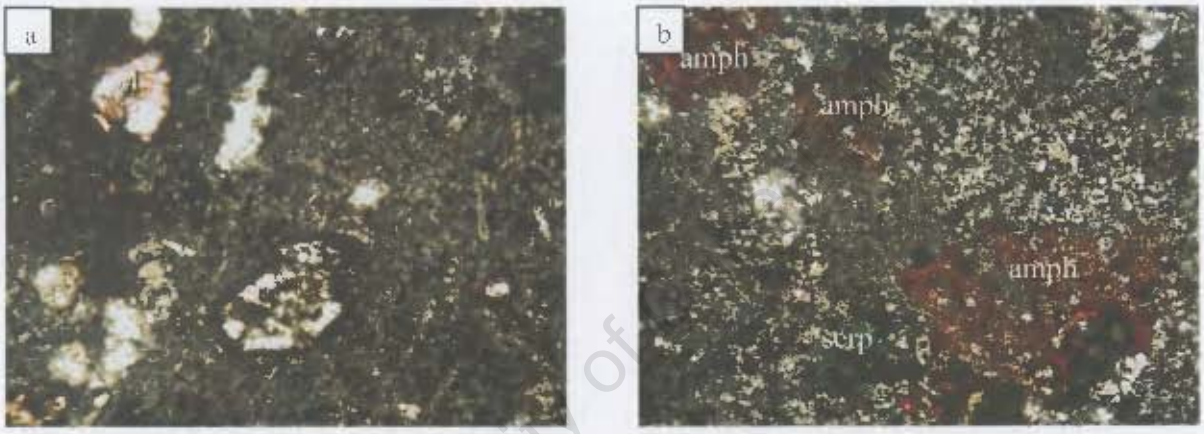

Fig. A.9 (a). ***AN-010:*** Altered olivine microphenocrysts enclosed in brown alteration rims. Under plane polarized light. Field of view is 1.3 mm across. (b) ***AN-011:*** Black opaque Fe-Ti oxides and secondary brown amphibole (amph) occur in the groundmass. Note the green secondary serpentine (serp), bottom centre. Under plane polarized light. Field of view is 2.5 mm across.

Fig. A.10 (a) ***AN-017:*** Subhedral olivine microphenocryst (upper left) with secondary alteration cracks. Field of view is 2.2 mm across. (b) ***AN-018:*** Euhedral olivine microphenocryst showing compositional zoning (under crossed polars). Field of view is 2 mm across.

A.4 Samples AN-016 and AN-019

AN-016: sparsely microporphyritic nephelinite

This sample is a very sparsely microporphyritic rock in which olivine microphenocrysts are set in a fine grained groundmass. Olivine microphenocrysts, 0.3 - 1.3 mm in size, constitute 5 vol.% of the rock, these are anhedral to rarely subhedral, and few are enclosed in serpentine rims or have alteration cracks filled by serpentine (Fig. A.11). Very rare clinopyroxene microphenocrysts, 0.3 - 1.3 mm, are very rare and constitute < 0.5 vol.% of the rock and most are anhedral with few being subhedral in habits. The fine grained groundmass is made up of olivine, clinopyroxene, pleochroic brown secondary amphibole and black Fe-Ti oxides. In comparison to the other Tsirub samples, Fe-Ti oxides of this sample are relatively coarser.

AN-019: very sparsely microporphyritic nephelinite

This sample is a very sparsely microporphyritic rock in which olivine and very minor clinopyroxene microphenocrysts are set in a fine grained groundmass. Olivine microphenocrysts, 0.3-1.4 mm in size, constitute 2.5 vol.% of the rock, majority are anhedral to rarely subhedral and few display zoning with darker rims than cores. Most of the crystals consist of thin alteration cracks occupied by serpentine. Very minor clinopyroxene crystals, << 0.5 vol.%, measure 0.3 - 0.4 mm in size, most are subhedral, few are anhedral and one single crystal is euhedral. A single euhedral crystal is zoned with a darker rim than the core (Fig. A.12). The fine grained groundmass is dominantly made up of clinopyroxene (6 vol.%) and less dominant amphibole (3 vol.%) and olivine (<1 vol.%) and moderate black Fe-Ti oxides. Fe-Ti oxides crystals are as similar in size to those in sample AN-016.

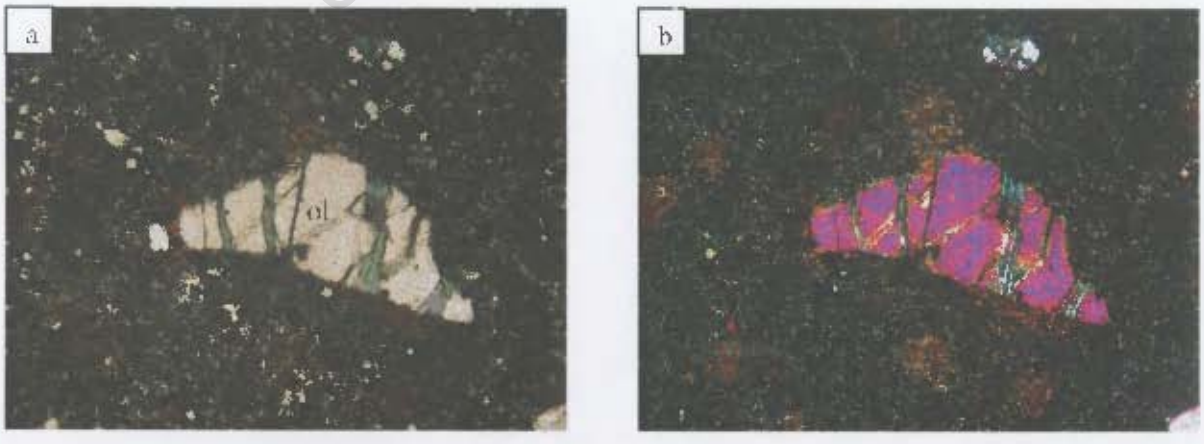

Fig. A.11 (a) ***AN-016:*** Anhedral olivine microphenocryst with interior alteration serpentine-filled cracks. Field of view is 2.1 mm across. (b) Under crossed polars. Note the scattered dark brown secondary amphibole within the groundmass.

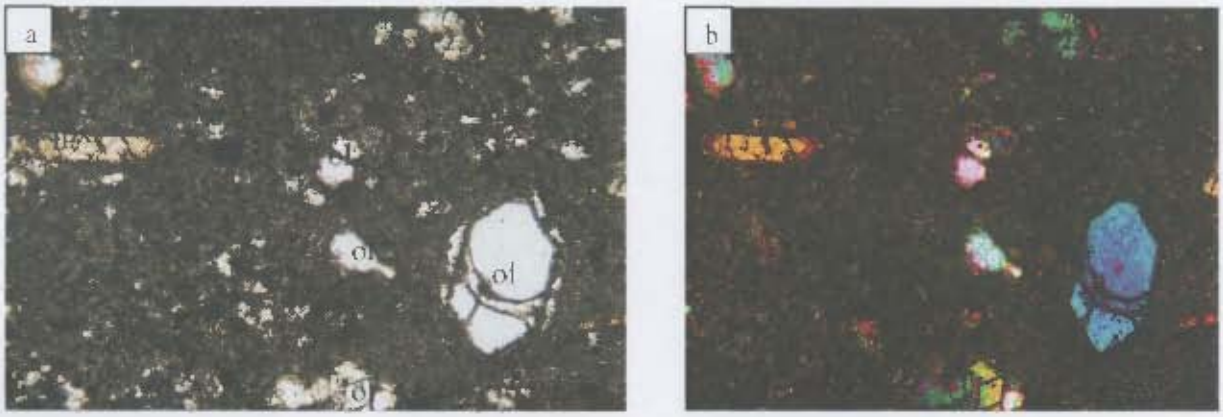

Fig. A.12 (a) *AN-019:* Euhedral olivine phenocryst (bottom right) and euhedral zoned clinopyroxene microphenocryst (top left) embedded in a fine grained groundmass. Field of view is 1.3 mm across. (b) Under crossed polars.

A.5 Tsirub South plug

AN-021: sparsely microporphyritic nephelinite

This sample is a sparsely microporphyritic rock in which olivine and rare brown clinopyroxene microphenocrysts are set in a fine to medium grained groundmass. Olivine microphenocrysts, 0.3 - 0.8 mm in size, constitute < 1 vol.% of the rock, most are anhedral and few are subhedral. Few crystals are enclosed in thin brown alteration rims of cracks whereas smaller crystals are completely replaced by serpentine. Minor clinopyroxene microphenocrysts, < 0.5 vol.%, measure 0.3 - 0.7 mm, majority are anhedral and a few show subhedral habits. A single microphenocryst shows zoning with a darker rim than core. The fine grained groundmass is made up of 6 vol.% lath-like clinopyroxene, 2 vol.% pleochroic secondary brown amphibole and black Fe-Ti oxides(Fig. A.13a).

AN-022: very sparsely microporphyritic nephelinite

This sample is a very sparsely microporphyritic rock in which very rare olivine and brown clinopyroxene microphenocrysts are set in a very fine grained groundmass. Olivine microphenocrysts, 0.3 - 0.9 mm, constitute < 0.5 vol.% of the rock, most are anhedral and few are subhedral. Many are enclosed in thick serpentine rims and few are completely replaced by serpentine (Fig. A.13b). Anhedral to rarely subhedral clinopyroxene microphenocrysts, 0.3 - 1.1 mm, make up < 0.5 vol.% of the rock and very few are zoned with darker rims than cores. The fine grained groundmass is made up of lath-like clinopyroxene, pleochroic brown secondary amphibole and black Fe-Ti oxides.

AN-023: sparsely microporphyritic nephelinite

This sample is a sparsely microporphyritic rock in which olivine (micro) phenocrysts (Fig. A.14a) and very rare brown clinopyroxene microphenocrysts are set in a fine grained groundmass. Olivine microphenocrysts, 0.3 - 1.1 mm, constitute < 1.5 vol.% of the rock, many are anhedral and very few are subhedral or euhedral in habits. Few are enclosed in, or completely replaced by, serpentine. A single olivine microphenocryst shows zoning with a darker rim than the core. Very rare clinopyroxene microphenocrysts, constitute < 0.5 vol.% of the rock and are all anhedral. The fine grained groundmass is made of lath-like clinopyroxene, pleochroic brown secondary amphibole and black Fe-Ti oxides (Fig. A.14b).

AN-024: sparsely microporphyritic nephelinite

This sample is a sparsely microporphyritic rock in which minor olivine and brown clinopyroxene microphenocrysts are set in a fine grained groundmass. Olivine microphenocrysts, 0.3 - 0.6 mm, make up < 0.5 vol.% of the rock, these are all anhedral and most are replaced, and few are rimmed, by serpentine. Clinopyroxene microphenocrysts, 0.3 - 0.7 mm in size, make up < 0.5 vol.% of the rock, many display anhedral habits, few are subhedral and a single crystal is euhedral (Fig. A.15). Few subhedral crystals exhibit zoning with darker rims than the cores. The fine grained groundmass is made up of lath-like clinopyroxene and black Fe-Ti oxides. Minor felsic xenoliths occur in this sample.

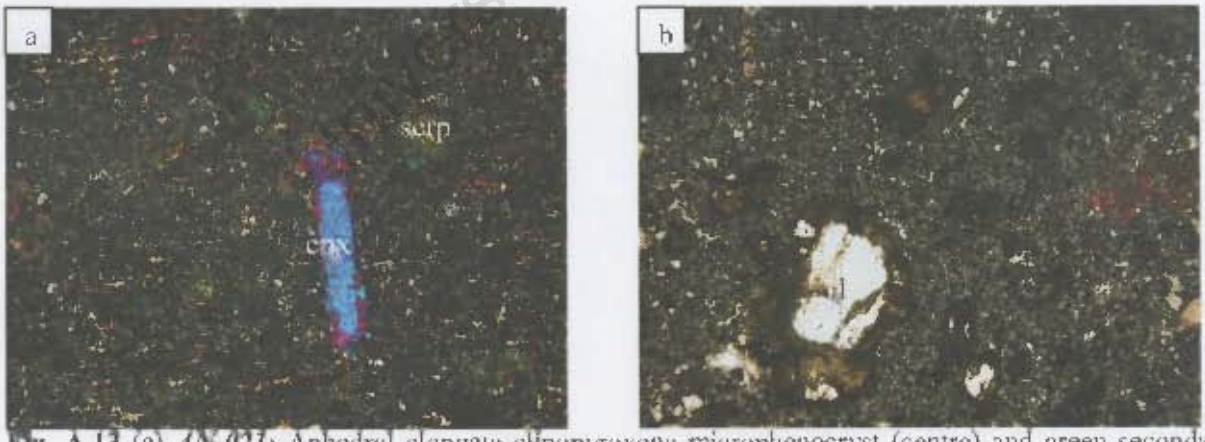

Fig. A.13 (a) *AN-021:* Anhedral elongate clinopyroxene microphenocryst (centre) and green secondary serpentine, which replaced some of the olivine microphenocrysts. Note the small clinopyroxene crystals (brown) in the fine grained groundmass, under crossed polars. Field of view is 1.4 mm across (b) *AN-022:* Anhedral olivine (micro) phenocrysts partially or completely bowlingite (under plane polarized light). Field of view is 1.8 mm across.

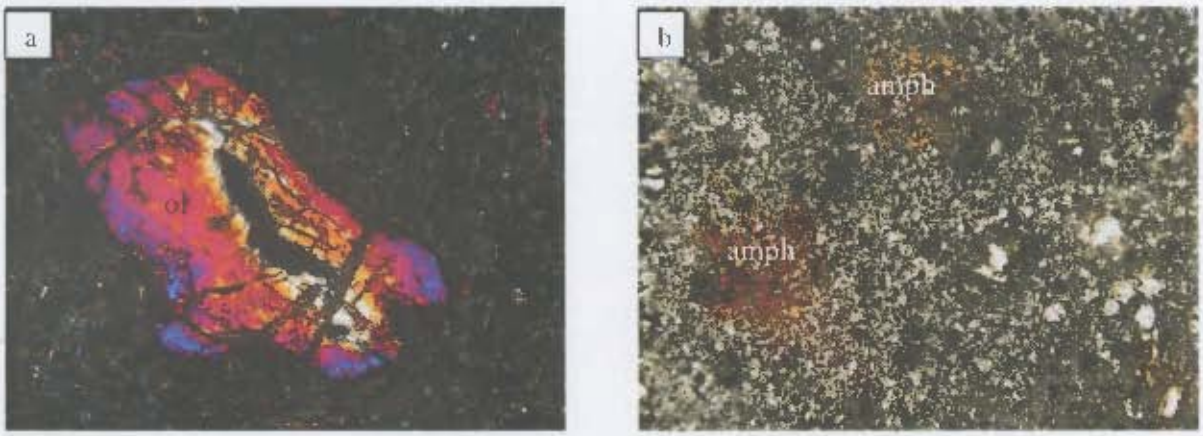

Fig. A.14 (a) ***AN-023:*** Altered subhedral olivine microphenocryst. Under crossed polars. Field of view is 1.2 mm across. (b) ***AN-023:*** Secondary brown amphibole and opaque Fe-Ti oxides from part of the groundmass. Field of view is 1.0 mm across.

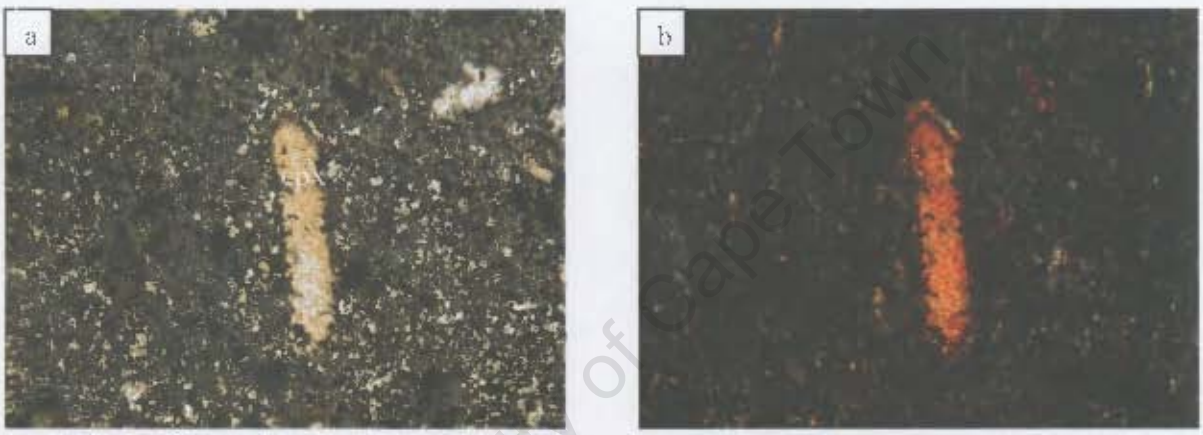

Fig. A.15 (a) **AN-024:** Euhedral clinopyroxene microphenocryst embedded in a fine grained groundmass. Under plane polarized light. Field of view is 1.0 mm across. (b) Under crossed polars.

Table A.1. Coordinates of individual samples collected during the study.

Tsirub dyke:		
AN-001	26° 73. 811' S	016° 02.037' E
Tsirub North (outer) plug:		
AN-003	26°69.150' S	016°07.845' E
AN-004	26°69.044' S	016°07.842' E
AN-005	26°69.132' S	016°07.827' E
AN-006	26°69.107' S	016°07.740' E
AN-006B	26°69.094' S	016°07.763' E
AN-013	26°69.032' S	016°07.884' E
AN-014	26°68.984' S	016°07.874' E
AN-014A	26°69.080' S	016°07.827' E
AN-015	26°68.910' S	016°07.867' E

Table A.1. Continued.

Tsirub North (inner) plug:		
AN-007	26°69.097' S	016°07.715' E
AN-007A	26°69.097' S	016°07.715' E
AN-008	26°69.093' S	016°07.685' E
AN-009	26°69.086' S	016°07.635' E
AN-010	26°69.063'S	016°07.759' E
AN-011	26°68.997' S	016°07.697' E
AN-017	26°68.816' S	016°07.681' E
AN-018	26°68.661' S	016°07.820' E
AN-016 and AN-019:		
AN-016	26°68.864' S	016°07.820' E
AN-019	26°68.524' S	016°07.853' E
Tsirub South plug:		
AN-021	26°80.777' S	016°13.109' E
AN-022	26°80.727' S	016°13.065' E
AN-023	26°80.611' S	016°13.067' E
AN-024	26°81.075' S	016°13.300' E

APPENDIX B

SAMPLE PREPARATION AND ANALYTICAL TECHNIQUES

B.1 Electron microprobe analyses

Mineral analyses were carried out on 30 μm thick, polished thin sections in the Department of Geological Sciences at the University of Cape Town (UCT) using a JEOL JXA-8100 electron probe microanalyzer. Operating conditions were 15 kV accelerating voltage for all the minerals, 20 nA beam current and 10 seconds counting time per element. An exception is Ni with peak counting time of 30 seconds. Olivine was analyzed at 25 kV accelerating voltage to ensure excitation of $Ni_{K\alpha}$. Analyses of the olivine and clinopyroxene standard are listed in Table B.1. Lower limits of detection for major element oxides in clinopyroxene are listed in Table B.2.

Table B.1. Average major elements concentrations (in wt.%) and 1σ error of olivine standard (Ma havati) and clinopyroxene standard (JJG1424-Cpx) obtained during the analyses of the Tsirub samples. Abbreviations: n = number of analysis

	Olivine n = 6	**Clinopyroxene** n = 9
SiO_2	40.15	54.28
TiO_2	0.01	0.25
Al_2O_3	0.01	3.00
Cr_2O_3	0.03	0.72
FeO	11.49	1.67
MnO	0.28	0.05
MgO	47.91	16.29
CaO	0.02	21.84
NiO	0.01	-
Na_2O	-	1.49
K_2O	-	0.01

Table B.2. Lower limits of detection (in wt.%) for major element oxides in clinopyroxene.

	LLD n = 10
SiO_2	0.010
TiO_2	0.012
Al_2O_3	0.008
Cr_2O_3	0.013
FeO	0.014
MnO	0.015
MgO	0.013
CaO	0.006
Na_2O	0.010
K_2O	0.004

B.2 X-Ray Fluorescence Spectrometry (XRF)

XRF technique was used to analyze major elements and 11 trace elements concentrations (Nb, Zr, Y, Sr, Rb, Zn, Cu, Ni, Co, Cr and V) using a Philips X'Unique wavelength dispersive spectrometer at UCT. Major elements were determined by analysis of fusion disks and trace elements were determined from pressed powder briquettes prepared as follows.

B.2.1 Preparation of Fusion Disks

Fusion disks were prepared for major element analyses as follows. Two grams of powdered sample were placed into pre-weighed empty porcelain crucibles and then weighed. The samples were then dried in an oven for 4 hours at 110°C and subsequently weighed to determine the weight percentage of H_2O^- present in each sample. In order to determine the weight percentage lost on ignition (LOI) the samples were dried overnight between 850°C and 1000°C. Lastly, 0.7 grams of each sample were mixed with 6 grams of $Li_2B_4O_7$-$LiBO_2$ flux. The prepared fusion disks were then stored in dessicator before they were analysed by a Philips X'Unique wavelength dispersive spectrometer.

B.2.2 Preparation of Briquettes

Briquettes were prepared by pressing 5 grams of powdered sample and a backing of boric acid (H_3BO_3) under 10-ton of pressure. The prepared briguettes were analyzed for selected trace elements (Nb, Zr, Y, Sr, Rb, Zn, Cu, Ni, Co, Cr and V) by XRF-technique. These trace elements were also analyzed by ICP-MS technique in order to compare the two techniques.

Analytical errors and detection limits for trace elements are similar to those reported by le Roex and Dick (1981) and Willis (1999). Analytical errors and lower detection limits of the mafic standard JB-1, analysed at UCT, by Willis (1999) are presented in Table B.3. For comparison, recommended values from Govindaraju (1989) are also reported in Table B.3.

Table B.3. Trace element data (in ppm) for reference standard JB-1 (Willis, 1999) together with analytical errors and lower detection limits. 1σ = 1σ error, LLD = lower limit of detection (in ppm). Recommended values are from Govindaraju (1989).

	UCT	1σ	LLD	Recommended
V	193	1.4	3.0	212
Cr	406	1.5	2.0	469
Co	37.0	0.9	2.3	38.7
Ni	139	0.7	1.0	139
Cu	55.0	0.5	1.1	56.3
Zn	84.0	0.4	0.9	83.0
Rb	39.0	0.2	0.6	41.0
Sr	444	0.3	0.5	435
Y	24.0	0.2	0.6	24.0
Zr	152	0.2	0.4	143
Nb	28.0	0.2	0.5	35.0
U	2.30	0.4	1.2	1.70

B.3 Inductively Coupled Plasma Mass Spectrometry (ICP-MS)

An ELAN 6000 Inductively Coupled Plasma Mass Spectrometer (ICP-MS) was used to determine the trace element abundances of Tsirub samples in the Department of Geological Sciences at UCT. Sample preparation for trace element analyses is outlined below.

B.3.1 Sample preparation

Approximately 50 milligrams of each sample were weighed out in beakers. Four millilitres of a solution containing hydrofluoric acid (HF) and nitric acid (HNO_3) in the ratio of 4Hf: 1 HNO_3 was added to each sample. The beakers containing the samples were then sealed and placed on a hotplate for 48 hours to allow the sample to digest, the lids of the beakers were then removed to dry down the samples on the same hot plate. Two milliliters of concentrated HNO_3 were then added to the samples and then dried down for about four hours. This step was repeated once. Four millilitres of 5% HNO_3 acid solution which contains 10 ppb of In, Re, Bi and Rh as internal standards were added. The samples were then kept in an ultrasonic bath for an hour to ensure complete dissolution. One drop of HF acid was added, in order to keep Ta in solution, and then about 50 grams of 5% HNO_3 were added to each sample. The samples were further diluted with 5% HNO_3 acid solution (containing 10 ppb of In, Re, Bi and Rh as internal standards) by a factor of 10.

Table B.4. Average trace elements concentrations (in ppm) of total procedural blanks (TPB) run with the Tsirub samples (n = number of analysis).

	TPB n = 9
Sc	0.0666
V	0.0321
Cr	0.0537
Co	0.0048
Ni	0.0448
Cu	0.0634
Rb	0.0031
Sr	0.0377
Y	0.0015
Zr	0.0491
Nb	0.0163
Cs	0.0012
Ba	0.3388
La	0.0020
Ce	0.0040
Pr	0.0007

	TPB n = 9
Nd	0.0016
Sm	0.0004
Eu	0.0002
Gd	0.0005
Tb	0.0001
Dy	0.0003
Ho	0.0001
Er	0.0002
Tm	0.0001
Yb	0.0002
Lu	0.0001
Hf	0.0013
Ta	0.0730
Pb	0.2677
Th	0.0005
U	0.0002

Total procedural blanks (TPB) were run during each analysis; the average trace elements concentrations of the TPB are shown in Table B.4. The international standard BHVO-1 was also run during each analysis. The results for BHVO-1 and recommended values for this standard are reported in Table B.4. Repeated analyses of BHVO-1 gave a precision of generally better than 3% relative for all trace elements Accuracy of the analyses can be quoted from Table B.5.

Most trace elements (except for example Nb) show a good comparison between values measured by XRF and ICP-MS techniques (Fig. B.1a). The Tsirub samples show slightly higher Ni concentrations when analysed by ICP-MS compared to XRF. Nb concentrations obtained by XRF technique are slightly higher than those obtained by ICP-MS technique. It should be noted that all the trace element concentrations reported in the main text are those analyzed by Inductively Coupled Plasma Mass Spectrometry (ICP-MS) except for Nb whose reported concentration is that analysed by XRF technique.

Table B.5. Average trace elements concentrations (in ppm) of the international standard BHVO-1 produced during trace elements analyses of Tsirub samples. Recommended values (Govindaraju, 1994) are reported for comparison. %RSD = relative standard deviation and n = number of analysis.

	AN-001 to AN-014		AN-014A to AN-024		Recommended
	BHVO-1	%RSD n = 5	BHVO-1	%RSD n = 4	values for BHVO-1
Sc	29.0	3.73	29.7	1.75	31.8
V	351	1.91	330	2.31	317
Cr	313	1.93	310	2.43	289
Co	42.8	1.17	44.9	1.66	45.0
Ni	116	1.14	128	1.71	121
Cu	134	1.75	133	1.71	136
Rb	8.96	1.69	9.52	1.94	11.0
Sr	406	1.19	419	1.30	403
Y	24.1	1.35	24.3	1.85	27.6
Zr	174	0.82	168	1.24	179
Nb	18.7	0.55	19.7	1.17	19.0
Cs	0.10	2.99	0.10	2.39	0.13
Ba	131	0.97	131	1.42	139
La	15.2	1.94	15.2	1.17	15.8
Ce	35.8	1.20	36.0	1.24	39.0
Pr	5.29	1.17	5.00	1.53	5.70
Nd	24.4	0.80	23.4	1.45	25.2
Sm	5.57	1.17	5.20	3.02	6.20
Eu	1.91	1.52	1.93	0.98	2.06
Gd	5.94	1.86	5.72	0.69	6.40
Tb	0.88	1.01	0.82	1.58	0.96
Dy	4.90	1.11	4.66	1.39	5.20
Ho	0.94	0.98	0.87	1.34	0.99
Er	2.31	0.68	2.19	1.26	2.40
Tm	0.31	1.23	0.28	1.54	0.33
Yb	1.80	0.33	1.72	1.01	2.02
Lu	0.26	0.90	0.24	1.73	0.29
Hf	3.83	0.93	3.65	0.65	4.38
Ta	1.54	3.57	1.15	0.54	1.23
Pb	2.13	1.42	2.38	0.82	2.60
Th	1.22	1.30	1.21	0.90	1.08
U	0.42	1.69	0.42	1.81	0.42

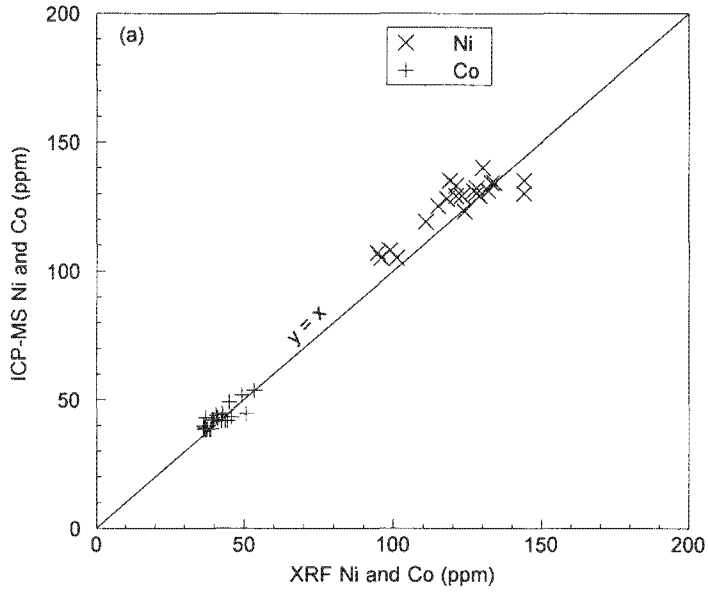

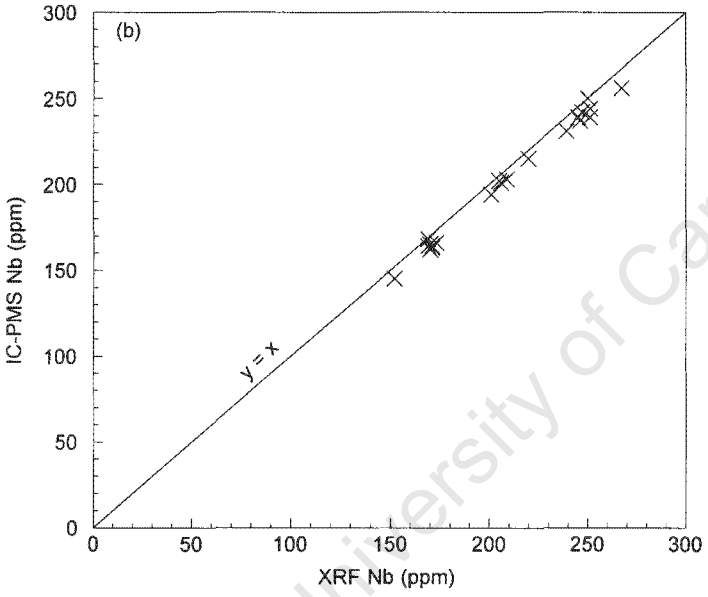

Fig. B.1. (a) Ni and Co content analyzed by ICP-MS versus Ni and Co content analyzed by XRF. (b) Nb content analyzed by ICP-MS versus Nb content analyzed by XRF.

B.4 Sr and Nd isotope analyses

Sr and Nd isotope analyses were carried out in the Department of Geological Sciences at UCT.

B.4.1 Sr isotope analysis

Four millilitres of a mixture of 4:1 HF/HNO_3 were added to 100mg of sample in a beaker. The beaker containing the samples were then sealed and placed on a hotplate (~75°C) for 48 hours to allow the samples to digest. The lids of the beakers were then removed in order to dry down the

samples. Three millilitres of 6.2M HCL were added to each sample in order to remove HNO_3 from the samples. The samples were then dried on a hot plate at 75°C (this step was repeated). After drying, 2.5M HCL was added to each sample in order to make up 1 millilitre of sample solution. The sample solutions were then centrifuged for 15 minutes in order to separate any undissolved sample material so that no undissolved sample material is loaded onto the ion exchange columns.

B.4.1.1 Sr separation using cation-exchange columns

Sr was separated from the other elements using standard cation exchange columns containing Dowex AG50WX8 cation resin following the method of Hart and Brooks (1977). Sr separation was achieved by loading 0.5 milliliters of sample solution onto primary cation exchange columns from which Sr was eluted with 2.5M HCL. The collected solution containing Sr was then placed on a hotplate in order to dry down the samples. The samples were pre-mixed with one drop of HNO_3 and one drop of H_2PO_3 before loading them, as nitrates, onto degassed single Ta filaments. Analyses were undertaken using a VG Sector 54 seven-collector thermal ionization mass spectrometer in the Department of Geological Sciences at UCT.

B.4.2 Nd isotope analysis

B.4.2.1 Nd separation using cation-exchange columns

REE elements including Nd were separated from the remaining residue, after Sr collection, by adding 6 ml of 6.2M HCL. The collected REE sample solution was then dried, and the taken up into solution by adding 0.25 ml of 0.25M HCL. The final REE solution (0.25 milliliters) was loaded onto standard secondary cation exchange columns containing a resin composed of teflon powder coated with HDEHP.

Nd was separated and eluted with 0.25M HCL following the method of Zindler (1980). The samples were pre-mixed with 1µl of a 1:1 HCL/ H_2PO_3 solution before loading them, as chlorides, onto double filaments consisting of Ta side filaments and Re centre filaments; the samples where loaded onto the Ta side filaments.

B.4.3 Reproducibility of Sr (NBS 987) and Nd (La Jolla) standards

Analyses of Sr standard NBS 987 produced $^{87}Sr/^{86}Sr$ ratio of 0.71023 ± 23 (n = 1) that is similar to the accepted value of 0.71025. To correct for mass fractionation effect the measured $^{87}Sr/^{86}Sr$ and $^{143}Nd/^{144}Nd$ were normalised to $^{86}Sr/^{88}Sr$ = 0.1194 and $^{146}Nd/^{144}Nd$ = 0.7219, respectively. Repeated measurements of La Jolla yielded average $^{143}Nd/^{144}Nd$ = 0.511809 ± 21 (2σ, n = 3) (Table B.6). Although no repeat analyses for the Sr standard were done the measured $^{87}Sr/^{86}Sr$ value of NBS 987 obtained during this study is within error of the accepted value and therefore the measured $^{87}Sr/^{86}Sr$ values of Tsirub samples reported in Chapter 6 are taken to be representative of these samples.

Table B.6 Average ratios for Sr and Nd standards and 2σ errors. Errors quoted for $^{87}Sr/^{86}Sr$ values and $^{143}Nd/^{144}Nd$ represent $2\sigma_{mean}$ on in-run statistics and apply to the last quoted digit of the analyzed ratio. Abbreviations: n = number of analysis.

Standard	Isotope ratio	Average	2σ error	n
NBS 987	$^{87}Sr/^{86}Sr$	0.710212	23	1
La Jolla	$^{143}Nd/^{144}Nd$	0.511809	21	3

APPENDIX C

CIPW NORMS AND MINERAL CHEMISTRY DATA

To enhance the readability of this thesis, only representative data are presented in the main text. Additional data and entire mineral data for the Tsirub samples are presented in this section. The additional data include calculated CIPW norms (Table C.1), calculated atomic proportions for olivine and clinopyroxene (Tables C.2 – C.4), major and trace element data of the country rock intruded by the Tsirub North plug (Table C.5).

Table C.1. Calculated CIPW norms for Tsirub samples. Abbreviations: or = orthoclase, ab = albite, an = anorthite, ne = nepheline, lc = leucite, di = diopside, ol = olivine, il = ilmenite, hap = apatite.

	Tsirub dyke	Tsirub North (outer) plug							
	AN-001	AN-003	AN-004	AN-005	AN-006	AN-012	AN-013	AN-014	AN-015
or	0.00	8.65	6.78	5.09	0.00	7.89	6.49	3.92	7.8
ab	0.00	2.92	4.13	0.00	0.00	5.62	2.11	6.91	0.00
an	6.41	9.77	6.44	11.0	0.22	11.2	9.47	21.2	8.42
ne	21.1	19.2	22.9	19.6	17.8	11.3	21.2	6.56	22.0
lc	8.86	0.00	0.00	3.87	18.2	0.00	0.00	0.00	0.75
di	29.2	32.8	34.1	34.2	30.4	31.6	34.2	37.7	34.6
ol	19.7	13.1	12.3	12.7	13.6	14.6	12.8	10.2	12.7
cs	1.43	0.00	0.00	0.00	2.81	0.00	0.00	0.00	0.00
cm	0.10	0.07	0.07	0.07	0.08	0.09	0.07	0.06	0.07
mt	4.26	4.34	4.30	4.29	4.90	5.46	4.42	4.27	4.40
il	5.54	6.76	6.52	6.54	8.98	9.69	6.74	6.40	6.80
hap	3.45	2.51	2.60	2.66	3.02	2.66	2.57	2.76	2.54

Table C.1. Continued.

	Tsirub North (inner) plug								AN-016 and AN-019	
	AN-007	AN-007A	AN-008	AN-009	AN-010	AN-011	AN-017	AN-018	AN-016	AN-019
or	0.00	1.07	7.28	4.19	0.00	1.26	0.00	0.00	2.06	0.00
ab	0.00	0.00	0.00	0.00	0.00	0.00	0.00	0.00	0.00	0.00
an	5.35	8.05	5.34	4.53	5.74	6.84	2.15	4.68	3.70	6.08
ne	23.0	20.0	24.0	25.3	23.2	20.9	23.3	23.6	22.8	24.2
lc	10.3	8.13	1.53	3.58	10.1	8.36	12.7	9.53	7.30	8.62
di	32.5	33.3	34.3	35.7	28.8	34.0	31.5	35.1	35.9	32.6
ol	13.5	14.3	12.6	12.2	15.2	13.6	13.5	12.4	12.5	14.1
cs	0.94	0.00	0.00	0.00	2.31	0.00	1.86	0.15	0.00	0.21
cm	0.06	0.06	0.05	0.05	0.05	0.05	0.05	0.05	0.07	0.05
mt	4.22	4.30	4.22	4.12	4.24	4.23	4.24	4.25	4.67	4.25
il	4.94	4.95	4.76	4.69	4.83	4.90	4.90	4.84	7.30	5.75
hap	5.39	6.04	5.94	5.71	5.60	5.95	5.90	5.47	3.75	4.31

Table C.1. Continued.

	Tsirub South plug			
	AN-021	**AN-022**	**AN-023**	**AN-024**
or	0.00	0.00	0.00	0.00
ab	0.00	0.00	0.00	0.00
an	4.70	3.20	4.95	6.96
ne	22.6	23.9	22.0	20.2
lc	11.7	12.0	13.4	11.8
di	28.9	28.5	22.3	29.2
ol	14.1	14.2	16.1	14.3
cs	3.24	3.76	6.58	2.87
cm	0.05	0.05	0.04	0.05
mt	4.56	4.45	4.46	4.49
il	6.42	6.28	6.43	6.35
hap	3.84	3.71	3.77	3.92

Table C.2. Atomic proportions calculated for olivine analyses from Tsirub intrusions on the basis of 4 oxygens.

	Tsirub dyke							
	AN-001							
	p(core)	p(rim)	p(core)	p(rim)	p	gm	gm	gm
SiO_2	42.08	42.15	41.99	41.73	41.74	41.54	42.12	41.65
TiO_2	-	0.01	0.03	0.00	0.01	0.01	0.01	0.00
Al_2O_3	0.02	0.03	0.02	0.04	0.03	0.02	0.02	0.07
Cr_2O_3	0.13	0.13	0.13	0.14	0.11	0.15	0.13	0.13
FeO	9.19	8.92	10.60	10.78	9.78	11.34	8.86	9.25
MnO	0.10	0.10	0.09	0.09	0.11	0.11	0.10	0.11
MgO	47.66	47.87	47.07	46.50	47.35	46.37	47.54	47.57
CaO	0.03	0.03	0.01	0.03	0.02	0.01	0.02	0.02
NiO	0.39	0.37	0.35	0.35	0.39	0.34	0.40	0.38
Total	99.59	99.60	100.28	99.67	99.55	99.89	99.20	99.18
Fo	90.3	90.5	88.8	88.5	89.6	88.00	90.5	90.2
Fa	9.8	9.5	11.2	11.5	10.4	12.10	9.5	9.8
	Number of cations on the basis of 4 oxygens:							
Si	1.030	1.030	1.027	1.028	1.025	1.024	1.033	1.025
Ti	-	0.000	0.000	0.000	0.000	0.000	0.000	0.000
Al	0.000	0.001	0.000	0.001	0.001	0.000	0.000	0.002
Fe^{2+}	0.188	0.182	0.217	0.222	0.201	0.234	0.182	0.190
Mn	0.003	0.003	0.003	0.003	0.002	0.003	0.003	0.003
Mg	1.739	1.744	1.716	1.708	1.734	1.705	1.738	1.745
Ca	0.003	0.003	0.002	0.002	0.003	0.003	0.003	0.003
Cr	0.000	0.000	0.000	0.000	0.000	0.000	0.000	0.000
Ni	0.008	0.007	0.007	0.007	0.008	0.007	0.008	0.008
Sum	2.970	2.970	2.973	2.972	2.974	2.976	2.966	2.974

Table C.2. Continued.

	Tsirub North (outer) plug												
	AN-003							AN-005					
	p	p	p	gm	gm	gm	gm	p (core)	p(rim)	p	p	p (core)	p (rim)
SiO_2	41.57	41.56	41.58	41.41	41.53	41.34	41.50	41.18	40.75	39.65	40.81	41.42	40.68
TiO_2	0.07	0.04	0.03	0.03	0.04	0.04	0.03	0.03	0.05	0.04	0.02	0.02	0.04
Al_2O_3	0.01	0.03	0.04	0.02	0.01	0.03	0.05	0.05	0.04	0.01	0.05	0.05	0.03
Cr_2O_3	0.03	0.02	0.03	0.02	0.04	0.04	0.02	0.03	0.03	0.02	-	0.03	0.01
FeO	14.64	14.37	13.90	14.00	14.20	14.11	14.59	13.81	16.16	22.17	17.72	14.59	18.71
MnO	0.24	0.27	0.23	0.24	0.23	0.25	0.26	0.21	0.33	0.57	0.34	0.25	0.40
MgO	43.22	43.45	43.99	43.75	43.70	43.48	43.70	43.93	42.44	37.82	41.16	42.94	40.10
CaO	0.40	0.39	0.28	0.33	0.37	0.35	0.33	0.28	0.35	0.45	0.28	0.30	0.34
NiO	0.15	0.17	0.18	0.17	0.14	0.15	0.14	0.17	0.15	0.08	0.14	0.16	0.11
Total	100.32	100.29	100.26	100.29	100.26	99.81	100.62	99.68	100.31	100.82	100.53	99.76	100.41
Fo	84.0	84.4	84.9	84.8	84.6	84.6	84.2	85.0	82.4	75.3	80.6	84.0	79.2
Fa	16.0	15.6	15.1	15.2	15.4	15.4	15.8	15.0	17.6	24.7	19.5	16.0	20.7
	Number of cations on the basis of 4 oxygens:												
Si	1.034	1.034	1.032	1.032	1.032	1.032	1.030	1.029	1.024	1.021	1.029	1.037	1.032
Ti	0.001	0.001	0.000	0.001	0.001	0.001	0.001	0.001	0.001	0.001	0.000	0.000	0.001
Al	0.000	0.001	0.001	0.000	0.000	0.001	0.001	0.001	0.001	0.000	0.001	0.001	0.001
Fe^{2+}	0.305	0.299	0.289	0.292	0.295	0.295	0.303	0.288	0.339	0.477	0.374	0.305	0.397
Mn	0.005	0.006	0.005	0.005	0.005	0.005	0.005	0.005	0.007	0.012	0.007	0.005	0.008
Mg	1.604	1.612	1.628	1.625	1.620	1.619	1.617	1.636	1.590	1.452	1.547	1.602	1.517
Ca	0.011	0.010	0.007	0.009	0.010	0.009	0.009	0.007	0.010	0.012	0.008	0.008	0.009
Cr	0.000	0.000	0.001	0.000	0.001	0.001	0.000	0.001	0.001	0.000	-	0.001	0.000
Ni	0.003	0.003	0.004	0.003	0.003	0.003	0.003	0.003	0.003	0.002	0.003	0.003	0.002
Sum	2.963	2.965	2.967	2.968	2.967	2.966	2.968	2.971	2.975	2.978	2.970	2.963	2.967

Table C.2. Continued.

	Tsirub North (outer) plug											
	AN-005				AN-013							
	gm	gm	gm	gm	p (core)	p(rim)	p (core)	p(rim)	p	gm	gm	gm
SiO_2	40.96	41.23	41.31	41.50	41.35	41.19	41.51	41.43	41.55	41.48	41.62	41.53
TiO_2	0.05	0.03	0.03	0.06	0.04	0.02	0.04	0.05	0.02	0.04	0.09	0.05
Al_2O_3	0.03	0.03	0.03	0.12	0.01	0.01	0.05	0.06	0.06	0.05	0.04	0.04
Cr_2O_3	0.03	0.01	0.02	0.02	0.03	0.02	0.04	0.04	0.02	0.03	0.03	0.04
FeO	17.12	16.30	16.53	14.93	14.46	16.04	13.52	14.32	14.04	14.82	15.36	14.02
MnO	0.37	0.28	0.32	0.28	0.26	0.32	0.23	0.24	0.23	0.23	0.25	0.23
MgO	41.66	42.30	41.55	43.09	43.57	42.11	44.40	43.52	43.47	43.57	42.74	44.26
CaO	0.32	0.34	0.36	0.33	0.37	0.50	0.29	0.32	0.32	0.32	0.31	0.32
NiO	0.15	0.16	0.14	0.21	0.13	0.11	0.18	0.15	0.16	0.15	0.16	0.17
Total	100.70	100.68	100.29	100.53	100.23	100.33	100.26	100.13	99.87	100.68	100.59	100.67
Fo	81.3	82.2	81.7	83.7	84.3	82.4	85.4	84.4	84.7	84.0	83.2	84.9
Fa	18.7	17.8	18.2	16.3	15.7	17.6	14.6	15.6	15.3	16.0	16.8	15.1
	Number of cations on the basis of 4 oxygens:											
Si	1.029	1.031	1.037	1.033	1.030	1.033	1.029	1.032	1.036	1.030	1.036	1.028
Ti	0.001	0.001	0.001	0.001	0.001	0.000	0.001	0.001	0.000	0.001	0.002	0.001
Al	0.001	0.001	0.001	0.003	0.000	0.000	0.001	0.001	0.001	0.001	0.001	0.001
Fe^{2+}	0.360	0.341	0.347	0.311	0.301	0.336	0.280	0.298	0.293	0.308	0.320	0.290
Mn	0.008	0.006	0.007	0.006	0.006	0.007	0.005	0.005	0.005	0.005	0.005	0.005
Mg	1.560	1.577	1.556	1.599	1.618	1.574	1.641	1.616	1.616	1.612	1.586	1.633
Ca	0.009	0.009	0.010	0.009	0.010	0.014	0.008	0.009	0.008	0.009	0.008	0.009
Cr	0.001	0.000	0.000	0.000	0.001	0.000	0.001	0.001	0.000	0.001	0.001	0.001
Ni	0.003	0.003	0.003	0.004	0.003	0.002	0.004	0.003	0.003	0.003	0.003	0.003
Sum	2.970	2.968	2.961	2.965	2.969	2.967	2.970	2.966	2.963	2.968	2.962	2.971

Table C.2. Continued.

	Tsirub North (inner) plug											
	AN-007								AN-017			
	p	p (core)	p(rim)	p	p	gm	gm	gm	p	p	p	p
SiO_2	41.87	41.40	41.65	41.57	41.76	41.49	41.40	41.37	40.96	41.55	42.17	40.30
TiO_2	0.03	0.03	0.03	0.00	0.04	0.03	0.04	0.04	0.04	0.03	0.01	0.01
Al_2O_3	0.04	0.03	0.02	0.02	0.03	0.04	0.03	0.04	0.01	0.02	0.01	0.01
Cr_2O_3	0.02	0.03	0.03	0.02	0.02	0.05	0.05	0.03	0.02	0.01	0.02	0.02
FeO	13.92	14.54	15.96	13.68	14.17	13.89	13.94	14.01	16.72	13.92	7.79	18.96
MnO	0.27	0.22	0.30	0.21	0.22	0.26	0.23	0.25	0.36	0.20	0.11	0.50
MgO	43.72	43.48	42.10	44.26	43.82	43.78	43.95	43.72	41.91	44.01	48.72	40.50
CaO	0.31	0.28	0.38	0.30	0.32	0.31	0.32	0.33	0.29	0.23	0.05	0.26
NiO	0.16	0.14	0.11	0.18	0.15	0.17	0.17	0.17	0.16	0.24	0.36	0.18
Total	100.34	100.15	100.58	100.25	100.53	100.00	100.13	99.96	100.47	100.22	99.24	100.74
Fo	84.9	84.2	82.5	85.2	84.7	84.9	84.9	84.7	81.7	84.9	91.8	79.2
Fa	15.2	15.8	17.5	14.8	15.4	15.1	15.1	15.2	18.3	15.1	8.2	20.8
	Number of cations on the basis of 4 oxygens:											
Si	1.038	1.032	1.040	1.031	1.035	1.033	1.029	1.031	1.029	1.032	1.029	1.022
Ti	0.001	0.001	0.001	0.000	0.001	0.001	0.001	0.001	0.001	0.001	0.000	0.000
Al	0.001	0.001	0.000	0.001	0.001	0.001	0.001	0.001	0.000	0.000	0.000	0.000
Fe^{2+}	0.289	0.303	0.333	0.284	0.294	0.289	0.290	0.292	0.351	0.289	0.159	0.402
Mn	0.006	0.005	0.006	0.004	0.005	0.005	0.005	0.005	0.008	0.004	0.002	0.011
Mg	1.616	1.616	1.567	1.637	1.619	1.625	1.630	1.625	1.570	1.630	1.772	1.531
Ca	0.008	0.007	0.010	0.008	0.009	0.008	0.008	0.009	0.008	0.006	0.001	0.007
Cr	0.000	0.001	0.001	0.000	0.000	0.001	0.001	0.001	0.000	0.000	0.000	0.000
Ni	0.003	0.003	0.002	0.004	0.003	0.003	0.003	0.003	0.003	0.005	0.007	0.004
Sum	2.961	2.967	2.960	2.969	2.965	2.966	2.968	2.967	2.971	2.968	2.971	2.978

Table C. 2. Continued.

	Tsirub South plug		
	AN-021		
	p	p	p
SiO_2	40.03	39.85	40.40
TiO_2	0.02	0.04	0.01
Al_2O_3	0.04	0.02	0.02
Cr_2O_3	-	0.01	0.02
FeO	22.80	22.96	20.03
MnO	0.74	0.78	0.54
MgO	36.91	37.46	40.35
CaO	0.48	0.44	0.33
NiO	0.08	0.07	0.09
Total	101.10	101.61	101.79
Fo	74.3	74.4	78.2
Fa	25.7	25.6	21.8
	Number of cations on the basis of 4 oxygens:		
Si	1.030	1.021	1.019
Ti	0.000	0.001	0.000
Al	0.001	0.000	0.000
Fe^{2+}	0.491	0.492	0.422
Mn	0.016	0.017	0.011
Mg	1.416	1.432	1.517
Ca	0.013	0.012	0.009
Cr	0.000	0.000	0.000
Ni	0.002	0.001	0.002
Sum	2.969	2.977	2.981

Table C.3. Major element analysis and atomic proportions for Tsirub clinopyroxenes, calculated on the basis of 6 oxygens.

	Tsirub dyke				
	AN-001				
	p (core)	p (rim)	p	p (core)	p (rim)
SiO_2	49.24	48.94	49.26	46.51	48.86
TiO_2	2.27	2.51	2.28	2.77	2.40
Al_2O_3	4.24	4.64	4.62	7.38	4.49
Cr_2O_3	0.13	0.24	0.20	0.09	0.24
FeO	6.08	5.51	5.53	6.80	5.67
MnO	0.08	0.09	0.08	0.07	0.11
MgO	14.39	14.36	14.32	12.56	14.29
CaO	23.62	23.79	23.76	23.09	23.76
Na_2O	0.37	0.36	0.36	0.67	0.37
K_2O	0.01	-	0.01	0.01	-
Total	100.43	100.44	100.41	99.95	100.19
Wo	48.8	49.5	49.5	50.3	49.4
En	41.4	41.6	41.5	38.1	41.4
Fs	9.8	8.9	9.0	11.6	9.2
Si	1.844	1.831	1.841	1.772	1.834
Al^{IV}	0.148	0.162	0.159	0.228	0.157
Al^{VI}	0.000	0.000	0.002	0.034	0.000
Ti	0.064	0.071	0.064	0.079	0.068
Fe^{2+}	0.190	0.172	0.173	0.217	0.178
Mn	0.003	0.003	0.003	0.002	0.003
Mg	0.803	0.801	0.798	0.713	0.800
Ca	0.948	0.954	0.952	0.943	0.956
Na	0.027	0.026	0.026	0.050	0.027
K	0.000	0.000	0.000	0.000	0.000
Cr	0.004	0.007	0.006	0.003	0.007
Sum	4.030	4.026	4.024	4.041	4.030

Table C.3. Continued.

	Tsirub North (outer) plug											
	AN-003								AN-005			
	p	p (core)	p (rim)	p (core)	p (rim)	gm	gm	gm	p (core)	p (rim)	p (core)	p (rim)
SiO_2	48.39	48.76	48.28	45.75	46.65	47.63	43.05	47.34	48.96	48.89	44.16	42.41
TiO_2	2.83	2.77	2.61	4.00	3.65	2.88	5.19	2.89	2.52	2.51	4.75	5.31
Al_2O_3	4.27	4.19	4.80	7.07	6.01	4.95	8.19	4.84	4.13	4.24	7.93	9.12
Cr_2O_3	0.20	0.02	0.10	0.34	0.37	0.32	0.27	0.25	0.20	0.21	0.01	0.26
FeO	6.46	6.52	6.78	6.50	6.50	6.42	7.36	6.87	5.81	6.01	7.52	7.54
MnO	0.14	0.10	0.14	0.05	0.10	0.10	0.13	0.11	0.11	0.07	0.09	0.09
MgO	14.29	14.14	14.33	13.02	13.28	14.28	11.97	14.43	14.56	14.55	12.13	11.63
CaO	23.08	23.37	22.70	23.30	23.03	23.21	23.11	22.72	23.34	23.46	23.08	23.14
Na_2O	0.35	0.46	0.35	0.53	0.66	0.43	0.59	0.41	0.37	0.38	0.54	0.51
K_2O	0.01	-	0.11	0.01	0.03	0.01	0.02	0.04	0.00	-	-	0.01
Total	100.03	100.32	100.20	100.58	100.27	100.23	99.87	99.90	100.01	100.31	100.21	100.02
Wo	48.1	48.6	47.4	50.1	49.4	48.3	50.8	47.2	48.5	48.5	50.4	51.2
En	41.4	40.9	41.6	39.9	39.7	41.3	36.6	41.7	42.1	41.8	36.8	35.8
Fs	10.5	10.6	11.0	10.9	10.9	10.4	12.6	11.1	9.4	9.7	12.8	13.0
	Number of cations on the basis of 6 oxygens											
Si	1.824	1.832	1.820	1.735	1.768	1.798	1.665	1.795	1.839	1.833	1.695	1.643
Al^{IV}	0.150	0.147	0.169	0.250	0.212	0.174	0.295	0.171	0.145	0.148	0.284	0.329
Al^{VI}	0.000	0.000	0.000	0.000	0.000	0.000	0.000	0.000	0.000	0.000	0.000	0.000
Ti	0.080	0.078	0.074	0.114	0.104	0.082	0.151	0.082	0.071	0.071	0.137	0.155
Fe^{2+}	0.204	0.205	0.214	0.206	0.206	0.203	0.238	0.218	0.182	0.188	0.241	0.244
Mn	0.005	0.003	0.005	0.002	0.003	0.003	0.004	0.004	0.003	0.002	0.003	0.003
Mg	0.803	0.792	0.805	0.736	0.751	0.804	0.690	0.816	0.815	0.813	0.694	0.672
Ca	0.932	0.941	0.917	0.947	0.935	0.939	0.958	0.923	0.939	0.943	0.949	0.961
Na	0.026	0.033	0.025	0.039	0.048	0.031	0.044	0.030	0.027	0.027	0.040	0.038
K	0.001	-	0.005	0.000	0.001	0.001	0.001	0.002	0.000	-	-	0.000
Cr	0.006	0.001	0.003	0.010	0.011	0.010	0.008	0.007	0.006	0.006	0.000	0.008
Sum	4.030	4.033	4.037	4.040	4.041	4.044	4.054	4.049	4.028	4.032	4.045	4.054

Table C.3. Continued.

	Tsirub North (outer) plug											
	AN-005				AN-013						AN-015	
	p (core)	p (rim)	gm	gm	p	p	p	p	gm	gm	p(core)	p(rim)
SiO_2	46.46	44.95	48.03	46.25	47.79	49.31	49.02	47.66	48.38	48.32	48.19	43.06
TiO_2	3.57	4.08	2.90	3.52	2.90	2.40	2.56	3.15	2.90	2.78	2.64	5.10
Al_2O_3	5.53	7.14	4.37	5.35	4.51	3.64	3.97	4.84	4.32	4.16	4.77	8.63
Cr_2O_3	-	0.43	0.01	0.04	0.16	0.20	0.30	0.07	0.11	0.05	0.23	0.02
FeO	7.36	6.53	7.38	7.40	6.74	5.75	6.10	6.72	6.64	6.66	6.28	8.05
MnO	0.09	0.05	0.16	0.12	0.18	0.09	0.10	0.18	0.14	0.09	0.09	0.11
MgO	13.29	12.80	13.29	13.75	14.34	14.81	14.90	14.31	14.21	14.20	14.56	11.39
CaO	23.14	23.08	22.97	23.05	23.38	23.58	23.41	23.41	23.41	23.29	22.78	22.90
Na_2O	0.43	0.50	0.75	0.45	0.35	0.37	0.37	0.41	0.30	0.40	0.36	0.71
K_2O	0.00	0.02	0.02	0.01	-	0.00	0.00	-	0.01	0.00	0.09	0.02
Total	99.87	99.59	99.87	99.95	100.35	100.15	100.73	100.75	100.42	99.96	99.99	100.00
Wo	48.8	50.2	48.6	48.1	48.1	48.4	47.9	48.2	48.4	48.3	47.5	50.8
En	39.0	38.7	39.2	39.9	41.1	42.3	42.4	41.0	40.9	41.0	42.3	35.2
Fs	12.1	11.1	12.2	12.0	10.8	9.2	9.7	10.8	10.7	10.8	10.2	14.0
	Number of cations on the basis of 6 oxygens:											
Si	1.773	1.725	1.824	1.765	1.801	1.846	1.829	1.791	1.818	1.823	1.817	1.668
Al^{IV}	0.197	0.255	0.155	0.190	0.102	0.084	0.089	0.110	0.102	0.098	0.168	0.312
Al^{VI}	0.000	0.000	0.000	0.000	0.000	0.000	0.000	0.000	0.000	0.000	0.000	0.000
Ti	0.102	0.118	0.083	0.101	0.128	0.102	0.111	0.137	0.122	0.118	0.075	0.149
Fe^{2+}	0.235	0.210	0.234	0.236	0.212	0.180	0.190	0.211	0.209	0.210	0.198	0.261
Mn	0.003	0.002	0.005	0.004	0.006	0.003	0.003	0.006	0.004	0.003	0.003	0.004
Mg	0.756	0.732	0.752	0.782	0.806	0.827	0.829	0.802	0.796	0.799	0.819	0.658
Ca	0.946	0.949	0.934	0.942	0.944	0.946	0.936	0.943	0.943	0.942	0.920	0.950
Na	0.032	0.037	0.055	0.033	0.025	0.027	0.027	0.030	0.022	0.029	0.026	0.053
K	0.000	0.001	0.001	0.001	-	0.000	0.000	-	0.001	0.000	0.004	0.001
Cr	-	0.013	0.000	0.001	0.005	0.006	0.009	0.002	0.003	0.002	0.007	0.001
Sum	4.044	4.042	4.043	4.056	4.030	4.021	4.024	4.031	4.020	4.024	4.037	4.056

Table C.3. Continued.

	Tsirub North (outer) plug			
	AN-015			
	p(core)	p(rim)	gm	gm
SiO_2	46.53	43.94	52.04	52.86
TiO_2	3.14	4.85	1.57	1.23
Al_2O_3	6.12	7.76	1.59	0.94
Cr_2O_3	0.55	0.14	0.03	-
FeO	6.43	7.29	5.92	6.37
MnO	0.07	0.09	0.20	0.18
MgO	13.65	12.20	15.09	15.00
CaO	23.19	23.18	23.45	22.77
Na_2O	0.48	0.45	0.71	0.98
K_2O	0.00	0.01	0.02	0.02
Total	100.16	99.91	100.62	100.35
Wo	49.1	50.6	47.8	46.8
En	40.2	37.0	42.8	42.9
Fs	10.6	12.4	9.4	10.2
Si	1.766	1.692	1.926	1.957
Al^{IV}	0.216	0.279	0.054	0.043
Al^{VI}	0.000	0.000	0.000	0.000
Ti	0.090	0.140	0.044	0.026
Fe^{2+}	0.204	0.235	0.183	0.197
Mn	0.002	0.003	0.006	0.006
Mg	0.772	0.700	0.833	0.828
Ca	0.943	0.956	0.930	0.903
Na	0.035	0.034	0.051	0.070
K	0.000	0.001	0.001	0.001
Cr	0.016	0.004	0.001	-
Sum	4.046	4.044	4.029	4.031

Table C.3. Continued.

	Tsirub North (inner) plug					
	AN-007					
	p	p	p	gm	gm	gm
SiO_2	49.68	47.91	48.50	49.13	47.36	48.84
TiO_2	2.23	3.06	2.81	2.65	3.26	2.55
Al_2O_3	3.63	4.64	4.29	4.07	4.90	3.79
Cr_2O_3	0.28	0.11	0.21	0.24	0.04	0.28
FeO	5.46	6.94	6.05	6.21	7.23	5.84
MnO	0.13	0.11	0.13	0.13	0.10	0.07
MgO	15.29	14.08	14.72	14.89	13.97	14.97
CaO	23.56	23.52	23.48	23.30	23.20	23.32
Na_2O	0.31	0.41	0.39	0.33	0.44	0.39
K_2O	0.01	0.00	0.01	0.01	0.01	0.01
Total	100.58	100.78	100.59	100.96	100.51	100.06
Wo	48.0	48.5	48.2	47.7	48.1	47.9
En	43.3	40.4	42.1	42.4	40.3	42.8
Fs	8.7	11.2	9.7	9.9	11.7	9.4
Si	1.848	1.800	1.815	1.829	1.788	1.833
Al^{IV}	0.077	0.107	0.098	0.092	0.115	0.089
Al^{VI}	0.000	0.000	0.000	0.000	0.000	0.000
Ti	0.102	0.131	0.121	0.114	0.139	0.107
Fe^{2+}	0.170	0.218	0.189	0.193	0.228	0.183
Mn	0.004	0.003	0.004	0.004	0.003	0.002
Mg	0.848	0.789	0.821	0.827	0.786	0.838
Ca	0.939	0.947	0.942	0.929	0.938	0.938
Na	0.022	0.030	0.028	0.024	0.032	0.028
K	0.000	0.000	0.001	0.000	0.001	0.001
Cr	0.008	0.003	0.006	0.007	0.001	0.008
Sum	4.019	4.028	4.025	4.020	4.032	4.026

Table C.5. Major (in wt.%) and trace (in ppm) element analyses of the country rock (AN-002) intruded by Tsirub North plug. All Fe reported as Fe_2O_3; Mg# = atomic Mg/(Mg + Fe^{2+}) calculated assuming $Fe_2O_3/FeO = 0.2$. *Analysed by XRF.

XRF:	AN-002	ICP-MS:	AN-002		AN-002
SiO_2	68.8	Sc	2.03	Th	60.9
TiO_2	0.47	Ni	7.54	U	1.08
Al_2O_3	14.4	Cr	41.1	La	170
Fe_2O_3	2.69	Co	2.78	Ce	326
MnO	0.03	V	26.6	Pr	34.2
MgO	0.68	Cu	12.5	Nd	107
CaO	1.65	Zn	65.8	Sm	10.4
Na_2O	2.80	Rb	229	Eu	1.62
K_2O	6.62	Sr	203	Gd	4.18
P_2O_5	0.14	Ba	1474	Tb	0.35
H_2O-	0.114	Y	3.21	Dy	1.03
LOI	0.76	Zr	61.8	Ho	0.14
Total	99.23	Nb*	12	Er	0.27
		Hf	1.53	Tm	0.03
Mg#	0.37	Ta	0.47	Yb	0.14
		Pb	42.1	Lu	0.02